THE UNIVERSITY *of* EDINBURGH

Advanced sparse sampling techniques for accelerating structural and quantitative MRI

Arnold Julian Vinoj Benjamin

A thesis submitted for the degree of Doctor of Philosophy.
The University of Edinburgh.
3 July 2019

Abstract

Magnetic Resonance Imaging (MRI) has become a routine clinical procedure for the screening, diagnosis and treatment monitoring of various clinical conditions. Although MRI has highly desirable properties such as being completely non-ionizing and providing excellent soft tissue contrast which has resulted in its widespread usage across the gamut of clinical applications, it is limited by a slow data acquisition process. Several techniques have been developed over the years that have considerably improved the speed of MRI but there is still a clinical need to further accelerate MRI for many clinical applications. This thesis focuses on two recent advances in MRI acceleration to reduce the overall patient scan time.

The first part of the thesis describes the development of a fast 3D neuroimaging methodology that has been implemented in a clinical Magnetic Resonance (MR) sequence which was accelerated using a combination of compressed sensing and sampling order optimization of acquired measurements. This methodology reduced the overall scan time by more than 60% compared to the normal scan time while also producing images of acceptable quality for clinical diagnosis. The clinical utility of accelerated neuroimaging is demonstrated by conducting a healthy volunteer study on eight subjects using this fast 3D MRI method. The results of the radiological diagnostic quality assessments that were carried out on the accelerated human brain MR images by four experienced neuroradiologists are presented. The results show that accelerated MR neuroimaging retained sufficient clinical diagnostic value for certain clinical applications.

The second part of the thesis describes the development of an accelerated Cartesian sampling scheme for a rapid quantitative MR method called Magnetic Resonance Fingerprinting (MRF). This method was able to simultaneously generate quantitative multi-parametric maps such as T1, T2 and proton density (PD) maps in a very short scan duration that is clinically acceptable. The developed Cartesian sampling method using Echo Planar Imaging (EPI) is compared with conventional spiral sampling that is generally used for MR fingerprinting. The ability of novel iterative reconstruction techniques to improve the multi-parametric estimation accuracy is also demonstrated. The results show that accelerated Cartesian MR fingerprinting can be an alternative to conventional spiral MR fingerprinting.

Lay Summary

Magnetic Resonance Imaging (MRI) is a non-invasive medical imaging technique that is used to image the internal organs of the body. It provides excellent soft tissue contrast and does not use any radiations that are harmful to the body. Therefore, it has become a routine clinical procedure for the screening, diagnosis and treatment monitoring of various diseases. However, it is limited by a slow acquisition process which limits the imaging speed. As a result, MRI scans are slow, time consuming, reduces patient comfort and are expensive due to the costs involved in the maintenance of the equipment. This work aims to reduce the overall scan time for patients by accelerating MRI sequences that are clinically used. The acceleration is carried out by using advanced techniques in data acquisition and image reconstruction in order to produce images of clinically acceptable quality. This work has the potential to reduce the overall patient scan time considerably, improve patient comfort inside the scanner, reduce the wait time in hospitals due to faster scanning and can result in operational cost savings for hospitals and clinics.

Declaration of originality

I hereby declare that the research recorded in this thesis and the thesis itself was composed and originated entirely by myself in the Institute for Digital Communications, School of Engineering at The University of Edinburgh.

Arnold Julian Vinoj Benjamin

Acknowledgements

I would like to acknowledge the fact that it would not have been possible to submit my thesis had it not been for the support and guidance of many people during the course of my PhD degree.

First and foremost, I would like to thank both my supervisors, Prof. Ian Marshall and Prof. Mike Davies for giving me the opportunity to be a part of this research project. They have both played an active role in this project, have been instrumental throughout the various stages of its development, have given me the freedom to explore while also suggesting new directions for the future. I would like to thank them both for their great support, expert guidance and immense patience throughout my study. I strongly believe that their excellent insights led to the high standard of research that was carried out and it has helped me to become a better researcher.

I also give thanks to my examiners Dr Kieren Hollingsworth and Dr Lucy Kershaw for their time evaluating the thesis, and their useful feedback and critique, which has allowed me to significantly improve the quality of this thesis.

I would also like to thank Dr Grant Mair, one of my clinical collaborators who showed great interest in the project and was responsible for driving it forward among the other clinicians. I would also like to thank the other clinical collaborators: Dr Gerard Thompson, Dr Ana Casado and Dr Carol di Perri for performing radiological assessments and for providing feedback on the manuscripts in spite of their extremely busy schedules.

I would also like to thank Dr Mohammad Golbabaee who helped me immensely with the reconstructions and simulations for the MR fingerprinting work. I would also like to thank the other researchers in my group, Ms Wajiha Bano and Dr Zaid Mahbub for their help with the experiments. I would also like to thank the radiographers at Western General Hospital for helping me with the MRI scanning and also agreeing to be volunteers for some of my experiments.

I would like to thank the Marie-Sklodowska Curie programme for giving me an opportunity to undertake an industrial secondment in Munich, Germany and an academic secondment in Athens, Greece during my PhD. I would like to thank the funding agencies: European Commission, Engineering and Physical Sciences Research Council and Scottish Research Partnership for their financial support that helped me to carry out my experiments and attend several conferences and training events.

I would like to thank Dr Marion Menzel from GE Global Research, Munich for introducing me to Dr Pedro Gomez, who made feel welcome and helped me with the reconstructions and experiments while I was in Munich. I would also like to thank him for conducting additional experiments that were required as part of the article publication process. I also want to thank Dr. Sergios Theodoridis, Dr Eleftherios Kofidis, Mr Christos Chatzichristos and Mr Manuel Morante for hosting me in Athens for my academic secondment.

I would like to thank my parents, family members, relatives and friends for their unwavering support and emotional guidance during my difficult moments. Finally, I want to thank all the friends that I have made since I arrived in Edinburgh for helping me to have an active social life, spending time with me during good and bad moments and for preventing me from feeling homesick.

Contents

List of figures

List of tables

Acronyms and abbreviations

ACS	acquisition signals
BLIP	Bloch matching response recovery through iterated projection
bSSFP	balanced steady state free precession
BW	bandwidth
CNNs	convolutional neural networks
CS	compressed sensing
CSF	cerebrospinal fluid
CS-PI	compressed sensing-parallel imaging
DCE	dynamic contrast enhanced
DM	dictionary matching
EPI	echo planar imaging
EPI-MRF	echo planar imaging-magnetic resonance fingerprinting
EPG	extended phase graph
ESPIRiT	eigen value SPIRiT
ETS	echo time shifting
FID	free induction decay
FA	flip angle
FFT	fast Fourier Transform
fMRI	functional magnetic resonance imaging
FOV	field of view
FS	fully sampled
GE	general electric
GM	grey matter
GRAPPA	generalized autocalibrating partially parallel acquisition
GRE	gradient echo
IHT	iterative hard thresholding
IPA	iterative projection algorithm
IR	inversion recovery
IR-SE	inversion recovery spin echo

MDM	magnetic dipole moment
MF	matched filter
MR	magnetic resonance
MRF	magnetic resonance fingerprinting
MRI	magnetic resonance imaging
MS	multiple sclerosis
MRA	magnetic resonance angiography
NUFFT	non uniform fast Fourier Transform
PACS	picture archiving and communication system
PD	proton density
PE	phase encoding
PI	parallel imaging
PPI	partially parallel imaging
q-MRI	quantitative MRI
R	acceleration factor / reduction factor
RF	radio frequency
RS	radiological scores
SD	standard deviation
SENSE	sensitivity encoding
SE	spin echo / standard error
SMASH	simultaneous acquisition of spatial harmonics
SNR	signal to noise ratio
Spiral-MRF	spiral-magnetic resonance fingerprinting
SPIRiT	iterative self-consistent parallel imaging reconstruction from arbitrary k-space
SSFP	steady state free precession
SVD	singular value decomposition
T1w	T1 weighted
T2w	T2 weighted
TE	echo time
TI	inversion time
TR	repetition time
TV	total variation
WM	white matter
ZF	zero filled

Nomenclature

B_0	external magnetic field
B_1	magnetic field of RF pulse
ω_0	precession frequency of hydrogen protons / Larmor frequency (in radians)
ω_1	frequency of RF pulse (in radians)
γ	gyromagnetic ratio
α	flip angle
M_z	longitudinal magnetization
M_{xy}	transverse magnetization
M_0	magnetization at thermal equilibrium
$T1$	longitudinal relaxation constant
$T2$	transverse relaxation constant
$T2^*$	transerverse relaxation constant with magnetic field inhomogeneities
Φ	undersampled Fourier operator weighted by coil sensitivities
Ψ	sparsifying operator
$\hat{X}$	estimated image
λ	regularization parameter
μ	step size
A	forward operator
A^H	backward / adjoint operator

Chapter 1
Introduction

1.1 Project Motivation and Scope

MRI is one of the most popular medical imaging modalities today [1, 2]. It is used in a wide range of clinical applications such as the diagnosis of tumours, neuro-degenerative diseases, stroke, epilepsy, muscular abnormalities and several others. It is also used for imaging various organs such as the brain, heart, neck, spine, knee, body, prostate etc. According to the statistics published by NHS England [3], more than 3 million MR scans were carried out in the UK alone in 2017. This figure is likely to increase further because of the ever-increasing range of emerging clinical MR applications (e.g. lymphangiography, opthalmology, etc.). The wide range of applications have made MRI a routine clinical procedure in hospitals and clinics where it has become indispensible.

MRI has two key advantages over other medical imaging modalities. It can provide excellent soft tissue contrast which is very difficult to achieve in other medical imaging techniques. In addition, MRI does not use ionizing radiations like X-ray or CT which makes it safer than other medical imaging methods. In spite of these advantages, MRI is significantly limited by its slow data acquisition process. The inherently long relaxation times of tissues in the body coupled with line-by-line data acquisition as a result of how spatial encoding is carried out in MRI lead to the following consequences: i) very long scan times (i.e. scan times can last upto 90 minutes) ii) reduced patient comfort due to the long scanning process iii) inability to acquire sufficient data within a time period in order to generate images or quantitative maps of acceptable quality (e.g. collecting sufficient data within a breath-hold, generating multi-parametric quantitative maps) iv) difficulty for patients to remain still or motionless within the MR scanner during the entire scanning process due to the high susceptibility of MRI to motion artefacts that reduce the image quality v) increase in the MR scanner operational cost in hospitals and clinics due to the long patient scan times and vi) becomes very expensive for patients especially those who live in countries where access to health care is costly since it is not provided by the government.

Several fast MRI sequences have been developed over the years to overcome some of the limi-

tations of the slow imaging speed. Conventionally, the speed of MRI data acquisition is usually enhanced by parallel imaging (PI) techniques that make use of spatial information from multiple receiver coils to reconstruct alias free images from accelerated acquisitions [4–7]. As a result, interest has grown in the undersampling of the acquired raw data for fast MRI. For example, a variety of subsampling patterns and PI reconstruction methods have been used to accelerate MRI data acquisition in organs such as the brain [8, 9] and the heart [10, 11]. Although some of these parallel imaging techniques are widely implemented in modern MRI scanners [5, 6], the increased speed comes at the expense of degradation in signal to noise ratio (SNR). Therefore, the degree of acceleration that can be applied to images acquired for clinical diagnosis is limited.

Recently however, compressed sensing (CS) [12] has emerged as a general framework for faster data acquisition that is widely applicable to many types of data including MR images. The basic premise is that images are in some way sparse and can, under certain circumstances be reconstructed from far fewer measurements than would be expected conventionally. CS can be used to reduce acquisition times for many types of MR examinations such as 3D structural imaging, dynamic 2D and 3D imaging since subsampling can be performed in more than one dimension leading to significant reduction in acquisition time. When used in conjunction with PI methods (i.e. CS-PI) [13, 14], further acceleration is possible with significantly less reduction in SNR when compared to conventional PI methods. CS-PI methods combine the data redundancy from multiple receiver coils with the transform sparsity of MR images and the spatial incoherence achieved by random subsampling to reconstruct alias free images with higher SNR thereby allowing for more acceleration to be applied to the acquisition without further compromising the diagnostic image quality.

The major goal of this work is to improve the imaging speed in MRI by using a combination of compressed sensing, parallel imaging and sparse sampling methods. Another objective is to implement prospective accelerated scanning in a clinical sequence and to show that accelerated neuroimaging has clinical diagnostic value. In this work, novel MR acceleration techniques have been applied to both structural and quantitative MRI. The results have been validated in phantoms and healthy volunteers in vivo.

1.2 Main Contributions

This thesis proposes advanced sparse sampling schemes for accelerating structural and quantitative MRI. The major contributions of this work are:

1. Application of CS-PI reconstruction technique on 3D structural Brain MR data for reducing scan time. By simulating undersampling retrospectively, optimization of acquisition and reconstruction parameters such as subsampling pattern, calibration size, acceleration factor and amount of regularization was carried out to improve the image quality of CS-PI reconstructions.

2. Implementation of accelerated prospective MR scanning in a clinical MR sequence by utilizing the optimized acquisition and reconstruction parameters that were obtained from retrospective simulations of undersampling.

3. Identification of the importance of sampling order optimization especially in IR-prepared sequences and the development of k-space acquisition order optimized subsampling patterns to preserve contrast in prospective accelerated 3D neuroimaging.

4. Evaluation of the clinical diagnostic utility of CS-PI accelerated neuroimaging through radiological assessment of accelerated brain datasets. The major factor that affected the radiological scoring was also identified.

5. Development of an accelerated Cartesian MR fingerprinting scheme based on multi-shot EPI and showing that it can be an alternative to conventional spiral MR fingerprinting.

6. The implementation of iterative reconstruction algorithms for improving the accuracy of estimated multi-parametric maps in MR fingerprinting.

1.2.1 Project Output

1.2.1.1 Journal Articles

1. A. J. V. Benjamin, P. A. Gómez, M. Golbabaee, Z. Mahbub, T. Sprenger, M. I. Menzel, M. Davies, and I. Marshall, "Multi-shot Echo Planar Imaging for accelerated Cartesian MR Fingerprinting: An alternative to conventional spiral MR Fingerprinting", *Magnetic resonance imaging*, vol. 61, pp. 20-32, 2019.

2. E. Ozturk-Isik, I. Marshall, P. Filipiak, A. J. Benjamin, V. G. Ones, R. O. Ramón, and M.

d. C. Valdés Hernández, "Workshop on reconstruction schemes for magnetic resonance data: summary of findings and recommendations", *R Soc open sci*, vol. 4, no. 2, 2017.

1.2.1.2 Conference Proceedings

1. A. J. V. Benjamin, W. Bano, G. Mair, G. Thompson, M. Davies, and I. Marshall, "The clinical condition to be assessed by radiological assessment significantly influences the radiological scores of compressed sensing accelerated 3D brain MRI", in *Proc Intl Soc Mag Reson Med*, #2992, 2019.

2. A. J. V. Benjamin, P. Gómez, M. Golbabaee, Z. Mahbub, T. Sprenger, M. I. Menzel,M. Davies, and I. Marshall, "Balanced multi-shot EPI for accelerated cartesian MR fingerprinting: An alternative to spiral MR fingerprinting, in *Proc Intl Soc Mag Reson Med*, #4265, 2018.

3. A. J. V. Benjamin, W. Bano, G. Mair, M. Davies, and I. Marshall, "Sampling order optimization preserves contrast and improves clinical diagnostic utility of accelerated prospective 3D brain MRI: a radiological assessment study on healthy volunteers", in *Proc Intl Soc Mag Reson Med*, #3189, 2018.

4. A. J. V. Benjamin, W. Bano, M. Davies, and I. Marshall, "Sampling Order Optimization for contrast preservation in accelerated prospective 3D MRI", in *Proc Eur Soc Mag Res Med Biol*, #463, 2017

1.3 Thesis Organization

The Background material for this research work is provided in Chapter 2. This includes introduction to MR Physics that explains the processes involved in the acquisition of an MR image, the k-space domain and basic MR pulse sequences. This is followed by an overview about the various techniques that have been used for accelerating MRI in order to reduce the overall patient scan time. The chapter ends with the description of some advanced reconstruction methods that are used extensively in this work.

In Chapter 3, an MRI reconstruction method which is based on a combination of compressed sensing and parallel imaging is applied to clinical 3D brain data. Undersampling is simulated and reconstruction parameters are optimized to improve the image quality. The optimized pa-

rameters are subsequently used to implement accelerated scanning on a clinical MR scanner at reduced scan times. Further optimization is carried out to preserve the contrast in the accelerated images.

In Chapter 4, a healthy volunteer study is conducted to test the clinical diagnostic efficacy of accelerated neuroimaging. Experienced neuro-radiologists were asked to evaluate the accelerated images for image quality and artefacts. The major factor that affected the radiological scoring was identified. The clinical value of accelerated neuroimaging was ascertained through the radiological assessments.

In Chapter 5, a novel Cartesian sampling scheme based on multi-shot Echo Planar Imaging is developed for performing rapid quantitative MRI. This method is a variant of the fast MR Fingerprinting method that can generate accurate quantitative multi-parametric maps in a clinically feasible scan time. The performance of the accelerated Cartesian sampling scheme is compared with the conventional spiral sampling scheme. The use of advanced iterative reconstruction methods to improve the accuracy of estimated quantitative maps is also discussed and implemented on phantom and healthy volunteers.

In Chapter 6, the major conclusions of this research work are summarized. Some preliminary work and other ideas for future work are also provided.

Chapter 2
Background

2.1 The need for accelerating MRI

Magnetic Resonance Imaging (MRI) is currently a well-established medical imaging technique that is widely used for the screening, diagnosis and treatment of diseases in various clinical applications like neurology, cardiology, cancer diagnosis and detection of soft tissue abnormalities. However, the performance of MRI is characterized by a slow data acquisition process which limits the imaging speed and makes it susceptible to various types of artefacts that appear in the reconstructed image [15]. Therefore, accelerating MRI is an essential part of MRI research and it has led to the development of various techniques to speed up MRI data acquisition. Besides, a typical MRI examination should be able to address issues such as clinical time constraints (i.e. maximum permissible time inside an MRI scanner, fast image reconstruction) and local motion (i.e. due to breathing, beating heart) as a result of the long data acquisition process. These practical difficulties highlight the clinical need for accelerated MRI data acquisition.

2.2 MRI Physics

MRI is a medical imaging technique that utilizes the abundance of water and fat molecules in the human body to produce detailed images of various internal organs and tissues within the body. Magnetic Resonance is fundamentally a quantum mechanics phenomenon which depends on the spins of the hydrogen protons in the body. It is based on the fact that spinning charged particles such as hydrogen atoms (or protons) present in the body generate an electromagnetic field and behave like magnetic dipoles [16]. A magnetic dipole is characterized by two parameters, (i.e.) strength or amplitude of magnetic field and orientation or phase and it is represented by the vector quantity magnetic dipole moment (μ). In equilibrium, the magnetic dipole moments (MDMs) of individual hydrogen protons are distributed in various orientations in space and therefore, the net magnetization (M_0) is zero. However, when placed in an external magnetic field, the MDMs orient themselves either in the direction of the external magnetic

field (spin-up direction) or in the direction opposite to the external magnetic field (spin-down direction). However, the number of MDM's that orient themselves in the spin-up direction is more than the MDM's in the spin-down direction resulting in a net magnetization called longitudinal magnetization along the direction of the external magnetic field (usually z direction). In addition, each hydrogen proton also experiences a turning force or torque when subjected to a strong external magnetic field which causes it to precess or wobble around the external magnetic field [17]. It is analogous to the motion of a spinning top that rotates around its vertical axis due to the torque generated by its angular momentum. This movement is called Larmor precession and the precession frequency is called Larmor frequency. It is proportional to the external magnetic field given by the Larmor equation

$$\omega_0 = \gamma B_0$$

where γ is a constant called gyromagnetic ratio and is equal to 42.57 MHz T^{-1} for a hydrogen nucleus or proton, ω_0 is the angular frequency $(2\pi f)$ and B_0 is the external magnetic field.

2.3 Resonance

When an electromagnetic radiation like an RF pulse of frequency ω_1 is transmitted perpendicular to the direction of an external magnetic field into a system of hydrogen protons that are already precessing about an external magnetic field B_0, it would cause the protons to simultaneously precess about the new magnetic field B_1 (associated with the RF pulse) according to the Larmor equation

$$\omega_1 = \gamma B_1$$

where ω_1 is the frequency of the RF pulse and B_1 is the magnetic field associated with the RF pulse. Therefore the RF pulse acts as a stimulus that causes the system to precess simultaneously about the magnetic fields B_0 and B_1. But if $B_1 << B_0$; this effect is negligible and it cannot be visualized. However, if the frequency of the RF pulse matches the frequency of precession of the protons, *i.e. if* $\omega_1 = \omega_0$ *(Larmor frequency)*, resonance occurs [18]. Resonance results in the RF pulse adding energy to the protons and causes the flipping of the net magnetization vector (i.e. longitudinal magnetization) from the z direction towards the x-y plane [18]. When viewed from the stationary point of reference (i.e. x-y-z coordinate system), the observer would witness a rapid precession around the z-axis that spirals down to the x-y plane. This motion is the result two precessional motions happenning simultaneously due to the B_0 and B_1 fields and is called nutation [18]. However, when viewed from a rotating frame of reference

where the observer is rotating at the same frequency as the external magnetic field B_0, the flipping of longitudinal magnetization will resemble a simple arc as shown in Figure 2.1 and the resulting magnetization in the x-y plane is called transverse magnetization. The strength of the RF pulse (B_1) and its duration (τ) control the flip angle (α) which can be determined by the following equation

$$\alpha = \gamma B_1 \tau$$

By using an RF pulse of appropriate duration and amplitude, the longitudinal magnetization can be completely flipped to the x-y plane. This is called 90° RF pulse which results in maximum transverse magnetization and zero longitudinal magnetization shown in Figure 2.1.

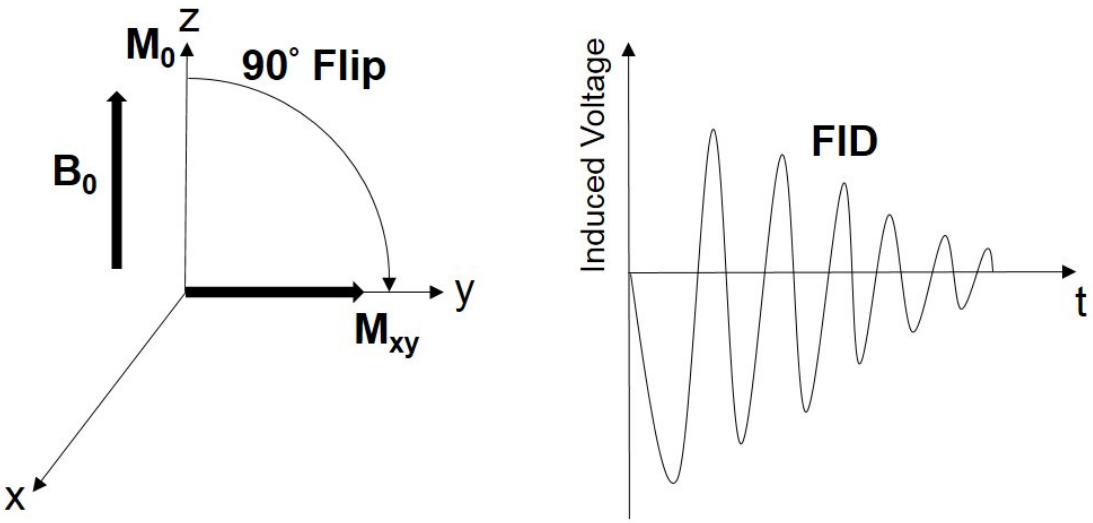

Figure 2.1: Left: *The effect of the 90° RF pulse that flips the entire longitudinal magnetization (M_z) into the transverse plane (M_{xy}).* ***Right:*** *The signal decay that is detected by the RF receiver coil from the transverse component of magnetization (M_{xy}). This signal decay is called Free Induction decay (FID).*

The flipping of longitudinal magnetization into transverse magnetization is only momentary since the transverse magnetization begins to decay after the application of the RF pulse due to the dephasing of protons in the transverse plane. The dephasing of protons occurs due to magnetic field inhomogeneities and spin-spin interactions between protons which follows an exponential decay curve and is called T2* relaxation. The dephasing of transverse magnetization due to magnetic field inhomogeneities is reversible and is usually done by applying a

180° RF pulse which rephases the transverse magnetization. After the application of a 180° RF pulse, the exponential decay of transverse magnetization occurs only due to spin-spin interactions between protons and is called transverse or T2 relaxation. The T2* decay is always shorter than T2 decay. Concurrently, the longitudinal magnetization begins to regrow and reaches its maximum value M_0 after some time [19]. This follows an exponential recovery curve and is called longitudinal (or) T1 relaxation. However, it should be noted that the longitudinal and transverse relaxation times are independent processes governed by different time constants T1 and T2 as shown in Figure 2.2. The exponential T2 decay time is usually not equal to the exponential T1 recovery time for most cases (e.g. T1 and T2 vary for different tissues, T1 is usually 5 to 10 times longer than T2 for tissues and fluids have high T1 and T2 values). The energy absorbed during resonance is released during relaxation and is detected by the RF receiver coil. The detected signal decays over time due to the dephasing of protons and is called free induction decay (FID) or echo shown in Figure 2.1. In other words, this signal is the MR signal that is detected by the receiver.

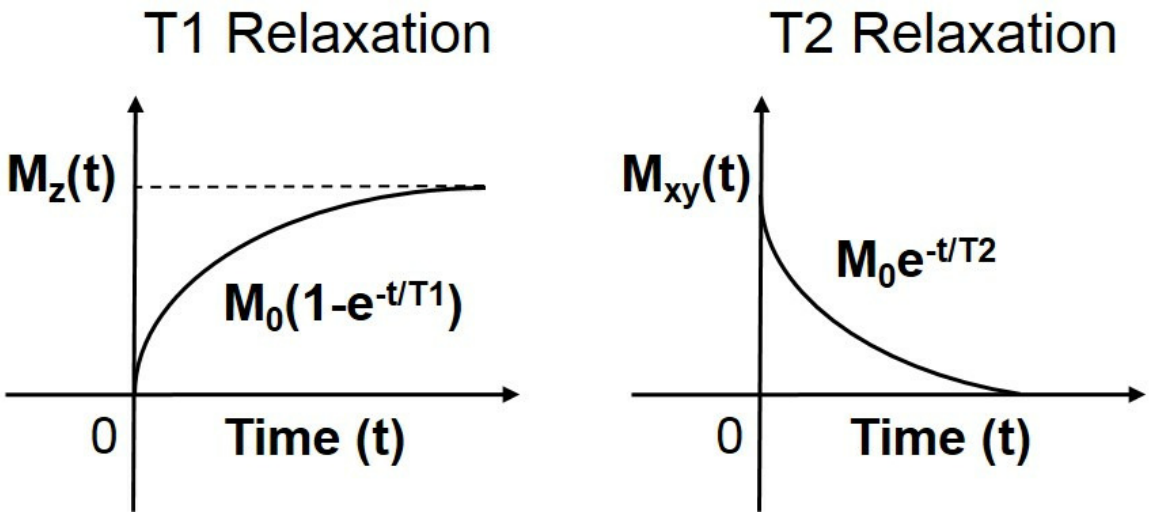

Figure 2.2: Left: *The graph of longitudinal magnetization* $(M_z(t)$ *recovery (i.e. T1 relaxation) with recovery rate governed by T1 time constant.* ***Right:*** *The graph of transverse magnetization* $(M_{xy}(t)$ *decay (i.e. T2 relaxation) with decay rate governed by T2 time constant*

2.4 Bloch Equations

Felix Bloch introduced the concept of relaxation time constants T1 and T2 and formulated equations for magnetization that accounted for T1 and T2 effects [20]. It was assumed that T1

and T2 followed first order kinetics and that single time constants were sufficient to describe this process according to the simplified Bloch equations [20] after a 90° RF pulse:

$$M_x(t) = M_0\, exp^{-t/T2} sin\omega_0 t$$

$$M_y(t) = M_0\, exp^{-t/T2} cos\omega_0 t$$

$$M_z(t) = M_0\,(1 - exp^{-t/T1})$$

where $M_x(t)$ and $M_y(t)$ are transverse magnetization components, $M_z(t)$ is the longitudinal magnetization component, M_0 is the magnetization at thermal equilibrium, T1 is longitudinal relaxation time constant and T2 is the transverse relaxation time constant. These equations predict that the net magnetization M will exhibit a spiraling precession around the external magnetic field B at the Larmor frequency with decay of transverse components back to zero and regrowth of the longitudinal component to its original maximum value M_0.

2.5 Spatial Encoding

The FID signal detected by the receiver has no spatial information about the location of the spins. This signal comes from the entire object being imaged. In order to localize the spins, the RF pulses and the external magnetic field have to be manipulated. Recall that RF pulse has to match the Larmor frequency of the precessing hydrogen protons to cause resonance and produce an FID signal. The protons whose Larmor frequencies are different from the frequency of the RF pulses will not produce any signal in the detector. This allows selective excitation at different locations. The Larmor frequency is proportional to the strength of the static magnetic field. A magnetic field gradient can be applied to induce a linear variation in the static magnetic field along the spatial direction in which the gradient is applied. This would cause the protons to have different Larmor frequencies along the specific spatial direction. This process is called spatial encoding. Spatial encoding is performed on all three directions using the G_x, G_y and G_z gradients to localize the three spatial directions.

Generally an RF pulse with a small frequency bandwidth is used to excite one slice of the object being imaged. The slice thickness is determined by the bandwidth of the RF pulse. The gradient (conventionally G_z) is turned on concurrently with the RF pulse to cause a linear spatial magnetic field variation along the z direction. The protons along the z direction will

now have different Larmor frequencies that would match with the different frequencies in the RF pulse resulting in an FID signal. As a result a slice at a particular z position is excited. Therefore, G_z is usually referred to as the slice-selection gradient. After the entire slice is excited, the gradient G_x is turned on which will cause the protons from the entire excited slice to precess at different frequencies along the x direction. This is called the readout gradient and the process is called frequency encoding. In the Fourier domain, signals with different spatial frequencies can be separated. Since the MRI signal is complex (i.e. it consists of both amplitude and phase); the phase in the MRI signal can be used for spatial encoding in the third direction. The G_y pulse is usually switched on just after the RF pulse and before the G_x gradient to introduce a linear phase shift that determines the spatial y position. Depending on the strength of the G_y pulse, only the protons having a specific Larmor frequency at a particular y position will match with one of the frequencies in the RF pulse. Therefore, the signals from this spatial y location will be read out along the x direction when the readout gradient G_x is switched on. This process is called phase encoding. The phase encoding must be repeated multiple times by varying the strength of the G_y gradient to read out signals from different points along the y direction. The speed of the data acquisition is therefore highly dependent on the number of phase encoding steps. The phase encoding process is time consuming and is directly responsible for the slow data acquisition process in MRI.

2.6 k-space

K-space is the spatial frequency domain or Fourier domain in which MRI data is acquired. It is defined as the space covered by the frequency encoding and phase encoding data. In a conventional 2D MR image, there is one frequency encoding direction (k_x) and one phase encoding direction (k_y). In 3D MRI, the frequency encoding direction is the same as 2D MRI but there are two phase encoding directions (k_y and k_z). The k-space represents the spatial frequency information in two or three dimensions of an object [21]. The relationship between the k-space and the desired image is the Fourier transformation. There is a one-to-one relationship between frequency encoding and x-position and between phase encoding gradient strength and y-position [18]. This relationship exists because the linear gradient in the x direction correlates sequential frequency increments with position; likewise, the linear gradient in the y direction correlates sequential phase gradient increments with position in the y direction [18].

K-space (i.e. original raw data) of a 2D brain MRI is shown in Figure 2.3. Each point in k-space contributes to all the pixels in the MR image. There is absolutely no direct relationship between the center of k-space and the center of the image. Likewise, there is no direct relationship between the edges of k-space and the edges of the image. The individual points (k_x, k_y) in k-space do not correspond one-to-one with individual pixels (x, y) in the image [22]. Each k-space point contains spatial frequency and phase information about every pixel in the final image. The centre of k-space contains low spatial frequency information, determining overall image contrast, brightness, and general shapes. The periphery of k-space contains information about the *fineness* of the image that includes edges, sharp transitions and fine details of the image.

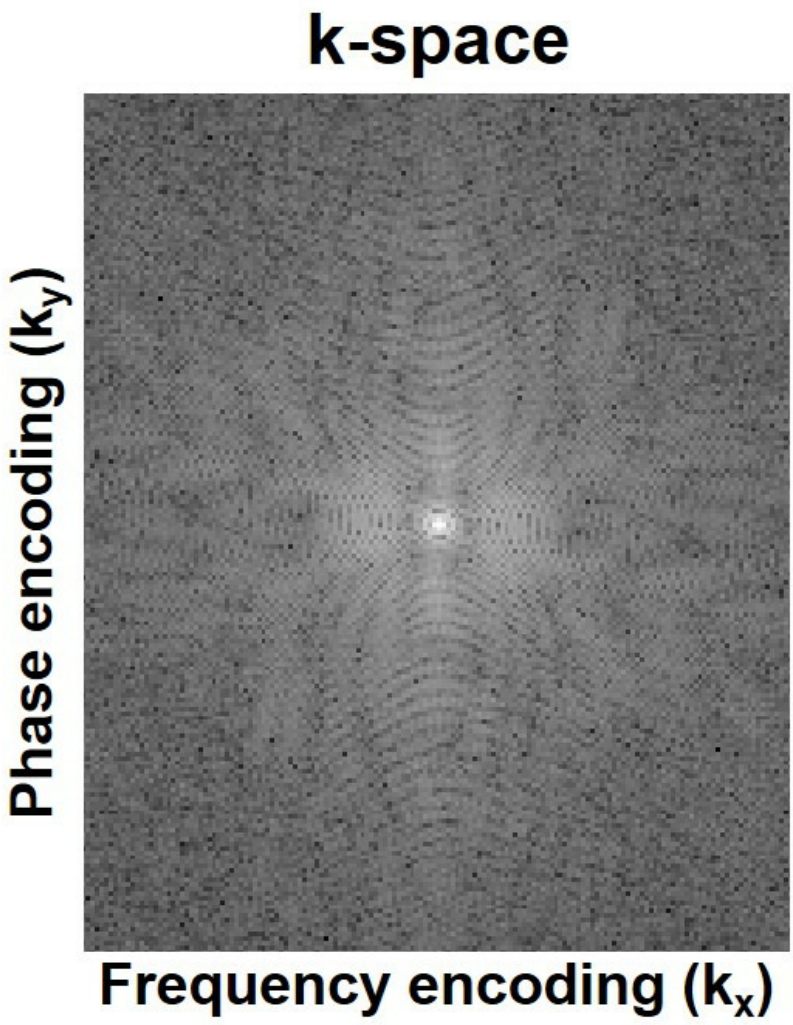

Figure 2.3: *The k-space (i.e. original raw data) of a 2D brain MRI*

Figure 2.4 shows the same 2D MR brain image reconstructed using full k-space, only using the central k-space and only using the k-space periphery. The images that are reconstructed using only the central k-space will contain the general shape of the image but the edges and sharp interfaces in the image will be coarse as shown in Figure 2.4 (middle). In contrast, images constructed using k-space periphery will only contain information about fine structures and edges which can been seen from Figure 2.4 (bottom).

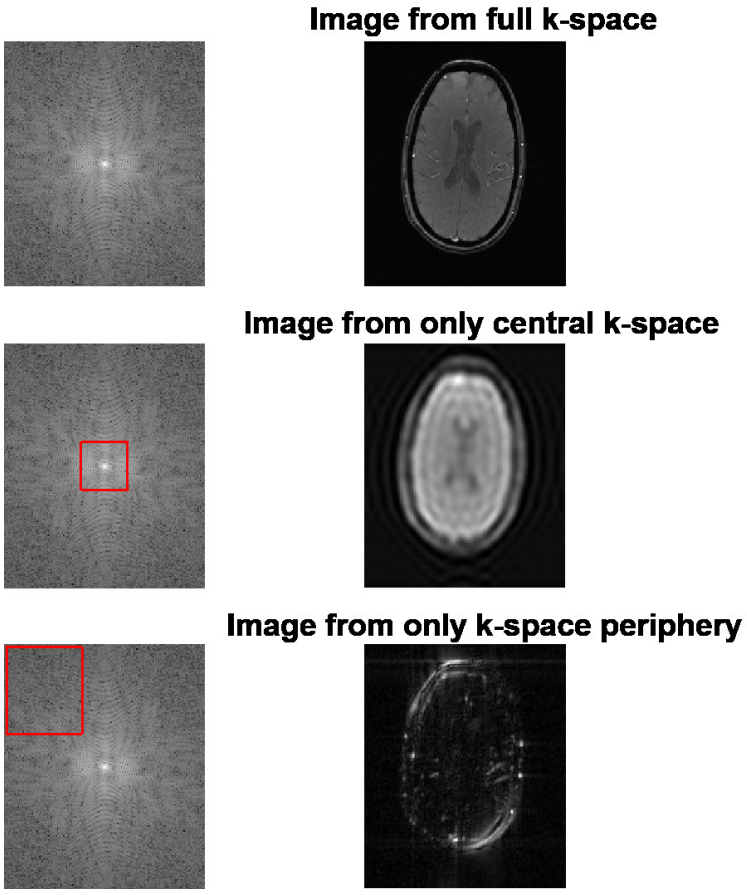

Figure 2.4: *Figure showing a 2D brain MR image reconstructed from full k-space (top), only central k-space(middle) and only k-space periphery (bottom)*

A complete coverage of the k-space will produce a fully sampled image whose resolution is determined by the number of acquired k-space lines. The route or path in which the k-space is traversed during data acquisition is called k-space trajectory. The most commonly used k-space trajectory is the Cartesian trajectory. The examples shown in Figure 2.3 and 2.4 are sampled on a Cartesian grid. The images can be obtained by directly applying a discrete Fourier transformation to the acquired k-space data. Other arbitrary k-space trajectories such as radial, spiral and

random trajectories have been proposed [12, 23] which are now being used more frequently. These arbritrary k-space trajectories require re-gridding of the samples onto a Cartesian grid before applying a Fourier transform in order to obtain the image.

2.7 MRI Pulse sequences

An MRI pulse sequence is a programmed set of changing RF pulses and magnetic gradients to control the data acquisition. The pulse sequence defines the type of k-space trajectory and the order in which the k-space samples are acquired which in turn would affect the image resolution, contrast, SNR and image artefacts. The pulse sequence also allows the manipulation of two important parameters that control the image contrast, namely repetition time (TR) and echo time (TE). TR is defined as the time between two successive excitation RF pulses. TE is defined as the time between the application of an excitation RF pulse and the peak signal induced in the receiver coil. Both TR and TE play an important role in the estimation of relaxation time constants T1 and T2. The overall scan duration is also controlled by these parameters.

The two basic pulse sequences commonly used in MRI are the spin echo sequence and gradient echo sequence. All other pulse sequences are derived from these two basic pulse sequences. The pulse sequences that were used for acceleration in chapters 3, 4 and 5 are based on the gradient echo sequence.

2.7.1 Spin Echo Sequence

The spin echo sequence (SE) is shown in Figure 2.5. It usually starts with a 90° RF pulse that tips the magnetization M_z to the transverse plane M_{xy}. The protons begin to dephase after the application of the 90° RF pulse. G_x, G_y and G_z are applied at the appropriate time as explained in Section 2.5. The only difference is that an additional 180° RF pulse is applied between the 90° pulse and the readout gradient G_x. This pulse flips M_{xy} to the opposite side in the transverse plane. As a result, the protons begin to rephase due to the flipping of magnetization in the opposite direction. The phase difference will be reduced to zero and a strong signal will appear at the echo time (TE). This signal is called the echo and the 180° RF pulse is called the refocusing pulse because it refocuses the protons. The application of the 180° RF pulse will rephase the magnetization decay caused by the magnetic field inhomogeneities and therefore

will make the tissue relax only according to the T2 relaxation time constant. After the echo time, the protons begin to dephase again. The process is repeated every repetition time (TR). TR is the time between successive 90° RF pulses.

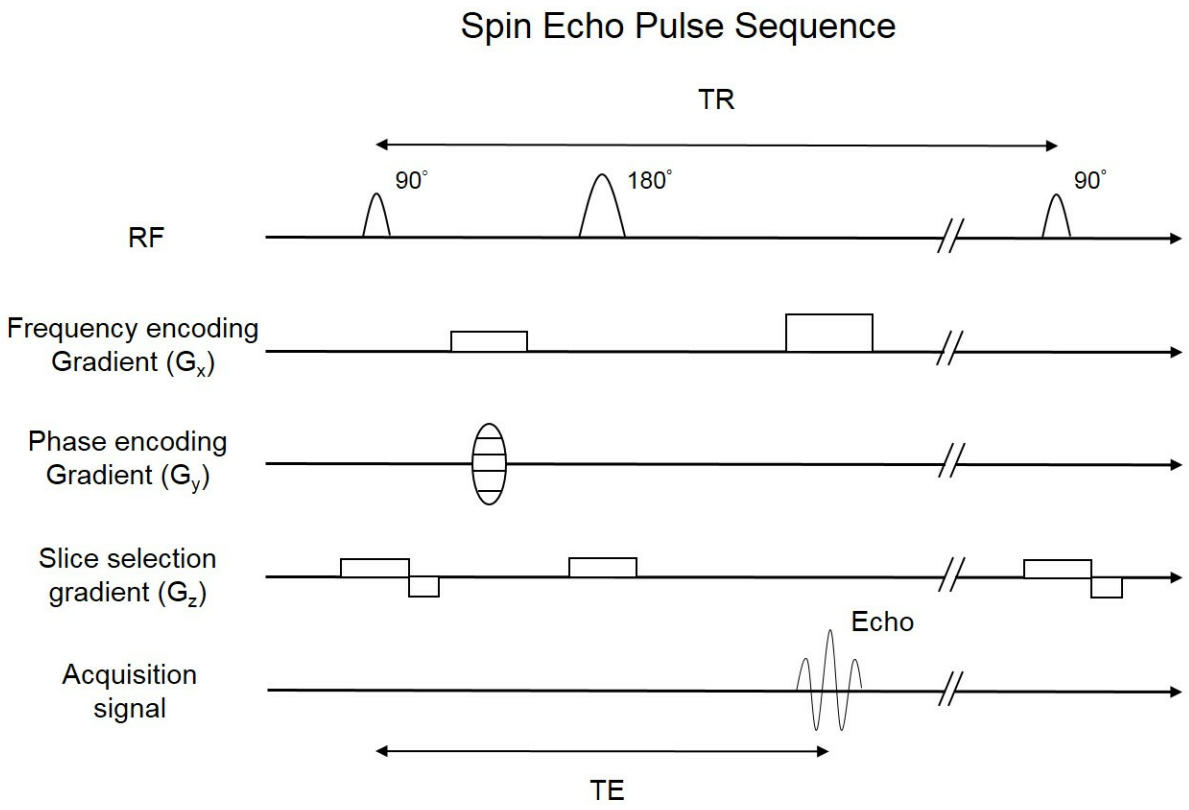

Figure 2.5: *Schematic diagram of the Spin Echo sequence.*

2.7.2 Gradient Echo Sequence

The gradient echo sequence (GRE) is shown in Figure 2.6. The GRE sequence uses gradients to dephase and rephase instead of using 180° refocusing pulses. In the absence of refocusing pulses, the transverse relaxation is also governed by local field inhomogeneities rather than just T2 relaxation. This relaxation is always shorter than T2 and is called $T2^*$ decay. Therefore, the GRE sequence is more sensitive to local field inhomogeneities than the SE sequence. However, the GRE sequence is faster (i.e. shorter TR and TE can be used) than SE due to absence of refocusing pulses. If the TR is short and if a 90° RF pulse is used, the longitudinal magnetization M_z may not be fully restored before the next 90° excitation pulse. So, the flip angles used in GRE sequences are usually smaller (i.e. between 10° to 60°) to restore M_z in a shorter

duration.

Note: In general, for GRE sequences, the transverse relaxation is due to $T2^*$ decay and not T2 as described above. However, if a series of rapid RF pulses are applied at very short TRs (i.e. $TR \ll T2^*$), there is no time for the transverse magnetization to decay completely before the next excitation. Stimulated echoes are generated due to the interaction between different RF pulses which results in T2 decay [24]. This is the reason for T2 weighting in Chapter 5 even though the sequence used is a GRE sequence.

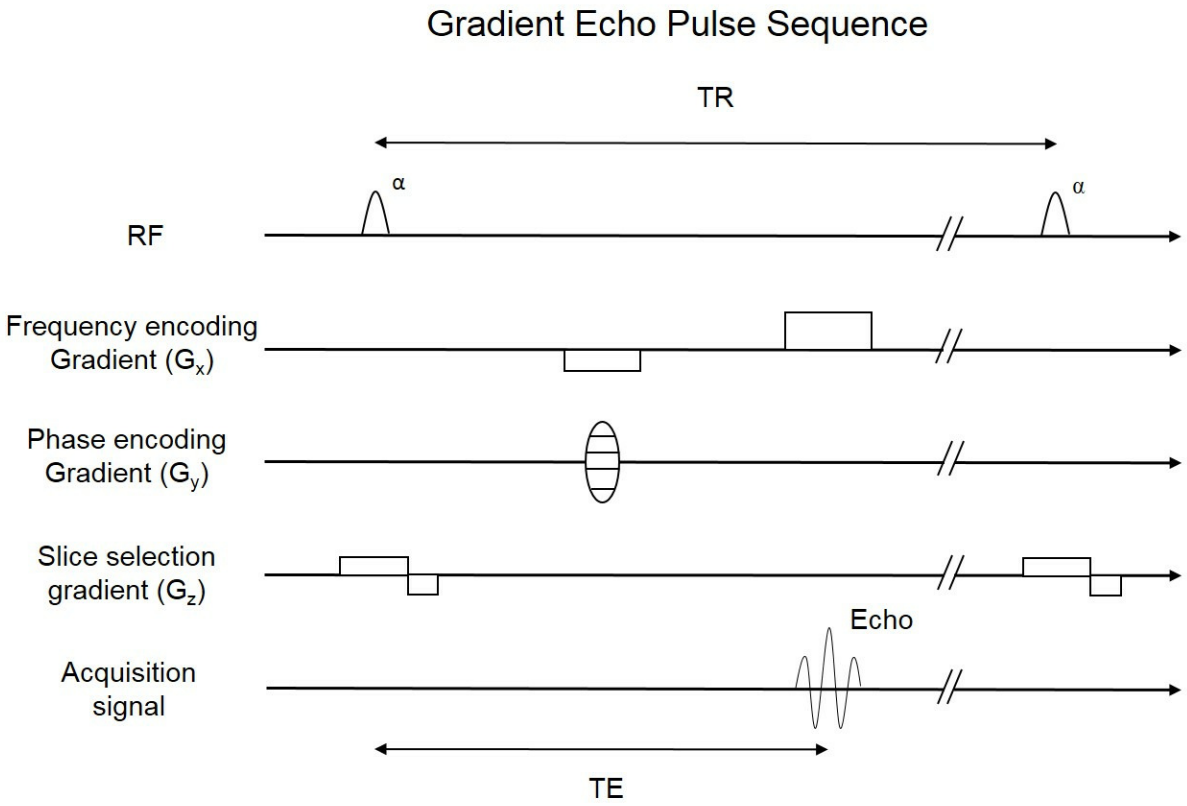

Figure 2.6: *Schematic diagram of the Gradient Echo sequence.*

2.8 Tissue Contrast in MRI

The tissue contrast in MRI is governed by the density of protons and the relaxation time constants T1 and T2 of various tissues in the human body. The MR signal is stronger if there is higher proton density because of the higher net magnetization. Since soft tissues and blood have greater proton density than bones, MRI is able to provide excellent soft tissue contrast.

Soft tissues such as gray matter (GM) and white matter (WM) in the brain have different T1 and T2 values and the variation in the values of relaxation time constants is exploited to provide contrast in an MR image. The T1 and T2 contrast can be modified by manipulating the TR and TE which is illustrated in Figure 2.7.

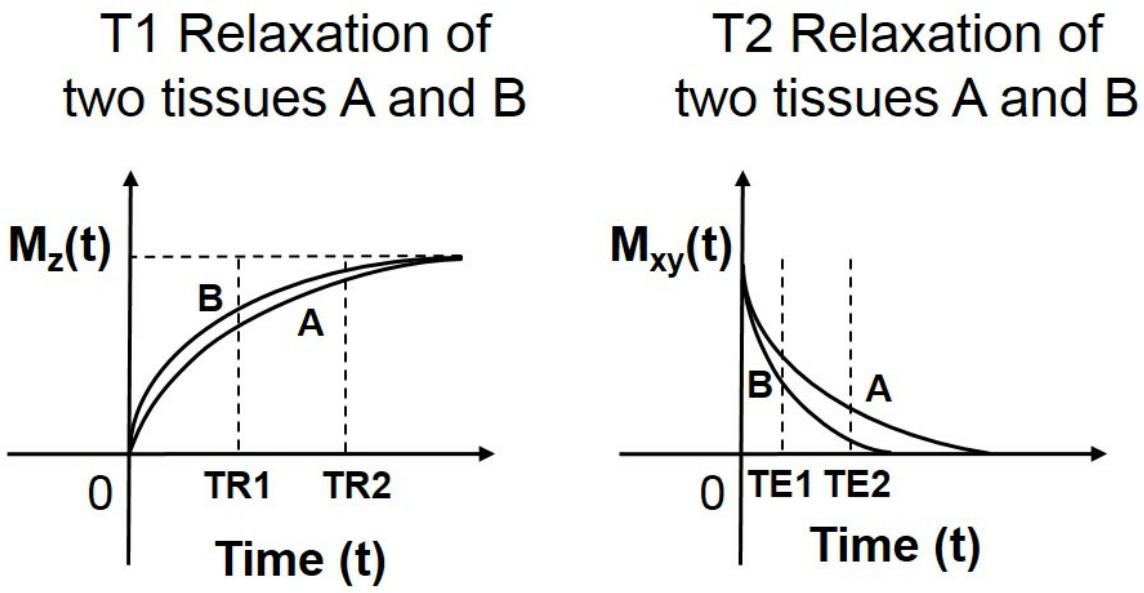

Figure 2.7: Left: *Figure showing that the T1 contrast variation between two tissues (A and B) having different T1 relaxation time constants can be modified by changing repetition time (TR).* ***Right:*** *Figure showing that the T2 contrast between two tissues (A and B) having different T2 relaxation time constants can be modified by changing Echo Time (TE).*

The T1 contrast becomes negligible when the TR is very long, i.e. four or five times of T1. In contrast, The T1 contrast is enhanced when a shorter TR is used as shown in Figure 2.7 (left). Therefore, the TR is chosen such that it is neither too short nor too long to achieve optimum contrast (typically close to the T1 of the tissue being imaged). In a similar way, the T2 contrast is enhanced at longer TE and diminished at shorter TE. Therefore, by choosing different TRs and TEs, images with varying T1 and T2 weighting can be obtained.

2.8.1 T1 weighted and T2 weighted images

MRI allows the user to have a certain degree of control over the image contrast through the manipulation of TR and TE settings during scanning. Figure 2.8 shows a 2D slice of a healthy volunteer brain imaged using different TR and TE settings that maximize either T1 or T2 contrasts to produce T1 weighted (T1w) and T2 weighted (T2w) images. T1 weighted images are obtained by using short TRs and short TEs while T2 weighted images are obtained by using long TRs and long TEs. In T1 weighted images, the CSF which has a high T1 value takes the longest to recover compared to WM and GM. Therefore it appears dark in the image. The GM recovers slower than WM which makes WM brighter than GM in a T1 weighted image. In T2 weighted images, the CSF signal takes the longest to dephase or decay compared to WM and GM and therefore, appears bright in a T2w image.

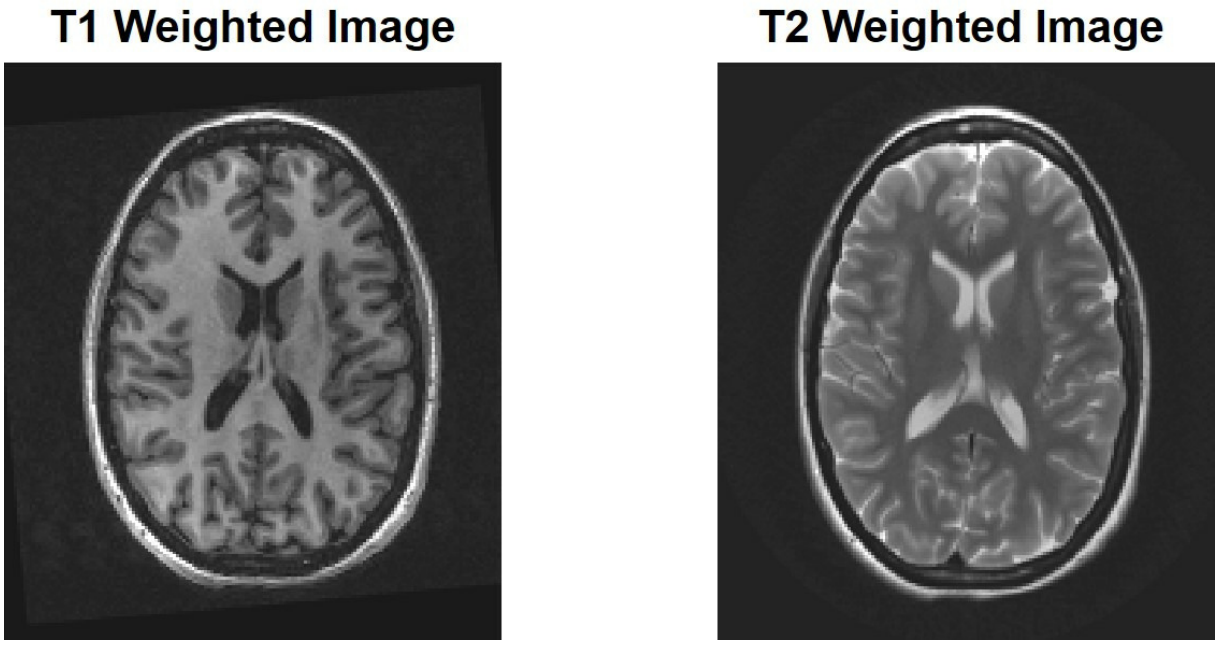

Figure 2.8: Left: *T1 weighted image.* ***Right:*** *T2 weighted image. TR and TE values have been chosen to provide maximum T1 and T2 contrast respectively between GM, WM and cerebrospinal fluid (CSF).*

2.8.2 Inversion Recovery Sequences

Inversion Recovery (IR) sequences or IR-prepped sequences were originally developed to generate heavily T1 weighted images. IR is a magnetization preparation technique that is used to maximize tissue contrast in MR images. The improved tissue contrast is obtained by selectively suppressing or nulling the signal of any given tissue based on its T1 value. As a result, a superior discrimination between tissues can be achieved based on their T1 relaxation constants. IR sequences typically contain a preparation module which is followed by an acquisition module. The preparation module consists of a 180° RF inversion pulse and associated gradients that flip the magnetization M_z to its negative value $-M_z$. Due to longitudinal relaxation, the magnetization M_z will begin to recover to its original value, passing through a null value. Tissues regain M_z at different longitudinal (T1) relaxation rates determined by their T1 relaxation times and therefore, the sequence is T1 weighted. The inversion pulse increases the T1 weighting of conventional SE and GRE sequence but is time-consuming due to the additional preparation module.

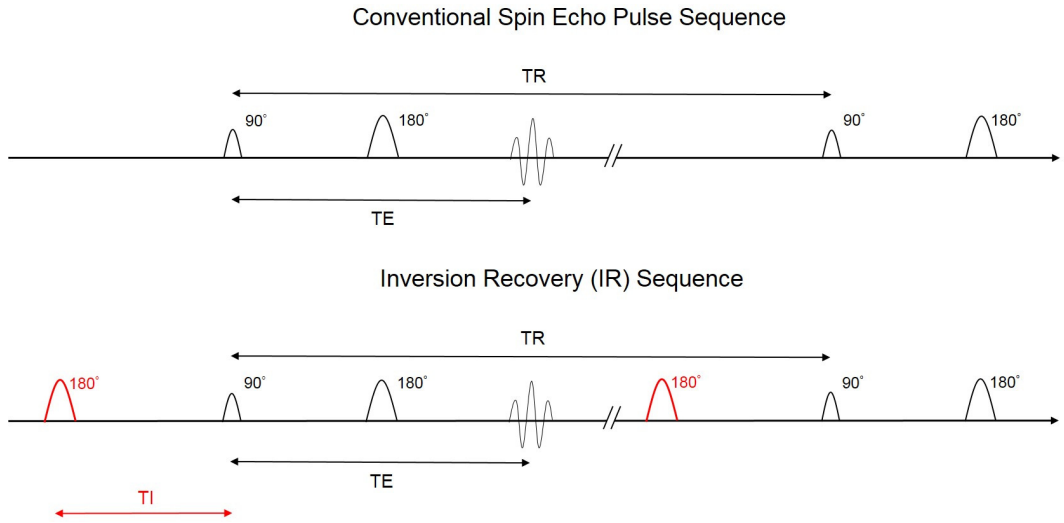

Figure 2.9: *Pulse sequence timing diagrams of a conventional Spin Echo (SE) sequence and an inversion recovery (IR) prepared SE sequence*

Selective suppression of tissue signals is achieved by applying a 90° readout pulse at the exact time when the longitudinal magnetization reaches the null point for the tissue that has been chosen to be suppressed. The time elapsed between the 180° inversion pulse and the 90° readout pulse is called time to inversion or inversion time (TI). By choosing an appropriate TI,

signals from particular tissues can be nulled (i.e. no signal will be detected from tissues at their null point due to absence of longitudinal magnetization). A comparison of a conventional SE sequence and an IR sequence is shown in Figure 2.9. The acquisition module follows the preparation module and is usually a generic SE or GRE sequence. In other words, IR sequences are usually a variation of the SE or GRE sequence preceded by a 180° preparation pulse to enhance T1 weighting. IR prepared sequences are widely used especially in neuroradiology and cardiac imaging applications.

An IR-prepared T1w 3D GRE sequence is generally used clinically to accentuate GM/WM tissue contrast. In this sequence, the image contrast between tissues is related to the time instant at which the data samples are acquired. The samples collected at the beginning of each readout have better contrast than samples collected towards the end of the readout due to T1 relaxation characteristics of different tissues. The TI is chosen to optimize tissue contrast and several k-space samples are read out after each TI [25]. The order in which k-space samples are acquired is therefore important as the contrast changes from readout to readout if the k-space samples are not acquired in the appropriate order. The image contrast plays an important role in clinical diagnosis for the effective discrimination of various tissue types including any abnormalities. Therefore, the k-space trajectory should be optimized to acquire central k-space data (that contains most of contrast information) at the beginning of each readout when GM/WM tissue contrast is maximum. Failure to optimize k-space acquisition order will lead to severe loss of contrast in reconstructed images, making them unsuitable for clinical diagnosis.

2.8.3 T2 Preparation Sequences

Similar to inversion recovery, T2 preparation can be added to any MR pulse sequence to enhance the T2 contrast in images. It is primarily used in cardiac MRI [26, 27] and MR Angiography [28, 29] to enhance the contrast between the myocardium and arterial blood signal. In such sequences, a 90° RF pulse is first applied to tip the longitudinal magnetization M_z into the $x - y$ plane. A series of non-selective 180° refocusing RF pulses are then applied to remove the decay caused by magnetic field inhomogeneities (T2* decay) and thereby induce pure T2 weighting. Finally, a -90° tip-up pulse is applied to conclude the T2 preparation phase. This tip-up pulse spoils the transverse magnetization and aids in the recovery of longitudinal relaxation, imparting enhanced T2 contrast between tissues. Tissues such as CSF, arterial blood that have long T2 relaxation times appear bright when compared to the myocardium or venous blood that have low T2 values. The time between the first 90° pulse and the -90° tip-up pulse

is called T2-prep time. The T2-prep time is usually between 30-50 ms. The T2 weighting can be changed by varying the time intervals between the different RF pulses.

2.9 Noise in MRI

Although the MRI signal that originates from the hydrogen protons in the body is localized spatially by the application of the gradient magnetic fields as described in Section 2.5, the noise in the image is not localized [30]. The major source of noise in MRI is the patient's body. A small portion of the RF energy is absorbed by the tissues of the body and dissipated in the form of heat which produces the noise in the image. The hardware components in an MRI scanner (coils, electronics etc.) also contribute to the noise. The noise is related to the sensitivity of the receiver coil which depends on its size, with smaller coils more sensitive than larger coils but covering a smaller region or Field of View (FOV) [31]. An increase in the coil size results in the increase in the FOV but it also increases the noise received by the area of the receiver coil. Therefore, multiple coils are used in most MRI scanners to increase the signal to noise ratio (SNR) in the acquired images.

2.10 MRI Artefacts

Any unintended effect or signal on an MR image is generally referred to as an artefact. Various artefacts can appear in MR images either because of the MRI scanner hardware or due to the interaction of the patient with the hardware [32]. These artefacts cause difficulty in the interpretation of MR images and may affect the clinical diagnosis. It is important to know the sources of these artefacts and learn how to avoid or eliminate them in order to prevent false diagnosis. Many different types of artefacts have been reported to appear in MR images [33] but can be broadly classified into the following categories, namely:

i) **Truncation artefacts:** In MRI, only a finite number of frequencies are sampled and approximating an image using relatively few harmonics in its Fourier representation would give rise to truncation artefacts. If the image is smoothly varying, only a few Fourier terms are needed to approximate the image. However, at high contrast interfaces, the truncation of Fourier terms would lead to significant artefacts. The most common truncation artefact is Gibbs ringing that appear as fine parallel lines adjacent to high contrast interfaces. Truncation artefacts are usually

minimized by increasing the number of phase encodes or by reducing the field of view [34].

ii) **Motion artefacts:** Motion artefacts are the most common MRI artefacts that can occur in many clinical MRI applications. The artefacts can be caused by patient motion, breathing, cardiac motion or blood flow. They usually appear as "ghosts" which cause blurring and reduce image quality. They can be reduced by breath hold, cardiac/respiratory gating or by using accelerated MR techniques such as parallel imaging [5, 6], compressed sensing [12] or a combination of both [13, 14].

iii) **Aliasing artefacts:** Aliasing artefacts arise if the field of view (FOV) does not cover the entire object or if a sufficient number of k-space lines are not sampled during acquisition. These artefacts can be removed either by increasing the FOV or by using parallel imaging reconstructions to approximate/synthesize missing k-space data.

iv) **Chemical Shift artefacts:** Chemical shift artefacts occur at fat-water interfaces especially in the case of fluid-filled structures surrounded by fat such as eye balls, bladder. They can be useful at times to confirm the presence of fat in lesions but in most cases, they are undesirable. They can be removed by fat suppression techniques using inversion recovery sequences [25].

v) **Other Artefacts:** There are other MRI artefacts such as banding artefact, blurring artefact, spike noise artefact, susceptibility artefacts, etc. [32] that do not fall into any of the above categories but it is important to be aware about them and know when they might occur so that they can be minimized or eliminated.

2.11 Acceleration techniques in MRI

Development of fast MRI schemes to reduce scan time have been an integral part of MRI research. Fast MRI sequences have numerous potential benefits across the gamut of clinical applications. The slowness of data acquisition is a major limiting factor in MRI when compared to other medical imaging modalities. The slow imaging speed is due to the inherently long relaxation times which necessitates a critical requirement for sequential line-by-line data collection.

MRI acceleration techniques can be broadly classified into:

i) Partial Fourier imaging
ii) Parallel Imaging (PI) techniques
iii) Compressed Sensing (CS) techniques

2.11.1 Partial Fourier Imaging

Partial Fourier imaging was one of the first techniques that was used for accelerating MR acquisition [35]. It was mainly used in scenarios where only the magnitude information of the image was necessary. It exploited the property that the Fourier transformation of a purely real function has complex conjugate symmetry in k-space [35]. This means that only half the k-space in the phase encoding direction needs to be acquired for a two fold gain in acceleration. As a result, the acquition time is reduced by half even though there is a corresponding fall in SNR [36]. Since more than half (commonly $\sim$60%) of phase information is generally needed in practice to provide robust phase correction, this method is not suitable for applications that require high resolution phase information.

2.11.2 Parallel Imaging techniques

Parallel Imaging (PI) or partially parallel imaging (PPI) has been widely used in MRI scanners to accelerate MRI data acquisition. The basic idea of PI is to reduce the number of phase encoding steps and utilize the inherent spatial encoding of multiple receiver coils to account for the reduction in the number of phase encodes [37]. In other words, small shifts can be induced in k-space by optimal weighting of the different coil sensitivity profiles of multiple coils while the sampling density can be reduced to accelerate the data acquisition [38]. The acceleration factor (R) also known as the reduction factor is used to represent the reduction in the number of lines acquired in k-space. In PI, the resulting gain in imaging time is directly proportional to the factor 1/R. PI techniques are broadly classified into two categories:

k-space methods:

PI techniques that primarily operate on signal data in the spatial frequency domain before being transformed into an image. The missing lines in k-space are first synthesised from adjacent k-space lines by using weighting functions derived from the fully acquired portion of

k-space [6, 39] and the final step is the Fourier transformation of the full k-space data to obtain the reconstructed image. Some examples are: SMASH (Simultaneous Acquisition of Spatial Harmonics), AUTO-SMASH (Autocalibrating SMASH), VD AUTO-SMASH (Variable Density AUTO-SMASH), PILS (Partially Parallel Imaging with Localized Sensitivities), GRAPPA (Generalized Autocalibrating Partially Parallel Acquisition), SPIRiT (Iterative Self-consistent Parallel Imaging Reconstruction From Arbitrary k-Space) [5].

Image domain methods:

These methods operate on the signal data in the image domain. Because of reduced data acquisition due to parallel imaging, the images are initially aliased. The aliasing is then corrected by the image reconstruction algorithm in order to obtain the original unaliased image. Example: SENSE (Sensitivity Encoding).

Noise in Parallel Imaging:

The geometry factor (g-factor) or noise amplification factor is unique to parallel imaging. It is due to the spatial dependence of the coil sensitivities and plays an important role in the SNR. It varies across the image and depends on the number of replicates in the aliased image [40]. The geometry factor analytically describes the spatially varying noise amplification due to the PI reconstruction, and is a measure of how easily the separation of aliased pixels can be performed with a specific coil array [41].

$$SNR_{parallel} = \frac{SNR}{g\sqrt{R}}$$

2.11.2.1 Simultaneous Acquisition of Spatial Harmonics (SMASH):

SMASH was invented by Sodickson et al. in 1997 and it was the first PI technique that was able to demonstrate significant reduction in imaging time for fast MRI [4]. It is a k-space method that exploited the inherent spatial information in multiple receiver coils to account for reduction in the number of acquired k-space lines. The missing k-space lines are nothing but spatial harmonics of the acquired k-space lines and are approximated by a linear combination of sensitivity profiles from multiple receiver coils. The missing k-space lines are synthesized and then Fourier transformed to obtain the image. The gain in imaging time is proportional to 1/R where R is the reduction or acceleration factor.

Limitations include the design of special coils with sinusoidal sensitivity profiles and the requirement of accurate estimation of coil sensitivity maps to generate optimal weights for approximating spatial harmonics. It also suffers from ghosting artefacts in the reconstructed image when the approximation of the harmonics is poor. In addition, the approximation error increases for estimation of higher order harmonics. Derivatives such as AUTO-SMASH [42] and VD AUTO-SMASH [39] have been developed to overcome some of the limitations of the SMASH technique.

2.11.2.2 Generalized Autocalibrating Partially Parallel Acquisition (GRAPPA):

GRAPPA is the most widely used PI technique in MRI applications that are very sensitive to motion (e.g. Cardiac imaging, abdominal imaging). It is an extension of both VD AUTO-SMASH [39] and PILS [43] as it utilizes the advantages of both techniques in image reconstruction. It follows a variable density sampling scheme (similar to VD AUTO-SMASH) and is also a coil by coil reconstruction technique (similar to PILS). Classical GRAPPA utilizes a sliding block reconstruction mechanism in which more than one reconstruction is possible for each missing line [6]. A block is defined as a single acquired line and missing lines adjacent to it. Using more than one block increases the fit accuracy and improves image quality but requires more reconstruction time.

The central k-space data that is collected is called the autocalibration signal (ACS). The GRAPPA reconstruction weights are generated from the central ACS which are then used to synthesize the missing k-space lines. Generation of GRAPPA reconstruction weights involves the learning of GRAPPA calibration kernels in the calibration or ACS region. The kernels are calculated by the linear combination of k-space neighbours of all coils and depend only on the acquired k-space lines.

Iterative Self-consistent Parallel Imaging Reconstruction from Arbitrary k-Space (SPIRiT):

A popular derivative of the GRAPPA technique is SPIRiT. SPIRiT is a generalized reconstruction framework that was invented in 2010 by Lustig et al. that is based on consistency with the calibration and acquired data [7]. In SPIRiT, the reconstruction problem is formulated as an optimization problem in which various regularization terms that arise from compressed sensing can be incorporated to improve reconstructed image quality [7]. It is a generalization of

the GRAPPA technique but unlike GRAPPA, it is an iterative reconstruction technique that enforces consistency of all points in the neighbourhood, whether acquired or not. As a result, the entire neighbourhood around each point is used to generate the reconstruction weights at each iteration. Because of this, it results in a higher SNR than GRAPPA and produces images of better quality [7].

2.11.2.3 Sensitivity Encoding (SENSE):

SENSE is the most commonly used PI technique for MR image reconstruction. Different MRI vendors use various acronyms for their own version of SENSE (eg. Philips-SENSE, Siemens-mSENSE, GE-ASSET, Hitachi- RAPID, Toshiba -SPEEDER). SENSE is based on the fact that receiver sensitivity generally has an encoding effect complementary to Fourier preparation by linear field gradients [5]. It is an image domain method in which the undersampled k-space data is first Fourier transformed to produce an aliased or folded image. The image is then unfolded by utilizing the coil sensitivity maps of multiple receiver coils. The estimation of the coil sensitivity maps is the most important step in SENSE reconstruction. Firstly, low resolution images at full FOV are acquired from each coil. A body coil image is then utilized to normalize the low resolution coil images. Filtering, thresholding and point estimation are then applied to generate a sensitivity map for each coil. These sensitivity maps quantify the relative weighting of signals that originate from the sensitive region of each coil. The popularity of SENSE is due to the fact that it can be easily adapted to arbitrary k-space sampling trajectories [23]. Although non-Cartesian sampling patterns require an iterative reconstruction technique, the simplicity of image reconstruction has made it possible to be implemented by several vendors in MRI scanners. However, SENSE reconstructions are highly susceptible to motion artefacts due to the need for a separate calibration scan. Therefore, SENSE is not utilized in MRI applications that are sensitive to motion such as cardiac imaging or abdominal imaging.

2.11.3 Compressed Sensing techniques

Compressed Sensing theory or Compressive Sampling (CS) states that signals or images can under certain conditions be accurately reconstructed from far fewer measurements than traditional methods that satisfy the Shannon-Nyquist theorem [44, 45]. CS is based on two principles, sparsity and incoherence. Sparsity refers to the small fraction of non-zero elements in a large dataset. It has been found that many naturally occurring signals are sparse in an appro-

priate domain (i.e. contain only few significant non-zero values) and this feature is exploited in CS. Incoherence refers to the fact that the signal can be sampled using a basis that is incoherent to the sparsity basis. Thereby each measurement is recording information of all components in the sparsity basis (i.e. none of the useful information in the sparsity basis is lost during the sampling process). CS also exploits the randomness in the subsampling scheme.

MRI is a special case of CS in which the Fourier coefficients are under sampled in k-space, thereby significantly reducing the number of measurements. Therefore, by using a CS reconstruction, the original image can be recovered from a small subset of k-space rather than the entire k-space grid [12]. Lustig et al. have shown that MR data acquisition can be designed to satisfy all the three requirements for a successful implementation of CS [12]:

i) Transform Sparsity: Some MRI images are inherently sparse (e.g. angiograms) but most MR images are sparse in some transform domain e.g. brain images are sparse in the wavelet domain [12, 15], sparsity can be enforced by an efficient Total Variation (TV) algorithm in applications such as cardiac MRI while dynamic MRI images are sparse when represented by low rank sparse matrix decomposition

ii) Incoherence: By utilizing an appropriate sampling scheme such as random sampling, the correlation between the sparse data entries in MRI can be greatly reduced (i.e. incoherence can be implemented in the subsampled data by choosing an appropriate undersampling scheme). Fourier measurements are naturally incoherent to signals that contain only a few significant coefficients (so angiography works well with random Fourier). However, wavelets are not completely incoherent with respect to Fourier (the low frequency components are highly correlated). Therefore, there is a need to use some form of variable density scan where the low frequencies are densely sampled if wavelets are used for reconstruction. Incoherence makes aliasing artefacts appear noise-like and enables efficient recovery of sparse signal coefficients.

iii) Non-linear reconstruction: Non-linear CS reconstruction algorithms capable of enforcing sparsity and data consistency are used to recover the sparse signals from the undersampled data. The non-linear reconstruction algorithms are iterative and generally make use of an appropriate regularization parameter to enforce sparsity [12, 46].

Compressed sensing recovery methods

Compressed sensing is an inverse problem where the objective is to accurately recover the signal/image from highly undersampled measurements. The idea is to exploit the sparsity in

the measurements to achieve efficient retrieval of the signal/image under specific conditions. Unlike conventional and parallel imaging reconstructions that use linear reconstructions such as inverse Fourier transformations or utilizing prior information to unfold the images (i.e. remove the aliasing) introduced by uniform subsampling, CS reconstruction is a non-linear iterative reconstruction technique that is used for the recovery of sparse coefficients.

In CS problems, the number of measurements (i.e. number of equations) M is always less than the signal length (i.e. dimension of the signal) N leading to an underdetermined system of equations. An underdetermined system of equations has an infinite number of solutions. However, if it is already known that the signal is sparse with sparsity k (i.e. it contains only k significant coefficients where $k \ll M$), under suitable conditions it is possible to obtain the k-sparse solution according to CS theory. This is usually done by using sparsity promoting recovery methods. Some sparsity promoting methods are discussed below:

i) $\ell 0$ **minimization:**

The best way to find the k-sparse solution to an inverse problem is to perform $\ell 0$ minimization which is mathematically written as:

$$\min\{\|x\|_0 : Ax = b\}$$

where the quantity $\|x\|_0$ (i.e. $\ell 0$ norm of x) denotes the number of non-zeros in x (i.e. the signal vector to be recovered), A is the unknown sensing matrix of dimension $M \times N$ where $M < N$ and b is the k-sparse measurement vector.

$\ell 0$ minimization provides the sparsest solution to the CS recovery problem but it is also a combinatorial optimization problem of high complexity, is computationally intractable (i.e. it requires a very long time to be solved making it unusable for practical scenarios) as well as not being robust to noise or signals that are only approximately sparse. Therefore, it is not generally used for solving practical CS problems.

ii) $\ell 1$ **minimization:**

An alternative method to solve the CS recovery problem is to replace the $\ell 0$ norm by $\ell 1$ norm that makes the solution computationally tractable (i.e. it can be solved in a reasonably quick

time that is acceptable for practical scenarios). It is mathematically written as:

$$\min\{\|x\|_1 : Ax = b\}$$

where the quantity $\|x\|_1$ (i.e. $\ell 1$ norm of x) is the summation of absolute values of the elements in x. Under favourable conditions, $\ell 0$ minimization and $\ell 1$ minimization problems share common solutions. The solution to both these problems become similar when the measurements are sufficiently sparse and if the sensing matrix A has highly incoherent column vectors (i.e. less correlation between columns). Otherwise, ℓ_1 minimization will not produce the sparsest solution. Therefore, it is possible to recover the sparse coefficients in MRI using the regularized $\ell 1$ minimization technique. CS reconstruction using $\ell 1$ minimization is discussed in more detail in section 2.13, 'Advanced Reconstruction Algorithms'.

2.11.3.1 Sparse MRI

Sparse MRI provides a framework for the application of CS techniques for rapid MR imaging [12]. Sparse MRI is a software package written in Matlab that consists of a series of implementations of CS on real MR images [12]. This framework was specifically developed for Cartesian MRI. CS reconstructions exploiting different types of sparsity have been demonstrated on various MRI applications such as brain imaging (i.e. wavelet sparsity), knee imaging (i.e. discrete cosine transform sparsity) and angiograms (i.e. finite differences sparsity). The reconstructions utilized ℓ_1 regularization to promote sparsity and ℓ_2 minimization to ensure data consistency. The regularization parameters in CS reconstructions depends on the type of application and must to be tuned appropriately in order to obtain better reconstructions.

2.11.3.2 Other CS models for capturing sparse representations in MRI

Several CS models have been developed for various MRI applications. These models can be broadly classified into:

i) **Methods based on regularization and sparsifying transform:** Various types of regularization and sparsifying transforms have been used for different MRI applications as described earlier. Some of these methods use phase regularization [47, 48], shearlets [49] and contourlets (i.e. combination of wavelets and curvelets) [50] to improve the sparsifying transform.

ii) **Dictionary Learning methods:** These methods exploit nonlocal similarity and sparse representation [51–53]. Smaller image patches are used to find sparse representations of the entire image and the dictionary is optimized adaptively based on current sparse coefficients. In these methods, the sparse approximations of the image are represented using adaptive transforms (dictionaries) which result in the increase in sparsity since they are learnt for the particular image instance or class of images.

iii) **Low rank methods:** In these methods [54], low rank matrix completion is used to recover components in an incomplete data matrix. It is mostly suited in the context of dynamic MRI where the highly correlated timeframes are approximated as a low rank component while the dynamic changes in each timeframe are formulated as a sparse component. The reconstruction is based on the combination of both low rank and sparse components [55].

2.11.4 Compressed Sensing-parallel imaging techniques

When CS is used in conjunction with PI methods (i.e. CS-PI) [13, 14], further acceleration is possible with significantly less reduction in SNR when compared to conventional PI methods. CS-PI methods combine the data redundancy from multiple receiver coils with the transform sparsity of MR images and the spatial incoherence achieved by random subsampling to reconstruct alias free images with higher SNR thereby allowing for more acceleration to be applied to the acquisition without further compromising the diagnostic image quality.

2.11.4.1 Eigen value SPIRiT (ESPIRiT):

ESPIRiT is one of the most popular and commonly used CS-PI reconstruction algorithms in MRI [14]. It combines the advantages of the two most popular parallel imaging techniques (i.e. SENSE and GRAPPA). It also incorporates CS into the reconstruction algorithm to perform CS-PI reconstructions. ESPIRiT is just one example of a CS-PI reconstruction algorithm that falls under a class of algorithms that perform convex relaxation/constrained optimization.

ESPIRiT is an iterative algorithm that works on a series of Singular Value Decompositions (SVDs). The central data or calibration data is utilized to perform calibration in k-space. Then, an Eigen decomposition is carried out in image space to compute the Eigen maps. The Eigen vectors that correspond to the Eigen value = 1 are the estimated coil sensitivity maps. If there is strong aliasing in the input data, more than one Eigen vector corresponds to 1 which results in

the appearance of multiple sensitivity maps for each receiver coil. Multiple sensitivity maps are utilized in the reconstruction algorithm to reconstruct the original image. Therefore, accurate sensitivity maps can be estimated even from aliased datasets. Besides, like GRAPPA it is also robust to motion artefacts since it does not require a separate calibration scan to generate sensitivity maps (i.e. PI part of algorithm). In addition, it allows a random undersampling scheme to be implemented and utilizes wavelet sparsity (i.e. CS part of the algorithm) to perform CS reconstruction. The combination of CS and PI (CS-PI) has the potential to be utilized in many MRI applications in order to provide an additional speed-up factor in MRI data acquisition without reducing the signal to noise ratio (SNR).

2.11.4.2 Other CS-PI Algorithms:

There are several CS-PI algorithms that are used for providing additional acceleration to conventional PI or CS techniques. Some examples include modifying PI algorithms to also incorporate CS [56], performing subsampling in both spatial and temporal domain (i.e. kt subsampling) for CS-PI reconstruction of dynamic MRI [57] and promoting joint sparsity for combining CS-PI reconstructions [58].

Table 2.1 shows the comparison of some PI, CS and CS-PI techniques in MRI:

Name	Acronyms	Reconstruction Domain	Autocalibration Signal (ACS)	Calibration Scan	Sampling trajectory	Reconstruction type	Limitations
Simultaneous Acquisition of Spatial Harmonics [4]	SMASH	k-space	No	Yes	only Cartesian	linear	requires special coil design, high approximation error
Generalized Autocalibrating Partially Parallel Acquisition [6]	Siemens - GRAPPA; General Electric - ARC	k-space	Yes	No	only Cartesian	linear	only supports uniform subsampling
Iterative Self-consistent Parallel Imaging Recon from Arbitrary k-Space [7]	SPIRiT	k-space	Yes	No	Works for arbitrary sampling patterns	nonlinear iterative	does not support CS reconstruction
Sensitivity Encoding [5]	Philips - SENSE; Siemens - mSENSE; GE - ASSET; Hitachi - RAPID Toshiba - SPEEDER	image space	No	Yes	Works for arbitrary sampling patterns	linear	highly susceptible to motion artefacts
Sparse MRI [12]	CSMRI	image space	No	Yes	only Cartesian	nonlinear iterative	requires proper tuning of regularization parameter
Eigen Value SPIRiT [14]	ESPIRiT	image space	Yes	No	Works for arbitrary sampling patterns	nonlinear iterative	requires proper tuning of regularization parameter

Table 2.1: *Comparison of parallel imaging (PI), compressed sensing (CS) and compressed sensing-parallel imaging (CS-PI) techniques in MRI*

2.11.5 Clinical applications of accelerated MRI

Various MRI applications could benefit from the implementation of CS-PI acceleration techniques. Some of them include:

Structural MRI:

Structural MRI is the most widely used MRI application in the world. It is generally used to examine the anatomy of the tissues in the human body. Abnormalities like tumours, micro bleeds, blood vessel leakage, blockage of blood vessels etc. can be detected from structural MRI images. Structural images provide excellent anatomical detail of the tissues being imaged but the resolution is limited by the scan time and susceptibility of the reconstruction technique to motion artefacts [59]. Moreover, typical MRI examinations require multiple scans to acquire images with complementary diagnostic information [60]. This entails the need to run multiple scans with varying contrast settings (such as T1-weighted, T2-weighted and $T2^*$ weighted sequences) for optimal visualization of tissue structure which results in a significant increase in scan time. Incorporation of CS-PI techniques in a MRI clinical protocol would significantly reduce the scan time while also preserving the image resolution to a certain extent.

Quantitative MRI:

Most of the MR images that are used clinically are qualitative in nature. However, quantitative MRI (q-MRI) is fast emerging as a clinically useful modality in diagnostic MR imaging because these images provide clinicians with additional information that helps in more accurate diagnosis [61, 62], improved disease monitoring [63, 64] and better treatment planning [65, 66]. q-MRI involves the estimation of tissue parameters such as proton density (PD), longitudinal relaxation time (T1), transverse relaxation time (T2) and transverse relaxation time with inherent magnetic field inhomogeneities ($T2^*$) from multiple MRI images of the same tissue with different parametric weighting to compute a parametric map whose individual pixels have a numerical or quantitative meaning (such as the value of T2, at each location of the brain) [67]. Quantitative parameters like proton density, T1 and T2 relaxation times etc. vary for normal and abnormal tissues and can give an indication of neurodegenerative disorders in the brain such as mild cognitive impairment [62], Parkinson's disease [61] and Huntington's disease [68] that cannot be detected from conventional structural MR images. The estimation of tissue parameters helps in greater tissue discrimination [67, 69, 70], segmentation [71, 72] and classification [73, 74] to improve disease detection [69, 75] and monitoring [63, 64]. However, a series of

structural images acquired with varying contrast settings is required to generate a quantitative map which makes the process time consuming [76]. In most cases, the data collected is insufficient to generate quantitative maps due to clinical time constraints. Therefore, accelerating q-MRI is of immense clinical importance and can be achieved by CS and PI techniques.

3D/ Multidimensional / dynamic MRI:

3D MRI acquisition has become popular in clinical applications like diagnostic radiology since it allows the acquisition of isotropic images with small size thickness. The 3D data set is acquired in one plane and images in any other plane can be subsequently reconstructed from the same 3D data set [77]. It is also useful in volumetric imaging that can be used to measure tissue volume loss while monitoring brain disorders or depression [78]. Moreover, additional "dimensions" can also be included to provide vascular information from which blood flow can be measured (i.e. multidimensional MRI) [79]. But, like other MRI applications, its performance is limited by the slow data acquisition process which increases the scan time considerably when compared to conventional 2D imaging. Moreover, motion artefacts appear in the images unless the patients remain motionless throughout the scan sequence. Therefore, CS and PI techniques have a vital role to play in reducing the imaging time in 3D/multidimensional MRI [80, 81]. Dynamic MRI, which gives information about physiological tissue characteristics by the use of external contrast agents can also benefit from an efficient implementation of CS-PI techniques [82]. Faster sampling also allows better fitting of theoretical models to the contrast agent uptake.

2.12 Quantitative MRI

2.12.1 The need for quantitative MRI (q-MRI)

Traditionally, clinical MRI relies on the acquisition of so-called weighted images, whose image contrast is affected by a combination of different factors, some intrinsic to the tissue (i.e. natural contrast between different tissues due to differences in proton density) and some dependent on the specifics of the experiment (i.e. user specified TE, TR, TI values that can enhance tissue contrast) [83]. Images of the same patient acquired from two separate scans with identical sequence parameters may appear different when MRI scanners from different vendors are used to acquire the images [84]. This is common in MRI because of the vendor specific variations in various clinical pulse sequences. There is a possibility that the diagnosis might be slightly biased if radiologists are not trained in evaluating images from different vendors. Likewise, there

can also be a discrepancy in diagnosis between different radiologists who evaluate the same images since signal intensities are relative in traditional MRI. These limitations have brought about the desire for images that can provide quantitative values of meaningful physical and chemical variables reflecting tissue characteristics that can be measured in physical units and compared between tissue regions and among subjects [83]. Such images are quantitative in nature and can reduce diagnostic bias between radiologists since quantitative maps can provide additional information about tissue parameters that can aid clinical diagnosis [85, 86]. Therefore, q-MRI is fast emerging as a clinically useful modality in diagnostic MR imaging because it can help in more accurate diagnosis, improved disease monitoring and better treatment planning [67, 87, 88].

2.12.2 Clinical q-MRI - Practical Difficulties

Although q-MRI has a great potential to improve diagnosis in several clinical applications, it is not a routine procedure in most clinical protocols. The limited use of q-MRI is due to the amount of time that is necessary to generate a quantitative T1 or T2 map. In general, in order to obtain a T1 or T2 map of a single slice, multiple scans of the same slice have to be carried out sequentially using different imaging parameters (such as TE and TR) to acquire a series of images that are either T1 weighted (T1w) or T2 weighted (T2w). Figure 2.8 shows an example of T1w and T2w MR image from a healthy volunteer brain. The multiple T1w and T2w images are used to mathematically fit the exponential signal recovery curve for T1 estimation and exponential signal decay curve for T2 estimation. Acquiring multiple T1w/T2w images is extremely time consuming which is not practical in a clinical scenario. Besides, multiple quantitative maps such as T1 and T2 maps are often necessary to diagnose various abnormalities which further adds to the overall scan time [89, 90]. The clinically permissible scan time for a single patient is usually not sufficient to perform all the necessary scans from which T1 and T2 maps can be generated. This practical difficulty has been mitigated to some extent by the emergence of several accelerated techniques [91–93] that considerably reduce the overall scan time for q-MRI and will be discussed in section 2.11. These acceleration techniques utilize several principles such as parallel imaging and compressed sensing to reduce the overall scan time. Even though the scan time can be sufficiently reduced for certain clinical applications using these acceleration techniques, separate scanning experiments requiring additional scan time are necessary to generate multiple quantitative maps. Techniques to simultaneously generate multiple quantitative parametric maps such as PD, T1, T2 in a very short scan duration

have been recently developed [94, 95] which has led to the immense interest in making q-MRI a routine procedure in clinics and hospitals worldwide.

2.12.3 Gold Standard T1 and T2 Measurements

Gold standard quantitative measurements are necessary to evaluate the accuracy of accelerated quantitative measurement techniques. Gold standard measurements often take a very long time and are usually impractical in a clinical setting. These measurements are often carried out on phantoms and are used to validate the performance of different quantitative measurement techniques. If the T1, T2 values from gold standard measurements agree with estimated values of a specific quantitative measurement technique, it is widely accepted as a proof of concept for that particular measurement technique.

The gold standard measurement technique for T1 measurement is the inversion recovery-spin echo (IR-SE) sequence. Multiple scans are carried out using varying inversion times (TIs) to acquire a set of T1w images. Inversion recovery is used to impart strong T1 weighting to the images. To calculate T1 values, the magnitude of IR-SE images are fit using pixel-wise nonlinear least-squares curve fitting to the following exponential recovery curve:

$$M_z(TI) = M_0(1 - 2e^{-TI/T1})$$

where M_0 is the magnetization at thermal equilibrium, M_z is the longitudinal magnetization that depends on the Inversion Time (TI) and T1 relaxation time of the IR-SE experiment.

The gold standard measurement technique for T2 measurement is the single echo spin echo (SE) sequence. Multiple scans are carried out using varying echo times (TEs) to acquire a set of T2w images. To calculate T2 values, the magnitude of the multiple SE images are fitted to the following exponential decay curve:

$$M_{xy}(TE) = M_0 e^{-TE/T2}$$

where M_0 is the magnetization at thermal equilibrium, M_{xy} is the transverse magnetization that depends on the Echo Time (TE) and T2 relaxation time of the SE experiment.

2.12.4 Magnetic Resonance Fingerprinting (MRF)

The emergence of rapid parametric mapping techniques such as Magnetic Resonance Fingerprinting (MRF) [94] and its various extensions [95–97] have shown that it is possible to generate multiple quantitative parametric maps simultaneously in a very short scan duration that is clinically feasible. MRF offers a new approach to rapidly quantify multiple tissue properties simultaneously within a single scan by acquiring the transient-state signal that is sensitive to multiple imaging parameters such as flip angle (FA) and repetition time (TR). In MRF, the uniqueness of the signal response in the temporal domain that is achieved due to the rapid, arbitrary variation of acquisition parameters is exploited to generate quantitative multi-parametric maps within a short acquisition time. By acquiring a series of subsampled images rapidly while constantly varying imaging parameters temporal incoherence is achieved resulting in unique signal evolutions that depend on the physical properties of various tissues, such as tissue relaxation times. These unique signal evolutions or fingerprints are matched to a precomputed dictionary to generate multi-parametric quantitative maps.

The entire MRF process can be broken down into two steps, namely:
i) data acquisition and
ii) pattern matching/dictionary matching (DM)

2.12.4.1 MRF Data Acquisition

The data acquisition in MRF is different to conventional MRI where the entire k-space data is acquired using the same acquisition parameters such as FA, TR and k-space trajectory to generate contrast weighted qualitative MR images as described in Section 2.8. In the MRF data acquisition process, acquisition parameters are deliberately varied throughout the acquisition and if these parameters are varied appropriately, unique signal timecourses for different tissue types can be generated [98]. The accuracy, time efficiency, the combination of tissue parameters to be estimated and clinical usefulness of MRF are governed by the manipulation of pulse sequence acquisition parameters.

One of the major advantages of MRF acquisition is that the acquired data can be highly subsampled. Severe undersampling artefacts are introduced in the individual images due to the subsampling process. However, these artefacts are not present in the generated quantitative maps since the DM algorithm used in MRF is robust to subsampling artefacts due to the temporal incoherence of the data. Therefore, temporal incoherence is an important design consideration

in MRF. Advanced reconstruction algorithms such as the iterative projection algorithm (IPA) [99, 100] or low rank alternating direction method of multipliers [101] can be used to remove aliasing in individual images and improve MRF quantification accuracy. Therefore, MRF has greatly reduced the time inefficiency of traditional mapping techniques.

MRF also provides a framework in which different sequences can be adopted to obtain relevant tissue properties [94, 97]. Various sequences such as balanced steady state free precession (bSSFP) [94], unbalanced SSFP [95, 102], pseudo SSFP [103], EPI [104] and other sequences [105] have been modified to perform MRF. Therefore, MRF provides greater freedom in sequence design when compared to conventional mapping techniques.

MRF data is typically acquired using an interleaved or variable-density spiral sampling strategy [94, 95, 102]. Spiral sampling provides more control for efficient traversal of the k-space trajectory than conventional Cartesian techniques as shorter pathways are required to cover a desired region and the data acquisition may start in the center of k-space [106]. Therefore, spiral sampling is faster than the conventional Cartesian sampling scheme. Spiral sampling has been used previously for fast imaging applications [107] and it is highly suitable for a rapid quantitative technique such as MR Fingerprinting. In addition, spirals have been shown to be more robust to motion and flow artefacts [108–110] and therefore can be more suitable for certain MR applications that require superior insensitivity to motion and flow artefacts (eg. cardiac MRI, vascular MRI, abdominal MRI). Even though the design of the variable density spiral is an important design criteria for MRF experiments, spiral design parameters such as the number of interleaves, the angle of rotation and readout length often vary for different MRF experiments and it is still unclear how these parameters may affect the accuracy of the estimated multi-parametric maps. Therefore, a systematic study of spirals with varying design parameters needs to be carried out for finding the optimal spiral design parameters for MRF.

Other sampling strategies such as radial sampling [103, 111], random subsampling [112] and single shot Cartesian sampling [104, 113, 114] have also been proposed for MRF. One of the major benefits of MRF is that it allows the acquired data to be highly subsampled. However, the single-shot Cartesian sampling strategies do not allow the same degree of subsampling as spirals or radials. Therefore, this leads to longer TRs than can be achieved using spiral or radial sampling. The difference in TRs between single-shot Cartesian and non-Cartesian methods affects the simultaneous T1-T2 sensitivity of the sequence and cannot be compared with each other (described in more detail in Chapter 5). In this thesis, an accelerated Cartesian MR

Fingerprinting technique that was developed using multi-shot EPI will be described in Chapter 5. It has the advantage of achieving TRs similar to those of Spiral-MRF while also providing entire k-space coverage over the course of the acquisition. The full k-space coverage eliminates the high frequency artefacts that arise due to non-sampling of k-space corners in Spiral-MRF. In addition, the absence of regridding and the use of the Fast Fourier Transform (FFT) instead of the non-uniform Fast Fourier Transform results in faster reconstruction than Spiral-MRF. Therefore, accelerated Cartesian MRF can be used as an alternative to conventional Spiral-MRF. In spite of the existence of several implementations of MRF using various sampling strategies as described above, the effect of the sampling strategy on the accuracy of generated multi-parametric maps is still an open question. Hence, more research is required to determine the optimum sampling strategy for MRF.

2.12.4.2 Dictionary Matching

The dictionary is a database containing all realistic combinations of signal evolutions or fingerprints with each entry having characteristic parameters (T1,T2). Several mathematical models such as Bloch equations [20], Extended Phase Graph (EPG) formalism [115, 116] and other complex models [105, 117] can be used to predict the signal evolution of the sequence and hence generate a dictionary of all possible signal evolutions. This dictionary of all possible fingerprints for a particular sequence is usually precomputed before the actual measurements are carried out. It is also possible to include other parameters such as diffusion, magnetization transfer and off-resonance effects into the dictionary [94].

Once the dictionary is generated, a pattern matching or dictionary matching (DM) algorithm is used to select a dictionary entry that best corresponds to the actual measurements [98]. DM is also sometimes referred to as matched filter (MF) reconstruction. DM provides a certain degree of tolerance to noise, artefacts and other errors as long as the acquired data is temporally incoherent [94]. For the DM process, the vector-dot product of the acquired signal with each simulated fingerprint signal in the dictionary is first calculated. One dictionary entry is picked as the best match from all possible signal evolutions in the dictionary for each measured voxel location. The dictionary entry with the highest dot product (i.e. correlation coefficient) is selected as most likely to represent the true signal evolution. The T1 and T2 values associated with the specific dictionary entry are assigned to that voxel. The M_0 value is computed as the multiplicative factor between the acquired and simulated fingerprints. Iterative algorithms

can be used to improve the accuracy of the DM process [100, 101]. The size of the dictionary increases exponentially based on the number of parameters to be estimated. Therefore, the DM process can be very time consuming if the dictionary size is very large. The time taken for DM can be reduced by compression in the time domain [101, 118, 119] and by using fast dictionary search algorithms [120, 121].

2.12.4.3 Applications of MRF

MRF has been in validated in phantoms, healthy volunteers and patients. Multi-parametric estimations using MRF have shown a good agreement with conventional T1 and T2 methods [95, 96, 104]. Current clinical applications have been primarily focused on brain relaxometry [122–125], cardiac imaging [96], prostate cancer [126], abdominal imaging [127], muskoskeletal imaging [128], perfusion imaging [105] and microvascular structure [117, 129] determination. The clinical applications of MRF have been gradually rising and are expected to increase further.

2.13 Advanced Reconstruction Algorithms

Advanced reconstruction algorithms are necessary for CS and MRF reconstructions. This section will describe two common approaches that are generally used for recovery of signals from incomplete measurements.

2.13.1 Constrained Convex Optimization (CS Reconstruction)

As described previously in section 2.12.2, CS theory states that signals can be recovered from far fewer measurements than necessary if the signal is either sparse or transform sparse (i.e. sparse in some transform domain). Mathematically, it entails solving a constrained optimization problem, e.g. finding an image that minimizes this form:

$$\begin{aligned} & \min_{X} \|\Psi X\|_1 \\ s.t. \quad & \|Y - \Phi X\|_2^2 < \epsilon \end{aligned} \tag{2.1}$$

where X is the reconstructed image, ΨX is the sparsified transform of X, Φ is the undersampled

Fourier matrix weighted by the estimated coil sensitivities and ϵ is the threshold parameter. ϵ controls the fidelity of the reconstruction to the measured data Y and is usually set below the expected noise level [12]. The constraint $\|Y - \Phi x\|_2^2 < \epsilon$ enforces data consistency. In words, among all solutions which are consistent with the acquired data, the $\ell 1$ minimization finds a solution which is compressible by the transform Ψ.

A convex function is one that has a unique global minimum. The optimization of the sparse or transform sparse MR image X is convex (i.e. it has a unique global minimum). The solution to the above problem can be obtained by performing any type of sparsity promoting regularization. Some examples of regularizers that promote sparsity are wavelets which promote sparsity in wavelet domain, total variation which utilizes finite differences to promote sparsity and low rank methods that promote dependency between rows or columns in matrices. Sparsity promoting $\ell 1$ regularization is suitable for MRI since MR images are non-smooth and contain sharp edges. The idea is to find the global minimum or sparse solution using $\ell 1$ minimization while ensuring that the sparse solution is consistent with the acquired measurements.

The above convex optimization problem can also be solved by the following equivalent formulation called the Least Absolute Shrinkage and Selection Operator (LASSO) formulation [130]:

$$\hat{X} = \underset{X}{\arg\min} \|Y - \Phi X\|_2^2 + \lambda \|\Psi X\|_1 \tag{2.2}$$

where $\hat{X}$ is the image to be estimated, Y is the acquired undersampled k-space data, Φ is the undersampled Fourier matrix weighted by the estimated coil sensitivities, ΨX is the sparsified transform of X and λ is the regularization parameter. The first term in the above equation ensures data consistency using $\ell 2$ minimization and the second term enforces sparsity by $\ell 1$ regularization, with the parameter λ controlling the relative weighting of the two constraints. $\ell 1$ minimization with wavelet regularization will be used to perform the CS-PI reconstructions in Chapters 3 and 4.

Several algorithms can be used to solve the $\ell 1$ minimization problem that is described above. Some popular algorithms include Iterative shrinkage-thresholding algorithm (ISTA) [131], fast ISTA (FISTA) [132], alternating direction method (ADM) [133], approximate message passing (AMP) [134] and projection onto convex sets (POCS) [135, 136].

2.13.1.1 Projection Onto Convex Sets Algorithm (POCS)

Among the several methods that can be used to solve $\ell 1$ minimization problem, the POCS algorithm has been shown to work very well for recovery of signals from undersampled k-space measurements in MRI [7, 14, 137]. The POCS algorithm is a general tool that is used to solve a constrained optimization problem. In this method, each constraint is defined as a convex set (i.e. the set has a unique global minimum). It uses alternating projections on each set iteratively to find the intersection between convex sets. If the constraints are well-defined, the algorithm converges in a few iterations. The $\ell 1$-ESPIRiT method that will be used for reconstructing the undersampled MR images in Chapters 3 and 4 makes use of the POCS algorithm to perform $\ell 1$ minimization.

2.13.2 Greedy Optimization

Greedy optimization refers to the use of a class of algorithms in which the best solution to an optimization problem is found by a series of incremental approximations in a number of steps [138]. Greedy algorithms make hard decisions on the constrained sets at each iteration during optimization. Some important greedy algorithms are matching pursuit (MP) [139], orthogonal matching pursuit (OMP) [140], orthogonal least squares (OLS) [141], iterative hard thresholding (IHT) [142] and gradient pursuits [143].

2.13.2.1 Iterative Hard Thresholding Algorithm (IHT)

Greedy algorithms have been widely used in compressive sensing applications [144]. Among the many algorithms, the IHT algorithm has been shown to be very useful in recovering sparse coefficients [142] and can be used within the MRF framework with modifications. The algorithm is based on a simple iterative procedure. Starting at $x^{(0)} = 0$, each iteration involves:

$$x^{n+1} = H_K(x^n + \mu^n \phi T(y - \phi x^n)) \tag{2.3}$$

where x^n is the reconstructed image at a specific iteration, x^{n+1} is the reconstructed image at the next iteration, H_k is a nonlinear hard thresholding operator that keeps the largest (in magnitude) K elements of a vector and sets the remaining elements to zero, μ^n is the step size that tries to minimize the difference between the estimated signal value at each iteration and the

K-sparse acquired measurements y.

2.13.2.2 Iterative Projection Algorithm (IPA)

The Iterative projection Algorithm (IPA) [145] is a general extension of the IHT algorithm. The BLoch matching response recovery through Iterated Projection (BLIP) algorithm is a special form of the IPA algorithm and is used to improve MR Fingerprinting reconstructions and generate more accurate multi-parametric maps [99, 100]. Cline et al. demonstrated the improved accuracy of multi-parametric estimations by the application of the IPA on healthy volunteer human brains [119]. The IPA algorithm will be used for MRF reconstructions in Chapter 5 to improve the accuracy of multi-parametric maps generated by the developed Cartesian MRF scheme based on multi-shot Echo Planar Imaging (EPI).

The IPA algorithm is based on the Landweber algorithm [145] that attempts to recover a signal X from from noisy measurements Y through iterative regularization. The IPA reconstruction is motivated by compressed sensing theory [12, 44, 142, 146] and is shown to be capable of removing aliasing artifacts (in the reconstructed images) resulting from severe k-space subsampling.

Briefly, in the BLIP form of IPA, each iteration consists of:

$$X^{j+1} = \rho_D \left(X^j - \mu A^H \left(A \left(X^j \right) - Y \right) \right) \tag{2.4}$$

where $Y \in C^{m \times N}$ are the undersampled k-space measurements, C denotes that the k-space measurements contain complex data (i.e. contain both real and imaginary parts), m refers to the number of coils, N refers to the number of temporal repetitions, μ is the step size which can be adaptively selected through line search [100], $X^j \in C^{n \times N}$ are the spatio-temporal reconstructed images at iteration 'j' and $D \in C^{d \times N}$ denotes the pre-computed dictionary with 'd' atoms. The forward and backward operators A, A^H model the multi-coil sensitivities and 2D Fourier Transforms for the acquired subsampled data. ρ_D denotes the DM step that is used in [100, 119] consisting of i) a search over the normalized dictionary atoms to replace the temporal pixels of X^{j+1} with the maximum correlated fingerprints and ii) proton density rescaling. Furthermore ρ_D can be seen as an orthogonal projection onto the constraint set defined by the dictionary model. Therefore, the first iteration of IPA could be interpreted as an

application of DM with proton density regularization [99, 100].

In IPA reconstruction, the subsampled images in each frame are simultaneously reconstructed to produce an alias free time series of images along with parameter estimation. The IPA algorithm reduces the relative error between the estimated T1 and T2 values and the MRF measurements at each iteration and improves the accuracy of the generated multi-parametric maps.

2.14 Summary

In this Chapter, the reader was given a brief introduction to MR Physics, MR Image formation and tissue contrast in MRI among other basics of MRI. The most commonly used pulse sequences were then presented which showed that MR data acquisition is a slow process and there is a great clinical need to increase MR imaging speed. After establishing the need for fast MRI, a literature review of conventional MR acceleration techniques was then provided. It was followed by describing two novel MR acceleration methods namely: CS-PI techniques that would be used for accelerating structural 3D MRI in Chapters 3 & 4 and MR fingerprinting that would be used for accelerating quantitative MRI in Chapter 5. These two acceleration techniques will be the major focus of this thesis. The main purpose of this chapter was to introduce the reader to the recent advancements in MR acceleration techniques and to describe the reconstruction methods that would be used in Chapters 3, 4 and 5.

Chapter 3

Optimizing acquisition and reconstruction parameters for CS-PI accelerated IR-prepared 3D MRI

This chapter introduces the reader to the need for optimization of acquisition and reconstruction parameters in CS-PI accelerated reconstructions. These parameters vary for different organs and MR pulse sequences and it is essential to perform optimization to improve the image quality of CS-PI reconstructions.

3.1 Introduction

Combination of compressed Sensing and parallel imaging (CS-PI) has become popular for MR acceleration since it has been demonstrated in many clinical applications such as paediatric MRI [147], dynamic contrast enhanced (DCE) MRI [148], MR angiography (MRA) [149], phase contrast MRI [150, 151]. CS-PI studies in MRI can be divided into two categories depending on whether the subsampling is real or simulated: i) retrospective CS and ii) prospective CS. Retrospective CS refers to the simulation of undersampling that can be applied to previously acquired fully sampled data. Retrospective subsampling is done by discarding part of the acquired k-space data prior to the Fourier transform. Retrospective studies are more convenient in a research setting as it allows the testing of various types of subsampling patterns and CS reconstruction algorithms without the need to acquire new data [152]. In contrast, prospective CS refers to the application of CS to perform accelerated scans on an MR scanner. Experimental prospective studies are more difficult to conduct due to the need for additional scans to acquire accelerated MR data.

High acceleration factors (≥ 4) with acceptable image quality have been achieved using CS-PI reconstructions in many retrospective CS-PI studies [12, 153] and prospective CS-PI studies that possess high inherent tissue contrast like MRA [149] or contrast enhanced studies such as

DCE MRI [148] that use external contrast agents. However, CS-PI studies in MR applications with low inherent contrast such as brain MRI [154] and spinal MRI [155] have shown that even a modest 2-fold acceleration caused severe blurring and global ringing artefacts. Although retrospective CS-PI neuroimaging studies [12, 14] show good reconstructions for higher acceleration factors (≥ 2), the radiological image quality assessment of prospective CS-PI accelerated neuroimaging [154, 156] showed that CS accelerated brain MR images have insufficient clinical diagnostic value.

The poor image quality of CS-PI accelerated brain images is usually attributed to the choice of subsampling pattern. Several studies have looked at different subsampling patterns and have shown that the choice of the subsampling pattern significantly affects the image quality of CS-PI accelerated reconstructions [157–160]. These studies also demonstrate that pseudo-randomness in the subsampling pattern improves the quality of CS-PI reconstructions. Since CS reconstructions rely heavily on the type of subsampling pattern [12], it is important to choose the subsampling pattern carefully to get the best image quality in reconstructed images. However, despite the use of pseudo-random subsampling patterns that were optimized retrospectively to improve the image quality of CS-PI reconstructions, prospective CS-PI implementations produced images that had significantly reduced quality than the predictions of retrospective experiments especially with the increase in acceleration factor [161]. This is primarily due to the non-optimization of the k-space trajectory and can be improved by optimizing the k-space acquisition order [161, 162]. Therefore, the k-space sampling order is another important acquisition parameter that needs to be optimized for prospective CS-PI implementations. The size of the calibration data, which is another acquisition parameter and reconstruction parameters such as the type of sparsifying transform and amount of regularization have also been shown to affect the quality of CS-PI reconstructions [152]. The focus of this chapter will be the optimization of CS-PI acquisition and reconstruction parameters to show that optimization is very important in CS-PI accelerated neuroimaging for producing images of acceptable clinical diagnostic quality.

3.2 Methods

3.2.1 Image Acquisition

The Scanning was performed on a 1.5 T GE Signa HDx scanner with an 8 channel receive only head RF coil (GE Medical Systems, Milwaukee, WI). Informed consent was obtained from the two healthy volunteers who participated in this proof of concept study. Initially, a fully sampled

dataset was acquired from two healthy volunteers using the IR-prepared 3D GRE sequence which is a widely used clinical T1w sequence. The fully sampled scan takes a fairly long time of about 8:08 minutes. It is challenging for many people to lie still inside the MR scanner for the entire scan duration of this sequence which often lead to motion artefacts in the 3D datasets. Therefore, the objective was to accelerate this 3D sequence using a combination of CS and PI techniques to reduce overall scan time. The 3D sequence was also chosen because subsampling could be performed in both the phase encode directions (i.e. k_y and k_z). The scanning protocol consisted of a localizer scan that was used to prescribe fully sampled and undersampled 3D T1-weighted IR-GRE scans. The localizer scan consists of a set of multiplanar, low resolution, large FOV images which are used to prepare the scan prescription (i.e. selecting the 3D imaging block, its angle and number of slices). Sequence parameters were: Repetition Time (TR)/Echo Time (TE)/TI = $10/4/500$ ms; flip angle = 8°; matrix 192 x 192 x 160 slices; isotropic 1.3 mm voxels. The image orientation was axial. Phase encoding was performed along the sagittal and coronal planes.

3.2.2 Reconstruction

The images were reconstructed offline using Matlab (Mathworks, Natick, MA) scripts. A decision was made to use the CS-PI based $\ell 1$-ESPIRiT [14] algorithm that used the wavelet sparsifying transform for reconstruction since it combined the advantages of both CS and PI techniques and was shown to be able to reconstruct good quality brain MR images from retrospective undersampling of fully sampled scans. This reconstruction algorithm uses the $\ell 1$ minimization technique that has been described in Section 2.13.1. A translation invariant Daubechies wavelet of order two (db2) and length four was used. The value of the regularization parameter λ was fixed in consultation with an experienced neuroradiologist to achieve a balanced trade-off between noisy images and overly smooth images. The methodology of fixing λ will be explained in Section 3.2.3. Approximately 15-20 iterations were required for the convergence of the $\ell 1$-ESPIRiT algorithm.

The idea was to initially test this reconstruction algorithm retrospectively on the acquired fully sampled data for determining optimal acquisition and reconstruction parameters that produced the highest image quality. Three types of subsampling patterns were tested: i) Poisson-disc subsampling, ii) random subsampling and iii) uniform subsampling. The Poisson-disk subsampling is a pseudo-random scheme where the samples are tightly packed but are separated

from each other by a minimum distance. In the random subsampling scheme, the samples are completely random but there is no distance criterion separating the samples. The absence of a minimum distance criteria leads to clusters of samples that are very close to each other in some regions while in some other regions there are holes with no samples. In the uniform subsampling scheme, a constant rate is used to subsample along both k_y and k_z directions. After retrospective experiments, the algorithm was then tested on CS accelerated prospective datasets that were acquired from a custom-built phantom [163, 164] and healthy volunteers to validate the practicality of CS accelerated neuroimaging.

3.2.3 Retrospective Experiments

CS-PI reconstructions were performed on retrospectively subsampled healthy volunteer brain data by varying CS acquisition and reconstruction parameters such as i) size of calibration data, ii) type of subsampling pattern, iii) degree of acceleration and iv) amount of regularization to determine optimal parameters that produced the highest image quality. Once the optimal calibration size, maximum acceleration factor and type of subsampling pattern were determined from the retrospective reconstructions, a sample dataset was reconstructed using different amounts of regularization and was then shown to an experienced neuroradiologist for feedback regarding the reconstructed image quality. The variation of the regularization parameter λ controlled the noise level and smoothness of the reconstructed images. The neuroradiologist was blinded to the value of λ and was asked to choose the most preferable reconstruction from among four different reconstructions with different values of λ (i.e. 0.001, 0.025, 0.3 and 1). The preferred reconstructed dataset which used $\lambda = 0.025$ had an acceptable trade-off between noisy reconstructions and overly smooth images. λ was fixed at this value for the rest of the study.

3.2.4 Prospective Experiments

After determining optimal CS acquisition and reconstruction parameters that produced the highest image quality through retrospective experiments, the same parameters were used for carrying out prospective experiments. The three different subsampling patterns used in this study were saved as look-up tables on the scanner by modifying the pulse sequence to incorporate prospective subsampling during data acquisition. Trial scans were then performed on a custom-built in-house phantom [163, 164] for proof of concept and subsequently on a healthy

volunteer to collect data at accelerated scan times. The phantom consisted of 9 tubes containing manganese chloride ($MnCl_2$) solution of various concentrations. The tubes were placed inside a cylindrical container that was filled with 1.5 g/l CuSO4 and 3.7 g/l NaCl solution. Each tube had varying T1 and T2 values due to the difference in the concentrations of $MnCl_2$ solution in each tube.

The images that were reconstructed from the prospectively subsampled healthy volunteer datasets showed a severe loss of contrast and elevated noise level in the reconstructions which led to degraded image quality of cerebral cortical deep grey matter brain structures such as thalamus, caudate, putamen and globus pallidus. It was found that the loss of contrast in prospectively subsampled images was due to the non-optimization of k-space acquisition order. Optimization of the k-space sampling order was then carried out and a healthy volunteer was prospectively scanned using sampling order optimized sampling patterns to show the importance of sampling order optimization in CS accelerated neuroimaging.

3.2.5 Optimization of k-space acquisition order (Sampling order optimization)

It has previously been argued in the literature that the optimization of the k-space acquisition order is important for CS-PI accelerated prospective scanning as there is a higher increase in noise and artefacts with increasing acceleration factor when compared to retrospective experiments [81, 161]. The increase in noise and artefact level in prospective experiments is much higher than predicted by retrospective experiments. This effect is observed since prospective acceleration is not exactly the same as retrospective simulation of acceleration. Retrospective subsampling from fully sampled data does not account for the increased noise level that arises due to the fast gradient switching during subsampling in prospective experiments. It is also hypothesized that there are increased eddy current effects in prospective experiments due to the random k-space trajectories and it has been shown that minimization of the overall k-space trajectory length largely reduced artefacts and improved image quality [161]. In certain clinical MRI sequences that use additional RF preparation pulses for contrast enhancement such as the IR-prepared 3D GRE sequence [25] used in this study, the k-space acquisition order becomes even more important due to continuous change in the inherent contrast of the sequence during the readout period. In such sequences, there is a preparation time after each preparation RF pulse where there is no acquisition and the image contrast between tissues is governed by the acquisition of data at the appropriate time when the inherent contrast of the sequence is

maximum.

Figure 3.1 shows the signal diagram of the IR-prepared 3D GRE sequence. In such IR sequences, additional RF inversion pulses are used before every readout period to either maximize the contrast between different tissues or to suppress the signal from a particular tissue type [25]. In this case, the sequence is optimized to maximize the tissue contrast between the GM and WM in the brain [25]. In order to suppress the signal from a particular tissue or to maximize contrast between two tissues of interest, the TI should be carefully chosen [165–169].

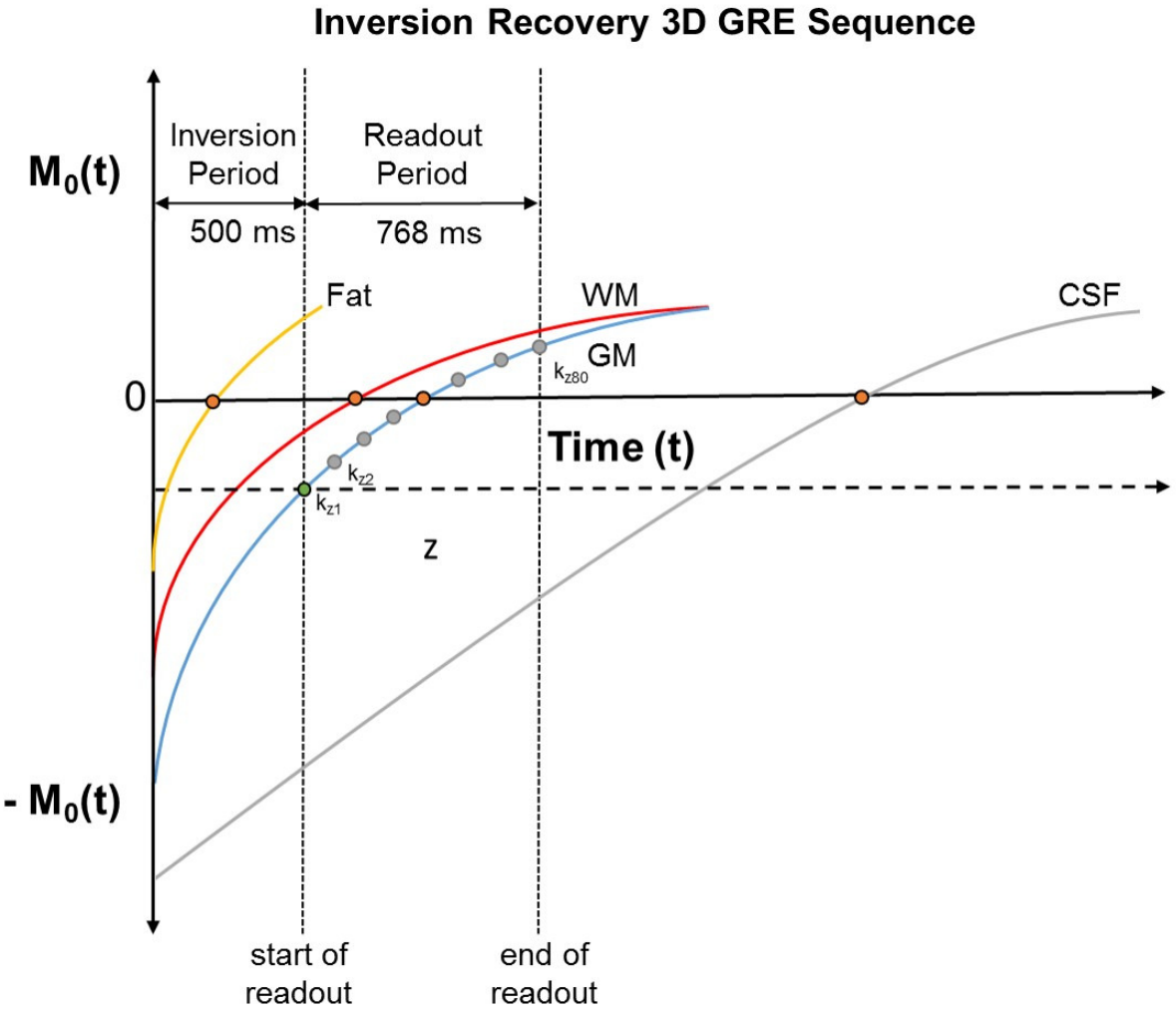

Figure 3.1: *Signal Diagram of the IR-prepared 3D GRE sequence*

The default TI of this sequence which has been set by the vendor for brain volume imaging is 500 ms since it has been shown previously that maximum contrast between GM & WM can be achieved by using TI values in the range between 400-500 ms [25]. It is also important to note that the definition of TI can vary between different MR scanner vendors for equivalent pulse sequences. Therefore, the inversion times used for a particular experiment can be vendor-specific (for example, equivalent IR-prepared sequences in GE and Siemens MR scanners use different inversion times due to the difference in the definition of TI). In this sequence, TI refers to the time between the application of the inversion pulse and the start of the readout period. The sequence consists of two phase encoding directions, k_y & k_z and the samples are usually acquired line-by-line along the k_z direction for a particular value of k_y. The process is repeated for different values of k_y to fill up the entire $k_y - k_z$ plane. Each sample in the $k_y - k_z$ plane corresponds to the acquisition of a full k-space line along the k_x direction.

The default fully sampled k-space acquisition ordering for the IR-prepared 3D GRE sequence (i.e. implemented by the manufacturer) is shown in Figure 3.2 and is described below. After an initial inversion pulse, the longitudinal magnetization is allowed to recover for a specific time period TI. As described earlier, the TI is chosen to maximize the GM & WM contrast. Exactly at the TI (i.e. 500 ms in this case), the readout starts and eighty k_z samples (i.e. one-half of k_z samples for a given k_y) are always acquired for a readout duration of 768 ms as shown in Figures 3.1 and 3.2. A second inversion pulse is then applied and the readout starts again after a period of 500 ms (i.e. TI) to collect the other half of k_z samples for the same k_y value. Hence, two inversion pulses are required to acquire a full line of 160 k_z samples for a given k_y. As there are 192 k_y phase encodes for the fully sampled acquisition, this process is repeated until the entire $k_y - k_z$ plane of 192 $\times$ 160 samples are acquired. Each k_x line consists of 192 frequency encodes. Therefore, the k_x, k_y, k_z dimensions of the acquired data for the fully sampled 3D acquisition is 192 $\times$ 192 $\times$ 160. The total duration of the fully sampled acquisition is 8:08 minutes.

In this sequence, the contrast between GM & WM is highest at the beginning of the readout (i.e exactly after an inversion time of 500 ms) since the value of TI was chosen to maximize this contrast . The contrast gradually decreases during the readout due to the T1 relaxation of GM and WM as shown in Figure 3.1. Therefore, the central k-space data which contains most of the contrast in the image must be acquired at the beginning of each readout when the inherent contrast is maximum.

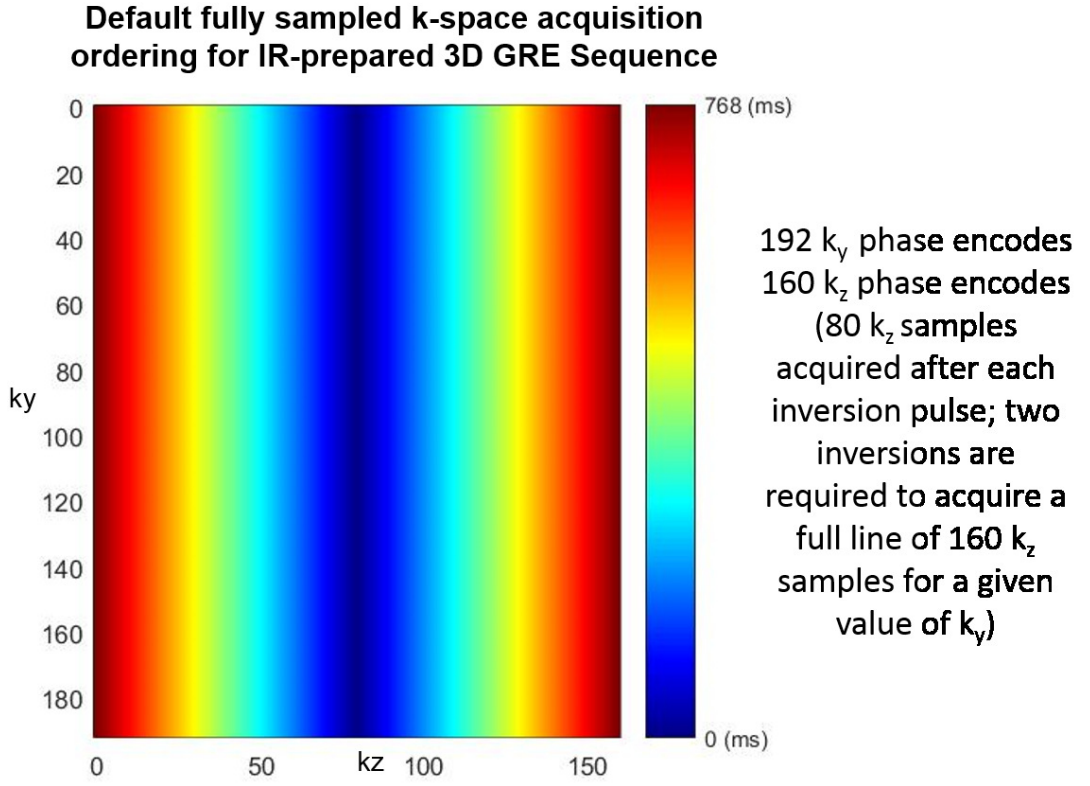

Figure 3.2: *The default k-space acquisition ordering for the inversion recovery 3D GRE sequence. The colourbars indicate the time instant at which k-space samples are acquired during the readout period of 768 ms duration. Note that the readout period starts after an inversion period of 500 ms duration as shown in Figure 3.1.*

The acceleration of the IR-prepared 3D GRE sequence is not trivial since the effect of the continuous change in the inherent contrast of the sequence during the readout period must be taken into consideration while designing subsampling patterns. The subsampling patterns that were used earlier in the chapter for both retrospective and prospective experiments were modified for the acquisition of k-space data at the maximum inherent contrast of the sequence by k-space sampling order optimization. The amount of acceleration that could be applied is additionally constrained by the fact that the number of samples that can be acquired after each inversion pulse and the timing between inversion pulses is fixed and cannot be modified for accelerated acquisitions. During the acquisition, it is important to ensure that the central data of each k-space line in the $k_y - k_z$ plane is acquired at the beginning of each readout when the inherent contrast of the sequence is maximum. The requirement for the acquisition

of a fixed number of k-space samples during each readout period of the IR-prepared GRE sequence affects the maximum amount of acceleration that can be achieved using sampling order optimization while being able to generate images of acceptable clinical quality using CS-PI reconstruction.

3.3 Results

Figure 3.3. shows the three different subsampling patterns that were used in this study. Poisson-disc, random and uniform subsampling patterns were generated to determine the most suitable undersampling pattern for $\ell 1$-ESPIRiT reconstruction. The reconstructed images were compared with the fully sampled images and the error maps were generated for the reconstructed images. Figure 3.4 shows a fully sampled image and four times accelerated $\ell 1$-ESPIRiT reconstructions for the three different subsampling patterns that were used in this study. The error maps for the retrospectively accelerated $\ell 1$-ESPIRiT reconstructions using the three subsampling patterns are also shown. The normalized root mean square (nRMSE) errors were 16.78%, 26.85% and 18.59% respectively for Poisson-disk, random and uniform subsampling patterns.

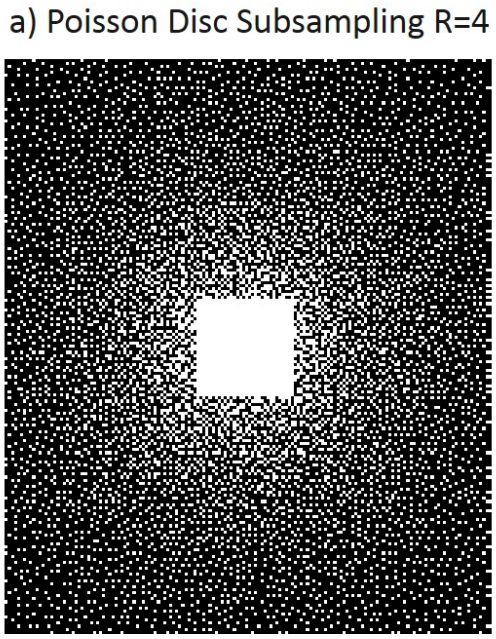

Figure 3.3: ***(a)*** *Poisson-disc subsampling pattern with four fold acceleration (i.e. R=4) that was used for retrospective simulation of undersampling and CS accelerated prospective experiments.*

b) Random Subsampling R=4

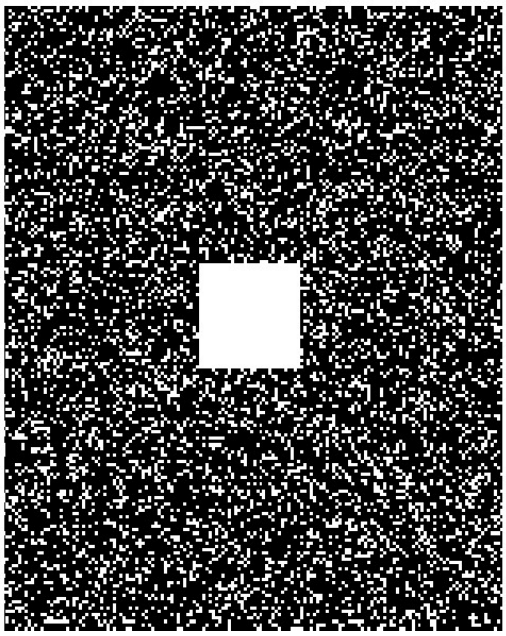

c) Uniform Subsampling R=4

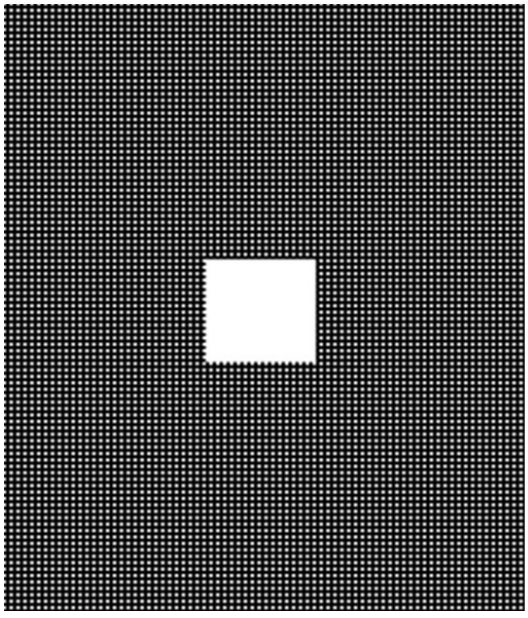

Figure 3.3: ***(b)*** *Random subsampling and* ***(c)*** *Uniform subsampling patterns with four fold undersampling (i.e. R=4) that was used for retrospective simulation of undersampling and CS accelerated prospective experiments.*

Figure 3.5 shows the effect of calibration size on the CS-PI reconstruction for 4-fold acceleration and Poisson-disc subsampling using a) 12x12 central k-space calibration, b) 16x16 central k-space calibration and c) 32x32 central k-space calibration. The nRMSE values were 28.72%, 23.12% and 18.14% for the three different calibration sizes respectively. In order to find the optimal acceleration factor R, subsampling patterns with varying acceleration factors were tested retrospectively using ℓ1-ESPIRiT reconstruction. Figure 3.6 shows three different ℓ1-ESPIRiT CS reconstructions with varying acceleration factors (i.e. R = 3,4,5) that used Poisson disc subsampling patterns. The nRMSE values were 16.09%, 18.21% and 29.42% respectively for acceleration factors of 3, 4 and 5 that are shown in Figure 3.6.

Figure 3.7 shows the fully sampled image of the phantom as well as CS accelerated prospective ℓ1-ESPIRiT reconstructions of the phantom for the three different subsampling patterns used in the study. The ℓ1-ESPIRiT reconstructions of all three subsampling patterns in Figure 3.7 were of good quality but there was a slight difference in the noise level between them. Figure 3.8 shows a fully sampled 2D brain section from a 3D acquisition of a healthy volunteer as well as four times (R=4) accelerated prospective ℓ1-ESPIRiT reconstructions for the three different subsampling patterns used in the study.

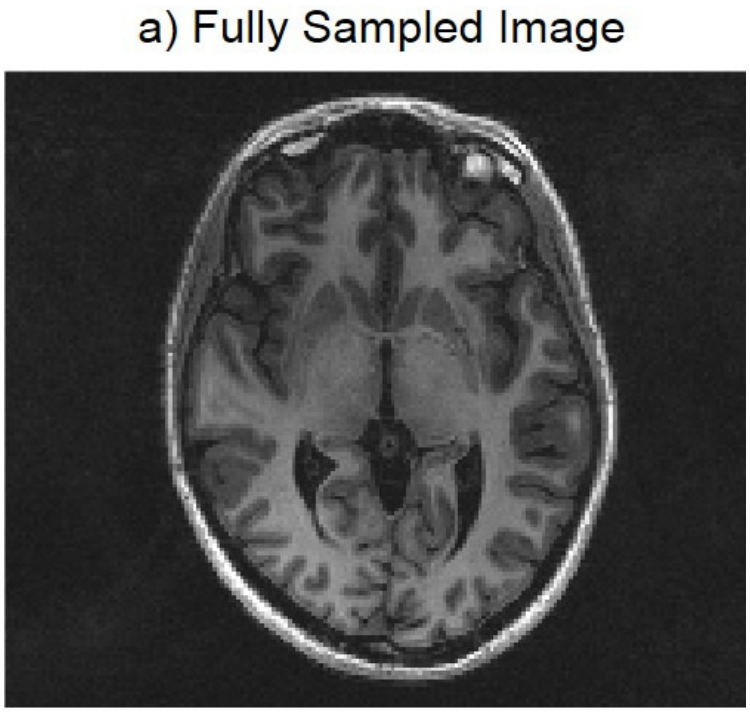

Figure 3.4: (a) *Fully sampled 2D section of a 3D acquisition from a healthy volunteer.*

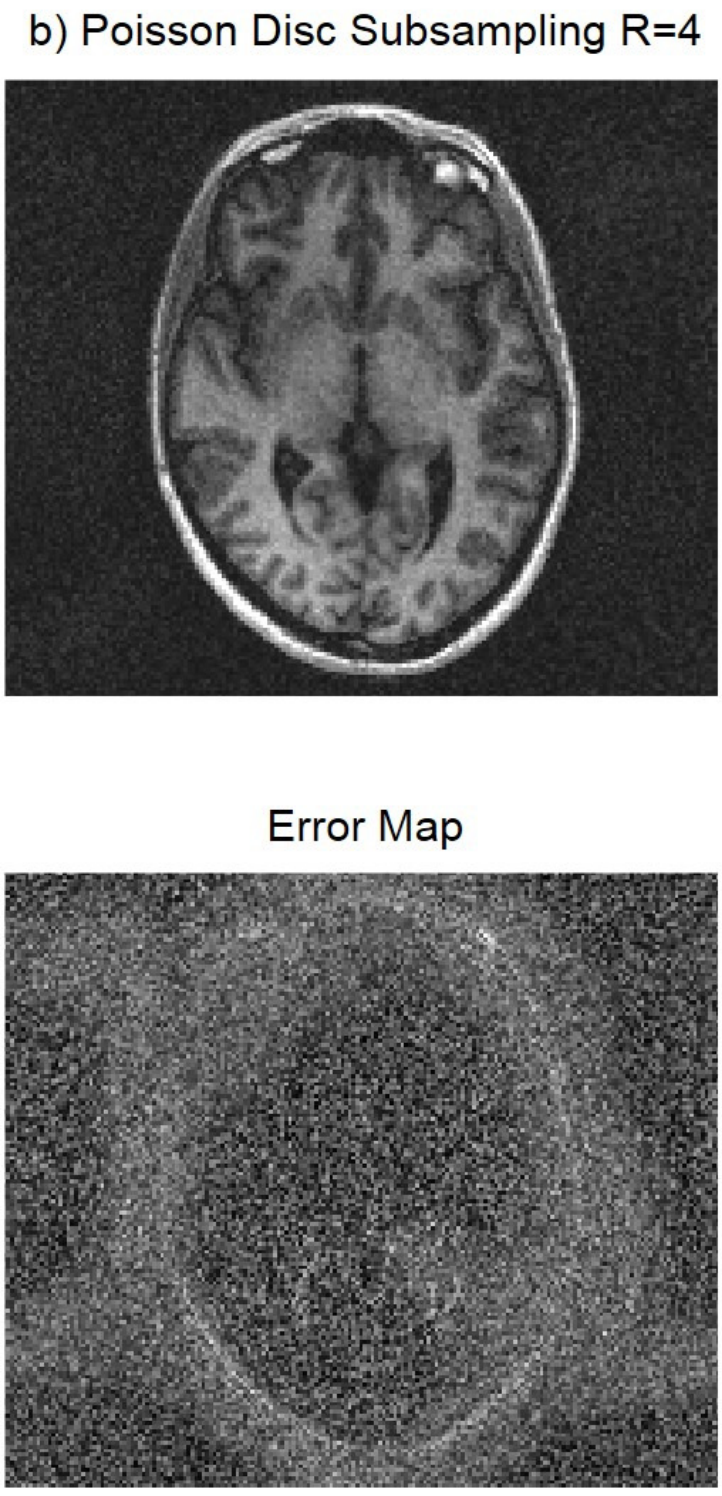

Figure 3.4: ***(b)*** *CS-PI (ℓ1-ESPIRiT) reconstruction and corresponding error map of a 2D section from a healthy volunteer 3D brain acquisition using Poisson-disc subsampling pattern with R=4.*

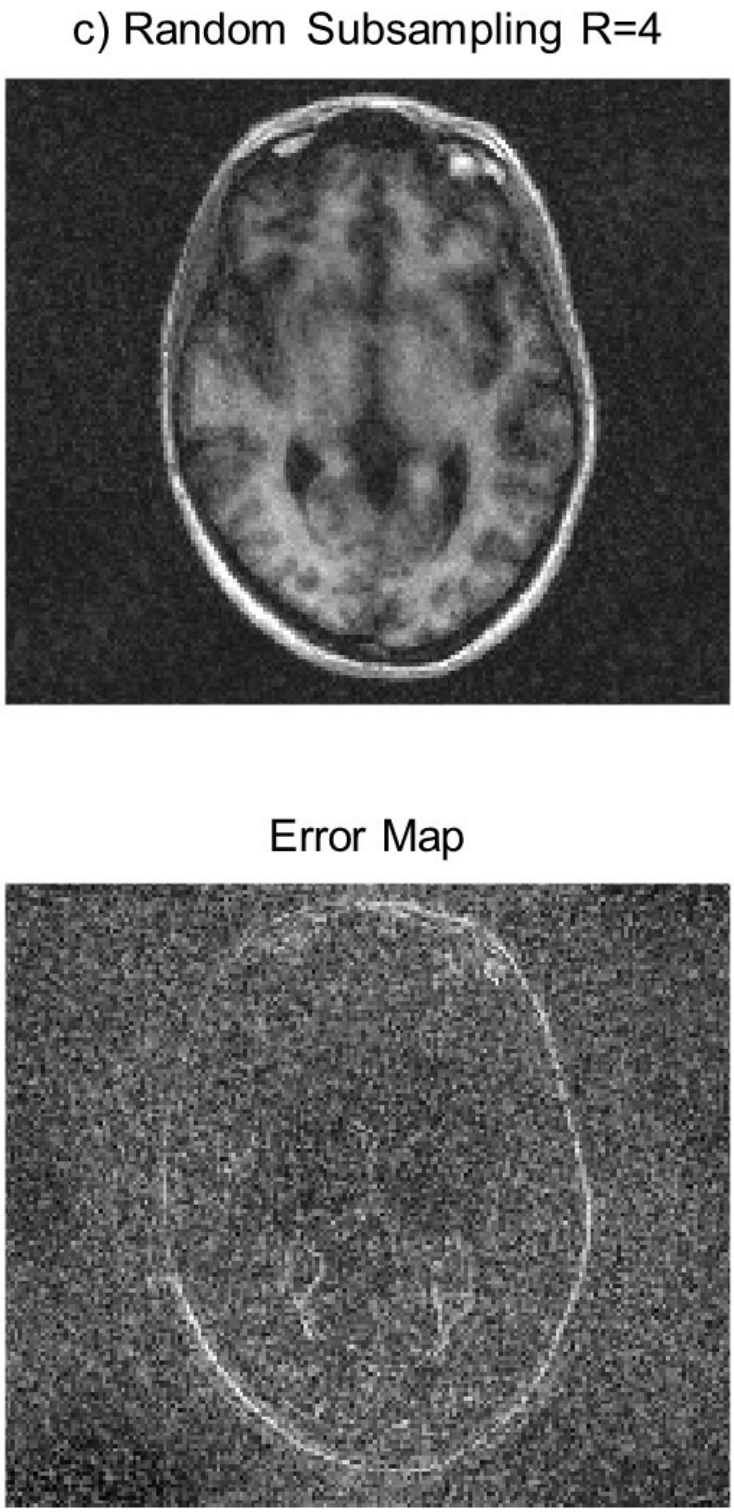

Figure 3.4: (c) *CS-PI $\ell(1$-ESPIRiT) reconstruction and corresponding error map of a 2D section from a healthy volunteer 3D brain acquisition using random subsampling pattern with R=4.*

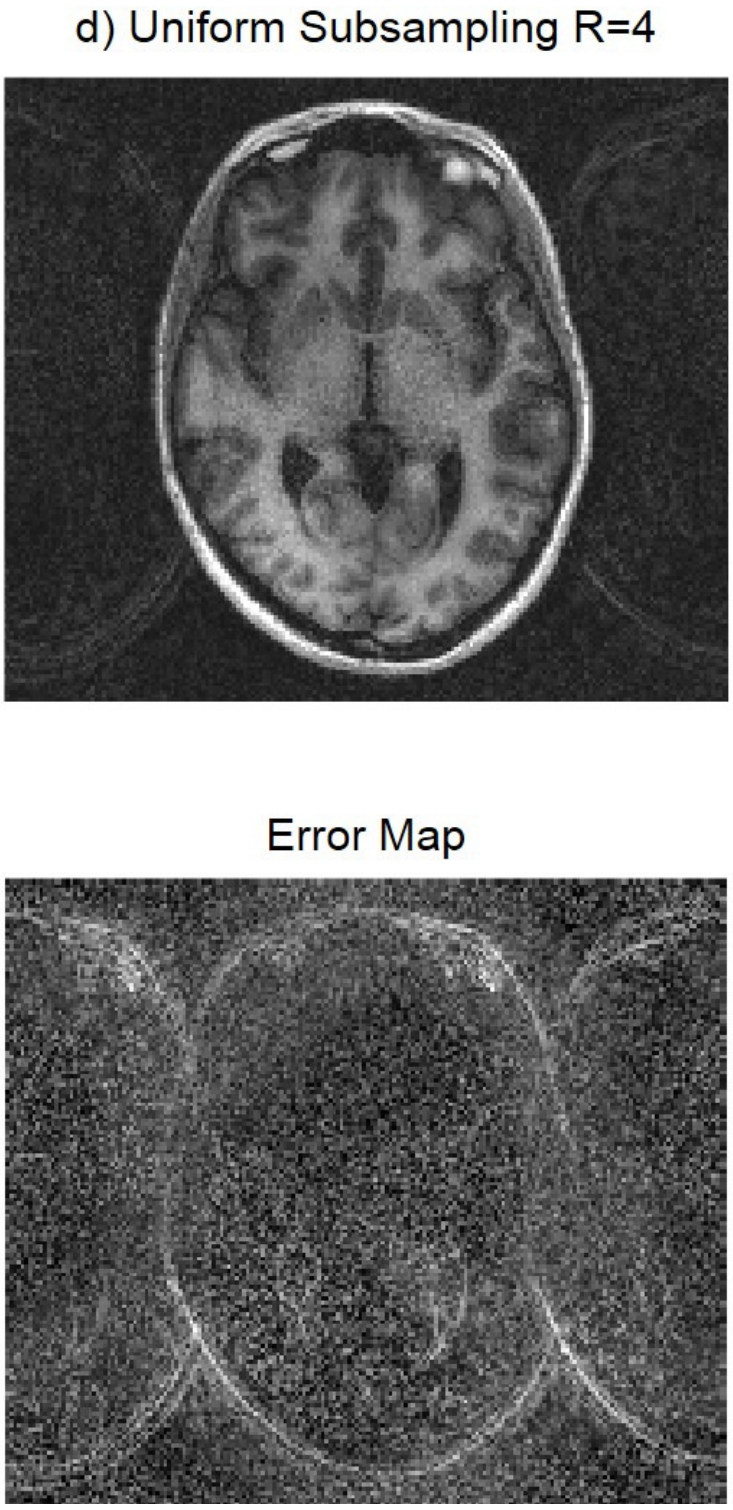

Figure 3.4: ***(d)*** *CS-PI (ℓ1-ESPIRiT) reconstruction and corresponding error map of a 2D section from a healthy volunteer 3D brain acquisition using uniform subsampling pattern with R=4.*

a) 12 x 12 central k-space calibration

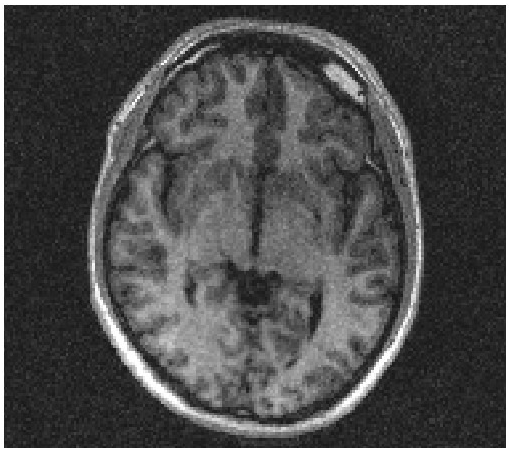

b) 16 x 16 central k-space calibration

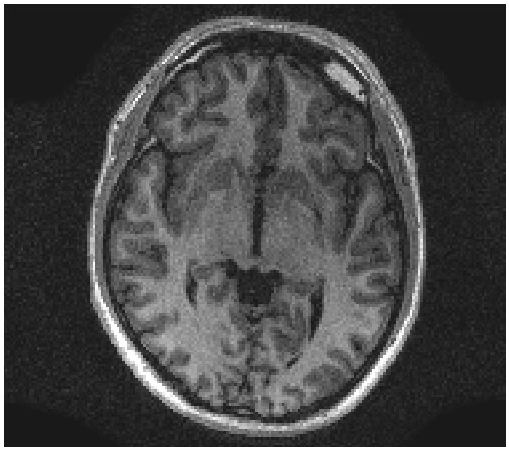

c) 32 x 32 central k-space calibration

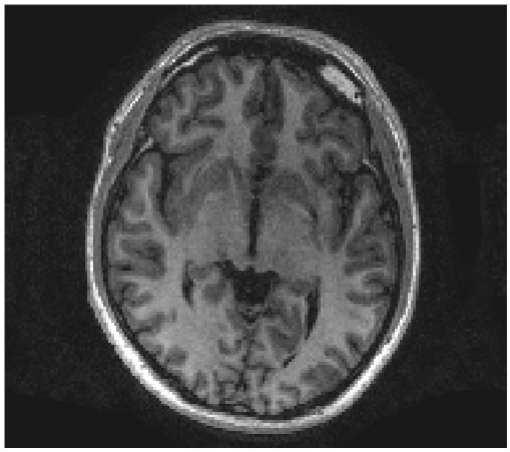

Figure 3.5: *CS-PI (ℓ1-ESPIRiT) reconstructions of a 2D brain section from a healthy volunteer 3D brain acquisition with R=4, Poisson-disc subsampling using* ***(a)*** *12 x 12 central k-space calibration* ***(b)*** *16 x 16 central k-space calibration and* ***(c)*** *32 x 32 central k-space calibration.*

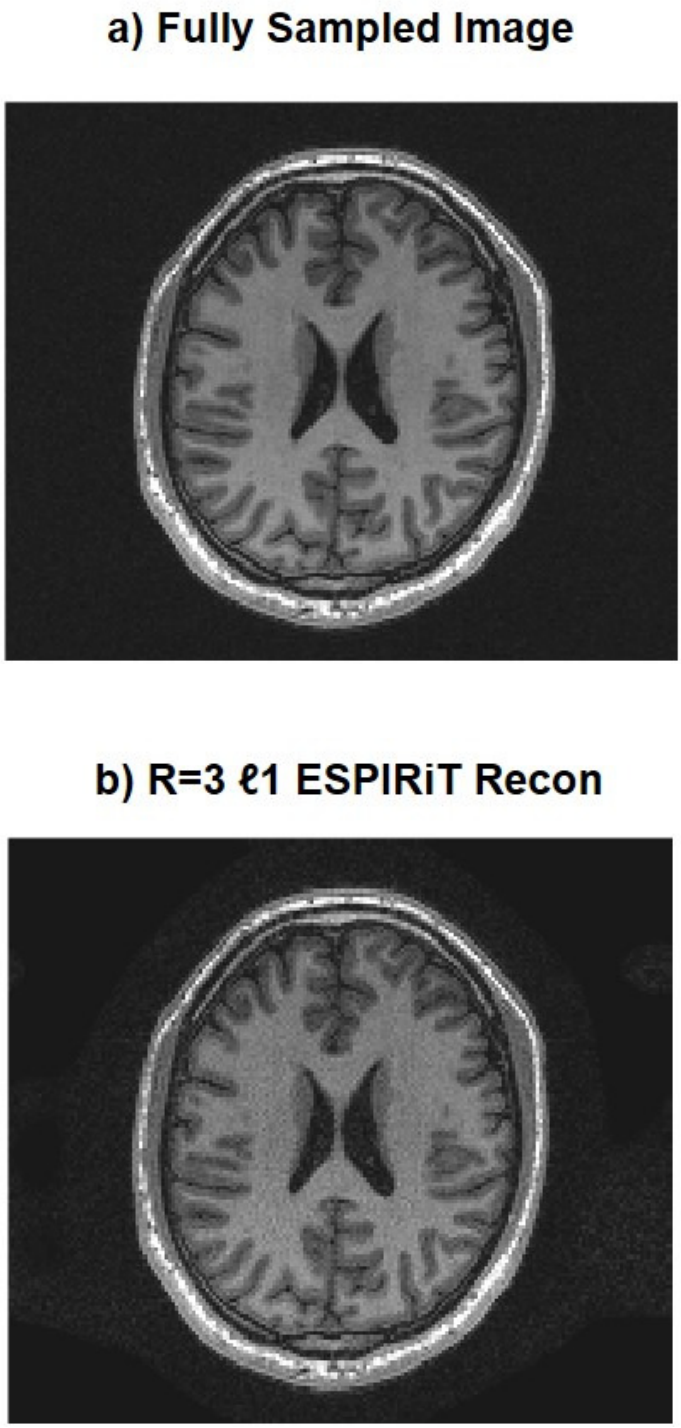

Figure 3.6: ***(a)*** *Fully sampled 2D section of a healthy volunteer 3D brain acquisition and* ***(b)*** *CS-PI (ℓ1-ESPIRiT) reconstruction of the same 2D section using Poisson-disc subsampling pattern and three fold acceleration (R=3).*

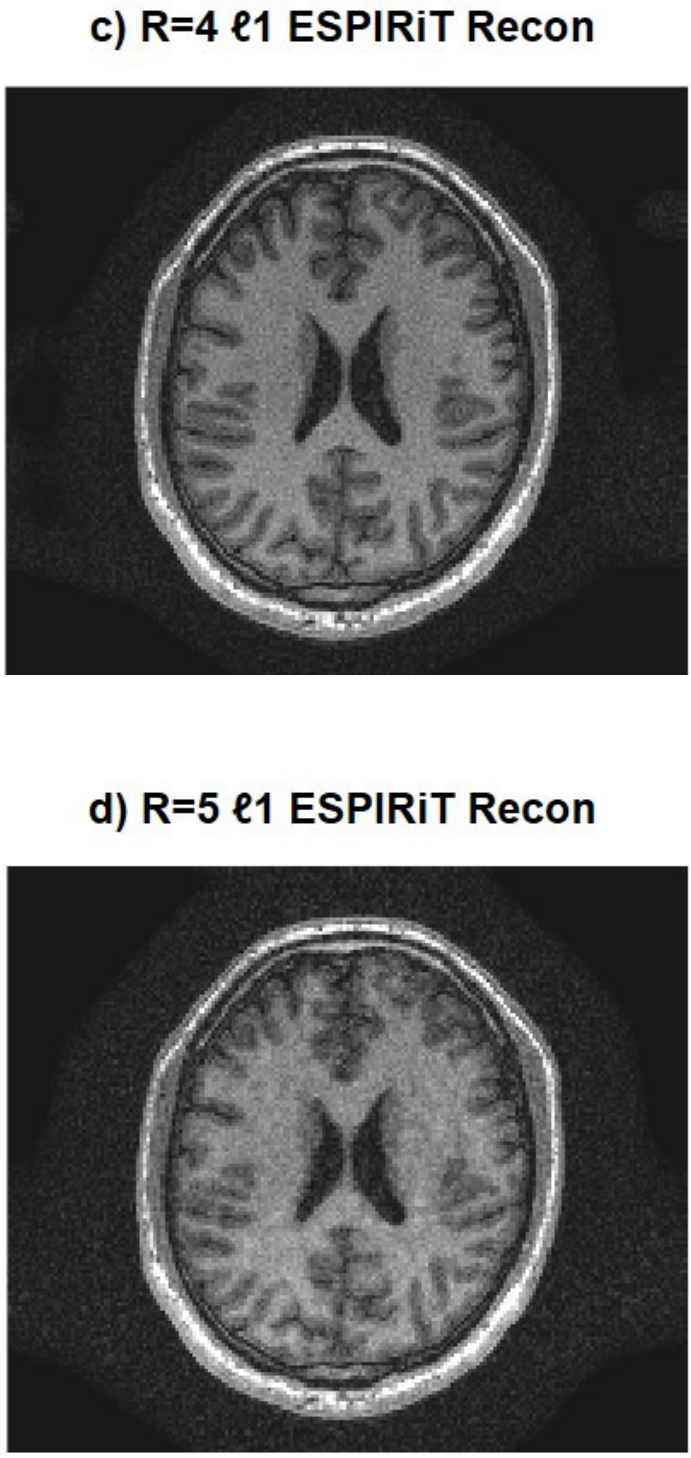

Figure 3.6: *CS-PI (ℓ1-ESPIRiT) reconstructions of a 2D brain section from a healthy volunteer 3D brain acquisition using Poisson-disc subsampling pattern with* ***(c)*** *four fold acceleration (R=4) and* ***(d)*** *five fold acceleration (R=5).*

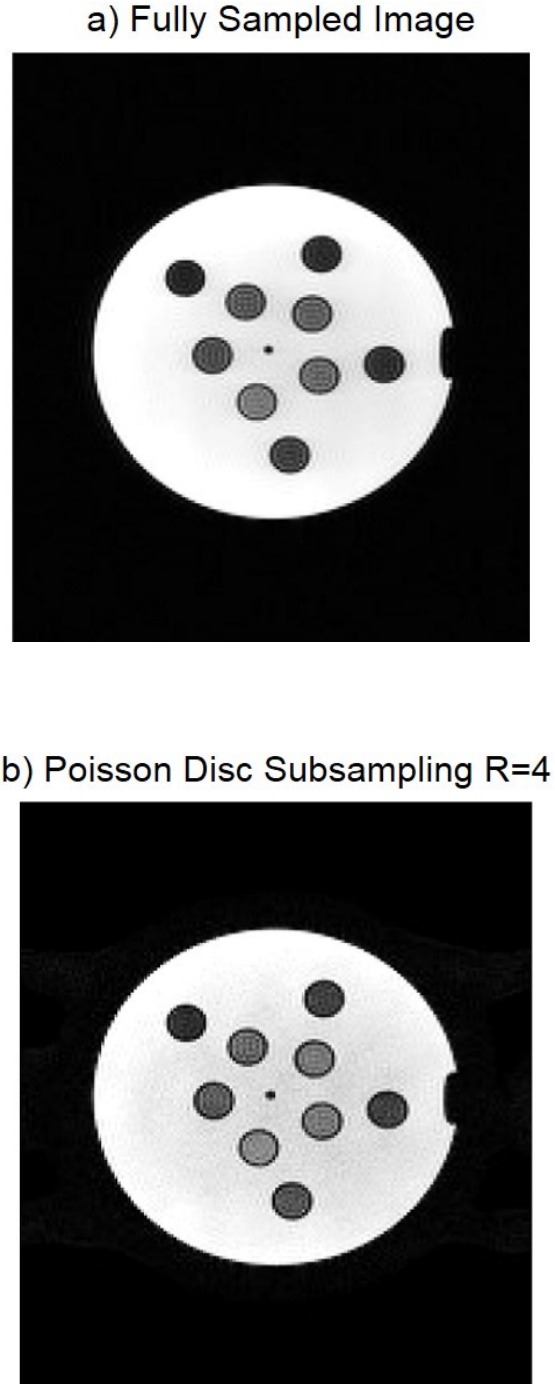

Figure 3.7: ***(a)*** *Fully sampled 2D section of a phantom from a 3D acquisition and* ***(b)*** *CS-PI (ℓ1-ESPIRiT) reconstruction of the same 2D section that is 'prospectively accelerated' four times (R=4) using Poisson-disc subsampling pattern. Note that the k-space acquisition order of the subsampling patterns were not optimized.*

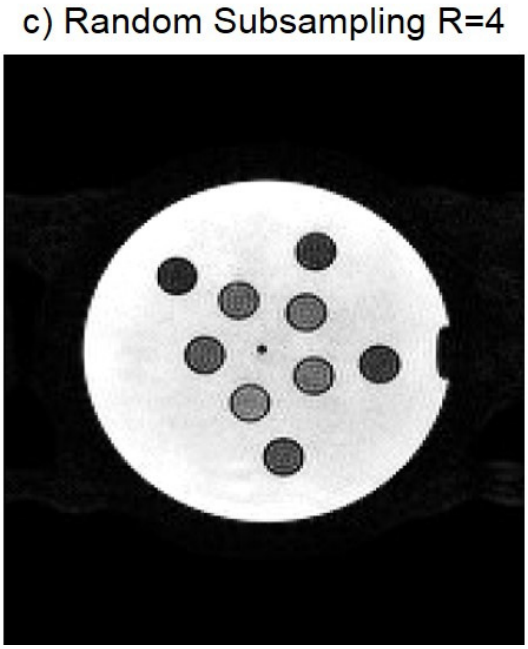

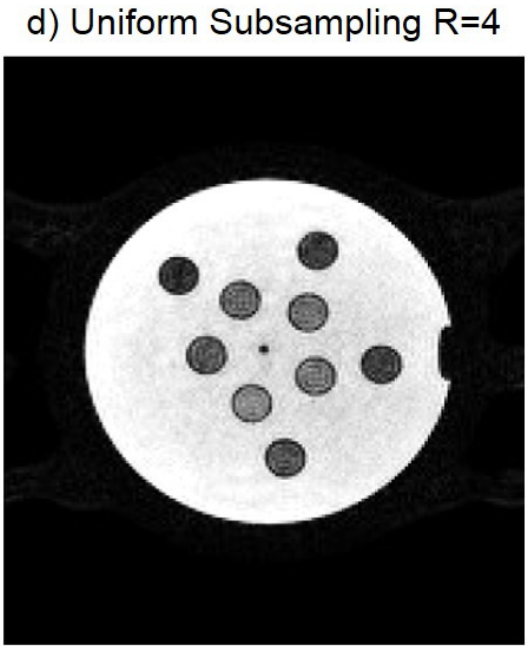

Figure 3.7: *CS-PI (ℓ1-ESPIRiT) reconstructions of a four times (R=4) 'prospectively accelerated' 2D section of a phantom from a 3D acquisition using* ***(c)*** *random subsampling pattern and* ***(d)*** *uniform subsampling pattern. Note that the k-space acquisition order of the subsampling patterns were not optimized.*

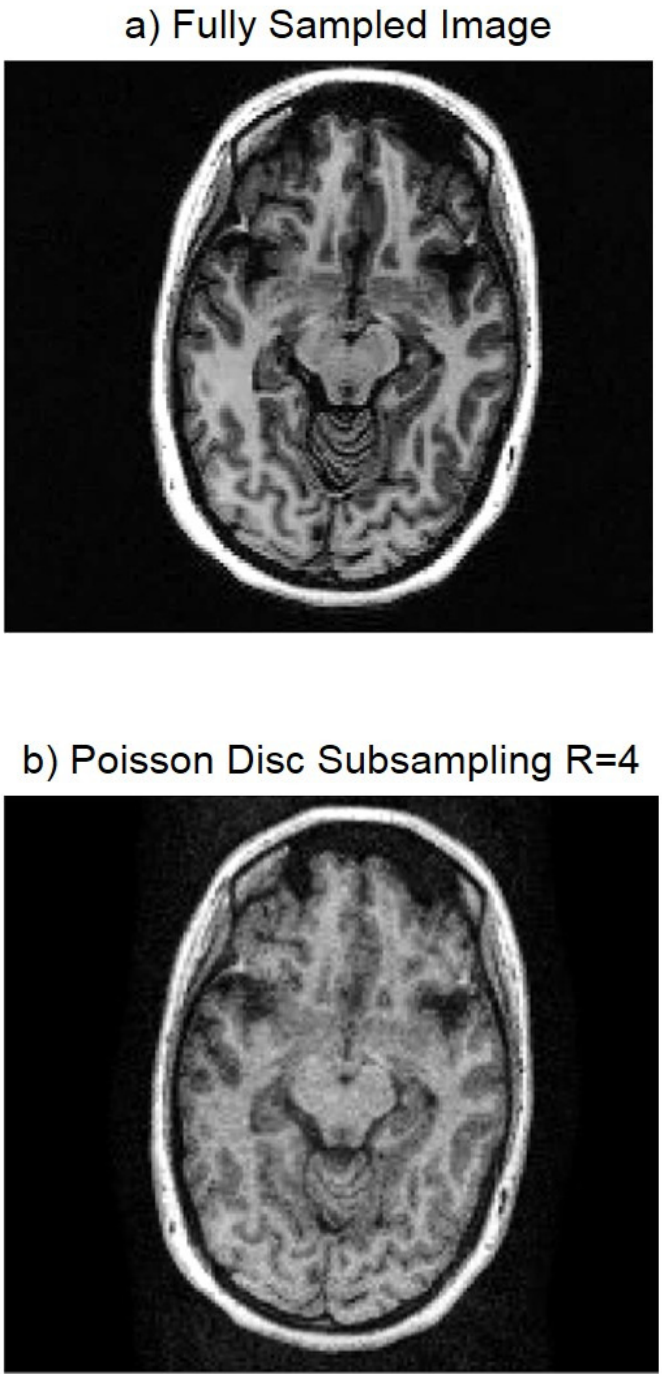

Figure 3.8: ***(a)*** *Fully sampled 2D section from a healthy volunteer 3D brain acquisition and* ***(b)*** *CS-PI (ℓ1-ESPIRiT) reconstruction of the same 2D section that is 'prospectively accelerated' four times (R=4) using Poisson-disc subsampling pattern. Note that the k-space acquisition order of the subsampling patterns were not optimized.*

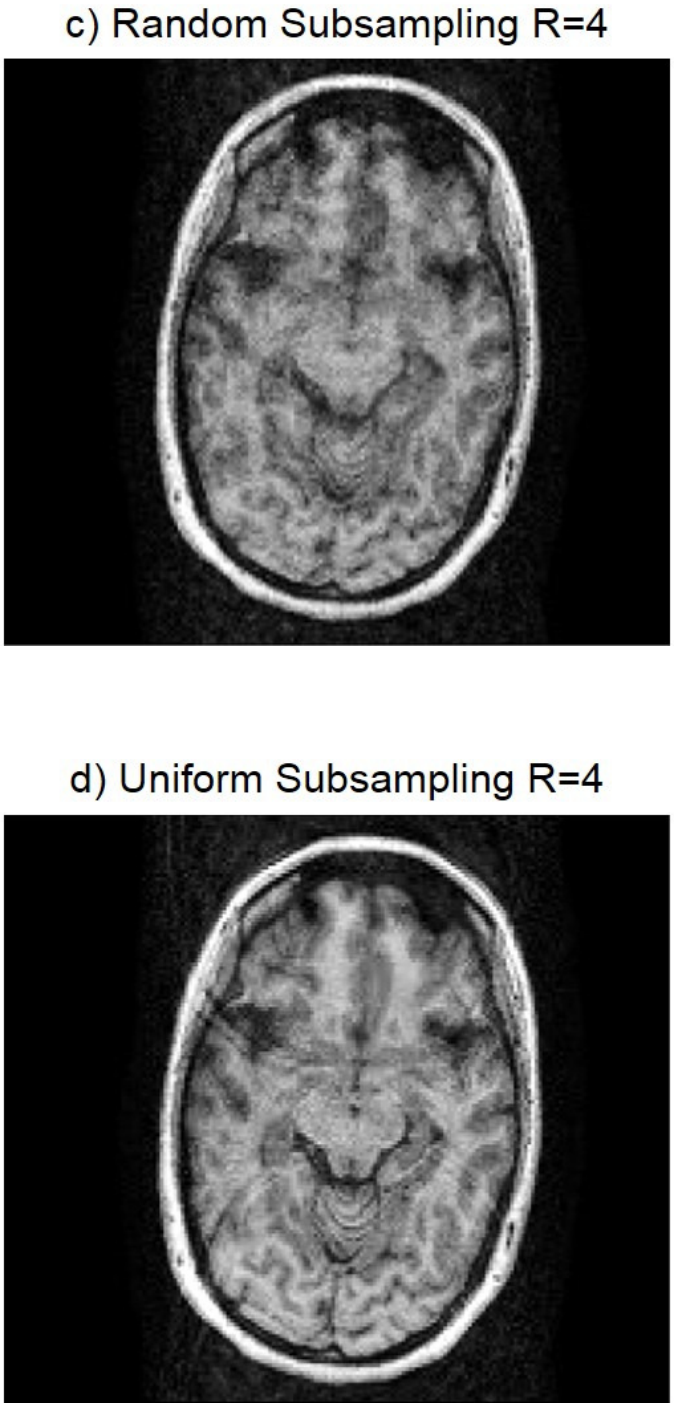

Figure 3.8: *CS-PI (ℓ1-ESPIRiT) reconstructions of a four times (R=4) 'prospectively accelerated' 2D section of a healthy volunteer 3D brain acquisition using* ***(c)*** *random subsampling pattern and* ***(d)*** *uniform subsampling pattern. Note that the k-space acquisition order of the subsampling patterns were not optimized.*

The importance of k-space acquisition order is illustrated in Figure 3.9 which shows two fully sampled brain datasets that were acquired using different sampling orders from the same healthy volunteer. In the first acquisition shown in Figure 3.9a, the samples were acquired at the maximum inherent contrast using a sampling order optimized pattern. However, in the second acquisition, the scan was repeated without sampling order optimization as shown in Figure 3.9b. The color bars in Figure 3.9 represent the time instant at which the samples were collected. The blue colour in Figure 3.9 represents the time instant at beginning of the readout period when the inherent contrast of the sequence is maximum while the red colour represents the time instant at the end of the readout period when the inherent contrast of the sequence is minimum. Acceleration of the IR-prepared 3D GRE sequence (with and without sampling order optimization) is shown in Figure 3.10. Two different subsampling patterns with 3-fold acceleration are shown in Figure 3.10a and 3.10b. In Figure 3.10a, the k-space acquisition is centric-ordered (i.e the acquisition starts from the centre and gradually moves outward in both directions at the start of each readout period). As a result, the central k-space data along the entire $k_y - k_z$ plane is acquired at the beginning of each readout period when the inherent contrast of the sequence is maximum. In Figure 3.10b, k-space ordering is from left to right (i.e. normal Cartesian acquisition). In this acquisition, the central k-space data is acquired at random time instants during the readout period as represented by the colours in the subsampling pattern. The comparison of the reconstructions shows the importance of sampling order optimization in CS accelerated neuroimaging of the IR-prepared 3D GRE sequence.

3.4 Discussion

As described in Section 3.2.3, retrospective simulation of undersampling was carried out on fully sampled healthy volunteer brain data to determine CS acquisition and acceleration parameters that produced the highest image quality. The CS-PI reconstructions and error maps in Figure 3.4 show that the CS-PI reconstruction using the Poisson disk subsampling pattern was able to recover the the image more accurately than the other two cases. This is validated by the smaller nRMSE value for the Poisson-disc subsampling scheme compared to random and uniform subsampling schemes. Among the three different subsampling patterns, the Poisson disk subsampling performed best since it had the smallest error and the best visual quality when compared to the fully sampled image. The other subsampling patterns produced aliasing artefacts and were more noisy than Poisson disc $\ell 1$-ESPIRiT reconstructions. Therefore, Poisson disk subsampling was chosen as the optimal subsampling pattern for this study.

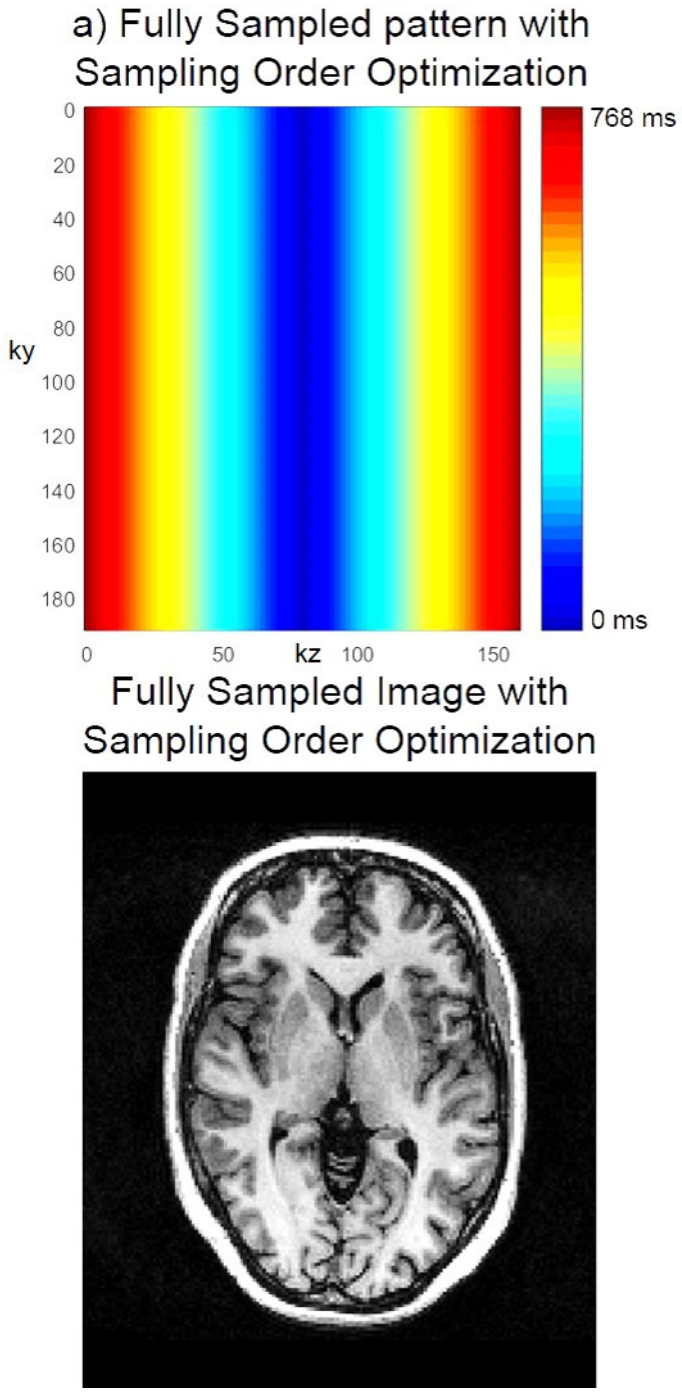

Figure 3.9: (a) *Fully sampled pattern with sampling order optimization along with a reconstructed 2D section from a healthy volunteer 3D brain acquisition.*

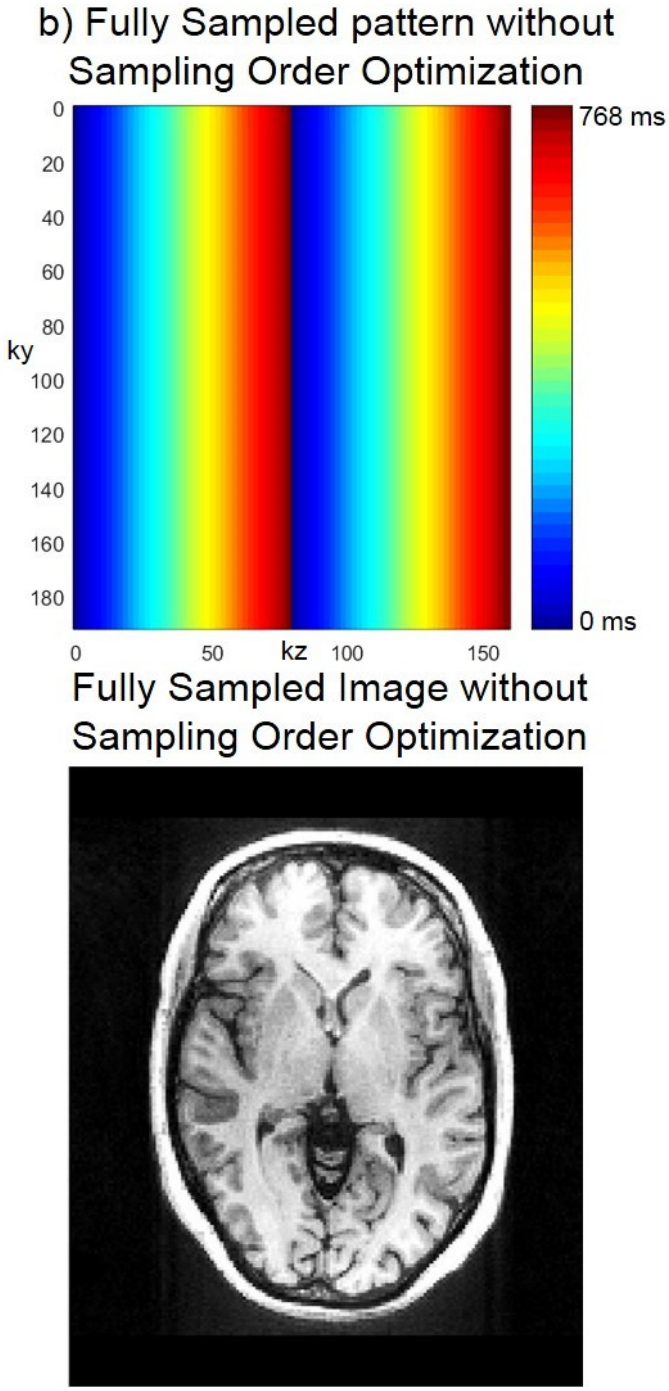

Figure 3.9: ***(b)*** *Fully sampled pattern without sampling order optimization along with a reconstructed 2D section from a healthy volunteer 3D brain acquisition. Note the difference in image contrast between the two reconstructed images in Figures 3.9a and 3.9b even though both acquisitions contained the same number of samples. The colour bars represent the time instant at which data samples were collected for each readout during acquisition.*

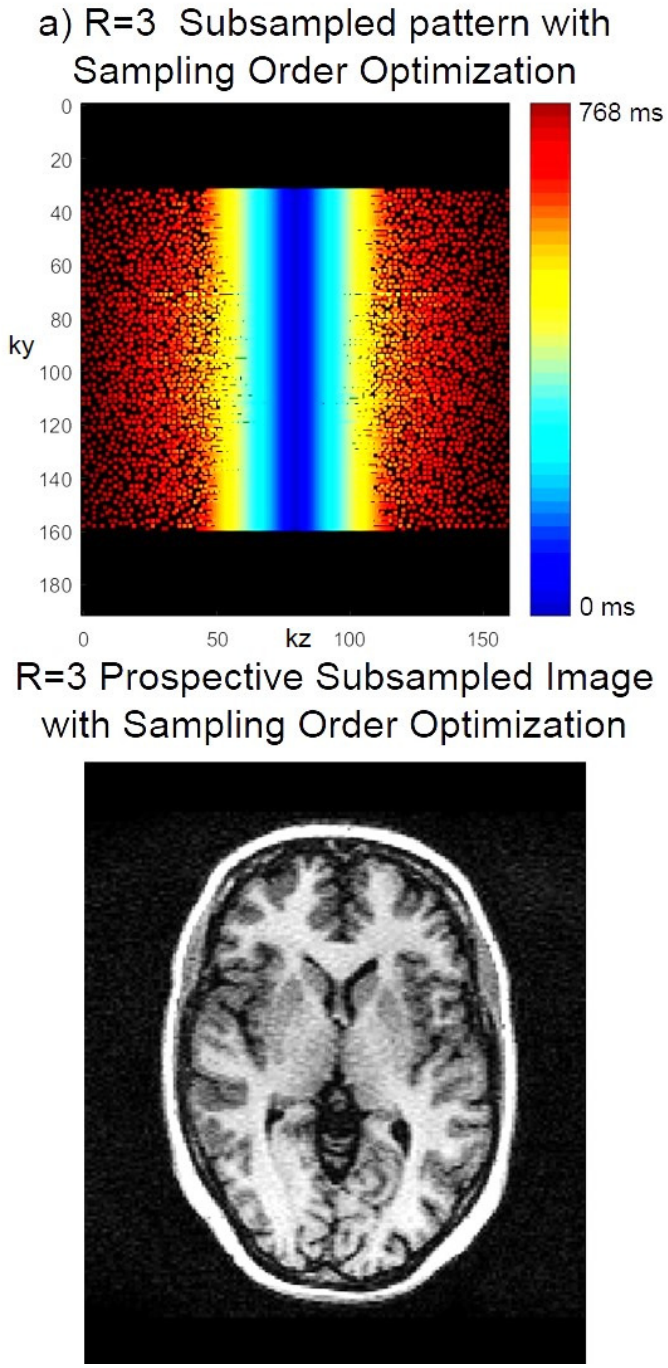

Figure 3.10: ***(a)*** *Three times accelerated (R=3) subsampling pattern with sampling order optimization along with a CS-PI (ℓ1-ESPIRiT) reconstructed 2D section from a healthy volunteer 3D brain acquisition that has been 'prospectively accelerated'.*

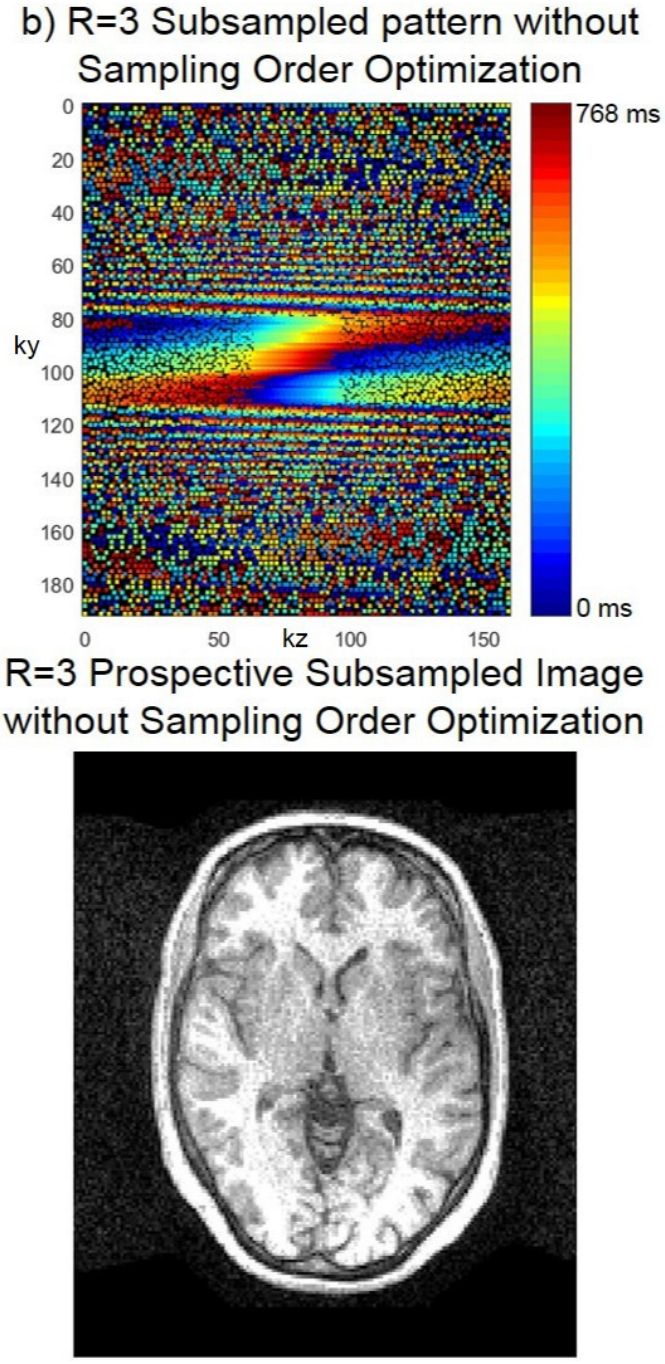

Figure 3.10: ***(b)*** *Three times accelerated (R=3) subsampling pattern without sampling order optimization along with a CS-PI (ℓ1-ESPIRiT) reconstructed 2D section from a healthy volunteer 3D brain acquisition that has been 'prospectively accelerated'. Note the loss in image contrast in Figure 3.10b due to the non-optimization of k-space acquisition order. Both acquisitions in shown in Figure 3.10 had the same acceleration factor (i.e. R=3). The colour bars represent the time instant at which data samples are collected for each readout during acquisition.*

The $\ell 1$-ESPIRiT algorithm uses the wavelet transformation as the sparsifying transform which has been shown to work well for accelerating MR images of the brain [14]. Since the wavelet transform contains highly correlated low frequency content, it is important to fully sample the k-space region that contains the low frequency information. The central k-space ($k_y - k_z$) region (i.e. sometimes called the calibration region) contains the low frequency features of the image and most of the contrast information. It should be fully sampled to capture the low frequency information of the image which are not sparse in the wavelet domain and to generate accurate sensitivity maps of multiple coils that significantly improve the image quality of CS-PI reconstructions. From Figure 3.5, it can be seen that a central calibration region of 32 $\times$ 32 samples sufficiently retained GM and WM brain structures, contained less noise and had a lower nRMSE value when compared to 16 $\times$ 16 or 12 $\times$ 12 central calibraion data. Increasing the calibration size to 64 $\times$ 64 central k-space samples showed a very small (i.e. 0.5%) decrease in nRMSE error while it did not visually improve the reconstruction. Therefore, for this study, the calibration size was set to 32 $\times$ 32 central k-space samples.

In general, for MR acceleration techniques, there is a trade-off between the amount of acceleration that can be applied and acceptable image quality. In order to find the optimal acceleration factor R, subsampling patterns with varying acceleration factors were tested retrospectively using $\ell 1$-ESPIRiT reconstruction. It can be seen from Figure 3.6 that CS-PI ($\ell 1$-ESPIRiT) reconstructions up to an acceleration factor of 4 retained all the important grey matter and white matter brain structures. Figure 3.6d shows that at an acceleration factor of 5, some structures within the brain (i.e. deep grey matter structures surrounding the ventricles) are highly blurred and the reconstructions are more noisy. Therefore, it was decided that that the highest acceptable acceleration factor was 4.

The regularization parameter, 'λ' plays an important role in the image quality of CS-PI based MR reconstructions [12, 46, 158]. It usually depends on the clinical application, sequence used for acquisition, acceleration factor and image intensity. The optimal value of the regularization parameter is usually calculated empirically by using a wide range of values during retrospective reconstructions [7, 14]. Very low values resulted in noisy reconstructions while high values resulted in overly smooth reconstructions which made the reconstructions look artificial. It should be noted that the value of λ can be subjective. As described in Section 3.2.3, the value was chosen in consultation with a neuroradiologist who preferred reconstructed images that had an acceptable trade-off between noisy reconstructions and overly smooth images. The

value of 'λ' was 0.025 in the preferred reconstruction among four different reconstructions with different values of 'λ' that were shown to the neuroradiologist. The regularization parameter 'λ' was fixed at this value for both the retrospective and prospective reconstructions.

After determining the parameters such as calibration size, type of subsampling pattern and maximum amount of acceleration from the retrospective experiments, the ℓ1-ESPIRiT algorithm was tested on CS accelerated prospective phantom and healthy volunteer brain data. The CS-PI reconstructions of the 4-fold accelerated prospective datasets of the phantom in Figure 3.7 show that all the three subsampling patterns (i.e. Poissson-disc, random and uniform subsampling) used in this study were able to produce good quality reconstructed images. In contrast, the CS-PI reconstructions of 4-fold accelerated prospective healthy volunteer brain in Figure 3.8 show that the quality of reconstructed images that utilized Poisson-disc subsampling is better when compared to random and uniform subsampling patterns. Even though the Poisson disk subsampling pattern provided the best image quality among the three different subsampling patterns which was also shown for the retrospective experiments in Figure 3.3, it should be noted that there is a clear loss of contrast between the fully sampled image in Figure 3.8a and prospectively accelerated brain images in Figures 3.8b, 3.8c and 3.8d. The loss of contrast in the prospectively accelerated brain images is due to the non-optimization of the k-space acquisition order which is an important parameter that needs to be carefully optimized while accelerating magnetization prepared sequences such as the IR prepared 3D GRE sequence used in this study.

The fact that the loss of contrast was not observed in the reconstructed images of the prospectively subsamped phantom might be due to two reasons: Firstly, the phantom is made up of simple uniform circular structures with high SNR compared to the brain. Therefore, the phantom proved to be an over-simplification of the complicated structures within the human brain leading to good-quality CS-PI prospective reconstructions. Secondly, the IR-prepared 3D GRE sequence used in this study is optimized to maximize T1 contrast in the brain and is not optimized for phantom scanning. The inversion time (TI) for this sequence is fixed and it is optimized to maximize the contrast between GM and WM in the brain. Hence, the TI should be changed to an appropriate value to maximize the contrast between the different tubes in order to observe differences in image contrast in the phantom. The reconstructions in Figure 3.7 show that it is important to choose a phantom that better represents the complex human anatomy and can mimic the complicated structures in the human body for validation of accelerated structural

MR imaging. It also highlights a significant drawback in using a simple phantom as a proof of concept for accelerated structural MR imaging of a complicated human anatomy such as the brain.

The major purpose of this study was to highlight the important role of k-space acquisition order optimization for preserving contrast in magnetization prepared sequences such as the IR-prepared 3D GRE sequence. In order to highlight the importance of sampling order, two fully sampled brain datasets with different acquisition orders were acquired from the same healthy volunteer. In the first acquisition, the samples were acquired at the maximum inherent contrast as shown in Figure 3.9a. However, in the second acquisition, the scan was repeated without sampling order optimization as shown in Figure 3.9b. In Figure 3.9a, the central k-space data was collected at the beginning of each readout during acquisition whereas in Figure 3.9b, only half of the central k-space data was collected with optimum contrast at the beginning of each readout. Since the k-space acquisition order in Figure 3.9b was not optimized for maximizing tissue contrast, a degradation in the image contrast can be clearly seen even though the number of samples and scan time were identical to Figure 3.9a which used a k-space acquisition order optimized sampling pattern for the fully sampled acquisition.

The sampling order optimization for CS accelerated prospective scanning was carried out as follows. Acceleration was performed along both phase encoding directions (i.e. k_y & k_z) to gain substantial reduction in overall scan time. Two different subsampling patterns with 3-fold acceleration are shown in Figure 3.10a and 3.10b. The subsampling pattern shown in Figure 3.10a is the proposed k-space acquisition order optimized subsampling pattern for preserving the contrast in accelerated prospective scanning. The k-space acquisition is centric-ordered (i.e the acquisition starts from the centre and gradually moves outward in both directions). Here, the number of k_z samples acquired for a given value of k_y is forced to be a sub-multiple (i.e. 40 in this case) of 80 which is the fixed number of k_z samples that is *always* acquired starting exactly at 500 ms after each inversion pulse.

The imposition of this constraint for each k_y value ensures that the start of acquisition of central k_z samples for each new k_y value corresponds with the beginning of each new readout period and occurs exactly at 500 ms after each inversion pulse. In this scenario, a single line of 80 k_z samples starting from the centre will be acquired for a given k_y value after the application of each inversion pulse. More importantly, the start of acquisition of k_z samples for the next k_y value will take place exactly after 500 ms of the next inversion pulse. Therefore, the central k_z

samples for all given values of k_y will be acquired at the highest contrast which results in the preservation of tissue contrast in accelerated scanning.

In the sampling pattern shown in Figure 3.10b, k-space ordering is from left to right (i.e. normal Cartesian acquisition). Subsampling results in the acquisition of a reduced number of k_z samples for a given k_y value. Even though the number of acquired samples along each line is reduced during the accelerated acquisition, the readout period (i.e. 768 ms) is fixed for this sequence and it controls the timing of the inversion pulses. As a result, 80 k_z samples are *always* acquired starting exactly at 500 ms after every inversion pulse. Therefore, the acquisition continues until 80 k_z samples are collected for each readout period of 768 ms duration. So, k_z samples of the next line (i.e. for a different k_y value) are acquired at a lower contrast in the middle of the current readout period until the required number of k_z samples (i.e. 80) are acquired for each readout period. For the next readout period, the acquisition does not start from the k-space centre at the beginning of the new readout period. Therefore, in this acquisition, central k-space samples which contain most of the contrast information in the image were not acquired at the appropriate time instant when there is maximum inherent contrast as shown by the colours in the subsampling pattern in Figure 3.10b. This type of acquisition leads to severe loss of contrast and elevated noise due to the non acquisition of central k-space data at the appropriate contrast setting as shown by the CS-PI reconstructed image in Figure 3.10b.

The importance of sampling order optimization for contrast preservation in CS accelerated IR-prepared 3D GRE sequence is illustrated in Figure 3.10a and 3.10b. Two different subsampling patterns with varying k-space acquisition ordering were used to acquire the data. Both subsampling patterns had the same acceleration factor (R=3) but sampling order optimization was performed only on one pattern. Figure 3.10a used a sampling order optimized k-space subsampling pattern while the subsampling pattern used in Figure 3.10b was without sampling order optimization. Optimization of k-space acquisition order is very important for accelerated prospective scanning because it not only helps in contrast preservation but also improves the clinical diagnostic utility of accelerated scans [170]. It is conspicuous from Figure 3.10a that the contrast was clearly preserved when the subsampling pattern with k-space acquisition order optimization was used for reconstruction. The reconstructions were less noisy and contained fewer artefacts compared to the subsampling pattern without sampling order optimization that was used in Figure 3.10b. The CS-PI reconstructed image in Figure 3.10b was clinically not useful due to the lack of contrast between various brain structures and the presence of elevated

noise in the reconstructed image.

It is also worth noting that further optimization of this sequence is possible but practical difficulties have limited its implementation in this study. Higher acceleration factors (>3) with acceptable image quality can be achieved according to retrospective experiments but it would require flexibility in the readout period after the application of each inversion pulse. The readout period is currently fixed and cannot be changed using the scanner software. The readout period must be modified according to the number of k_z samples acquired for each k_y value. This would mean that the time interval between two consecutive inversion pulses would need to vary between two readout periods to ensure that the start of acquisition for every k_y value occurs at the k-space centre with maximum inherent contrast setting (i.e. beginning of the each readout period). The inversion pulses should be applied at different time intervals depending on the number of samples acquired for a given k_y value. In order to change the readout period in this sequence, modification of the sequence timing in the pulse sequence source code is required which can be difficult and extremely time-consuming due to the need for advanced programming knowledge in the C++ based GE EPIC (Environment for Pulse programming In C) environment. Therefore, this implementation was not possible in this study but can be an avenue for future research.

It is also important to mention that the use of perceptual metrics such as structural similarity index (SSIM) [171] and perception based image quality evaluator (PIQE) [172] for quantifying the degradation of image quality could have benefited the optimization of CS acquisition and reconstruction parameters. In this study, the nRMSE value was used to quantify the error in the CS-PI reconstructions and it generally does not represent the visual degradation of image quality [173–175]. Lower nRMSE values does not always mean better visual image quality and vice versa. It has been shown previously that images with low nRMSE values can have have very poor visual quality [173–175] and this is illustrated by the CS-PI reconstruction in Figure 3.4d. Even though the difference in nRMSE value is less than 2% when compared to Figure 3.4b, the visual quality of Figure 3.4d is much worse than that of Figure 3.4b as it contains prominent ghosting artefacts. In such cases, SSIM and PIQE could give better indication of the degradation of image quality. Secondly, the fixing of the regularization parameter in this study was subjective and was based on the feedback of image quality from a neuroradiologist. The optimal value of the regularization parameter can be estimated by quantitative evaluation of the images using SSIM and nRMSE values which has been previously reported in the liter-

ature [176, 177]. The regularization parameter can also be robustly estimated using data driven approaches that do not require the empirical tuning of the regularization parameter [178, 179]. Such methods are more objective and could have been beneficial as it would have eliminated the subjectiveness in this study.

In this study, we have shown the significance of k-space acquisition optimization for preserving contrast in magnetization prepared sequences such as the IR-prepared 3D GRE sequence that can be used for CS accelerated neuroimaging. The next step is to test whether the accelerated brain images are clinically usable by performing diagnostic quality assessment of CS accelerated brain images from a cohort of healthy volunteers. The clinical utility of CS accelerated neuroimaging is explored in Chapter 4.

3.5 Conclusion

In conclusion, this study showed that the optimization of CS acquisition and reconstruction parameters improved the image quality of CS accelerated reconstructions for brain MRI . More importantly, for CS accelerated prospective neuroimaging, optimization of the k-space sampling order was essential for preserving image contrast. Sampling order optimization could potentially improve the clinical usability of CS-PI accelerated neuroimaging.

Chapter 4

Diagnostic Quality Assessment of IR-prepared 3D Magnetic Resonance Neuroimaging accelerated using compressed sensing and sampling order optimization

In the previous chapter, the importance of sampling order optimization for contrast preservation in CS accelerated neuroimaging was established. This chapter shows the clinical diagnostic efficacy of CS accelerated neuroimaging through radiological evaluations for image quality and artefacts . In addition, the factors that affect the radiological scoring of CS accelerated MR images will be discussed.

4.1 Introduction

As described in Section 1.1, MRI data acquisition is slow and therefore, acceleration of MRI has become an integral part of MR research. There are numerous potential benefits of fast MRI due to the strong clinical need for further MR acceleration. In brief, MRI was traditionally accelerated by PI methods. The emergence of CS showed that further acceleration was possible. By combining CS and PI methods, accelerated MR images with less degradation of image quality and higher SNR can be produced.

Despite the availablity of numerous algorithms and reconstruction methods based on CS-PI techniques [13, 137, 180–182], few studies have carried out diagnostic quality assessment to evaluate the clinical diagnostic utility of CS accelerated acquisitions. Vasanawala et al. [147] found that paediatric images reconstructed using CS techniques were rated more highly than those reconstructed with standard parallel imaging. In contrast, Sharma et al. [154] found significant artefacts that degraded 2D brain images even with an acceleration factor of only

two. However, it must be noted that the amount of acceleration that can be applied to 2D multislice imaging is limited since subsampling can be performed in only one phase encoding direction for reduction in acquisition time. Higher acceleration can be achieved in 3D brain imaging because undersampling can be carried out in two phase encoding directions. Marshall et al. [156] reported that CS accelerated T1 weighted images that were acquired using a 3D inversion recovery sequence showed reduced contrast and degraded image quality, especially for the identification of deep grey matter brain structures such as basal ganglia. Additionally, Kayvanrad et al. [183] concluded that only mild accelerations between two and three were possible in CS accelerated clinical neuroimaging sequences such as fluid attenuated inversion recovery (FLAIR), fast imaging employing steady state acquisition (FIESTA), time of flight and spoiled gradient echo (SPGR) sequences while maintaining diagnostic image quality. Although the clinical usefulness of CS accelerated MRI has been demonstrated in organs such as the heart, knee and abdomen [147], existing studies have shown that the clinical diagnostic utility of CS accelerated neuroimaging is minimal [154, 156, 183].

In this study, we aim to show that IR-prepared 3D neuroimaging accelerated by CS and sampling order optimization retains sufficient clinical diagnostic value for the gross structural assessment of the brain. Through the radiological evaluation of subsampled healthy volunteer 3D brain datasets, we show that CS accelerated neuroimaging has adequate clinical usefulness and can potentially be used for the screening of large tumours. We also demonstrate how the clinical condition to be investigated by radiological assessment significantly influences the radiological scores (RS) and impacts the diagnostic utility of CS accelerated neuroimaging.

4.2 Methods

4.2.1 Image Acquisition

Scanning was performed on a 1.5 T GE Signa HDx scanner with an 8 channel receive only head RF coil (GE Medical Systems, Milwaukee, WI). We obtained informed consent from eight healthy volunteers (3 female; age range 25-50). Fully sampled and accelerated scans were carried out on all eight volunteers using the manufacturer's IR-prepared 3D GRE sequence. The k-space acquisition order was varied for both the fully sampled and accelerated scans in order to evaluate its effect on image quality and contrast. The protocol consisted of a localizer scan that was used to prescribe fully sampled and undersampled 3D T1-weighted IR-GRE scans.

Sequence parameters were: Repetition Time (TR)/Echo Time (TE)/TI = $10/4/500$ ms; flip angle = 8°; matrix 192 x 192 x 160 slices; isotropic 1.3 mm voxels. The image orientation was axial. Phase encoding was performed along the sagittal and coronal planes. The scan time was 8:08 minutes for the fully sampled case and was reduced to a minimum of 2:42 minutes for 3-fold acceleration.

A total of thirty two MRI datasets were collected from the eight healthy volunteers (i.e. 8/32 datasets were fully sampled and 24/32 were subsampled datasets). Three different optimized subsampling patterns with different accelerations (R = 2.34, 2.59, 3) were used to acquire data. K-space acquisition order optimized datasets with higher acceleration factors (R = 3.84, 4.13) were collected from one of the volunteers in addition to the fully sampled and three sampling order optimized subsampled datasets to demonstrate the trade-off between the amount of acceleration and acceptable image quality. The central region of k_y-k_z space was fully sampled while the sampling density was gradually reduced towards the k-space periphery. Sampling patterns were saved as look-up tables on the scanner to replace the standard sequential Cartesian sampling order.

4.2.2 Generation of sampling order optimized subsampling patterns

Figure 4.1 shows the four different sampling order optimized k-space sampling patterns used in this study. Generally, for generating sampling order optimized subsampling patterns, a variable density subsampling is performed. The k-space centre is densely sampled and the sampling density is reduced towards the k-space periphery along the k_y direction. As described in Section 3.3.6, the amount of acceleration that can be applied is restricted by the fact that the time interval between two consecutive inversion pulses for the IR-prepared GRE sequence is fixed and cannot be modified for accelerated acquisitions. This constraint leads to different sampling densities along k_y and k_z directions.

The generation of sampling order optimized subsampling patterns is as follows. A naively subsampled Poisson disc subsampling pattern without sampling order optimization which has been shown previously in Figure 3.9b is used as the starting point to perform sampling order optimization. Firstly, the central k-space data (32 central $k_y - k_z$ samples) are either fully sampled or accelerated by a factor of 2 along the k_z direction. As we move away from the 32 central k-space lines along the k_y direction, the number of k_z samples that are acquired for a given k_y value is gradually reduced. In general, the number of k_z samples that are acquired for

a given k_y value is forced to be a sub-multiple (40, 20, 10) of 80 which is the fixed number of k_z samples that is *'always'* acquired starting from the TI after each inversion pulse. This is done to ensure that the central k_z samples for each subsequent k_y value is acquired at the beginning of each readout period with maximum inherent contrast exactly at 500 ms (i.e. TI) after each inversion pulse.

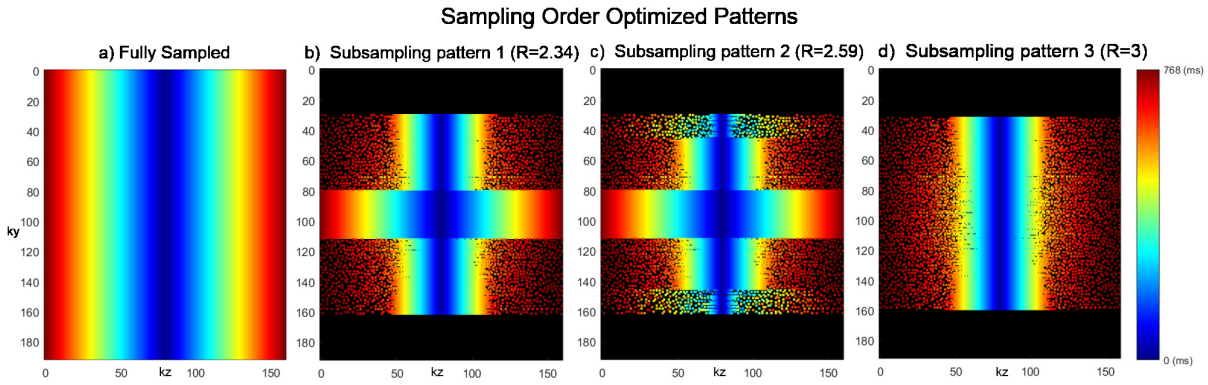

***Figure 4.1:**: Figure showing the k-space acquisition order optimized sampling patterns used in the healthy volunteer study (n=8 subjects). A fully sampled pattern and three subsampling patterns with varying acceleration factors (i.e. R=2.34, 2.59, 3) were used in the study.The colour bars represent the time instant at which data samples are collected for each readout during acquisition.*

During the optimization process, the number of k_z samples acquired for each k_y value in the original Poission disc subsampling pattern shown in Figure 3.9b is first calculated. Remember that k_y runs from k_{y1} at the top left corner to k_{y192} at the bottom left corner. For example, consider a single value of k_y from Figure 4.1b, say k_{y75}. For k_{y75}, the required number of k_z samples from the centre to the periphery on one side is set to 40. The sampling order optimization is performed in two steps:

i) If the number of acquired k_z samples in the original Poisson disc subsampling pattern for k_{y75} exceeded 40, k_z samples would be removed one by one from the periphery to the centre in the original subsampling pattern until the total number of k_z samples for k_{y75} is exactly equal to 40.

ii) If the number of acquired k_z samples in the original Poisson disc subsampling pattern for k_{y75} is less than 40, k_z samples would be added one by one from the centre to the periphery in the original subsampling pattern until the total number of k_z samples for k_{y75} is exactly equal

to 40.

This process is repeated for all k_y values in which the required number of k_z samples is either set to 80, 40, 20 or 10 depending on the distance from the k-space centre. The final step is not to sample some high frequency k_z samples at the k-space extremities as they do not contain enough contrast information. This is the general process that would result in one of the optimized subsampling patterns shown in Figure 4.1. By varying the subsampling density along the k_y direction, different acceleration factors can be achieved. It should however be noted that subsampling patterns with an arbitrary number of k-space samples will not be useful in this scenario as it would not account for the optimization of k-space acquisition ordering and would result in loss of contrast in prospective experiments.

4.2.3 Reconstruction

The images were reconstructed offline using Matlab (Mathworks, Natick, MA) scripts. The reconstructions were based on the compressed sensing-parallel imaging based $\ell 1$-ESPIRiT algorithm [14]. In the first step, estimates of the sensitivity maps of the individual head coil elements were computed from the central region of k-space using the eigenvector approach [14]. This yields high quality sensitivity maps which are crucial for good image reconstruction. In the next step, the CS algorithm solves the minimization problem:

$$\hat{X} = \underset{X}{\operatorname{argmin}} \|Y - \Phi X\|_2^2 + \lambda \|\Psi X\|_1$$

where X is the ground truth and $\hat{X}$ is the estimated image, Y is the acquired undersampled k-space data, Φ is the undersampled Fourier matrix weighted by the estimated coil sensitivities, and ΨX computes the translation invariant wavelet transform of X. A translation invariant Daubechies wavelet of order two (db2) and length four was used. The first term in the above equation ensures data consistency and the second term enforces sparsity in the wavelet domain, with the parameter λ controlling the relative weighting of the two constraints [46]. As described in Section 3.2.3, the value of λ was fixed in consultation with an experienced neuroradiologist to achieve a balanced trade-off between noisy reconstructions and overly smooth images.

4.2.4 Radiological Assessment

Radiological Assessment was carried out to test the clinical applicability of the undersampled 3D Brain Images. The acquired fully sampled and undersampled image datasets from the eight healthy volunteers were anonymized, randomly coded and transferred to a picture archiving and communication system (PACS) for storage, retrieval and review. Images were accessed using Carestream PACS (v11, Carestream Health Inc. Rochester. NY, USA) and viewed as multiplanar reformats. Four experienced neuroradiologists, blinded to the acceleration factor and subsampling pattern, independently assessed image quality and artefacts. The neuroradiologists were not given any specific instructions before the radiological evaluation on what type of clinical question was being investigated. This led to one neuroradiologist performing the radiological assessment based on a more stringent clinical question compared to the other three neuroradiologists.

RADIOLOGICAL SCORING KEY	
SCORE	**SPATIAL RESOLUTION SCORING**
0	Non-diagnostic
1	Poor quality (partly non-diagnostic)
2	Moderate quality (fully diagnostic)
3	Good quality
4	Excellent quality
SCORE	**ARTEFACT SCORING**
0	Severe artefact
1	Moderate artefact (partly non-diagnostic)
2	Minor artefact (fully diagnostic)
3	No artefact
Four different brain regions namely precentral gyrus, temporal gyri, brainstem and basal nuclei were each scored from 0 to 4 and the artefacts were scored from 0 to 3. The maximum possible overall score was 19.	

Table 4.1: *Table showing the radiological scoring key that was used for radiological assessment. The scores ranged from 0 (i.e. completely non-diagnostic) to 19 (i.e. excellent quality). The scoring was done to evaluate image quality of four different brain regions and for assessing the amount of artefacts that were present in the images.*

Of the four neuroradiologists, three of them (i.e. Radiologist 1, 2 & 3) evaluated the image datasets for routine structural assessment as might be applied in patients with non-specific headache and a clinical requirement to exclude tumour (based largely on grey and white matter boundaries, and cerebrospinal fluid distribution). One neuroradiologist (i.e. Radiologist 4) evaluated the same image datasets for tasks that required high spatial resolution and grey-white matter differentiation such as seeking developmental lesions responsible for epilepsy. The grading was based on a radiological scoring key from the literature that was previously used for evaluating 100 infant human brain examinations for image quality and artefacts [184]. The scoring key is shown in Table 4.1 with 0 being non-diagnostic and 4 being excellent quality for four different brain regions namely precentral gyrus, temporal gyri, brainstem and basal nuclei, while the artefacts were scored as 0 for severe artefact and 3 for no artefact. Image quality was rated for spatial resolution based on corticomedullary differentiation of the precentral gyrus and temporal gyri; delineation of the brain stem nuclei and basal ganglia. Scores were summed resulting in a range from 0 (very poor quality with severe imaging artefacts) to 19 (excellent quality with no imaging artefacts). The mean radiological scores (RS) of each neuroradiologist was calculated and analyzed for each of the four different brain regions and also for imaging artefacts.

4.3 Results

The CS-PI reconstructions of three representative axial slices of the fully sampled and undersampled acquisitions are shown in Figure 4.2 for three healthy volunteers selected randomly from the entire cohort. The image quality of undersampled images is comparable to fully sampled images and shows clear differentiation between different brain tissues including deep grey matter structures such as the basal ganglia. Figure 4.3 shows the independent radiological assessments of three neuroradiologists who carried out gross structural assessment and one neuroradiologist who performed high spatial resolution assessment. These assessments also show the mean $\pm$ standard error (SE) of fully sampled and three optimized CS accelerated image datasets for four different brain regions along with the mean artefact scoring.

Figure 4.4 shows the comparison of the mean RS of all four neuroradiologists who carried out radiological assessment for image quality and artefacts. The Bland Altman analysis in Figure 4.5 shows the radiological scoring agreement between the two different clinical conditions explored in this study (i.e. gross structural assessment vs high spatial resolution assessment).

Furthermore, visible degradation of brain structures was clearly seen for higher acceleration factors (i.e. R = 3.84, 4.13) even though the k-space acquisition order was optimized as shown in Figure 4.6. Therefore acceleration factors greater than 3 were considered not useful for clinical diagnosis due to strong deterioration in image quality and the presence of severe artefacts.

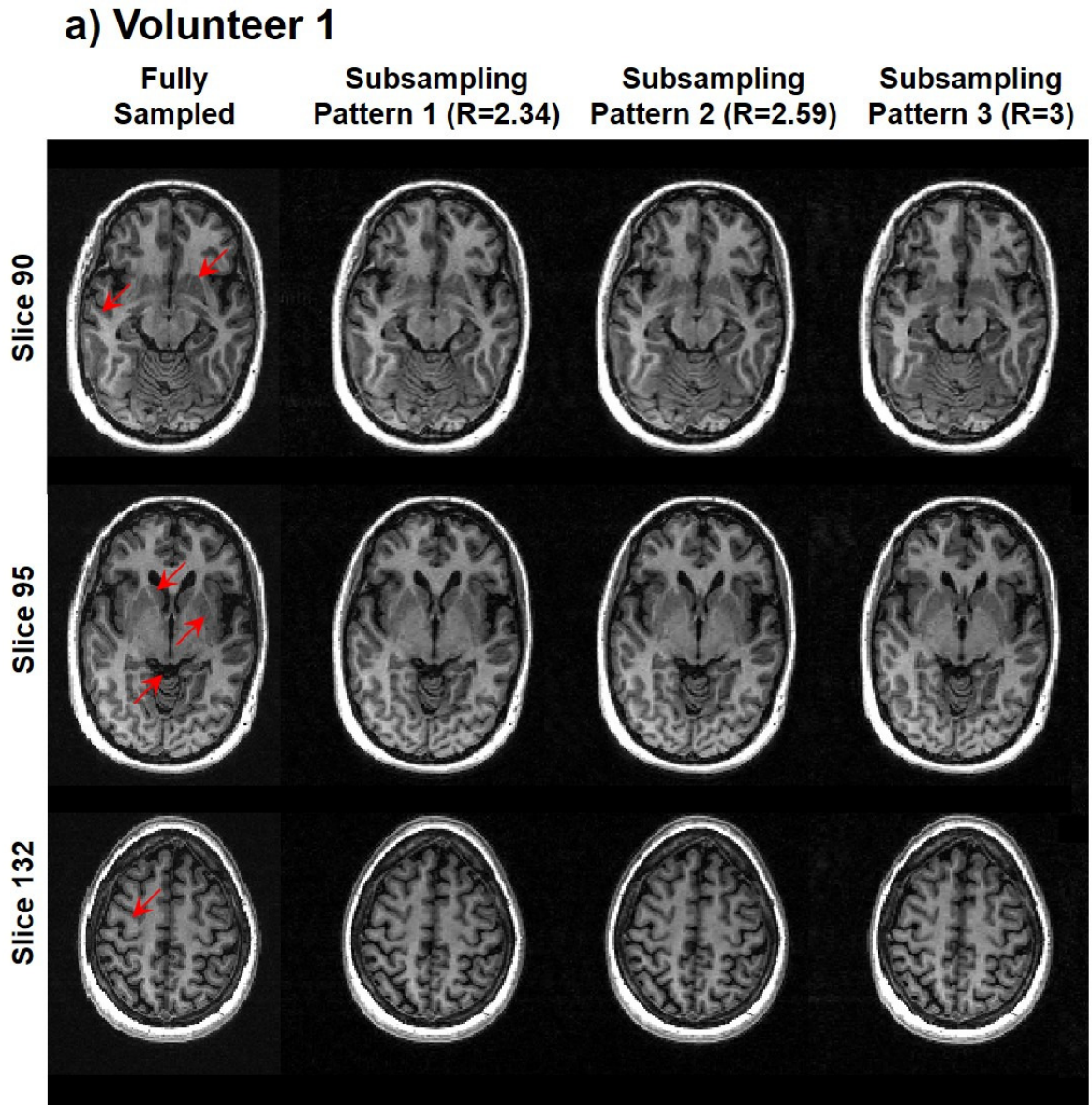

Figure 4.2: (a) *Figure showing the CS-PI reconstructions of k-space acquisition order optimized sampling patterns used in the healthy volunteer study (n=8 subjects). The reconstructions using fully sampled pattern and three subsampling patterns with varying acceleration factors (i.e. R=2.34, 2.59, 3) are shown for volunteer 1 selected randomly from the cohort. Three representative axial slices were selected for illustration.*

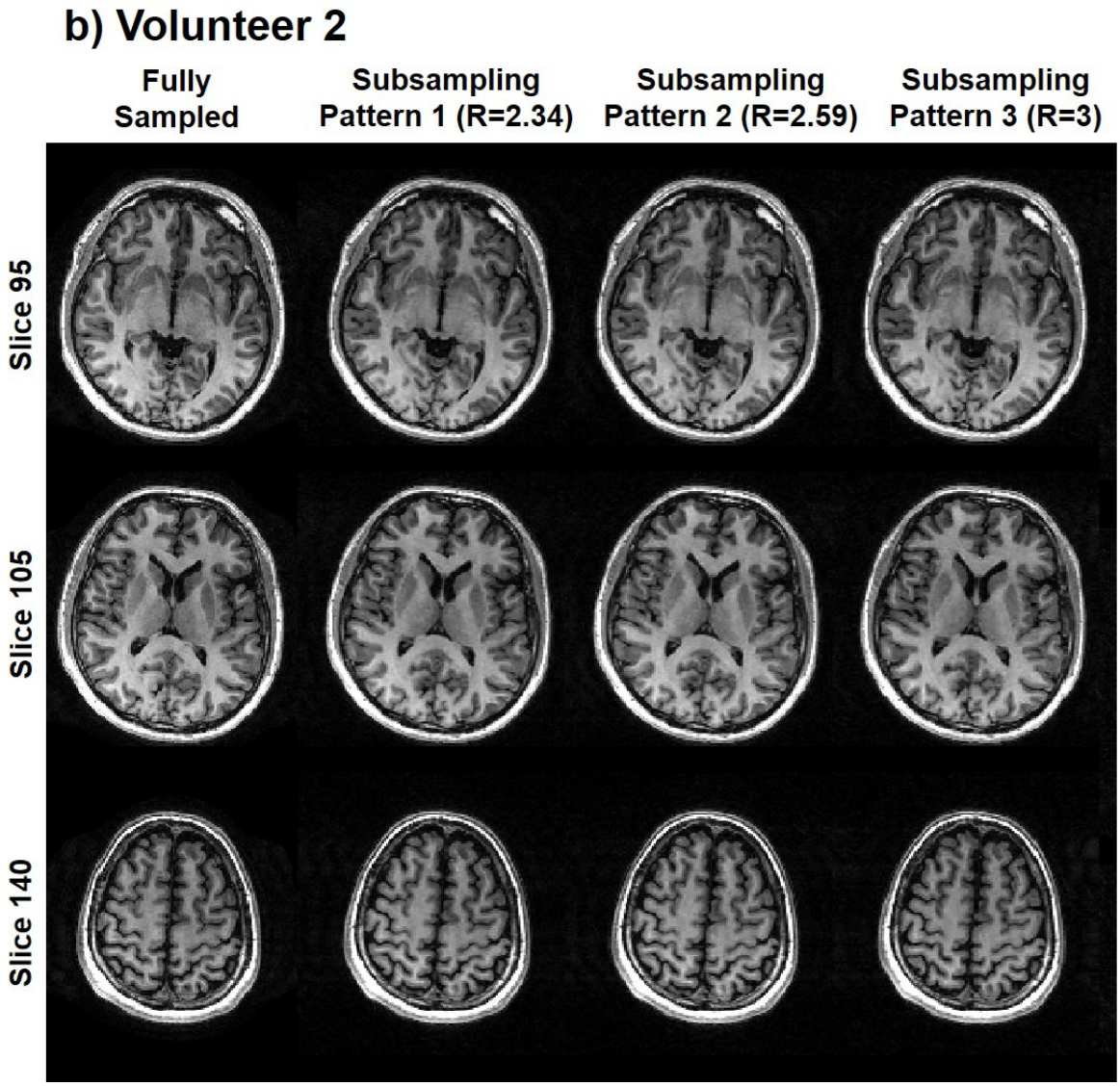

Figure 4.2: (b) *Figure showing the CS-PI reconstructions of k-space acquisition order optimized sampling patterns used in the healthy volunteer study (n=8 subjects). The reconstructions using fully sampled pattern and three subsampling patterns with varying acceleration factors (i.e. R=2.34, 2.59, 3) are shown for volunteer 2 selected randomly from the cohort. Three representative axial slices were selected for illustration.*

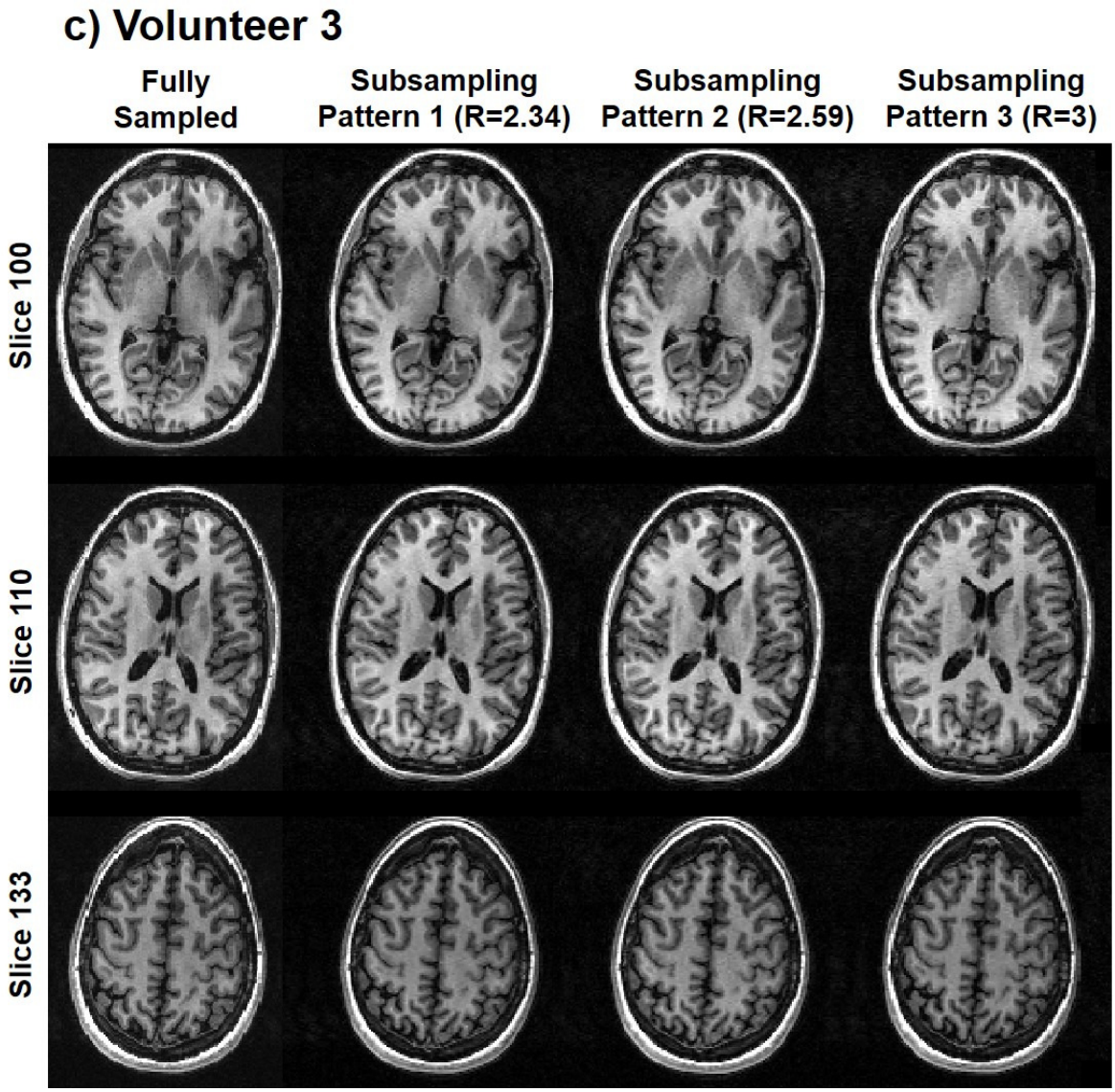

Figure 4.2: ***(c)*** *Figure showing the CS-PI reconstructions of k-space acquisition order optimized sampling patterns used in the healthy volunteer study (n=8 subjects). The reconstructions using fully sampled pattern and three subsampling patterns with varying acceleration factors (i.e. R=2.34, 2.59, 3) are shown for volunteer 3 selected randomly from the cohort. Three representative axial slices were selected for illustration.*

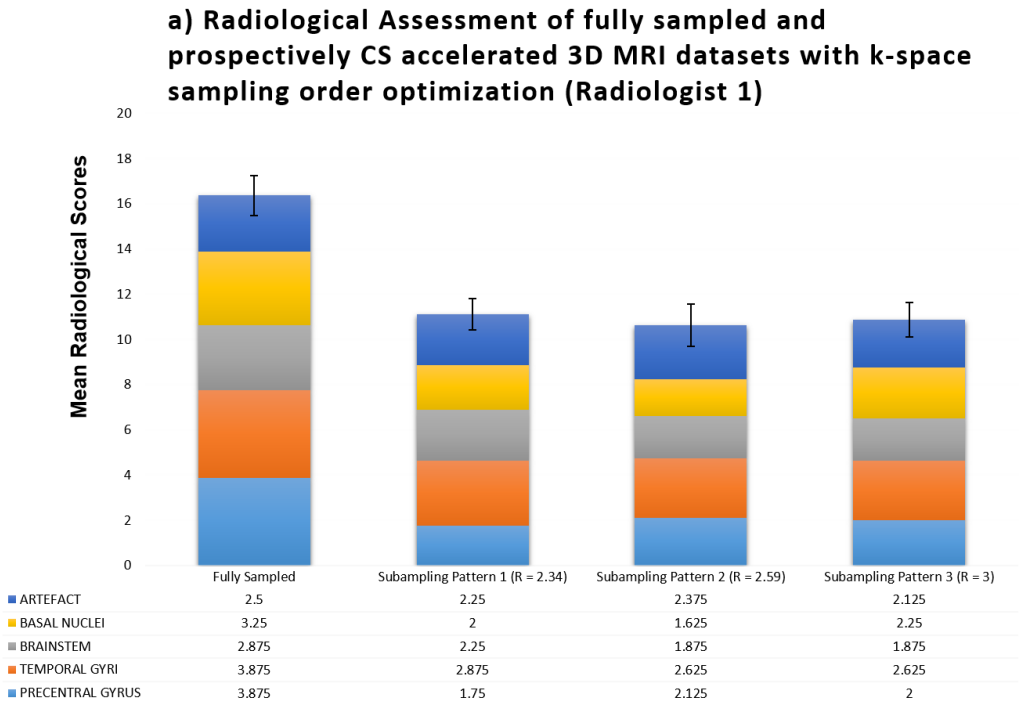

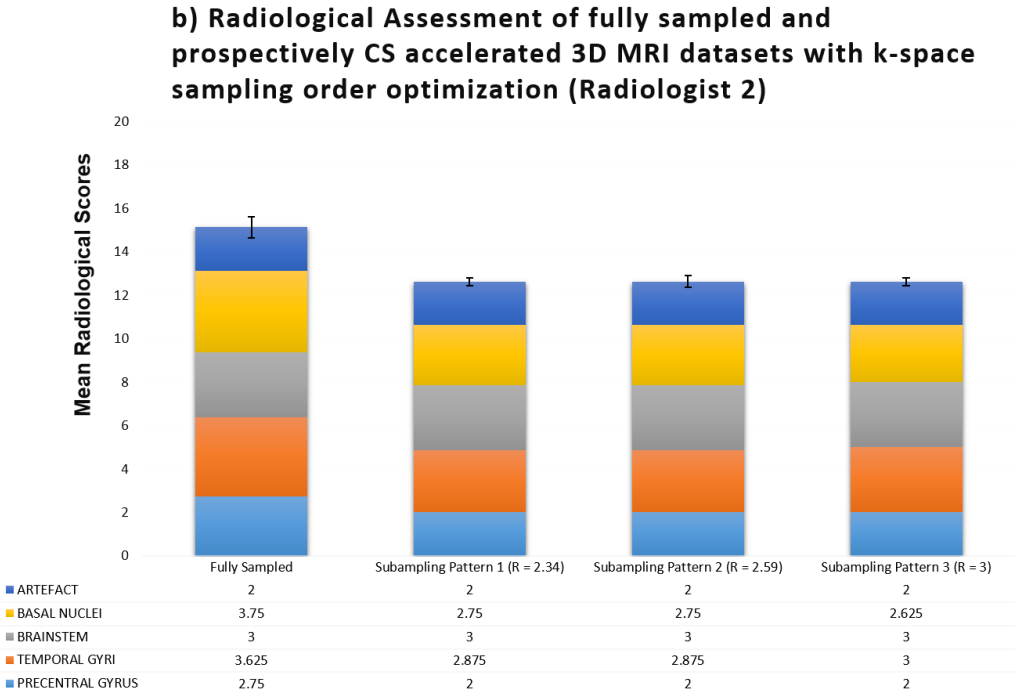

Figure 4.3: *Mean Radiological Scores (RS) along with ± standard error (SE) of independent radiological assessments carried out by* ***(a)*** *Radiologist 1 and* ***(b)*** *Radiologist 2 for the gross structural assessment of the brain for 8 healthy volunteers.*

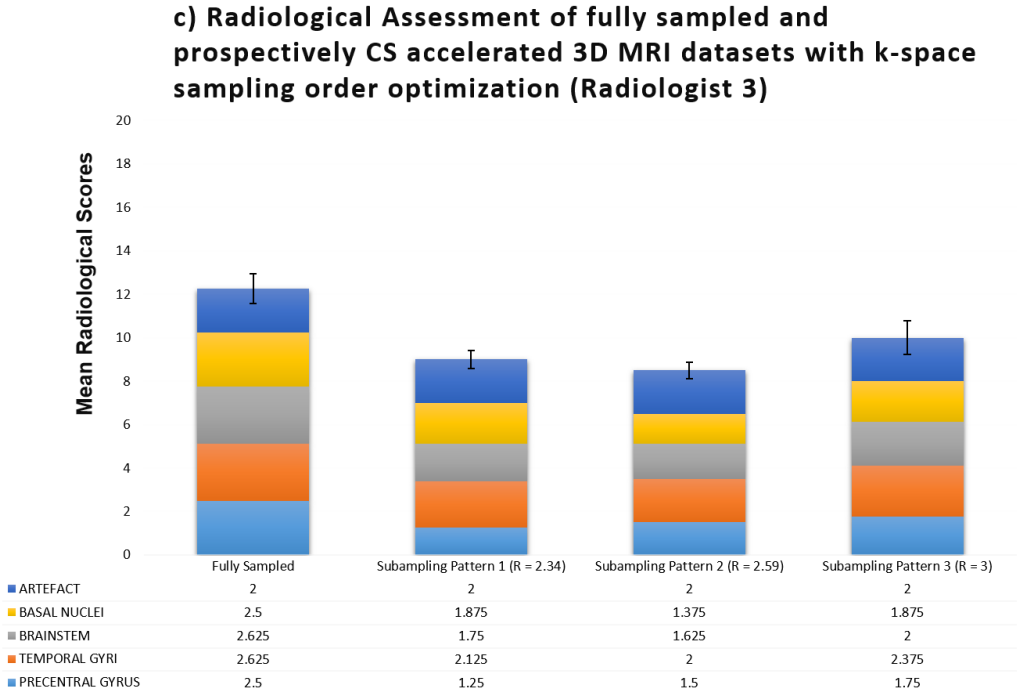

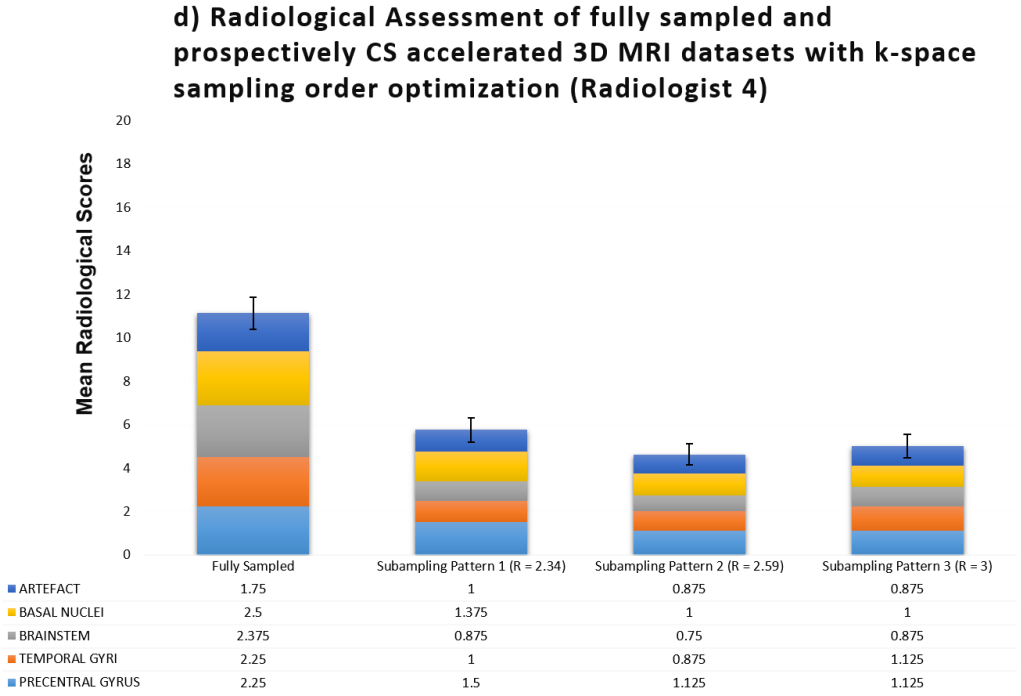

Figure 4.3: *Mean RS along with ± SE of independent radiological assessments carried out by* ***(c)*** *Radiologist 3 for the gross structural assessment of the brain and* ***(d)*** *Radiologist 4 for high spatial resolution assessment for 8 healthy volunteers. The mean RS of CS accelerated images show that there is sufficient clinical diagnostic value for gross structural assessment but not for high spatial resolution assessment. Note that higher scores mean better image quality.*

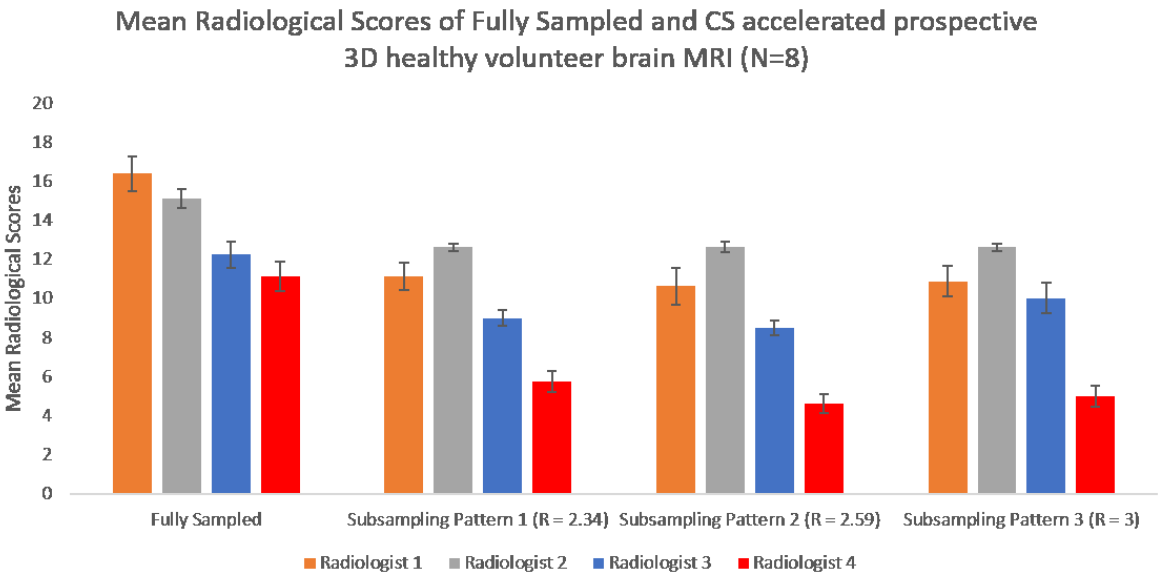

Figure 4.4: *Figure showing the comparison of mean radiological scores along with standard error (SE) of four different neuroradiologists who graded fully sampled (FS) and compressed sensing (CS) accelerated subsampled datasets. Higher scores mean better image quality. Note that three radiologists (i.e. Radiologist 1, 2 & 3) carried out gross structural assessment of the brain while one radiologist (i.e. Radiologist 4) performed high spatial resolution assessment.*

4.4 Discussion

The importance of sampling order optimization for preserving tissue contrast in neuroimaging has been previously described in Section 3.2.5. Figure 4.2 also illustrates the necessity for k-space acquisition order optimization by showing the contrast preservation and clear demarcation between different tissue types in accelerated scans for three representative axial slices of three volunteers who were randomly selected from the entire cohort of eight healthy volunteers. The CS-PI reconstructions of sampling order optimized accelerated scans in Figure 4.2 show that the deep grey matter structures can be clearly resolved; thereby improving its usefulness for clinical diagnosis.

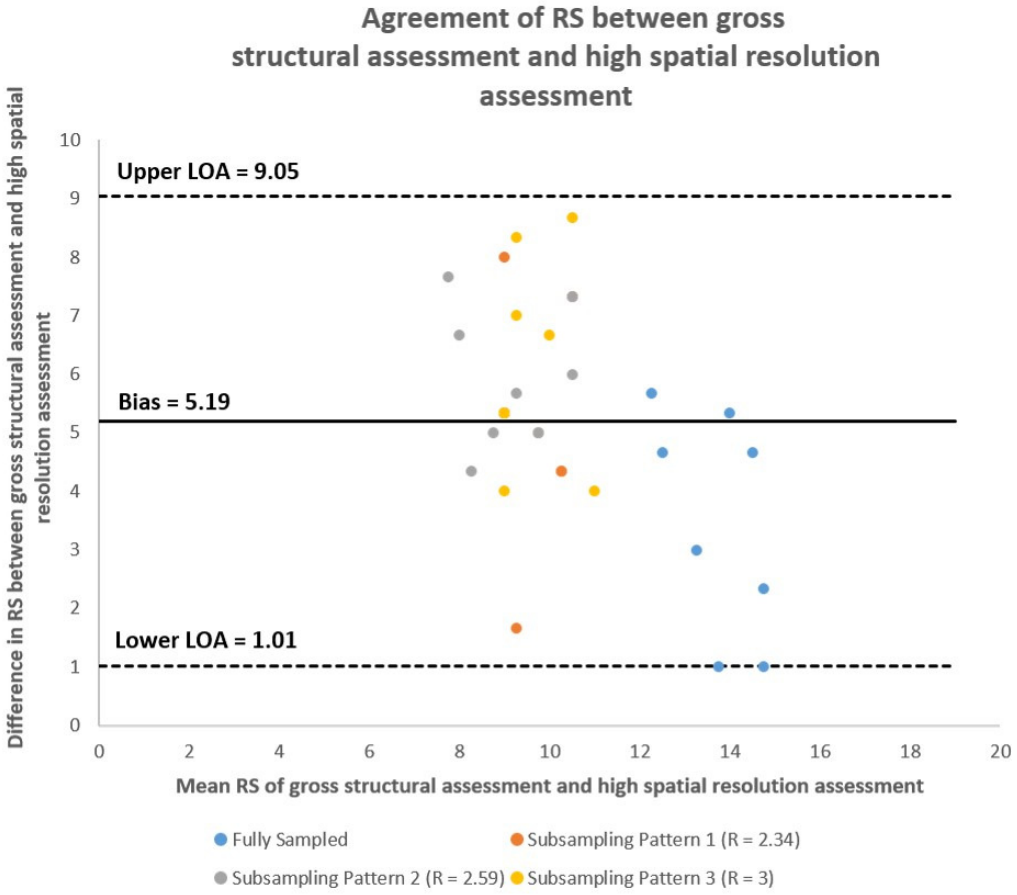

Figure 4.5: *Bland Altman plot showing the degree of agreement between neuroradiological assessments that graded two different practical clinical scenarios (i.e. gross structural assessment vs high spatial resolution assessment) for all datasets (8 subjects x 4 datasets each = 32 datasets). Note that the mean radiological scores (RS) of the first three radiologists were used since they answered the same clinical question.*

From Figures 3.9, 3.10 (refer Chapter 3) and 4.2, we have shown that the optimization of k-space acquisition order is essential for preserving contrast in CS accelerated 3D neuroimaging. Diagnostic quality assessment of 3D brain datasets accelerated using CS and sampling order optimization showed that the mean RS were generally high enough to perform a gross structural assessment of the brain confidently. In general, the fully sampled scans had higher scores compared to CS accelerated scans. The diagnostic quality assessments in Figure 4.3 show that there is a degree of variability in the RS between the different radiologists which is expected since each radiologist will have a slightly different idea of what level of image quality is acceptable for diagnosis. Despite this variability, the gross structural brain assessments in Figure 4.3a,

4.3b and 4.3c show that most of the subsampled image datasets (19/24 datasets for Radiologist 1, 24/24 datasets for Radiologist 2 and 16/24 datasets for Radiologist 3) had a mean RS of at least 9 with each brain region being graded with a mean RS of atleast 2 (i,e. fully diagnostic) predominantly. However, the grey-white matter differentiation in the precentral gyrus and the brainstem were graded to be partly non-diagnostic with a mean RS less than 2 by Radiologist 1 and 3 for some of the subsampled datasets which suggests stricter grading when compared to Radiologist 2. Even though the mean RS were lower in subsampled datasets than the fully sampled cases, a radiological grading of 2 (fully diagnostic) for the different brain regions and artefacts for many of the subsampled datasets by the different radiologists indicate that there is adequate confidence for performing gross structural brain assessment accelerated by CS and sampling order optimization. This means that the radiologists were able to adequately visualize large brain structures and could potentially identify large lesions or tumours for tumour diagnosis which is the planned next step in this work.

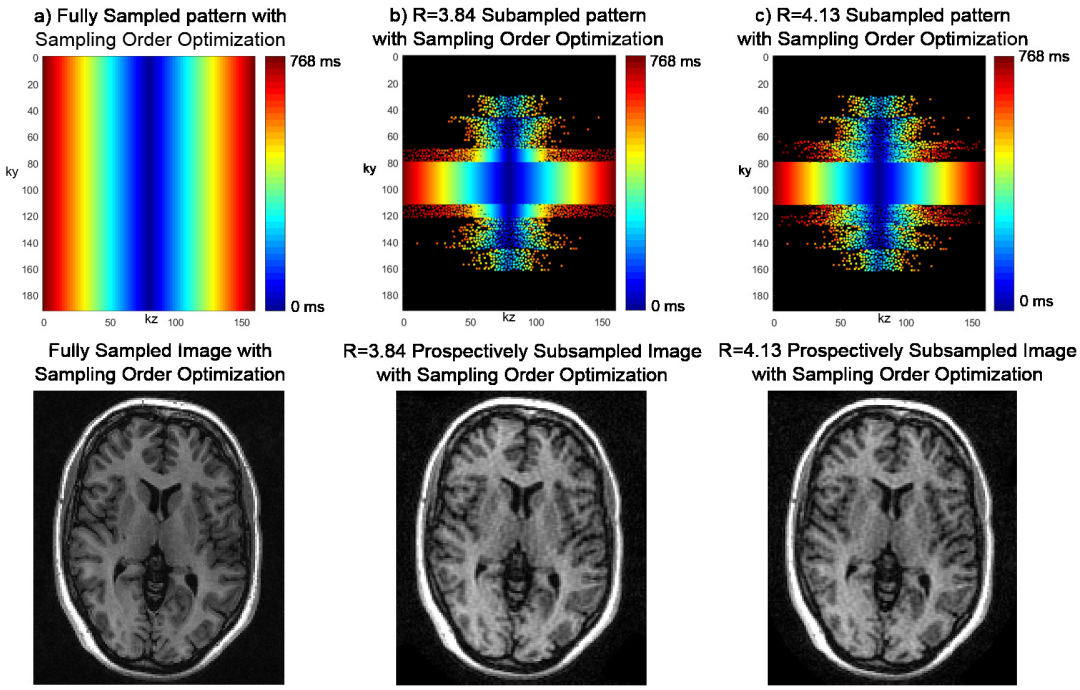

***Figure 4.6:**: Figure showing a fully sampled (a) and two subsampled patterns with R=3.84 (b) and R=4.13 (c). The k-space acquisition order is optimized for the three sampling patterns. The corresponding CS-PI reconstructed images are also shown. Note the degradation in image quality in (b) and (c) since the acceleration factor is too high. There is a clear deterioration of certain brain structures especially deep grey matter structures such as basal ganglia. The colour bars represent the time instant at which data samples are collected for each readout during acquisition.*

Another important factor that affects the clinical usability of CS accelerated neuroimaging is the clinical question that forms the basis of the diagnostic quality assessment [185]. The clinical problem that is being investigated should be clearly defined and established before the neuroradiological assessment is carried out since the RS are highly dependent on the clinical question that is being addressed by the radiological assessment (see Figs. 4.3 and 4.4). Although CS accelerated brain scans with optimized k-space acquisition order can be good enough for gross structural assessment of the brain, the CS-PI reconstructed images were not suitable for high spatial resolution assessments like finding subtle developmental abnormalities of cortex such as dysplasia, measuring cortical thickness or seeking developmental lesions for diagnosing epilepsy (see Fig. 4.3d). Even though the same radiological scoring key was used for addressing both these clinical scenarios, the RS varied significantly depending on the clinical condition to be assessed by the radiological grading.

For tasks that required high spatial resolution and grey-white matter differentiation, the artefacts due to CS reconstruction were deemed to be more severe and impeded the clarity of certain brain structures like brainstem, cortical grey-white margins and basal ganglia, leading to lower scores for image quality and artefacts. The amount of penalization that was applied to the RS was highly dependent on the practical clinical scenario. This effect can be seen from the Bland-Altman analysis in Figure 4.5 which shows an average bias of more than 5 in RS for the two different clinical scenarios. The bias in RS indicates that the threshold/cut-off that was used for acceptable image quality was different for both clinical scenarios. The Bland-Altman plot shows that there is a certain degree of agreement between the two different clinical assessments since all the datasets lie within the limits of agreement. However, it does not show which subsampling pattern had the best degree of agreement between the two different clinical assessments. Therefore, it is important to consider and clearly define the relevant clinical question before evaluating the diagnostic utility of CS accelerated prospective 3D brain scans. Consequently, the selection of the degree of CS, as with other acceleration schemes, could be guided by the proposed clinical application, i.e. higher for standard clinical assessments, but reduced for usage scenarios where better tissue discrimination is needed as with epilepsy investigation.

In abdominal paediatric imaging with Gadolinium contrast, Vasanawala et al. [147] found that CS reconstruction led to better image quality scores than standard parallel imaging because the algorithm used (ℓ1-SPIRIT) [137] reduced high image noise whilst preserving anatomical features. This behavior is expected in high contrast images that are inherently sparse [12].

However, in a neuroimaging study with lower inherent contrast, Sharma et al. [154] found that CS with a modest two-fold acceleration of 2D images caused blurring and global ringing artefacts. They attributed the ringing artefacts to the sampling pattern that was used for acquisition. However, it should be noted that the acceleration that could be achieved in this type of study is limited due to the presence of only one phase encoding direction.

Although we observed minor reconstruction artefacts in our work, the majority of the accelerated datasets were still deemed to be fully diagnostic since structures such as WM, GM and deep grey matter structures were clearly visible with distinct demarcation between the different structures in accelerated scans. Contrast preservation due to optimization of k-space acquisition order resulted in improved RS in accelerated brain scans when compared to the RS of a previous CS accelerated neuroimaging study in which k-space acquisition order was not optimized [156]. The higher RS were due to the clear visualization of deep brain structures such as basal ganglia which were previously reported to be degraded in CS accelerated brain scans [156]. Our accelerated brain images were of reasonable quality and contained minor artefacts that did not affect the diagnostic interpretation of brain structures such as basal ganglia, precentral gyrus, temporal gyrus and brainstem up to an acceleration factor of 3 (see Fig. 4.2). However, at higher acceleration factors (i.e. R = 3.84, 4.13), brain structures such as subcortical grey matter become indistinguishable due to the elevated presence of artefacts and noise which is introduced by CS-PI reconstruction (see Fig. 4.6). There is also a sharp degradation in image quality suggesting that there should be a trade-off between the amount of acceleration and acceptable image quality.

In this study, a 3D T1w volume sequence was deliberately chosen since it is a workhorse in many studies of ageing and neurodegeneration, and has a relatively long scan time. In addition to that, the T1-weighted volume image is also apt for tumour diagnostics since it is now the recommended T1-weighted imaging approach under the British Tumour Imaging Protocol for brain structural assessments [186]. Furthermore, with the 3D imaging sequence, undersampling was possible in the two phase encoding directions, which is expected to improve the performance of CS reconstruction by spreading incoherent artefacts [12]. A significant limitation of this study is that we examined only a small cohort of healthy volunteers who were not expected to (and did not) have significant lesions. It is therefore not possible in our analysis to comment on the suitability of accelerated scans for assessing clinically important brain lesions, for example those due to multiple sclerosis or cerebrovascular disease. A larger study including

patients with neurological disorders and older volunteers would be necessary to evaluate this important aspect. Likewise, most neurological studies rely on review of multiple sequences such as T1, T2, FLAIR, $T2^*$, DWI [21, 26, 27] for diagnosis. The clinical utility of CS accelerated brain scans on other sequences has not been evaluated here and would be an avenue for future research. Testing CS in people with lesions and additional work in CS accelerated T2-weighted imaging are the planned next steps in this work.

In conclusion, this study showed that the clinical usefulness of CS accelerated neuroimaging was task dependent. It could be used clinically for applications such as routine screening of patients. However, it is not yet recommended for clinical scenarios that require higher tissue discrimination such as epilepsy investigation. These conclusions show that CS has potential, but requires optimization to maintain tissue contrast, and is better suited to some diagnostic tasks than others.

Chapter 5

Multi-shot Echo Planar Imaging for accelerated Cartesian MR Fingerprinting: an alternative to conventional spiral MR Fingerprinting

In chapters 3 and 4, the main focus was on sparse sampling schemes for structural MRI acceleration. In this chapter, the attention now moves to the issue of accelerated quantitative imaging. This chapter introduces a Cartesian sampling scheme for rapid quantitative MRI. The sampling scheme will be based on a multi-shot EPI sequence that will be used to perform accelerated Cartesian MR Fingerprinting. This work is one of the main contributing chapters of this thesis and has resulted in a journal article that has been published as [187].

5.1 Introduction

The clinical usefulness and need for q-MRI has been previously described in Section 2.12. The estimation of quantitative multi-parametric maps helps in greater tissue discrimination, segmentation and classification to improve disease detection and monitoring. For example, T1 mapping has various applications such as the detection of neuro-degenerative disorders like multiple sclerosis (MS) [188], Alzheimer's disease [189], assessment of myocardial infarction [190] and characterizing fiber bundle anatomy in diffusion MRI [191] while T2 mapping is used for applications in ageing and cognitive decline [192], quantification of myocardial edema [193] and evaluation of articular cartilage damage in the knee [194, 195]. However, clinical time constraints have prevented the widespread clinical use of parametric mapping techniques [196, 197]. Recent emergence of rapid parametric mapping techniques such as Magnetic Resonance Fingerprinting (MRF) [94] and its various extensions [95–97] have shown that it is possible to generate multiple quantitative parametric maps simultaneously in a very short scan duration that is clinically feasible. MRF offers a new approach to simultaneously quantify multiple tissue

properties rapidly within a single scan by acquiring the transient-state signal that is sensitive to multiple imaging parameters such as flip angle (FA) and repetition time (TR). Acquiring a series of subsampled images rapidly while constantly varying imaging parameters leads to spatial and temporal incoherence resulting in characteristic signal evolutions, which depend on the physical properties of the underlying tissue, such as relaxation times. The unique signal evolutions or '*fingerprints*' are matched to a precomputed dictionary to generate multiparametric quantitative maps.

The first MRF implementation was able to simultaneously quantify T1, T2 and off-resonance effects and was based on a balanced steady state free precession (bSSFP) sequence which was sensitive to field inhomogenities and produced banding artefacts [94]. These effects were mitigated by the use of an unbalanced steady state free precession sequence (SSFP) for multiparametric quantification [95, 102, 127, 198]. The most commonly used sampling strategy in MRF is interleaved spiral sampling because it allows considerable subsampling of k-space and also provides more control for efficient traversal of the k-space trajectory [94, 95]. Despite its numerous advantages, the spiral sampling scheme has been shown to be susceptible to gradient inaccuracies [199] and high frequency artefacts due to non-sampling of k-space corners [119] and its availability is limited which prevents its widespread use in clinical protocols [106].

Cartesian sampling schemes for MRF primarily based on single-shot Echo Planar Imaging (EPI) that have been proposed are promising but are not a like-for-like comparison with the spiral sampling strategy for MRF [104, 113, 114, 200, 201]. This is because single-shot EPI implementations do not allow subsampling in a similar manner to the spiral scheme and therefore the entire k-space has to be traversed for every frame during acquisition. This results in much longer TRs than would be achievable with spiral sampling and also places a burden on the gradient performance of the scanner due to the short echo spacing necessary to minimise image distortions in single-shot EPI [202]. Simulation results show that shorter TRs result in better T1 and T2 sensitivity for the unbalanced SSFP MRF sequence that was used in this study (see Fig. 5.1).

In this study, a multi-shot EPI-MRF approach is proposed that not only allows considerable k-space subsampling but can also achieve shorter TRs that are comparable to conventional Spiral-MRF implementations in a sufficiently short scan duration. Multi-shot EPI can yield better SNR, reduced blurring and lower ghost intensity while it also reduces the burden on gradients and RF hardware such as gradient amplitude and slew rate compared to single-shot EPI

[202, 203]. It also has the advantage of reduced distortions due to magnetic field inhomogeneity [204]. Unlike Spiral-MRF, multi-shot EPI-MRF has a solid theoretical basis in terms of compressed sensing theory [99, 100].

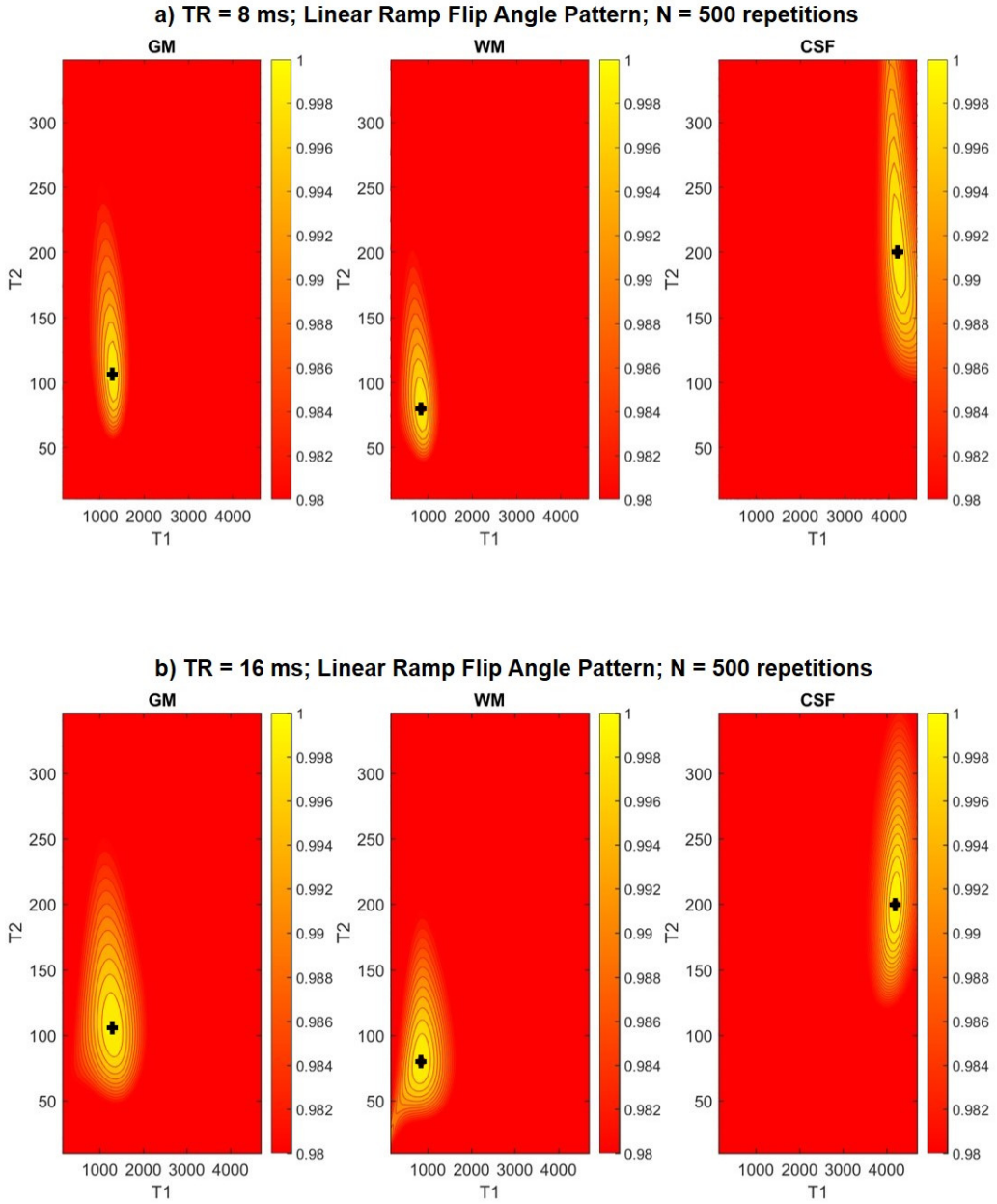

Figure 5.1: *T1-T2 sensitivity of exemplary values of grey matter (GM; T1 = 1300 ms, T2 = 105 ms), white matter (WM; T1 = 850 ms, T2 = 80 ms) and cerebrospinal fluid (CSF; T1 = 4200 ms, T2 = 200 ms) at 3T that were simulated for the unbalanced SSFP sequence with Linear Ramp FA and N = 500 repetitions for* ***(a)*** *TR = 8 ms and* ***(b)*** *TR = 16 ms.*

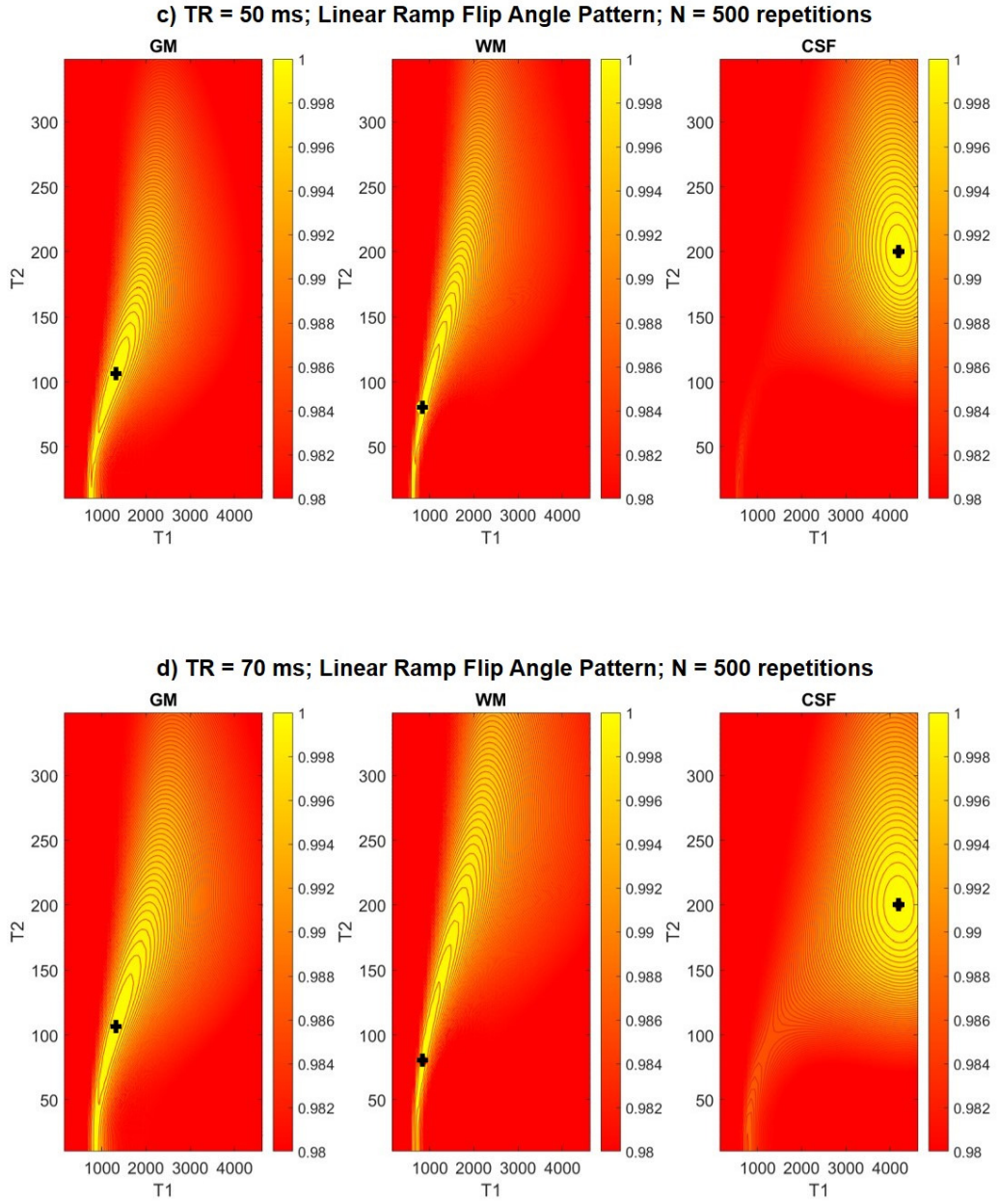

Figure 5.1: *T1-T2 sensitivity of exemplary values of GM, WM and CSF at 3T that were simulated for the unbalanced SSFP sequence with Linear Ramp FA and N = 500 repetitions for* ***(c)*** *TR = 50 ms and* ***(d)*** *TR = 70 ms. Note that shorter TR's have better sensitivity.*

A multi-shot EPI readout is used in this study to generate T1 and T2 maps for comparison with Spiral-MRF. An Iterative Projection Algorithm (IPA) called BLoch matching response recovery through Iterated Projection (BLIP) is used to improve the accuracy of the generated parametric maps [99, 100]. Sequence parameters such as RF pulse, Inversion Time, FA train, TR and bandwidth are identical for both EPI-MRF and Spiral-MRF experiments in order to quantitatively assess the agreement of both methods.

5.2 Methods

5.2.1 Pulse Sequence Design

The original MRF paper that was based on a bSSFP sequence was sensitive to banding artefacts [94]. In order to overcome this, Jiang et al. [95] suggested the use of an unbalanced SSFP sequence which is also sometimes referred to as a FISP sequence. In the multishot EPI-MRF method introduced here, we also used an unbalanced SSFP sequence but we made the following changes compared to previous papers:

(i) a variable flip angle ramp instead of a pseudorandom FA schedule was used to improve the T1 and T2 quantification efficiency in a fewer number of repetitions (N) [102] than the original FISP-MRF sequence [95]. Figure 5.2 shows the T1-T2 sensitivity of exemplary values of grey matter (GM), white matter (WM) and cerebrospinal fluid (CSF) at 3T that were simulated for the unbalanced SSFP sequence using the Extended Phase Graph (EPG) model [115, 116] for two different FA schedules, namely:
a) Linear Ramp FA Pattern from 1° to 70° with N = 500 repetitions and b) Pseudorandom FA pattern with N = 1000 repetitions that was used by Jiang et al. [95].

(ii) a subsampled Cartesian readout (with readout time 6.976 ms) using 16-shot EPI (see Fig. 5.3a) was used to eliminate regridding, perform faster reconstruction and avoid high frequency artefacts that appear in spiral readouts due to the non-sampling of k-space corners as shown by Cline et al. [119].

The sensitivity is defined as the correlation coefficient (i.e. the normalized inner product) measuring the correlation between a query T1-T2 pair within the dictionary and the responses for a range of T1-T2 values. It depends on the shape of the magnetization response and is a function of the flip angle schedule, number of repetitions, TR, Echo Time (TE), Inversion Time

(TI) and the readout time. The sensitivity plots are calculated using the same EPG model used to construct the dictionary which is mathematically described in [115, 116]. Figure 5.2 also shows that by using the Linear Ramp FA pattern, a very similar T1-T2 sensitivity for GM and WM is achieved in only half the number of repetitions and a significantly better T1-T2 sensitivity for CSF can be achieved when compared to the pseudorandom FA pattern. The FA was incremented by $(70-1)°/500 = 0.138°$ for every repetition.

5.2.2 Sequence Parameters

Scanning was carried out at GE Global Research, Munich during a secondment visit. The scanning was performed on a 3T GE MR750w scanner with a 12 channel receive only head RF coil (GE Medical Systems, Milwaukee, WI). The study was approved by the local ethics committee. Both EPI-MRF and Spiral-MRF data were acquired from phantom and healthy volunteer brains using the variable FA ramp that has been described in section 5.2.1.

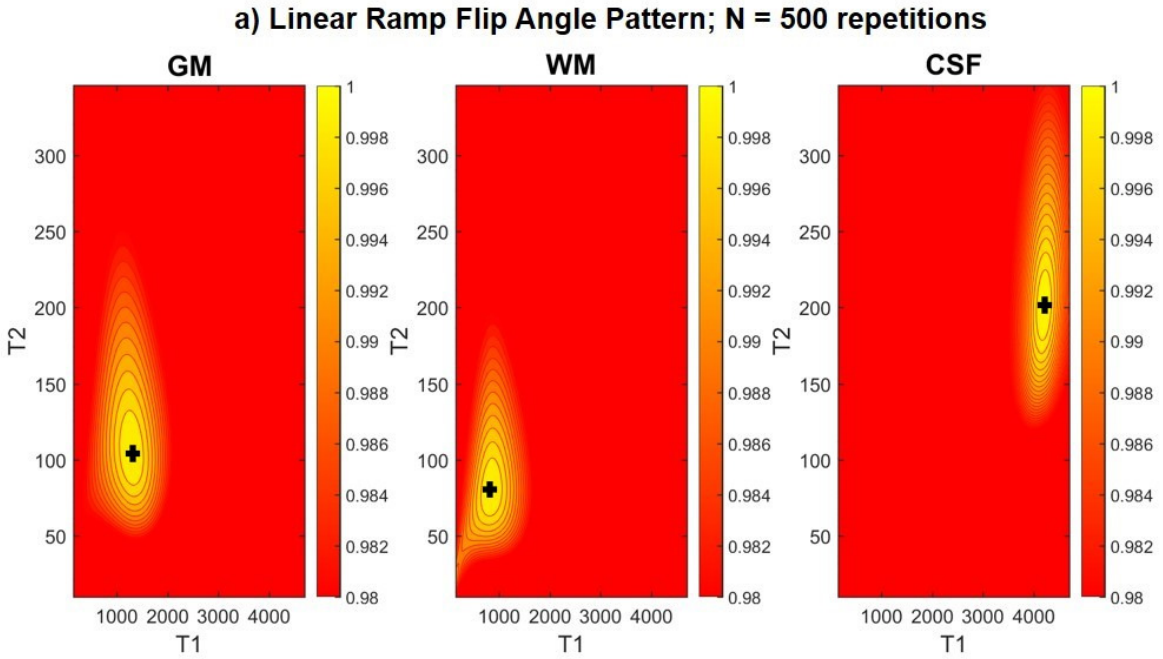

Figure 5.2: ***(a)*** *T1-T2 sensitivity of exemplary values of grey matter (GM; T1 = 1300 ms, T2 = 105 ms), white matter (WM; T1 = 850 ms, T2 = 80 ms) and cerebrospinal fluid (CSF; T1 = 4200 ms, T2 = 200 ms) at 3T that were simulated for the unbalanced SSFP sequence using the EPG model for Linear Ramp FA Pattern from 1° to 70° with N = 500 repetitions*

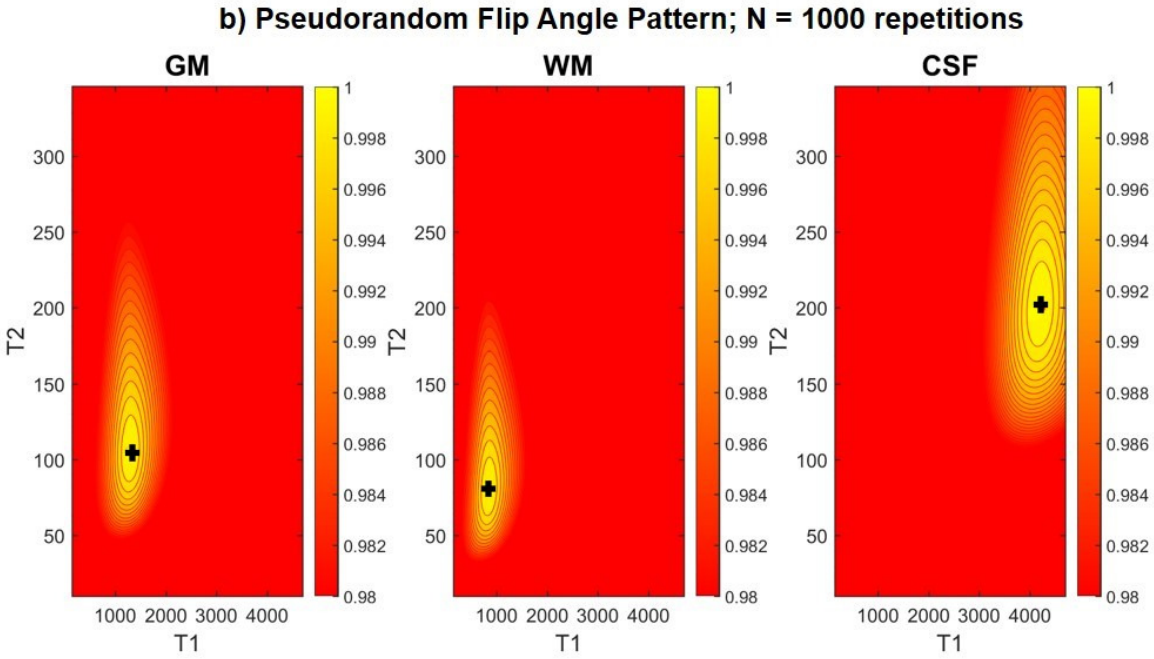

Figure 5.2: (b) *T1-T2 sensitivity of exemplary values of GM, WM and CSF at 3T that were simulated for Pseudorandom FA pattern with N = 1000 repetitions that was used by Jiang et al. [68]. The sensitivity measures the similarity between different T1-T2 responses and hence specifies the accuracy with which a query T1-T2 pair can be matched to the correct dictionary entry in the presence of noise. The tighter the contours, the smaller the range of T1 and T2 valued dictionary atoms to which the query is likely to be matched. Note that both sensitivity plots have the same contour levels for direct comparison between the two FA schedules.*

Figure 5.3 shows the Cartesian implementation of the unbalanced SSFP sequence for MR fingerprinting using 16-shot EPI readout. The EPI trajectory was implemented using the fidall imaging sequence from the Multinuclear Spectroscopy (MNS) research pack (GE Global Research, Munich, Germany). The EPI-MRF acquisition used about 58% of the readout time (i.e. 4.096 ms) to collect 8 unique lines of k_y-space data for every shot. A reference scan with the EPI blips turned off was performed for phase correction of EPI raw data. Gradient spoiling of about three and a half cycles was introduced by the spoiler gradient Gz (see Fig. 5.3a) to make it an unbalanced SSFP acquisition. The zero order gradient moments for G_x and G_y were nulled towards the end of every readout (between 6.464 ms and 6.976 ms) to ensure constant magnetization for each shot throughout the acquisition (see Fig. 5.3b).

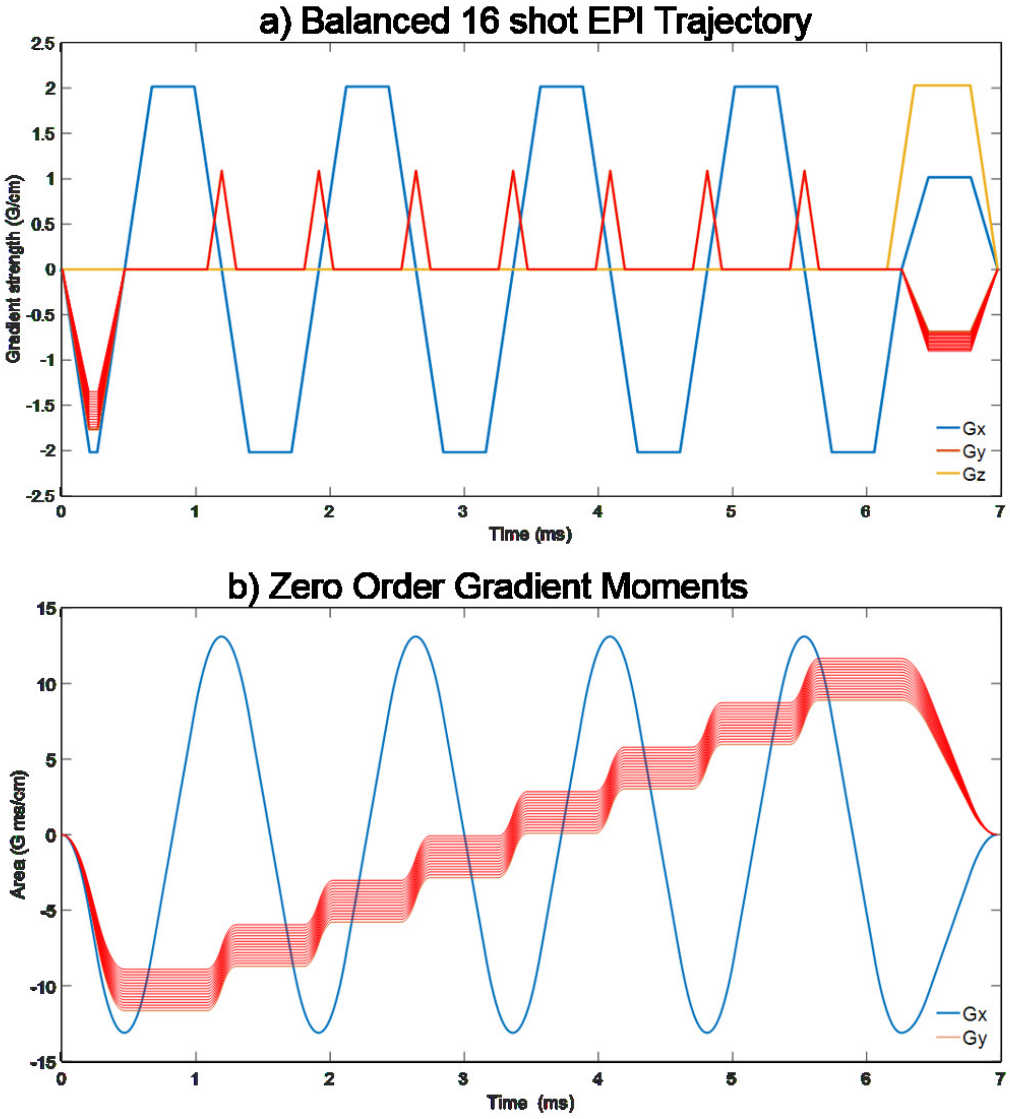

Figure 5.3: ***(a)*** *The 16 shot EPI trajectory showing G_x, G_y and G_z gradients. Note that the G_y gradients are slightly different for each of the 16 shots indicating that different lines of k_y space are acquired at every shot. The spoiler gradient G_z dephases the transverse magnetization for every TR making the sequence unbalanced [68].* ***(b)*** *The corresponding x and y zero order gradient moments for G_x and G_y were nulled to ensure constant residual magnetization for each shot throughout the acquisition.*

A variable density spiral trajectory with 89 interleaves was used to collect Spiral-MRF data. Each interleave was rotated by a golden-ratio angle (i.e. 111.246°). The duration of spiral readout was 4.096 ms. No reference measurements were made for the spiral trajectory.

The minimum achievable TR for EPI (i.e. 16 ms) was used for both EPI-MRF and Spiral-MRF acquisitions for fair comparison even though the TR could be further reduced for Spiral-MRF. Both acquisitions had bandwidth (BW) = 250 kHz, Field of View (FOV) = 22.5 x 22.5 cm^2, 128 x 128 matrix size and 5 mm slice thickness. A global inversion pulse with TI = 18 ms was used at the beginning of the acquisition to increase the T1 sensitivity of the sequence. The TI was chosen such that it maximized the temporal separation of the signals from GM, WM and CSF [102]. The TE was 2 ms and 3.488 ms respectively for the spiral and EPI acquisitions. TE is defined as the time at which the centre of k-space is sampled and is assumed to be constant for every shot (approximately half the readout time). The acquisition time for a single slice was 8 s.

5.2.3 Phantom Scans

16-shot EPI-MRF and Spiral-MRF datasets using a variable FA ramp [102] were acquired for 500 repetitions from a gel based phantom (Diagnostic Sonar, Livingston, UK) which consisted of 12 tubes, each having different T1 and T2 values. The gels were made from agarose doped with gadolinium which represent an ideal test material for MR imaging studies as gels with any desired T1 and T2 value can be produced by varying the material composition. Reference T1 and T2 values measured under controlled conditions were provided by the manufacturer and were used for comparison with the multi-parametric values estimated by the two MRF methods (i.e. EPI-MRF and Spiral-MRF).

5.2.3.1 Gold Standard T1 and T2 Spin Echo Measurements

The T1 and T2 values of the phantom were characterized by using the gold standard Inversion Recovery Spin Echo sequence for T1 estimation and single echo spin echo method (SE) for T2 estimation. These values were compared to the T1 and T2 values estimated by EPI-MRF and Spiral-MRF.

The T1 values of the different tubes in the phantom were measured by the IR-SE sequence with 32 inversion times ranging from 0.05 s to 4 s, parallel imaging ASSET factor 2, TR of 12s, a matrix size of 128 $\times$ 128, FOV of 22.5 cm, and a slice thickness of 5 mm. The scan time

for each T1 experiment was 12.8 minutes and the total scan time for the entire gold standard T1 experiment was 409.6 minutes. To calculate T1 values, pixel-based nonlinear least-squares curve fitting was used to fit the magnitude of the IR-SE images to

$$M_z(TI) = M_0(1 - 2e^{-TI/T1})$$

where, M_0 is the magnetization at thermal equilibrium, M_z is the longitudinal magnetization that depends on the Inversion Time (TI) and T1 relaxation time of the IR-SE experiment.

The T2 values were measured by multiple single echo-spin echo experiments with 12 echo times ranging from 0.02 s to 1 s, parallel imaging ASSET factor 2, TR of 12s, a matrix size of 128 $\times$ 128, FOV of 22.5 cm, and a slice thickness of 5 mm. The scan time for each SE experiment was 12.8 minutes and the total scan time for the entire gold standard T2 experiment was 153.6 minutes. To calculate T2 values, the magnitude values from the multiple single echo spin echo images were fit to

$$M_{xy}(TE) = M_0 e^{-TE/T2}$$

where, M_0 is the magnetization at thermal equilibrium, M_{xy} is the transverse magnetization that depends on the Echo Time (TE) and T2 relaxation time of the SE experiment.

5.2.4 Healthy Volunteer Brain Scans

16-shot EPI-MRF and Spiral-MRF datasets were acquired from three healthy volunteer brains using the linear ramp FA schedule from 1° to 70° for 500 repetitions. The T1 and T2 values estimated by EPI-MRF and Spiral-MRF methods from healthy volunteer brains were compared with conventional T1 and T2 values previously reported in literature [205] and also to T1 and T2 values estimated by an established Spiral-MRF method with pseudorandom FA variation [95]. WM and GM regions were extracted from the healthy volunteer brain images to calculate the accuracy of T1 and T2 quantification. The segmentation was performed by thresholding using the T1 maps. The Matlab Image Processing Toolbox was used for segmentation.

5.2.5 Reconstruction

The MRF dictionary of magnetic resonance responses was pre-computed offline using a Matlab implementation of the EPG formalism [115, 116]. The EPG model is an efficient computational tool for quantitative simulations of signals [95, 115, 198] obtained from various MRI pulse sequences and is also widely used for characterizing signal evolutions in sequences used for relaxometry (i.e. characterizing relaxation parameters) [128, 206, 207]. This model is used to numerically compute the dictionary for MRF sequences by effectively modelling the pathways that lead to the formation of echoes [102, 128, 198]. A high resolution dictionary having a total of 23866 dictionary atoms was used with T1 values ranging from 40 ms to 2 s in steps of 20 ms and 2 s to 6 s in steps of 100 ms. The T2 values ranged from 20 ms to 120 ms in steps of 1ms, 120ms to 200ms in steps of 2 ms and 200 ms to 600 ms in steps of 10 ms. For the dictionary matching process, the inner product of each of the dictionary atoms and the measured response for each pixel was first computed and the parametric values of the dictionary atom that had the maximum correlation with the measured response was assigned to each pixel.

The dictionary was computed in approximately 5 minutes on a typical laptop computer with standard specifications (i.e. Intel Core i7 Processor with 16GB RAM). Figure 5.4 illustrates the sensitivity of a subset of the dictionary elements. The T1 sensitivity (16 fingerprints of dictionary elements with varying T1 ranging from 100 ms to 700 ms in steps of 40 ms and constant T2 = 100 ms) and T2 sensitivity (17 fingerprints of dictionary elements with varying T2 ranging from 20 ms to 100 ms in steps of 5 ms and constant T1 = 1000 ms) of the sequence for discriminating dictionary elements using a linear ramp FA variation from 1° to 70° are shown for 500 frames. Figure 5.4a shows that the T1 sensitivity is high throughout the acquisition whereas Figure 5.4b shows that the T2 sensitivity occurs mostly at higher flip angles ($> 20^\circ$). Therefore, higher flip angles are needed for efficient T2 discrimination.

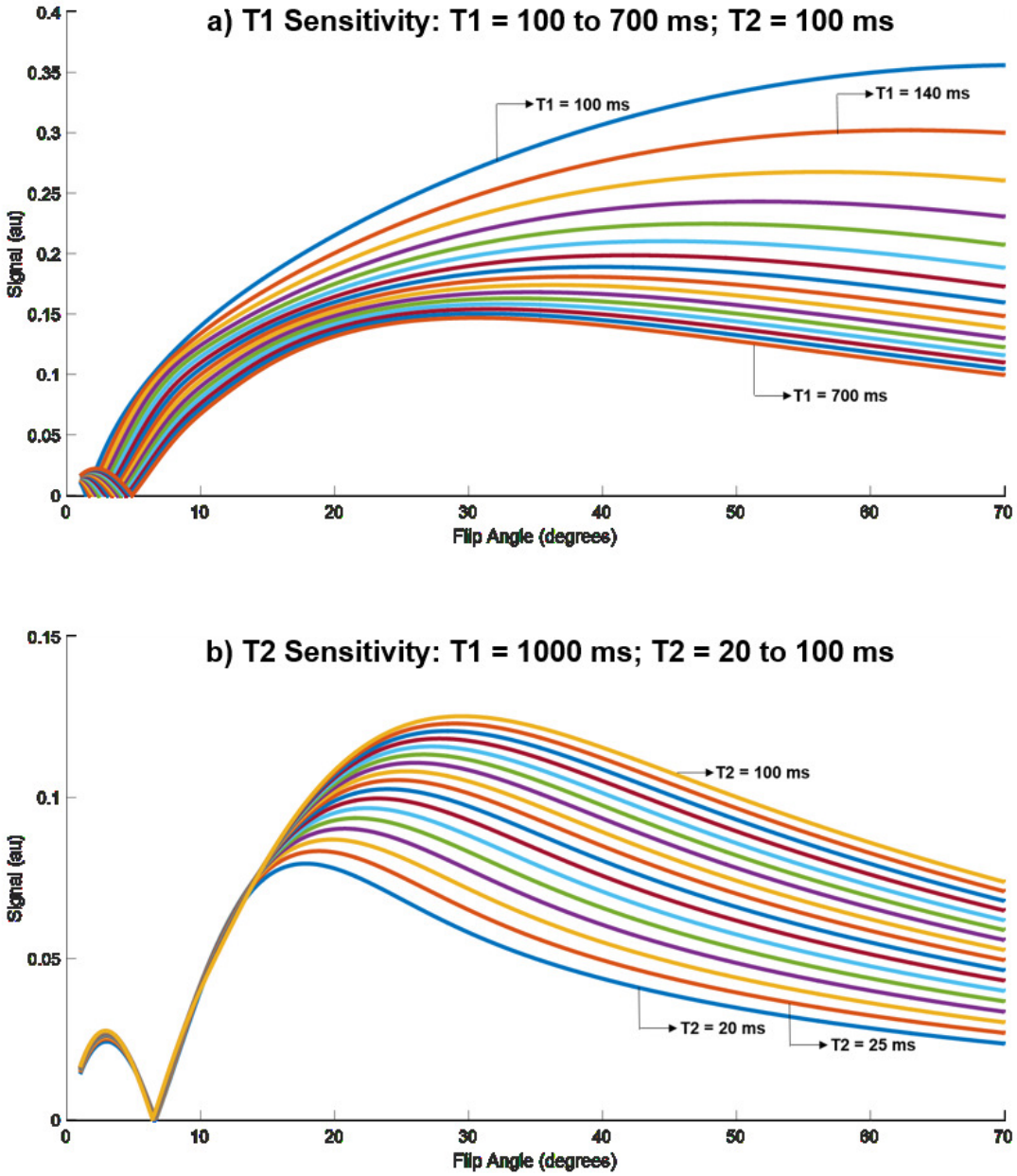

Figure 5.4: ***(a)*** *Figure showing the T1 sensitivity and* ***(b)*** *T2 sensitivity of the sequence for discriminating dictionary atoms when a variable flip angle ramp that linearly varied between 1° to 70° was used during the acquisition for 500 repetitions/frames. The FA for the 1st frame was 1° while the FA for the 500th frame was 70°. Note that the Inversion pulse causes the initial T1 discrimination in (a). These sensitivities were observed at practical T1 and T2 values. Only a subset of the high resolution dictionary is plotted for better visualization. It is also equivalent to label the x-axis in time-points (i.e. seconds). The total acquisition time for a single slice was 8s.*

The reconstruction was done entirely in Matlab using the code adapted from the works by Ma et al. [94] and Davies et al. [99, 100]. Two classes of reconstruction were considered: an IPA reconstruction that included Singular Value Decomposition (SVD) Compression in the Time Domain [101, 118, 119, 208]; and Dictionary matching (DM) sometimes called Matched Filter reconstruction as proposed in the original work on MRF [94] and is described previously in Section 2.12.4.2. The DM is applied to the backprojected undersampled data. The IPA reconstruction is motivated by compressed sensing theory [12, 44, 142, 146] and is shown to be capable of removing aliasing artifacts (in the reconstructed images) resulting from severe EPI style k-space subsampling. In the first iteration of IPA which is equivalent to the DM reconstruction, DM was performed on the highly subsampled measurements that were back projected. The back projection included combining multi-coil measurements, a 2D inverse Fast Fourier Transform (FFT) for each temporal slice and a linear temporal compression where the compression bases were pre-calculated using the dominant SVD components of the fingerprint dictionary [101, 119]. The temporal compression was performed primarily to reduce the reconstruction time. The 12 channel multi-coil data was combined coherently using sensitivity maps that were computed from the acquired data [5, 14, 180].

Briefly, each iteration of IPA consists of:

$$X^{j+1} = \rho_D \left(X^j - \mu A^H \left(A \left(X^j \right) - Y \right) \right)$$

where, $Y \in C^{m \times N}$ are the undersampled k-space measurements across N temporal repetitions and multiple coils, μ is the step size which is adaptively selected through line search [100], $X^j \in C^{n \times N}$ are the spatio-temporal reconstructed images at iteration 'j' and $D \in C^{d \times N}$ denotes the pre-computed dictionary with 'd' atoms (d = 23866 atoms in this case). The forward and backward operators A, A^H model the multi-coil sensitivities and 2D Fourier Transforms for the acquired subsampled data. The forward and adjoint operators were implemented using the non-uniform fast Fourier Transform (NUFFT) for the spiral reconstruction. Since the spiral readout acquires much denser samples from the centre of k-space than the outer regions, density compensation was performed in both forward and adjoint operations for faster convergence. ρ_D denotes the DM step that is used in [100, 119] consisting of i) a search over the normalized dictionary atoms to replace the temporal pixels of X^{j+1} with the maximum correlated fingerprints and ii) proton density rescaling.

Therefore, the first iteration of IPA could be interpreted as an application of DM with proton density normalization [99, 100]. SVD compression-decompression was also used in the IPA reconstruction to reduce the complexity of the reconstruction [101, 119]. The first 20 dominant singular values were enough to robustly compress the dictionary. The IPA reconstruction was allowed to converge through multiple iterations to improve the data fidelity (i.e. to reduce the relative error between the quantitative estimates of predicted T1 and T2 values and the MRF measurements at each iteration) resulting in more accurate tissue parametric estimations. The convergence occured when the decrease in relative error between the model fit and acquired measurements did not exceed the specified tolerance level (i.e. 10^{-6}) in successive iterations or if the maximum number of iterations (i.e. 100) had been reached (whichever occurred sooner).

5.2.6 Brainweb Digital Phantom Experiment

The Brainweb digital phantom is a realistic, high-resolution, digital, volumetric phantom of the human brain. This three-dimensional digital brain phantom defines the spatial distribution for different brain tissues such as grey matter, white matter, cerebrospinal fluid and muscle, where voxel intensity is proportional to the fraction of tissue within the voxel [209, 210]. Since the contribution of each tissue type to each voxel in the brain phantom is known, it can be used as the gold standard to test analysis algorithms such as DM and iterative reconstruction algorithms. The Brainweb digital phantom with known T1 and T2 values, 16-shot EPI subsampling and N = 200 repetitions was used in this study to demonstrate the advantages of iterative reconstruction over non-iterative DM method.

5.3 Results

Figure 5.5a and 5.5b show a subsampled zero-filled (ZF) EPI image of a phantom and a healthy volunteer respectively at a single time-point (t = 1) and the temporal signal curve of one representative voxel over the entire time-series of 500 repetitions together with its corresponding matched dictionary entry. Although both the phantom and healthy volunteer images are dominated by subsampling artefacts, the DM algorithm is still able to find the corresponding dictionary entry that has the maximum corelation with the acquired data showing its robustness to undersampling artefacts. Note that undersampling artefacts are regular due to uniform subsampling but the signal along the temporal domain is still noise-like which is similar to the

Spiral-MRF case as shown by Jiang et al. [95]. This noise-like behavior of the signal in the temporal domain facilitates effective discrimination between dictionary elements resulting in an accurate dictionary match.

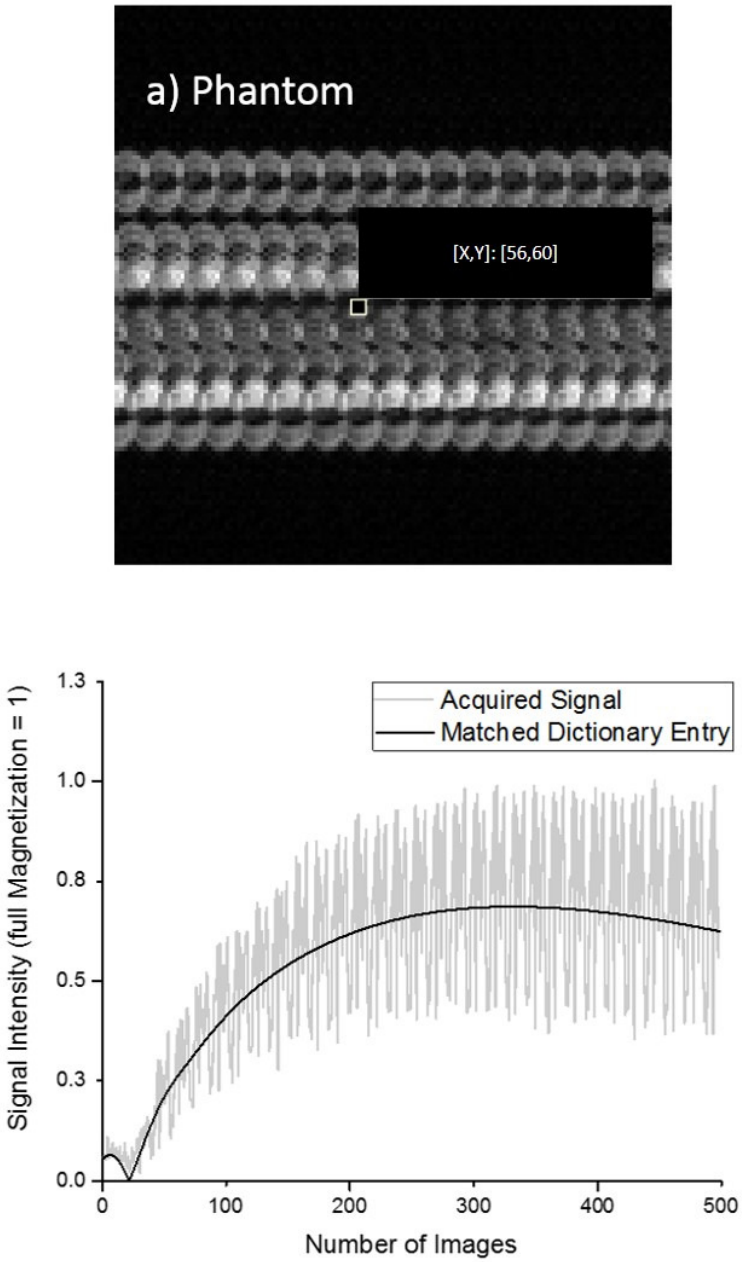

Figure 5.5: ***(a)*** *Subsampled zero-filled (ZF) EPI image of phantom at a single time-point (t = 1) and the temporal signal curve of one representative voxel over the entire time-series of 500 repetitions together with its corresponding matched dictionary entry.*

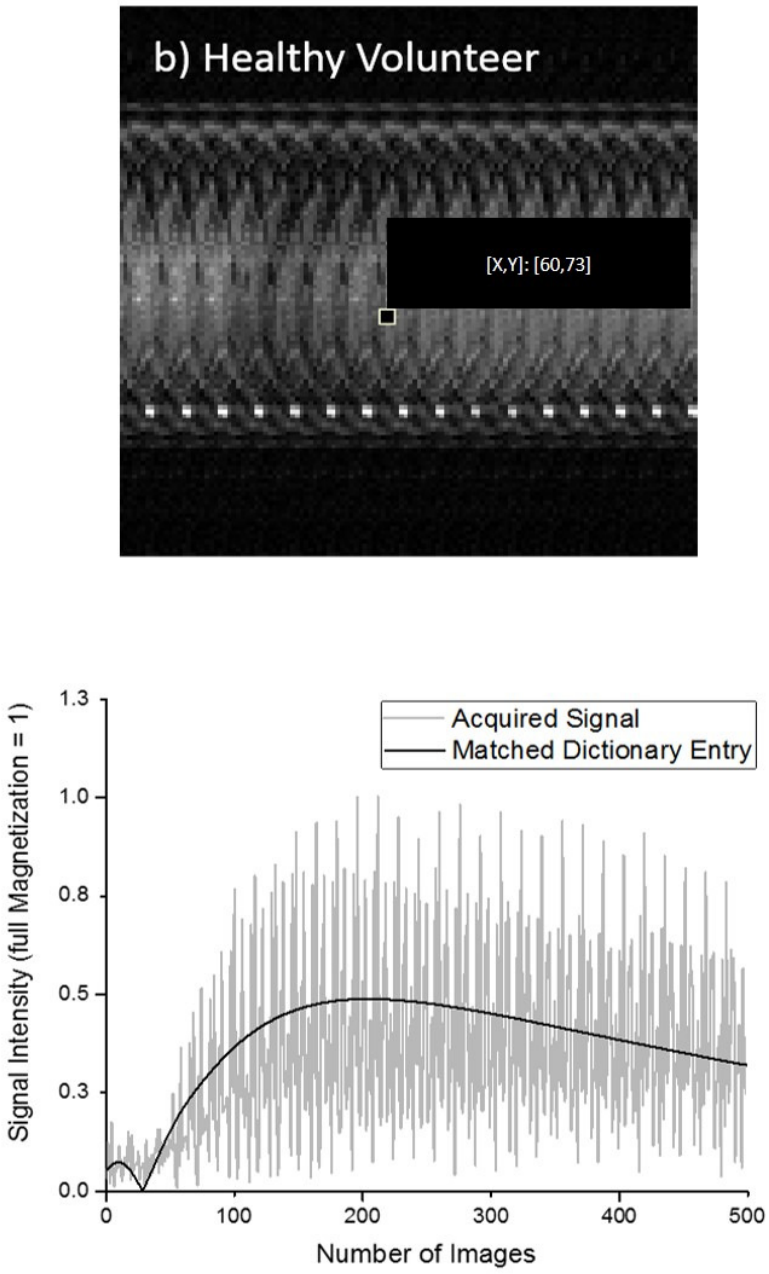

Figure 5.5: (b) *Subsampled zero-filled (ZF) EPI image of healthy volunteer at a single time-point (t = 1) and the temporal signal curve of one representative voxel over the entire time-series of 500 repetitions together with its corresponding matched dictionary entry. Note that dictionary matching (DM) still works even in the presence of uniform subsampling artefacts in the image due to the noise-like behavior of the signal in the temporal domain.*

Figure 5.6 shows the highly aliased zero-filled (ZF) images and Iterative Projection Algorithm (IPA) reconstructed images of the tube phantom and healthy volunteer at specific time-points (i.e. t = 44, 60, 250, 380, 420). It can be seen from the IPA reconstructed images that at lower repetition indexes (i.e. t = 44, 60) the images are predominantly T1 weighted. At higher repetition indexes (i.e. t = 350, 420) the images are more T2-weighted which is in agreement with the parameter encoding (i.e. FA train) used during acquisition. The signal intensity gradually increases due to the linear increase in the flip angles.

Figure 5.7a shows the comparison of T1 and T2 maps of i) Spiral-MRF and ii) multi-shot EPI-MRF for the tube phantom which were generated after DM (i.e. single iteration of IPA). The parametric maps are visually comparable for the two methods. Figures 5.7b and 5.7c show the mean ($\pm$ standard deviation) T1 and T2 values of each tube in the phantom comparing i) Spiral-MRF (ramp FA, TR = 16 ms and N = 500 repetitions) in orange; ii) EPI-MRF (ramp FA, TR = 16 ms and N = 500 repetitions) in grey; iii) reference values from the manufacturer supplied reference document in blue and iv) gold standard measurements in green (i.e. inversion recovery spin echo - IR-SE for T1 estimation and single echo spin echo - SE for T2 estimation). The mean T1 values are in close agreement for all the methods (less than 4% variation) while the mean T2 values of Spiral-MRF (in orange) and EPI-MRF (in grey) were similarly close (less than 3.5% variation) for all the 12 tubes in the phantom.

Figure 5.8a shows the generated multi-parametric maps of three healthy volunteer brains after the application of DM for i) Spiral-MRF and ii) EPI-MRF. Structures such as GM, WM and CSF can be clearly seen in the parametric maps of the healthy volunteer brains in both methods. The mean and standard deviations of WM and GM regions for the cohort of three healthy volunteer brains shown in Figures 5.8b and 5.8c are similar for both methods (i.e. less than 3% variation for T1 and less than 6% variation for T2). These values are also compared with T1 and T2 literature values of an individual healthy volunteer brain that was estimated using an established Spiral-MRF technique with pseudorandom FA, varying TR and N = 1000 repetitions [95] and the gold standard method for conventional T1 and T2 healthy volunteer brain measurements [205].

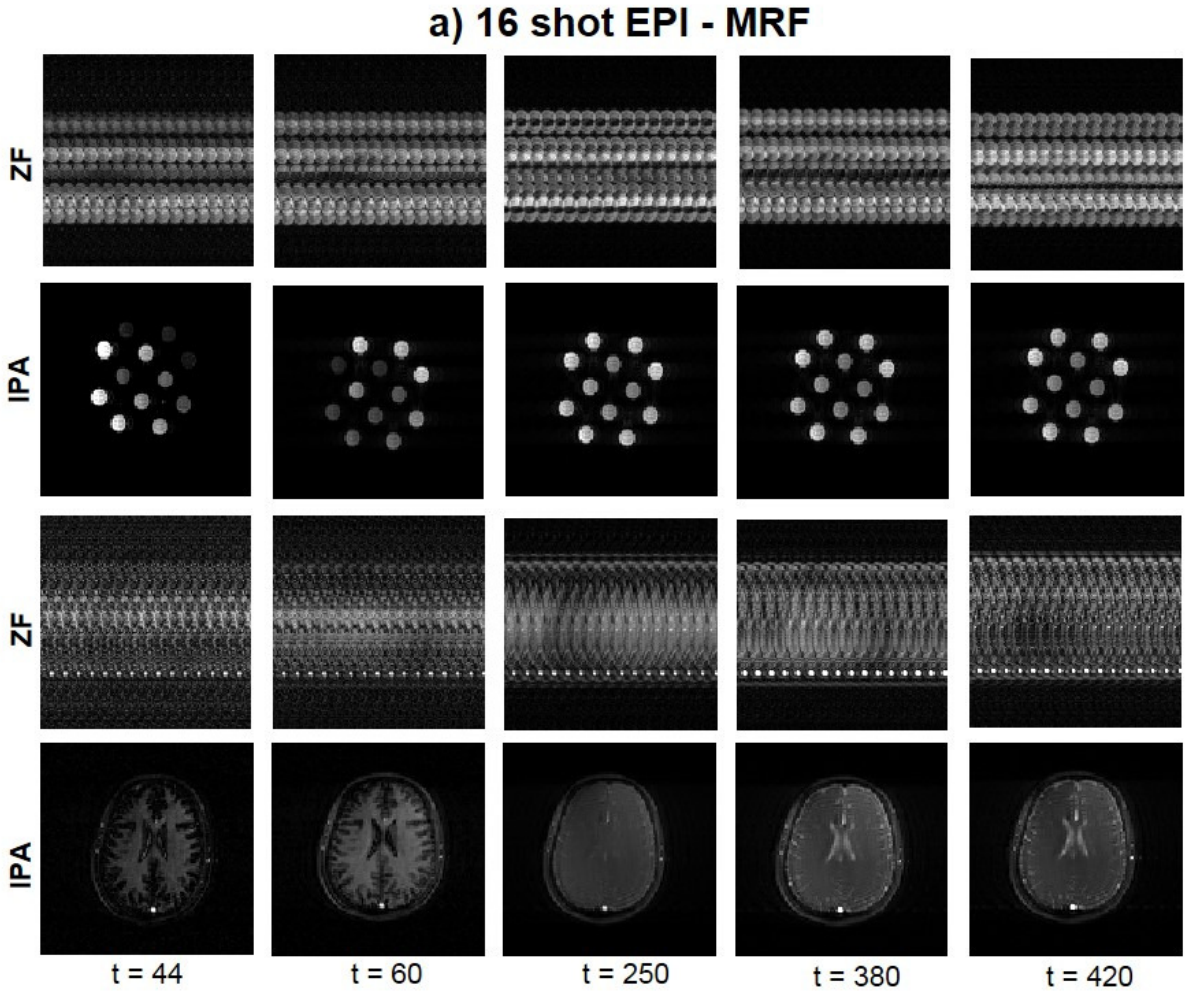

Figure 5.6: **(a)** *Highly aliased zero-filled (ZF) images and Iterative Projection Algorithm (IPA) reconstructed images at specific time-points (i.e. t = 44, 60, 250, 380, 420) of the tube phantom and the healthy volunteer for EPI-MRF (ramped FA, TR = 16 ms, N = 500 repetitions)*

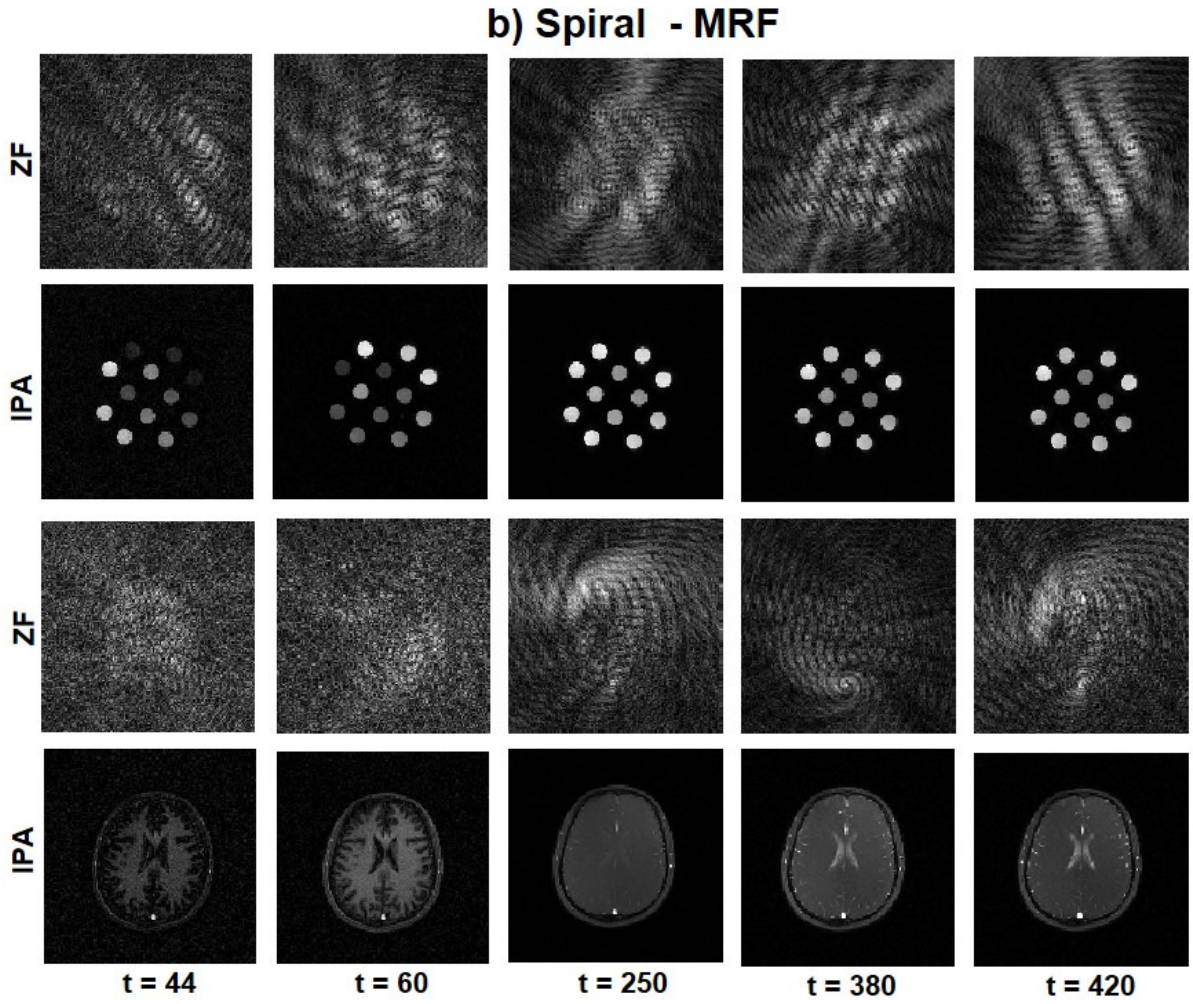

Figure 5.6: ***(b)*** *Highly aliased zero-filled (ZF) images and Iterative Projection Algorithm (IPA) reconstructed images at specific time-points (i.e. t = 44, 60, 250, 380, 420) of the tube phantom and the healthy volunteer for Spiral-MRF (ramped FA, TR = 16 ms, N = 500 repetitions). For DM, the subsampled/aliased ZF images at each frame are used for parameter estimation which is consistent with other work in MRF. However this image sequence should not be considered as an estimate of the actual alias free time series of images. Instead the DM estimates average out the aliasing artefacts. In contrast, for IPA, the subsampled images in each frame are simultaneously reconstructed to produce an alias free time series of images along with parameter estimation.*

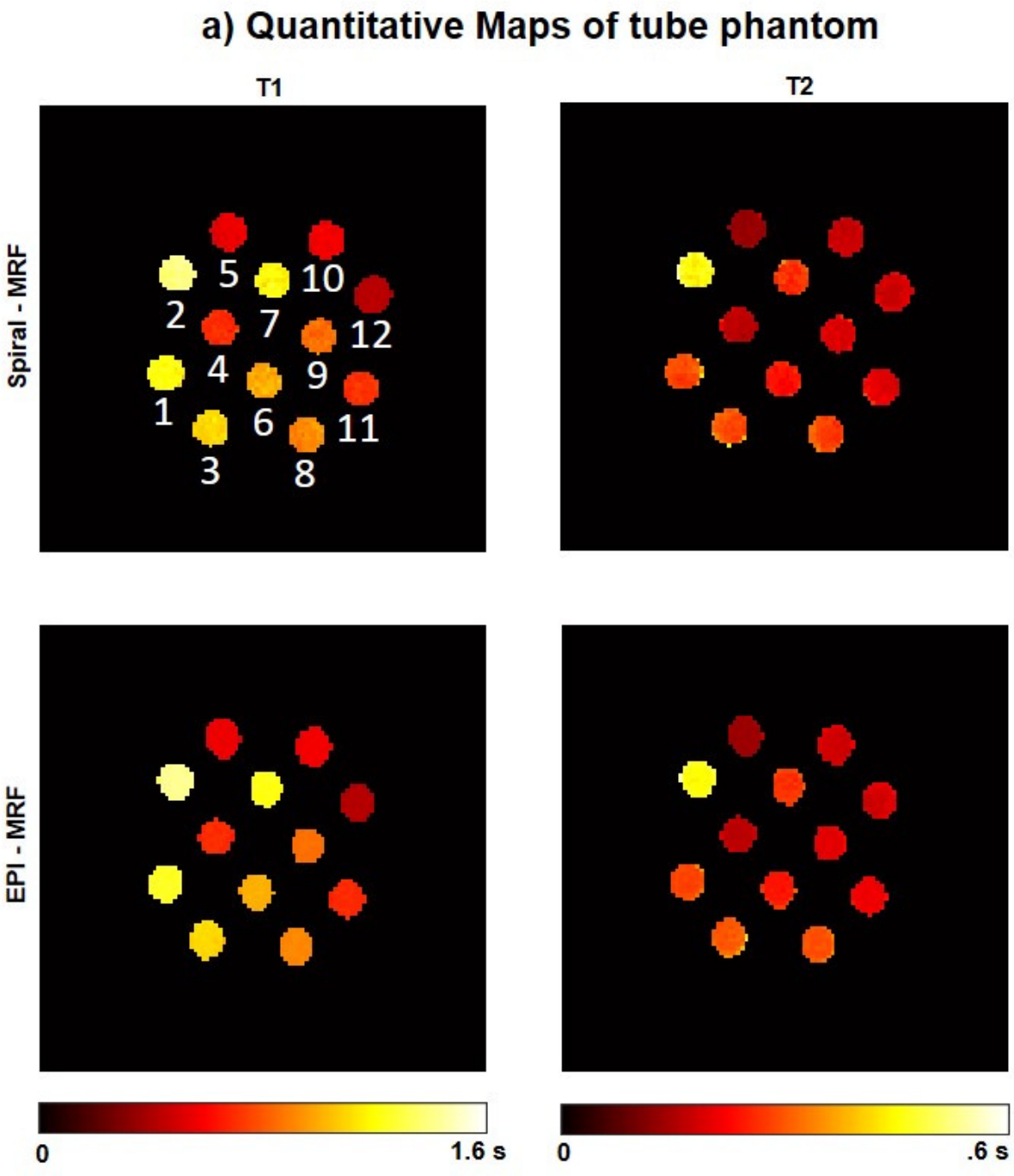

Figure 5.7: ***(a)*** *T1 and T2 maps (in seconds) of the tube phantom generated after Dictionary Matching (DM) for i) Spiral-MRF (ramped FA, TR = 16 ms, N = 500 repetitions) and ii) EPI-MRF (ramped FA, TR = 16 ms, N = 500 repetitions).*

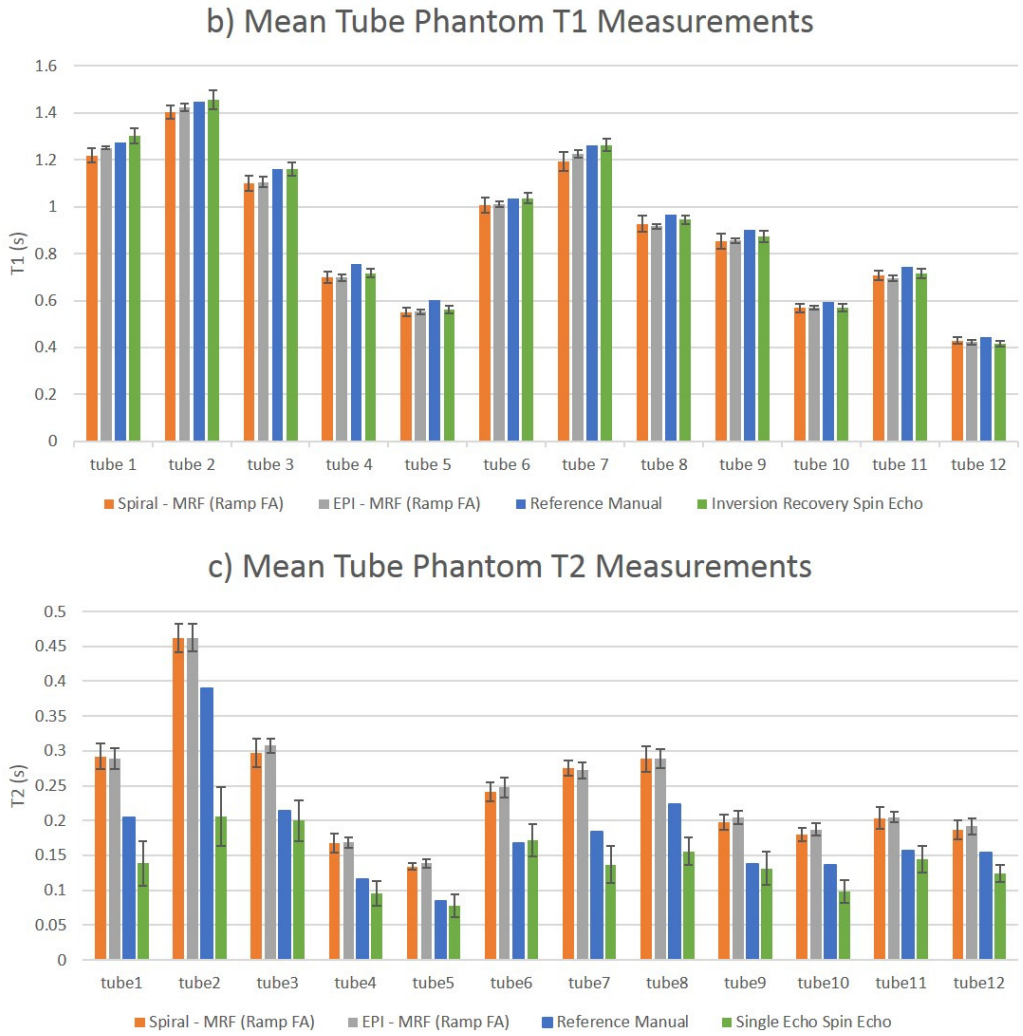

Figure 5.7: ***(b)*** *Mean T1 (± standard deviation) of all tubes in phantom comparing i) Spiral-MRF (ramp FA, TR = 16 ms and N = 500 repetitions) in orange; ii) EPI-MRF (ramp FA, TR = 16 ms and N = 500 repetitions) in grey; iii) reference values from the manufacturer supplied reference document in blue and iv) gold standard measurements in green.* ***(c)*** *Corresponding mean T2 values (± standard deviation). The tubes are numbered in (a) to point out the corresponding tubes in (b) and (c). Note that inversion recovery spin echo (IR-SE) and single echo spin echo (SE) were the gold standard experiments respectively for T1 and T2 estimation. The reference manual supplied by the manufacturer (i.e. Diagnostic Sonar, Livingston, UK) contained reference T1 and T2 values of all the tubes in the phantom.*

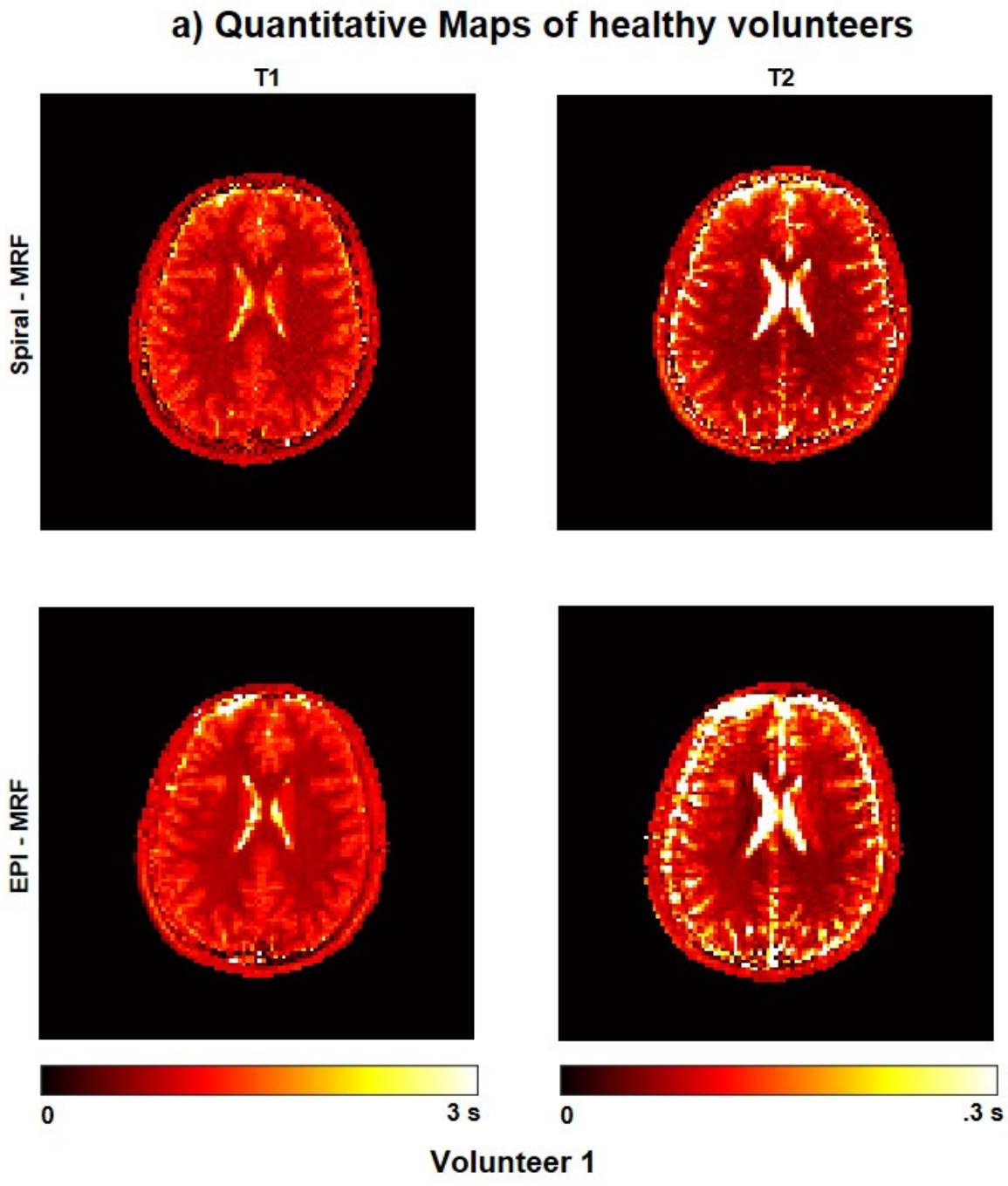

Figure 5.8: ***(a)*** *i) T1 and T2 maps (in seconds) of healthy volunteer 1 generated after Dictionary Matching (DM) for i) Spiral-MRF (ramped FA, TR = 16 ms, N = 500 repetitions) and ii) EPI-MRF (ramped FA, TR = 16 ms, N = 500 repetitions). Note the signal loss and signal accrual effects (i.e. susceptibility artefacts) to the left and right of the brain ventricles in the EPI-MRF T2 maps.*

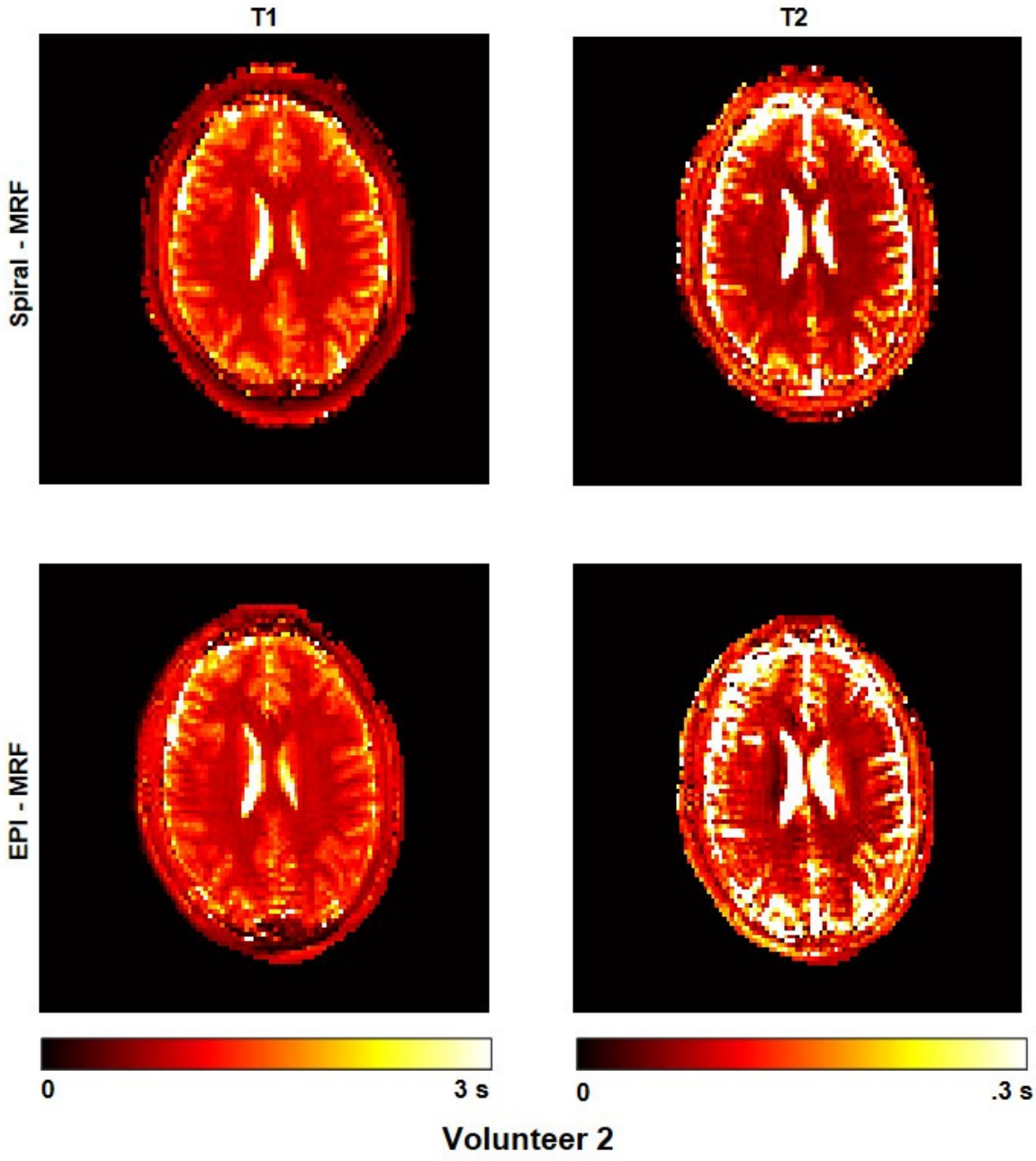

Figure 5.8: (a) *ii) T1 and T2 maps (in seconds) of healthy volunteer 2 generated after Dictionary Matching (DM) for i) Spiral-MRF (ramped FA, TR = 16 ms, N = 500 repetitions) and ii) EPI-MRF (ramped FA, TR = 16 ms, N = 500 repetitions). Note the signal loss and signal accrual effects (i.e. susceptibility artefacts) to the left and right of the brain ventricles in the EPI-MRF T2 maps.*

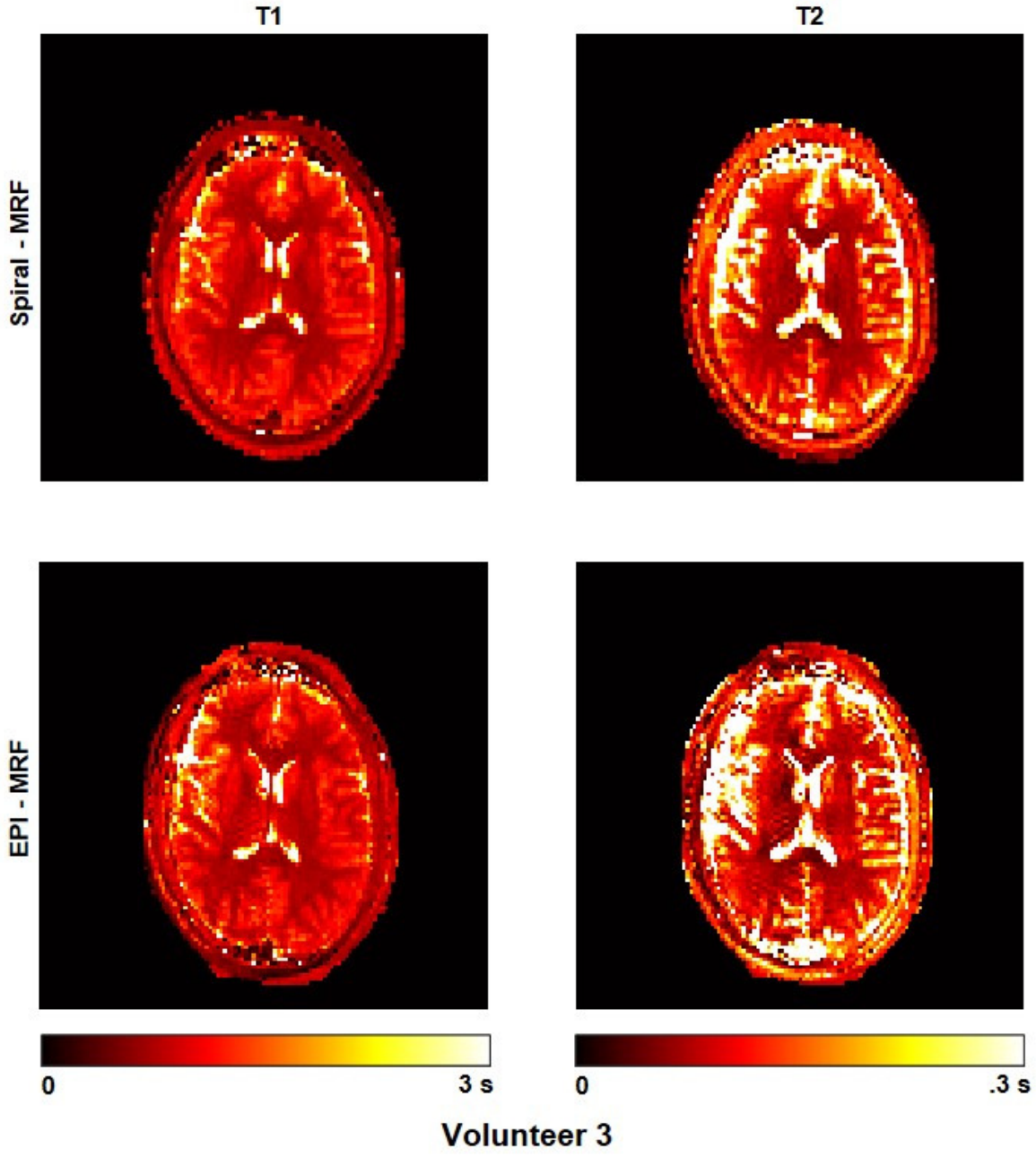

Figure 5.8: (a) *iii) T1 and T2 maps (in seconds) of healthy volunteer 3 generated after Dictionary Matching (DM) for i) Spiral-MRF (ramped FA, TR = 16 ms, N = 500 repetitions) and ii) EPI-MRF (ramped FA, TR = 16 ms, N = 500 repetitions). Note the signal loss and signal accrual effects (i.e. susceptibility artefacts) to the left and right of the brain ventricles in the EPI-MRF T2 maps.*

Figure 5.8: ***(b)*** *Mean T1 (± standard deviation) of WM and GM regions of a cohort of three healthy volunteers comparing i) Spiral-MRF (ramp FA, TR = 16 ms and N = 500 repetitions) in orange and EPI-MRF (ramp FA, TR = 16 ms and N = 500 repetitions) in grey. These values are also compared with T1 and T2 literature values of an individual healthy volunteer brain that was estimated using an iii) established Spiral-MRF technique (pseudorandom FA, varying TR and N = 1000 repetitions) in blue [68] and iv) previously reported conventional literature values of a healthy volunteer cohort in green [153].* ***(c)*** *Corresponding mean T2 values (± standard deviation) for WM and GM regions from three healthy volunteers.*

Figure 5.9a shows the original T1, T2 maps of the Brainweb digital phantom [209, 210] with corresponding known parameters (T1 s and T2 s) for GM (1.3, 0.105), WM (0.85, 0.08) and CSF (4.2, 0.2) along with the estimated T1 and T2 maps using Dictionary Matching and IPA reconstruction from single-coil Brainweb phantom data. Figure 5.9b shows the T1 and T2 difference error maps for Dictionary Matching and IPA reconstruction. Figure 5.10 shows the T1 estimations of EPI-MRF for a healthy volunteer brain when IPA was used for reconstruction. Also shown are the T1 maps generated after DM and difference map for comparison. The IPA reconstruction reduces the relative error between the quantitative estimates of predicted T1 and T2 values and the MRF measurements at every iteration and converges when this error becomes very small. Iterative reconstructions are particularly beneficial when we have limited data and its benefits are further highlighted for a reduced coil scenario in Figure 5.11. Figure 5.12 shows the corresponding T1 map for Spiral-MRF after IPA reconstruction. In the spiral case, we observe checker board like artefacts (similar to observations reported by Cline et al. [119]) which arise due to lack of samples from the edges of k-space as a result of the spiral sampling strategy. This can be seen as an issue of the null space of the forward operator [119] and is not an algorithmic issue.

5.4 Discussion

In this study, a new MRF scheme based on a vastly subsampled Cartesian readout that utilizes multi-shot EPI (i.e. multi-shot EPI-MRF) has been introduced. Good quantification of T1 and T2 maps has been achieved both in phantom and three healthy volunteer brains in about 8 s per slice for the range of T1 and T2 values that normally occur in the human brain. The generated parametric maps of the proposed EPI-MRF method have been compared and are shown to be in good agreement with Spiral-MRF; thereby demonstrating the potential of Cartesian MRF as a suitable alternative to Spiral-MRF. Moreover, EPI sequences have been used clinically for over 20 years and the artefacts that arise from EPI are better understood by clinicians when compared to spirals. Therefore, it has a great potential to be easily adopted in clinical protocols.

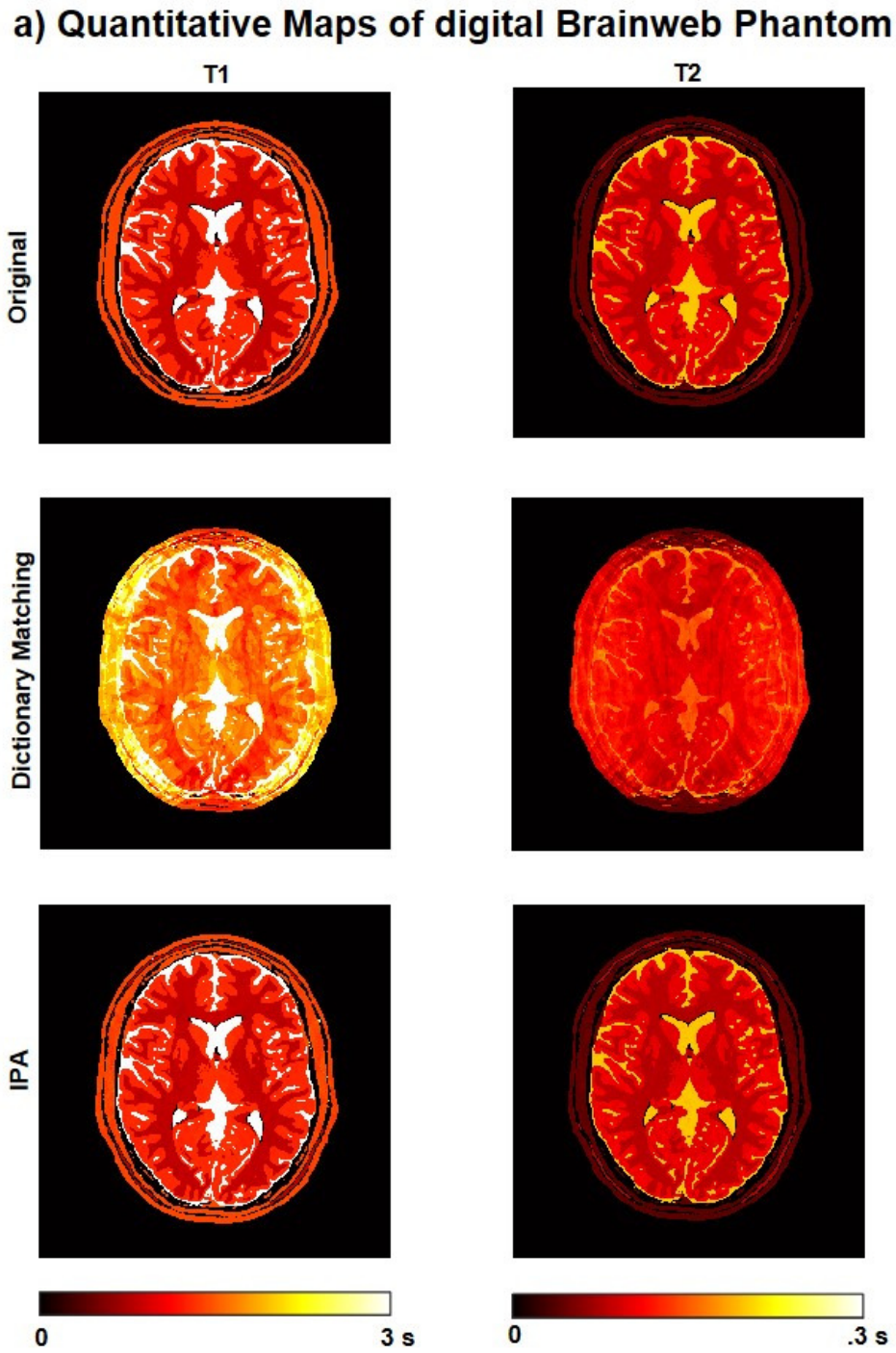

Figure 5.9: ***(a)*** The original T1,T2 maps of the digital Brainweb Phantom with corresponding known parameters (T1 s and T2 s) for GM (1.3, .105), WM (0.85,0.08) and CSF (4.2 and 0.2) along with the estimated T1 and T2 maps using Dictionary Matching and IPA reconstruction from single-coil Brainweb digital phantom data.Aliasing effects are still present inside the brain for DM reconstruction while aliasing is completely resolved when IPA reconstruction is used.

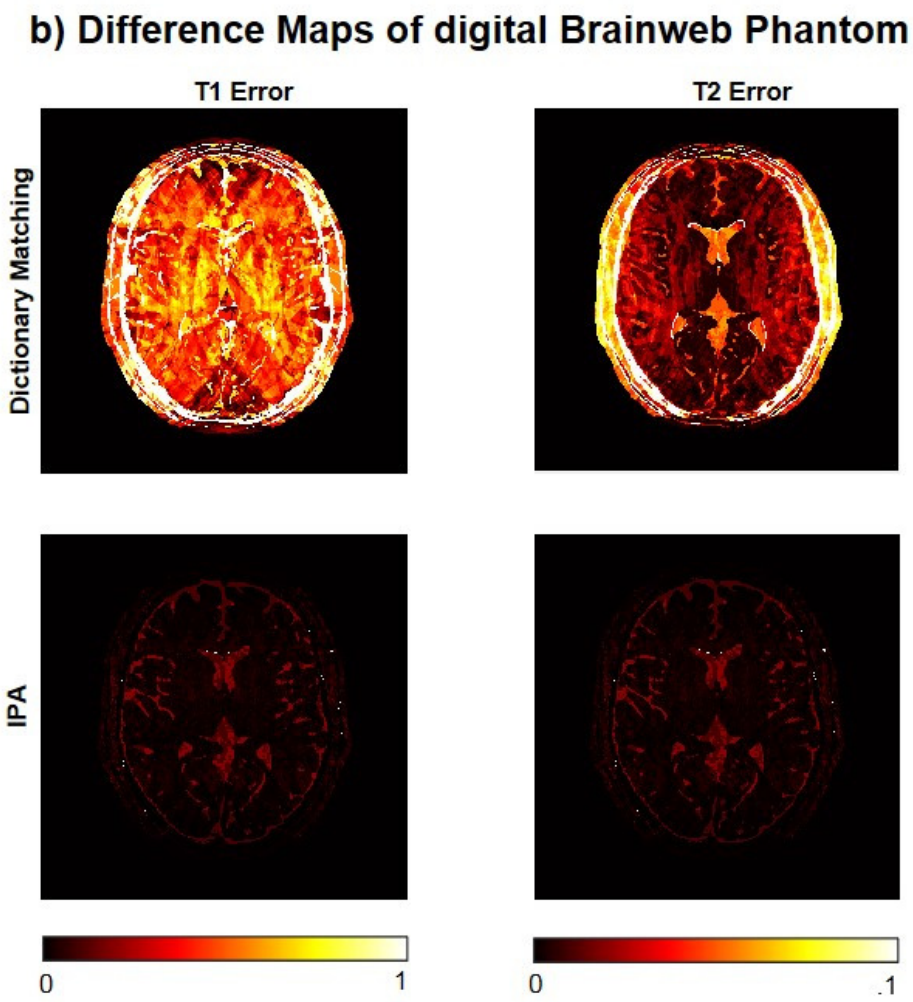

Figure 5.9: ***(b)*** *The T1 and T2 difference error maps for Dictionary Matching and IPA reconstruction. The maximum T1 and T2 error using DM was 38% and 35% respectively whereas the maximum T1 and T2 error using IPA was 3.9% and 5% respectively.*

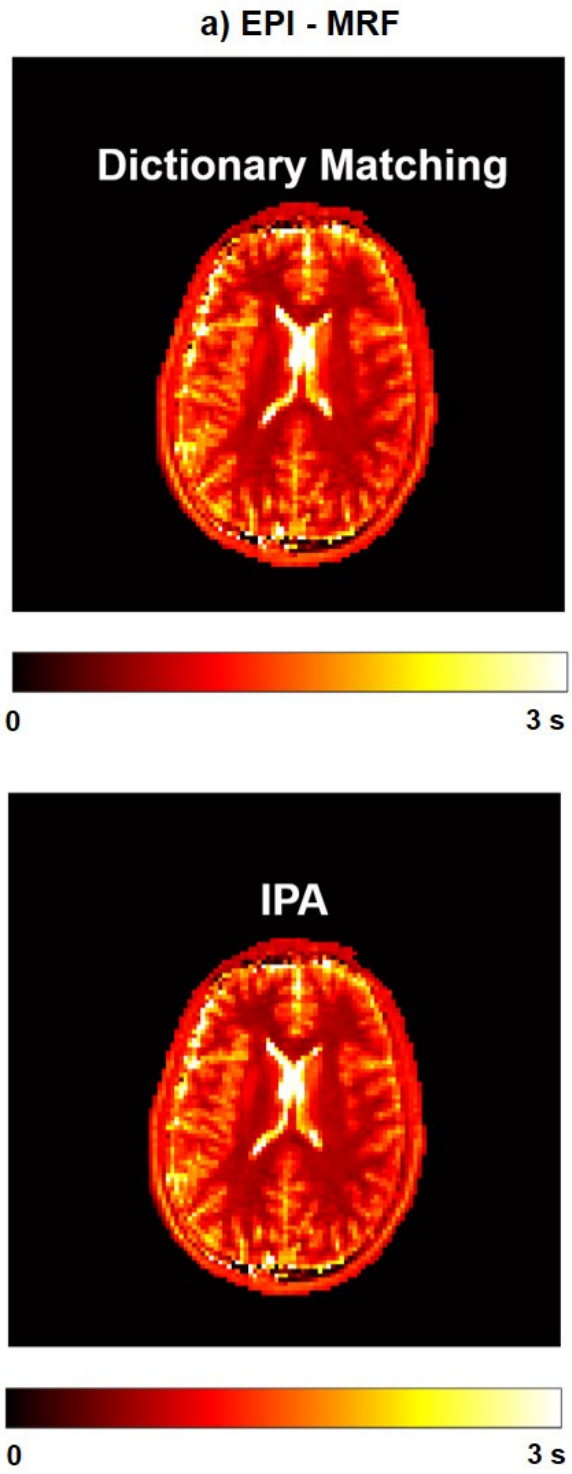

Figure 5.10: ***(a)*** *T1 maps generated using Dictionary Matching (DM) and Iterative Projection Algorithm (IPA) from multi-coil healthy volunteer data.*

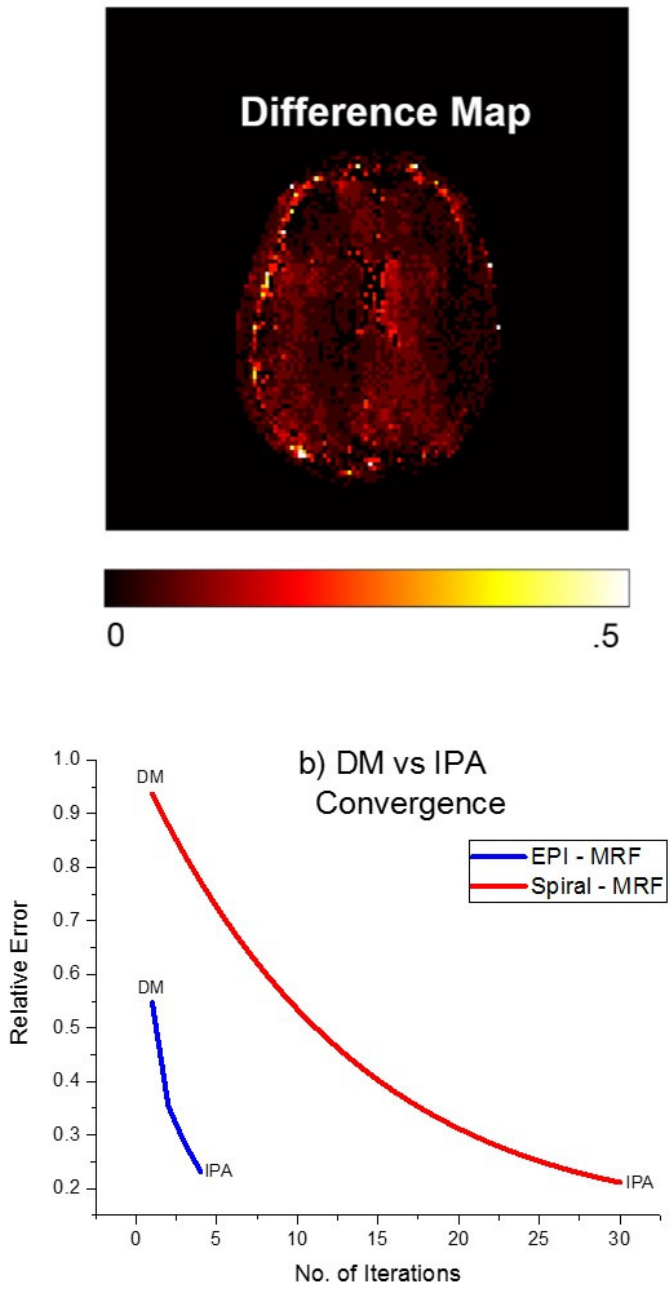

Figure 5.10: *The difference map between IPA and DM reconstruction for EPI-MRF.* ***(b)*** *A comparison of IPA convergence is shown for EPI-MRF and Spiral-MRF. The multi-coil healthy volunteer brain data considerably improves the performance of the DM method since most of the aliasing inside the brain due to subsampling is removed by using the multiple coils (in a similar way to parallel imaging).*

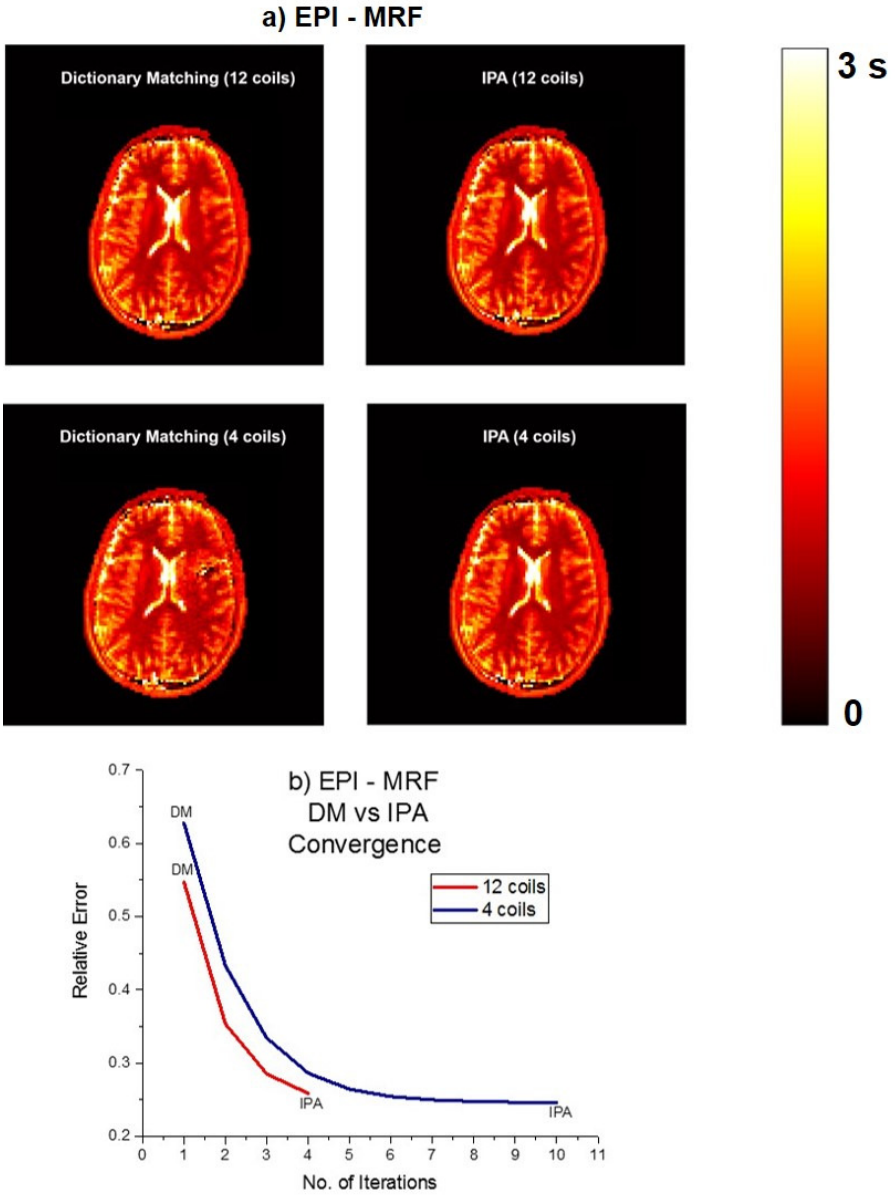

Figure 5.11: ***(a)*** *Figure showing the T1 maps of a healthy volunteer generated using 12 coils and 4 coils respectively for Dictionary Matching (DM) and Iterative Projection Algorithm (IPA) for EPI-MRF. The IPA algorithm is able to reconstruct T1 maps similar to the 12 coils case even though only 4 coils are used (this highlights the benefit of IPA in a reduced coil scenario). However, DM does not perform as well in a 4 coil scenario and produces noisy T1 maps as shown in the Figure.* ***(b)*** *The convergence of IPA algorithm using different number of coils are shown for EPI-MRF. Note that DM is equivalent to a single iteration of IPA.*

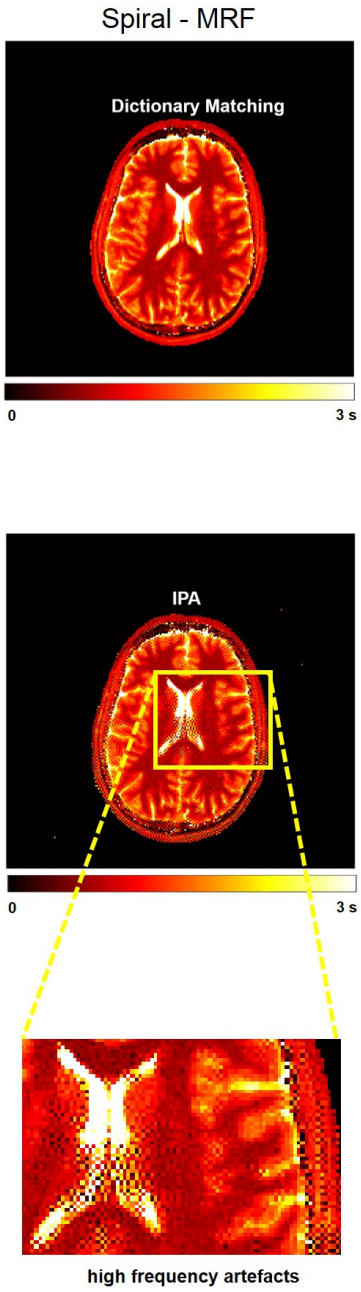

Figure 5.12: *T1 maps of a healthy volunteer generated using Dictionary Matching (DM) and Iterative Projection Algorithm (IPA) respectively for Spiral-MRF. The enlarged image shows the appearance of high frequency artefacts after iterative reconstruction.*

On comparison of the T1 and T2 maps of the tube phantom for EPI-MRF and Spiral-MRF in Figure 5.7a, it can be seen that both T1 and T2 maps are visually comparable for both methods. The mean T1 and T2 values (see Figs. 5.7b and 5.7c) for each of the 12 tubes in the phantom are in close agreement with less than 4% deviation for T1 and less than 3.5% deviation for T2. The mean T1 values of Spiral-MRF and EPI-MRF were also similarly in very good agreement with the gold standard IR-SE T1 measurements and with the known reference T1 values from the manual (see Fig. 5.7b). This is due to the high T1 sensitivity of the encoding scheme used for the acquisition resulting in a good T1 quantification. However, despite the good T2 agreement between EPI-MRF and Spiral-MRF for the phantom, we observe that T2 estimates of the tube phantom overestimate the reference values (see Fig 5.7c). In contrast, the gold standard SE measurements appear to slightly underestimate the reference values (and quite considerably in the case of tube 2). The T2 overestimation in MRF may be caused by slice profile and B1 effects which have been previously reported in other MRF studies [198, 211–213]. In addition to this, previous MRF studies have reported that T2 variability is greater than T1 in certain gel based phantoms suggesting that T2 is affected more by B1 and temperature fluctuations [96, 214]. This T2 discrepancy highlights an inherent limitation of the standard MRF model and not just the proposed methods. This is an important and under-reported issue in MRF even though attempts have been made to incorporate correction factors in standard MRF by simulating the radiofrequency pulse in the dictionary, estimating an additional B1 map during the MRF acquisition or by acquiring a B1 field map in a separate scan [198, 211]. The main focus of this study is to demonstrate that two different MRF methods (i.e. Spiral-MRF and EPI-MRF) that use the standard MRF model are in agreement with each other for both phantom and healthy volunteer scans. It does not completely account for the many correction factors necessary to improve the quantitative accuracy of the standard MRF model and is acknowledged as the major disadvantage of this work. Furthermore, it has also been shown in other studies that gold standard T2 measurements are also affected by B1 effects which cause a T2 bias when fitting to the mono-exponential T2 decay curve [215, 216]. Additional B1 measurements can also be used to reduce this bias and potentially decrease the discrepancy between MRF and gold standard T2 measurements.

The mean T1 and T2 values of white matter (WM) and grey matter (GM) for three healthy volunteer brains shown in Figures 5.8b and 5.8c for Spiral-MRF and EPI-MRF are almost identical (less than 3% deviation for T1 and less than 6% deviation for T2) and this demonstrates good T1 and T2 quantification for the three healthy volunteer brains. The mean T1 and T2 values

of EPI-MRF and Spiral-MRF are also in close agreement with the values obtained by an established Spiral-MRF acquisition with pseudorandom FA schedule, varying TR and N = 1000 repetitions [95] and with gold standard T1 and T2 values of healthy volunteers previously reported in the literature [205] (see Figs. 5.8b and 5.8c). These results show that the proposed multi-shot Cartesian EPI-MRF approach can be used to generate T1 and T2 maps similar to Spiral-MRF in human brains and can be a good alternative to the Spiral-MRF implementation.

This study also shows the advantages of using iterative reconstruction over the non-iterative DM method. The Brainweb digital phantom [209, 210] with known T1 and T2 values, 16-shot EPI subsampling and N = 200 repetitions was used to demonstrate the need for iterative reconstruction (see Figure 5.9). Iterative reconstructions become more beneficial when the number of repetitions are low and is highlighted by Figure 5.9 in which only 200 repetitions were used instead of 500 repetitions that were used for the tube phantom and healthy volunteer study. From the T1 and T2 estimates of DM and IPA reconstructions in Figure 5.9a, we can see that a considerable improvement in accuracy was achieved when IPA reconstruction was used. The error maps in Figure 5.9b show the reduced error for IPA reconstruction when compared to the DM method. Figure 5.10b also shows that there is a reduction in the relative error for EPI-MRF and Spiral-MRF at each iteration until the convergence of the IPA algorithm. The relative error showed an approximate five-fold decrease for EPI-MRF and eight-fold decrease for Spiral-MRF (see Fig. 5.10 b). The IPA reconstructions of multi-shot EPI-MRF converged very quickly (in about 4 iterations) compared to the Spiral-MRF implementation (30 iterations) and could therefore result in a very fast implementation on the scanner. The monotonic decay of the relative error (i.e.measurement fidelity error) implies that iterative reconstructions improved data consistency as compared to the non-iterative DM scheme. Since the entire k-space is sampled in EPI (including high frequency information from the k-space corners), iterative reconstruction improved the T1 estimation and resulted in a very fast convergence especially with the availability of multi-coil data (see. Figure 5.10a). The DM method shows poor results in Figure 5.9 since the Brainweb digital phantom data contains only single-coil data. The multi-coil healthy volunteer brain data used in Figure 5.10 considerably improves the performance of the DM method since most of the aliasing due to subsampling is removed by using the multiple coils (in a similar way to parallel imaging). While good reconstructions are possible with non-iterative schemes such as DM when multi-coil data is used, iterative methods are beneficial when there is less available data. Here we demonstrated this with a reduced number of coils but it should also be of value when optimizing shorter sequences. In contrast, for the spiral

case, due to the lack of sufficient high frequency content, errors appeared in the iterative reconstruction in the form of checker board like artefacts (similar to the ones reported by Cline et al. [119]) although there was a monotonic decay in the relative error (see Fig. 5.12). These errors could be removed either by using a spatial-smoothing regularization [132] or by reconstructing images at a lower spatial resolution. These high frequency artefacts coupled with the errors due to re-gridding highlight a fundamental limitation of the spiral sampling strategy [119] which is independent of the algorithm used for reconstruction. Therefore, IPA EPI-MRF may offer a possible route to higher resolution MRF due to its complete k-space coverage. [119, 120].

The reconstruction times were heavily dependent on the SVD compression-decompression that was used when moving from k-space to image space (i.e.backward or adjoint operation) and vice versa (i.e. forward operation) [101, 119]. Each iteration used SVD compression in the backward operation and SVD decompression in the forward operation. This provided a considerable reduction in reconstruction time. The reconstruction time was increased from 22 seconds to 206 seconds for EPI-MRF and from 482 seconds to approximately 6 hours for Spiral-MRF when SVD compression-decompression was not used in the reconstruction. The reconstructions were performed on a normal laptop computer with standard specifications (i.e.Intel Core i7 Processor with 16GB RAM). The convergence of the Spiral-MRF implementation was usually slower (i.e. both in time and in the number of iterations required) when compared to EPI-MRF (see Fig. 5.10b). This appears to be due to the bad conditioning of the spiral sampling problem and the need for re-gridding to reconstruct spiral data [119]. In addition, each iteration was more expensive because spiral sampling uses a costlier NUFFT compared to the FFT used in EPI. Therefore, SVD compression-decompression is highly beneficial especially for Spiral-MRF in order to speed up the reconstruction time. Further reductions in the computation time are possible using an adaptive iterative algorithm with fast nearest neighbor searches for the DM step in the reconstruction [120]. The fast convergence of EPI-MRF and its robustness to high frequency artefacts make it naturally suitable for iterative reconstructions.

Despite the enormous potential and numerous advantages of MRF, T1 and T2 quantification through the MRF framework also has some underlying drawbacks that also extend to the proposed EPI-MRF approach. The quantification is not accurate in MRF when T1 and T2 values are very high (i.e. T1 $>$ 2500 ms and T2 $>$ 400 ms) due to the difficulty of discriminating dictionary entries at these values and this can be seen from the underestimation of T2 cerebrospinal fluid (CSF) values in both EPI-MRF and Spiral - MRF in Figure 5.8a. In addition, The TR that

was used for both EPI and spiral acquisitions was the same. It was set to the minimum achievable TR for EPI (i.e. 16 ms) for fair comparison even though the TR could be further reduced for the case of Spiral-MRF. We have observed in other experiments that there were variations in T2 estimates when different TRs were used (i.e. longer TRs resulting in higher estimates) suggesting that the idealized EPG model used for the dictionary may have some inconsistencies and it merits further research. It is also important to note that EPI sequences are more sensitive to B_0 inhomogeneity caused by magnetic susceptibility variations that occur in the form of signal loss/leakage in the phase encoding (PE) direction [204, 217, 218] than spirals. The higher sensitivity of EPI to B_0 inhomogeneity is due to its reduced bandwidth in the PE direction. In the human brain, we observe a small signal shift/leakage around the CSF region (i.e. to the left and right of the ventricles in the brain) which is a susceptibility artefact and can be seen from the EPI-MRF T2 maps in Figure 5.8a. This is because the CSF has a low susceptibility compared to the iron rich regions surrounding it. However, these local magnetic susceptibility differences are small and do not appear to significantly affect the T2 estimations of GM and WM in human brains as shown by the similar means and standard deviations of EPI-MRF and Spiral-MRF in Figure 5.8c. Geometric distortions which are common in EPI are also present in the T2 maps in Figure 5.8a and might be caused by imperfect phase correction leading to phase errors. It could be reduced by using Echo Time Shifting (ETS) that could be used to improve the phase error function in multi-shot EPI [219]. Due to the high T1 sensitivity of the acquisition, these artefacts were suppressed in the T1 maps but they affected the T2 maps. By enhancing the T2 sensitivity during the acquisition using an optimized FA train, these artefacts could be potentially reduced.

A study of optimized FA schedules is of great interest for our future work that could depend on many factors such as the sequence used (i.e. bSSFP or unbalanced SSFP), excitation sequence length, TRs, the type of variation in flip angles (i.e. smoothly varying, pseudo-random, random, piecewise constant etc.), the amount of subsampling and the type of sampling (i.e. Cartesian, Spiral or Radial). In addition, this future work would include methods to accurately correct for magnetic susceptibility variations, phase errors and also explore high resolution MRF using IPA EPI-MRF. FA schedule optimization, reduction of phase errors and incorporation of correction factors to compensate for T2 quantification errors could potentially improve the robustness of the proposed EPI-MRF method.

5.5 Conclusion

The multi-shot EPI-MRF method introduced here was able to provide joint quantification of multi-parametric maps such as T1 and T2 in a short scan duration (i.e. 8s per slice) similar to Spiral-MRF. This method was able to significantly reduce the reconstruction time when compared to Spiral-MRF. This method also eliminated the high frequency artefacts that appeared in iterative Spiral-MRF reconstructions due to the full k-space coverage provided by the Cartesian sampling trajectory.

Chapter 6
Conclusions and Future Works

6.1 Conclusions

The ultimate goal of this work was to use a combination of CS, PI and sparse sampling methods to accelerate structural and quantitative MRI. Another important objective was to implement prospective accelerated scanning in a clinical MR scanner and to establish the diagnostic value of accelerated neuroimaging through radiological evaluation. The results show that the major goals of this project were accomplished.

The following conclusions were drawn from the sequence optimization in Chapter 3: optimization of acquisition and reconstruction parameters such as subsampling pattern, calibration size, acceleration factor, amount of regularization and k-space acquisition order was essential for improving the image quality of CS-PI reconstructions. If the acquisition and reconstruction parameters were not optimized, the reconstructed images showed higher presence of noise and artefacts that impeded the clarity of certain brain structures. Likewise, it was also very important to optimize the k-space acquisition order for preserving image contrast in certain clinical sequences like the IR-prepared 3D GRE sequence that was used in this work. Non-optimization of the sampling order resulted in severe loss of contrast and made CS accelerated brain images clinically unusable. In addition, this chapter also showed that accelerated prospective scanning with sampling order optimization which was implemented in a clinical MR scanner preserved contrast and reduced the scan time from 8:08 minutes to 2:42 minutes for 3-fold acceleration.

The diagnostic quality assessments in Chapter 4 resulted in the following conclusions. The mean radiological scores showed that the majority of accelerated MR brain datasets were considered to be fully diagnostic when they were evaluated for gross structural brain assessment. However, when the same datasets were evaluated using a more stringent clinical question which required high spatial resolution discrimination, a higher penalty was applied to the radiological scores which made the accelerated images non-diagnostic. The radiological assessments demonstrated that the clinical question that was being investigated radiologically should be clearly defined prior to the diagnostic quality assessment. It also showed that CS acceler-

ated neuroimmaging has clinical diagnostic value if sampling order optimization is carried out. From the radiological assessments, we can conclude that CS accelerated neuroimaging is only suitable for certain clinical applications such as the routine screening of patients for tumours while it is not yet recommended for tasks that require high spatial resolution such as epilepsy investigation.

The accelerated Cartesian MR fingerprinting scheme in Chapter 5 presented the following conclusions. Firstly, it was shown that multi-parametric quantitative maps such as T1 and T2 maps similar to Spiral-MRF could be produced by using an accelerated Cartesian sampling scheme based on multi-shot EPI. Therefore, multi-shot EPI-MRF could serve as an alternative to conventional Spiral-MRF. In addition, it was demonstrated that a linear ramp FA schedule could produce T1-T2 sensitivity similar to that found for a pseudorandom FA schedule in only half the number of timeframes even though it was not the optimal FA schedule. This observation showed that further FA schedule optimization in MRF is possible. Secondly, it was shown that advanced iterative reconstruction techniques improved the accuracy of multi-parametric maps when compared to the non-iterative DM method. Thirdly, it was shown that the Cartesian sampling strategy resulted in faster reconstructions while it also suppressed high frequency artefacts in reconstructed maps due to its full k-space coverage.

With these observations, it can be concluded that the developed MR acceleration techniques are very promising and can be successfully used for reducing the scan time in structural and quantitative MRI. Several extensions to this work are also possible and will be discussed in Section 6.2.

6.2 Future Work

6.2.1 CS-PI accelerated multi-sequence neuroimaging and patient studies

Even though the clinical diagnostic utility of CS accelerated neuroimaging for IR-prepared 3D GRE sequence has been demonstrated in this thesis, it has not been applied to other sequences that are also used in neuroimaging. Many neurological studies rely on multiple sequences such as T1w, T2w, T2*, Diffusion Weighted Imaging (DWI) and Fluid Attenuated Inversion Recovery (FLAIR) sequences that produce images of different contrasts for diagnostic purposes [154, 183]. Therefore, it is important to implement CS-PI acceleration on multiple sequences and validate the usefulness of CS-PI accelerated neuroimaging. It is expected that for mag-

netization prepared sequences such as T2w imaging, optimization of the k-space acquisition order would be important to improve the image quality of CS-PI reconstructions as shown in Chapters 3 and 4.

As shown in Chapter 4, CS-PI accelerated neuroimaging with sampling order optimization retained sufficient diagnostic value for routine screening of patients with large tumours or lesions. However, the study was conducted on healthy volunteers who were not expected and did not have any tumours or lesions in the MR images. As the study was not performed on patients with tumours, it is difficult to comment on the usefulness of CS accelerated neuroimaging for discriminating clinically relevant tumours. A possible next step to extending this work would be to carry out a study on patients and perform radiological assessments of CS accelerated MR datasets of patients.

6.2.2 Deep Learning based reconstructions for accelerated MRI

The newest trend in accelerated MRI is the use of deep learning methods involving convolutional neural networks (CNNs) to perform reconstructions of accelerated MRI data. Several studies have shown that deep learning based reconstruction methods methods can produce high quality MR images from highly undersampled MR measurements [220–222]. One of the other advantages is that CNN based reconstruction techniques are extremely fast and have a huge potential to be implemented in various clinical protocols in the future. Similarly, CNNs have been used in other studies to reduce artefacts and noise from undersampled MR measurements and the results obtained are very promising [223, 224]. So, a combination of CS acquisition with deep learning acquisition would be an interesting future direction for this project. It should also be noted that challenges such as amount of data required to train CNNs, the optimal training process and the widespread availability of medical images for training purposes are still prevalent and must be be dealt with so that these techniques gain more widespread usage. There are also ethical issues in deep learning based reconstruction techniques that need to be guarded against. It is important to ensure that ethnical biases are not inadvertently built into deep learning algorithms which may reflect biases inherent in the data used to train them [225]. There is also the need to to regulate deep learning in the context of medical device development, the accountability of deep learning techniques under the law, and the implications of data protection and cybersecurity [225]. Since the clinical adoption of deep learning based techniques is still in its infancy, there is plenty of work that needs to be done for these techniques to become a

routine procedure in clinics and hospitals.

6.2.3 Optimization of standard MR fingerprinting model

As shown in Chapter 5, very good quantification of T1 values was possible using the standard MRF model [95] that was used in the study and was validated in the tube phantom by using the gold standard IR spin echo T1 experiment. However, the T2 values were overestimated by both the MRF sequences (i.e. EPI-MRF and Spiral-MRF) when compared to the T2 values estimated by the gold standard spin echo T2 experiment. This discrepancy may have been caused by slice profile and B_0 effects [198, 211–213]. A future direction would be to include these additional effects into the standard MRF model and compensate for the T2 discrepancy. Including more parameters into the dictionary will exponentially increase the size of the dictionary and therefore will significantly increase the reconstruction time. Such a scenario will warrant the need to develop fast dictionary searching algorithms and fast reconstruction techniques to minimize the reconstruction time.

Likewise, there is also a big scope for the optimization of the FA schedule, the type of variation in the FA pattern, type of sequence, subsampling patterns and TR that can be used in MRF. It would also be interesting to design a unique, optimal set of parameters for all the different types of MRF sequences (i.e. bSSFP, unbalanced SSFP, pseudo SSFP) that are currently in use. The high flexibility offered by the MRF framework can be exploited to extend this work in the future.

In summary, we have shown in this thesis that advanced sparse sampling strategies can be used in conjunction with parallel imaging and compressed sensing techniques for accelerating both structural and quantitative MRI. The proposed techniques are ready to be integrated in clinical protocols and can potentially provide clinically useful information to radiologists for diagnostic quality assessments. It would be interesting to see how the proposed techniques would help in the screening, diagnosis and treatment monitoring of diseases in clinics and hospitals.

References

[1] C. Guy and D. Ffytche, *An introduction to the principles of medical imaging*. World Scientific, 2005.

[2] J. L. Prince and J. M. Links, *Medical imaging signals and systems*. Pearson Prentice Hall Upper Saddle River, 2006.

[3] "Diagnostic Imaging Dataset Annual Statistical Release 2017/18 - NHS England." https://digital.nhs.uk/data-and-information/data-collections-and-data-sets/data-sets/diagnostic-imaging-data-set.

[4] D. K. Sodickson and W. J. Manning, "Simultaneous acquisition of spatial harmonics (SMASH): fast imaging with radiofrequency coil arrays," *Magn Reson Med*, vol. 38, no. 4, pp. 591–603, 1997.

[5] K. P. Pruessmann, M. Weiger, M. B. Scheidegger, and P. Boesiger, "SENSE: Sensitivity encoding for fast MRI," *Magn Reson Med*, vol. 42, no. 5, pp. 952–962, 1999.

[6] M. A. Griswold, P. M. Jakob, R. M. Heidemann, M. Nittka, V. Jellus, J. Wang, B. Kiefer, and A. Haase, "Generalized autocalibrating partially parallel acquisitions (GRAPPA)," *Magn Reson Med*, vol. 47, no. 6, pp. 1202–1210, 2002.

[7] M. Lustig and J. M. Pauly, "SPIRiT: iterative self-consistent parallel imaging reconstruction from arbitrary k-space," *Magn Reson Med*, vol. 64, no. 2, pp. 457–471, 2010.

[8] M. Weiger, K. P. Pruessmann, and P. Boesiger, "2D SENSE for faster 3D MRI," *MAGMA*, vol. 14, no. 1, pp. 10–19, 2002.

[9] M. Lyu, Y. Liu, V. B. Xie, Y. Feng, H. Guo, and E. X. Wu, "A New Joint-Blade SENSE Reconstruction for Accelerated PROPELLER MRI," *Scientific reports*, vol. 7, p. 42602, 2017.

[10] B. Madore, G. H. Glover, and N. J. Pelc, "Unaliasing by Fourier-encoding the overlaps using the temporal dimension (UNFOLD), applied to cardiac imaging and fMRI," *Magn Reson Med*, vol. 42, no. 5, pp. 813–828, 1999.

[11] J. Tsao, P. Boesiger, and K. P. Pruessmann, "k-t BLAST and k-t SENSE: dynamic MRI with high frame rate exploiting spatiotemporal correlations," *Magn Reson Med*, vol. 50, no. 5, pp. 1031–1042, 2003.

[12] M. Lustig, D. Donoho, and J. M. Pauly, "Sparse MRI: The application of compressed sensing for rapid MR imaging," *Magn Reson Med*, vol. 58, no. 6, pp. 1182–1195, 2007.

[13] S. Becker, J. Bobin, and E. J. Candès, "NESTA: A fast and accurate first-order method for sparse recovery," *SIAM J Imaging Sci*, vol. 4, no. 1, pp. 1–39, 2011.

[14] M. Uecker, P. Lai, M. J. Murphy, P. Virtue, M. Elad, J. M. Pauly, S. S. Vasanawala, and M. Lustig, "ESPIRiT - an eigenvalue approach to autocalibrating parallel MRI: where SENSE meets GRAPPA," *Magn Reson Med*, vol. 71, no. 3, pp. 990–1001, 2014.

[15] M. Lustig, D. L. Donoho, J. M. Santos, and J. M. Pauly, "Compressed Sensing MRI," *IEEE signal processing magazine*, vol. 25, no. 2, p. 72, 2008.

[16] H. S. Chrysikopoulos, "Clinical MR imaging and physics," *Verlag Berlin Heidelberg: Springer*, 2009.

[17] D. W. McRobbie, E. A. Moore, M. J. Graves, and M. R. Prince, *MRI from Picture to Proton*. Cambridge university press, 2017.

[18] R. H. Hashemi, W. G. Bradley, and C. J. Lisanti, *MRI: The Basics*. Lippincott Williams & Wilkins, 2012.

[19] L. Schröder and C. Faber, *In vivo NMR Imaging*. Springer, 2011.

[20] F. Bloch, "Nuclear induction," *Physical review*, vol. 70, no. 7-8, p. 460, 1946.

[21] D. Moratal, A. Valles-Luch, L. Martí-Bonmatí, and M. E. Brummer, "k-space tutorial: an MRI educational tool for a better understanding of k-space," *Biomedical imaging and intervention journal*, vol. 4, no. 1, 2008.

[22] R. Mezrich, "A perspective on K-space.," *Radiology*, vol. 195, no. 2, pp. 297–315, 1995.

[23] K. P. Pruessmann, M. Weiger, P. Börnert, and P. Boesiger, "Advances in sensitivity encoding with arbitrary k-space trajectories," *Magn Reson Med*, vol. 46, no. 4, pp. 638–651, 2001.

[24] G. B. Chavhan, P. S. Babyn, B. G. Jankharia, H.-L. M. Cheng, and M. M. Shroff, "Steady-state MR imaging sequences: physics, classification, and clinical applications," *Radiographics*, vol. 28, no. 4, pp. 1147–1160, 2008.

[25] T. Foo, A. M. Sawyer, W. H. Faulkner, and D. G. Mills, "Inversion in the steady state: contrast optimization and reduced imaging time with fast three-dimensional inversion-recovery-prepared GRE pulse sequences.," *Radiology*, vol. 191, no. 1, pp. 85–90, 1994.

[26] P. Kellman, A. H. Aletras, C. Mancini, E. R. McVeigh, and A. E. Arai, "T2-prepared SSFP improves diagnostic confidence in edema imaging in acute myocardial infarction compared to turbo spin echo," *Magn Reson Med*, vol. 57, no. 5, pp. 891–897, 2007.

[27] P. Montant, M. Sigovan, D. Revel, and P. Douek, "MR imaging assessment of myocardial edema with T2 mapping," *Diagnostic and interventional imaging*, vol. 96, no. 9, pp. 885–890, 2015.

[28] J. H. Brittain, B. S. Hu, G. A. Wright, C. H. Meyer, A. Macovski, and D. G. Nishimura, "Coronary angiography with magnetization-prepared T2 contrast," *Magn Reson Med*, vol. 33, no. 5, pp. 689–696, 1995.

[29] R. M. Botnar, M. Stuber, P. G. Danias, K. V. Kissinger, and W. J. Manning, "Improved coronary artery definition with T2-weighted, free-breathing, three-dimensional coronary MRA," *Circulation*, vol. 99, no. 24, pp. 3139–3148, 1999.

[30] M. Blaimer, F. Breuer, M. Mueller, R. M. Heidemann, M. A. Griswold, and P. M. Jakob, "SMASH, SENSE, PILS, GRAPPA: how to choose the optimal method," *Top Magn Reson Imaging*, vol. 15, no. 4, pp. 223–236, 2004.

[31] M. A. Brown and R. C. Semelka, *MRI: basic principles and applications*. John Wiley & Sons, 2011.

[32] M. J. Graves and D. G. Mitchell, "Body MRI artifacts in clinical practice: a physicist's and radiologist's perspective," *J Magn Reson Imaging*, vol. 38, no. 2, pp. 269–287, 2013.

[33] K. Krupa and M. Bekiesińska-Figatowska, "Artifacts in magnetic resonance imaging," *Polish journal of radiology*, vol. 80, p. 93, 2015.

[34] K. T. Block, M. Uecker, and J. Frahm, "Suppression of MRI truncation artifacts using total variation constrained data extrapolation," *International journal of biomedical imaging*, vol. 2008, 2008.

[35] D. A. Feinberg, J. D. Hale, J. C. Watts, L. Kaufman, and A. Mark, "Halving mr imaging time by conjugation: demonstration at 3.5 kg.," *Radiology*, vol. 161, no. 2, pp. 527–531, 1986.

[36] K. G. Hollingsworth, "Reducing acquisition time in clinical mri by data undersampling and compressed sensing reconstruction," *Physics in Medicine & Biology*, vol. 60, no. 21, p. R297, 2015.

[37] A. Baert, *Parallel imaging in clinical MR applications*. Springer Science & Business Media, 2007.

[38] G. Schultz, *Magnetic resonance imaging with nonlinear gradient fields: signal encoding and image reconstruction*. Springer Science & Business Media, 2013.

[39] R. M. Heidemann, M. A. Griswold, A. Haase, and P. M. Jakob, "VD-AUTO-SMASH imaging," *Magn Reson Med*, vol. 45, no. 6, pp. 1066–1074, 2001.

[40] S. Aja-Fernández, G. Vegas-Sánchez-Ferrero, and A. Tristán-Vega, "Noise estimation in parallel MRI: GRAPPA and SENSE," *Magn Reson Imaging*, vol. 32, no. 3, pp. 281–290, 2014.

[41] M. Blaimer, F. A. Breuer, N. Seiberlich, M. F. Mueller, R. M. Heidemann, V. Jellus, G. Wiggins, L. L. Wald, M. A. Griswold, and P. M. Jakob, "Accelerated volumetric MRI with a SENSE/GRAPPA combination," *J Magn Reson Imaging*, vol. 24, no. 2, pp. 444–450, 2006.

[42] P. M. Jakob, M. A. Grisowld, R. R. Edelman, and D. K. Sodickson, "AUTO-SMASH: a self-calibrating technique for SMASH imaging," *MAGMA*, vol. 7, no. 1, pp. 42–54, 1998.

[43] M. A. Griswold, P. M. Jakob, M. Nittka, J. W. Goldfarb, and A. Haase, "Partially parallel imaging with localized sensitivities (PILS)," *Magn Reson Med*, vol. 44, no. 4, pp. 602–609, 2000.

[44] D. L. Donoho, "Compressed sensing," *IEEE Trans Inf Theory*, vol. 52, no. 4, pp. 1289–1306, 2006.

[45] E. J. Candès and M. B. Wakin, "An introduction to compressive sampling [a sensing/sampling paradigm that goes against the common knowledge in data acquisition]," *IEEE signal processing magazine*, vol. 25, no. 2, pp. 21–30, 2008.

[46] K. G. Hollingsworth, D. M. Higgins, M. McCallum, L. Ward, A. Coombs, and V. Straub, "Investigating the quantitative fidelity of prospectively undersampled chemical shift imaging in muscular dystrophy with compressed sensing and parallel imaging reconstruction," *Magn Reson Med*, vol. 72, no. 6, pp. 1610–1619, 2014.

[47] M. V. Zibetti and A. R. De Pierro, "Separate magnitude and phase regularization in MRI with incomplete data: Preliminary results," in *2010 IEEE International Symposium on Biomedical Imaging: From Nano to Macro*, pp. 736–739, IEEE, 2010.

[48] F. Zhao, D. C. Noll, J.-F. Nielsen, and J. A. Fessler, "Separate magnitude and phase regularization via compressed sensing," *IEEE Trans Med Imaging*, vol. 31, no. 9, pp. 1713–1723, 2012.

[49] W. Guo, J. Qin, and W. Yin, "A new detail-preserving regularization scheme," *SIAM J Imaging Sci*, vol. 7, no. 2, pp. 1309–1334, 2014.

[50] X. Qu, X. Cao, D. Guo, C. Hu, and Z. Chen, "Combined sparsifying transforms for compressed sensing MRI," *Electronics letters*, vol. 46, no. 2, pp. 121–123, 2010.

[51] R. Otazo and D. Sodickson, "Adaptive compressed sensing MRI," in *Proc Intl Soc Mag Reson Med*, p. #4867, 2010.

[52] S. Ravishankar and Y. Bresler, "MR image reconstruction from highly undersampled k-space data by dictionary learning," *IEEE Trans Med Imaging*, vol. 30, no. 5, pp. 1028–1041, 2011.

[53] H. Lu, J. Wei, Q. Liu, Y. Wang, and X. Deng, "A dictionary learning method with total generalized variation for MRI reconstruction," *International journal of biomedical imaging*, vol. 2016, 2016.

[54] S. G. Lingala, E. DiBella, and M. Jacob, "Deformation corrected compressed sensing (DC-CS): a novel framework for accelerated dynamic MRI," *IEEE Trans Med Imaging*, vol. 34, no. 1, pp. 72–85, 2015.

[55] R. Otazo, E. Candès, and D. K. Sodickson, "Low-rank plus sparse matrix decomposition for accelerated dynamic MRI with separation of background and dynamic components," *Magn Reson Med*, vol. 73, no. 3, pp. 1125–1136, 2015.

[56] M. Murphy, K. Keutzer, S. Vasanawala, and M. Lustig, "Clinically feasible reconstruction time for L1-SPIRiT parallel imaging and compressed sensing MRI," in *Proc Intl Soc Mag Reson Med*, p. #4854, 2010.

[57] Y. Zhou, Y. Chang, D. Liang, and L. Ying, "kt CSPI: A dynamic MRI reconstruction framework for combining compressed sensing and parallel imaging," in *2012 9th IEEE International Symposium on Biomedical Imaging (ISBI)*, pp. 410–413, IEEE, 2012.

[58] I. Y. Chun, B. Adcock, and T. M. Talavage, "Efficient compressed sensing SENSE parallel MRI reconstruction with joint sparsity promotion and mutual incoherence enhancement," in *2014 36th Annual International Conference of the IEEE Engineering in Medicine and Biology Society*, pp. 2424–2427, IEEE, 2014.

[59] M. Symms, H. Jäger, K. Schmierer, and T. Yousry, "A review of structural magnetic resonance neuroimaging," *Journal of Neurology, Neurosurgery & Psychiatry*, vol. 75, no. 9, pp. 1235–1244, 2004.

[60] E. Gong, F. Huang, K. Ying, W. Wu, S. Wang, and C. Yuan, "PROMISE: Parallel-imaging and compressed-sensing reconstruction of multicontrast imaging using SharablE information," *Magn Reson Med*, vol. 73, no. 2, pp. 523–535, 2015.

[61] L. Nürnberger, R.-M. Gracien, P. Hok, S.-M. Hof, U. Rüb, H. Steinmetz, R. Hilker, J. C. Klein, R. Deichmann, and S. Baudrexel, "Longitudinal changes of cortical microstructure in Parkinson's disease assessed with T1 relaxometry," *NeuroImage: Clinical*, vol. 13, pp. 405–414, 2017.

[62] M. J. Knight, A. Wearn, E. Coulthard, and R. A. Kauppinen, "T2 relaxometry and diffusion tensor indices of the hippocampus and entorhinal cortex improve sensitivity and specificity of MRI to detect amnestic mild cognitive impairment and Alzheimer's disease dementia," *Journal of Magnetic Resonance Imaging*, vol. 49, no. 2, pp. 445–455, 2019.

[63] U. W. Kaunzner and S. A. Gauthier, "Mri in the assessment and monitoring of multiple sclerosis: an update on best practice," *Therapeutic advances in neurological disorders*, vol. 10, no. 6, pp. 247–261, 2017.

[64] A. R. Martin, B. De Leener, J. Cohen-Adad, S. Kalsi-Ryan, D. W. Cadotte, J. R. Wilson, L. Tetreault, A. Nouri, A. Crawley, D. J. Mikulis, *et al.*, "Monitoring for myelopathic progression with multiparametric quantitative mri," *PloS one*, vol. 13, no. 4, p. e0195733, 2018.

[65] A. Fatemi, M. Bart Morris, M. R. Kanakamedala, S. Taghizadeh, and S. Vijayakumar, "Multiparametric quantitative mri as a metric for radiation treatment planning," *Nov Appro in Can Study*, vol. 1, no. 1, pp. 8–15, 2017.

[66] E. S. Kooreman, P. J. van Houdt, M. E. Nowee, V. W. van Pelt, R. H. Tijssen, E. S. Paulson, O. J. Gurney-Champion, J. Wang, F. Koetsveld, L. D. van Buuren, *et al.*, "Feasibility and accuracy of quantitative imaging on a 1.5 t mr-linear accelerator," *Radiotherapy and Oncology*, vol. 133, pp. 156–162, 2019.

[67] P. S. Tofts, "Chapter 1 - Concepts: Measurement and MR," in *Quantitative MRI of the Brain : Measuring Changes Caused by Disease*, pp. 3–16, Wiley, 2004.

[68] M. Syka, J. Keller, J. Klempíř, A. M. Rulseh, J. Roth, R. Jech, I. Vorisek, and J. Vymazal, "Correlation between relaxometry and diffusion tensor imaging in the globus pallidus of Huntingtons disease patients," *PloS one*, vol. 10, no. 3, p. e0118907, 2015.

[69] R. A. Pessini, A. C. d. Santos, and C. E. G. Salmon, "Quantitative mri data in multiple sclerosis patients: a pattern recognition study," *Research on Biomedical Engineering*, vol. 34, no. 2, pp. 138–146, 2018.

[70] X. Li, W. Huang, E. A. Morris, L. A. Tudorica, V. E. Seshan, W. D. Rooney, I. Tagge, Y. Wang, J. Xu, and C. S. Springer, "Dynamic nmr effects in breast cancer dynamic-contrast-enhanced mri," *Proceedings of the National Academy of Sciences*, vol. 105, no. 46, pp. 17937–17942, 2008.

[71] J. West, J. Warntjes, and P. Lundberg, "Novel whole brain segmentation and volume estimation using quantitative mri," *European radiology*, vol. 22, no. 5, pp. 998–1007, 2012.

[72] J. West, I. Blystad, M. Engström, J. B. Warntjes, and P. Lundberg, "Application of quantitative mri for brain tissue segmentation at 1.5 t and 3.0 t field strengths," *PloS one*, vol. 8, no. 9, p. e74795, 2013.

[73] S. Lorio, S. Fresard, S. Adaszewski, F. Kherif, R. Chowdhury, R. S. Frackowiak, J. Ashburner, G. Helms, N. Weiskopf, A. Lutti, *et al.*, "New tissue priors for improved automated classification of subcortical brain structures on mri," *Neuroimage*, vol. 130, pp. 157–166, 2016.

[74] H. Alizai, W. Virayavanich, G. B. Joseph, L. Nardo, F. Liu, H. Liebl, M. C. Nevitt, J. A. Lynch, C. E. McCulloch, and T. M. Link, "Cartilage lesion score: comparison of a quantitative assessment score with established semiquantitative mr scoring systems," *Radiology*, vol. 271, no. 2, pp. 479–487, 2014.

[75] S. J. Matzat, J. van Tiel, G. E. Gold, and E. H. Oei, "Quantitative mri techniques of cartilage composition," *Quantitative imaging in medicine and surgery*, vol. 3, no. 3, p. 162, 2013.

[76] S. C. Deoni, B. K. Rutt, and T. M. Peters, "Rapid combined T1 and T2 mapping using gradient recalled acquisition in the steady state," *Magn Reson Med*, vol. 49, no. 3, pp. 515–526, 2003.

[77] R. Tongdee, V. Narra, E. Oliveira, W. Chapman, K. Elsayes, and J. Brown, "Utility of 3D magnetic resonance imaging in preoperative evaluation of hepatobiliary diseases," *HPB*, vol. 8, no. 4, pp. 311–317, 2006.

[78] Y. I. Sheline, "3D MRI studies of neuroanatomic changes in unipolar major depression: the role of stress and medical comorbidity," *Biol Psychiatry*, vol. 48, no. 8, pp. 791–800, 2000.

[79] J. Fluckiger, B. Allen, K. Caldock, M. Markl, and J. Schneider, "Compressed sensing accelerated 4d-flow mri in the murine aorta," *Journal of Cardiovascular Magnetic Resonance*, vol. 15, no. S1, p. W37, 2013.

[80] Y. Tao, G. Rilling, M. Davies, and I. Marshall, "Carotid blood flow measurement accelerated by compressed sensing: validation in healthy volunteers," *Magn Reson Imaging*, vol. 31, no. 9, pp. 1485–1491, 2013.

[81] A. Cristobal-Huerta, D. Poot, M. Vogel, G. Krestin, and J. Hernandez-Tamames, "Compressed sensing 3d-grase for faster high-resolution mri," *Magnetic resonance in medicine*, vol. 82, no. 3, pp. 984–999, 2019.

[82] M. R. Espagnet, L. Bangiyev, M. Haber, K. Block, J. Babb, V. Ruggiero, F. Boada, O. Gonen, and G. Fatterpekar, "High-resolution dce-mri of the pituitary gland using radial k-space acquisition with compressed sensing reconstruction," *American Journal of Neuroradiology*, vol. 36, no. 8, pp. 1444–1449, 2015.

[83] C. Pierpaoli, "Quantitative brain MRI," *Top Magn Reson Imaging*, vol. 21, no. 2, p. 63, 2010.

[84] F. C. Schmeel, "Variability in quantitative diffusion-weighted mr imaging (dwi) across different scanners and imaging sites: is there a potential consensus that can help reducing the limits of expected bias?," 2019.

[85] S. B. Reeder and C. B. Sirlin, "Quantification of liver fat with magnetic resonance imaging," *Magnetic Resonance Imaging Clinics*, vol. 18, no. 3, pp. 337–357, 2010.

[86] R. Metere, T. Kober, H. E. Möller, and A. Schäfer, "Simultaneous quantitative mri mapping of t1, t2* and magnetic susceptibility with multi-echo mp2rage," *PloS one*, vol. 12, no. 1, p. e0169265, 2017.

[87] J. Warntjes, O. Dahlqvist, and P. Lundberg, "Novel method for rapid, simultaneous T1, T2*, and proton density quantification," *Magn Reson Med*, vol. 57, no. 3, pp. 528–537, 2007.

[88] S. C. Deoni, "Quantitative relaxometry of the brain," *Top Magn Reson Imaging*, vol. 21, no. 2, pp. 101–113, 2010.

[89] K. J. Chang and H. Jara, "Applications of quantitative t1, t2, and proton density to diagnosis.," *Applied radiology*, vol. 34, 2005.

[90] J. Sanz, G. LaRocca, and J. G. Mirelis, "Myocardial mapping with cardiac magnetic resonance: The diagnostic value of novel sequences," *Revista Española de Cardiología (English Edition)*, vol. 69, no. 9, pp. 849–861, 2016.

[91] K. T. Block, M. Uecker, and J. Frahm, "Model-based iterative reconstruction for radial fast spin-echo MRI," *IEEE Trans Med Imaging*, vol. 28, no. 11, pp. 1759–1769, 2009.

[92] T. J. Sumpf, M. Uecker, S. Boretius, and J. Frahm, "Model-based nonlinear inverse reconstruction for T2 mapping using highly undersampled spin-echo MRI," *J Magn Reson Imaging*, vol. 34, no. 2, pp. 420–428, 2011.

[93] M. Doneva, P. Börnert, H. Eggers, C. Stehning, J. Sénégas, and A. Mertins, "Compressed sensing reconstruction for magnetic resonance parameter mapping," *Magn Reson Med*, vol. 64, no. 4, pp. 1114–1120, 2010.

[94] D. Ma, V. Gulani, N. Seiberlich, K. Liu, J. L. Sunshine, J. L. Duerk, and M. A. Griswold, "Magnetic resonance fingerprinting," *Nature*, vol. 495, no. 7440, pp. 187–192, 2013.

[95] Y. Jiang, D. Ma, N. Seiberlich, V. Gulani, and M. A. Griswold, "MR fingerprinting using fast imaging with steady state precession (FISP) with spiral readout," *Magn Reson Med*, vol. 74, no. 6, pp. 1621–1631, 2015.

[96] J. I. Hamilton, Y. Jiang, Y. Chen, D. Ma, W.-C. Lo, M. Griswold, and N. Seiberlich, "MR fingerprinting for rapid quantification of myocardial T1, T2, and proton spin density," *Magn Reson Med*, vol. 77, no. 4, pp. 1446–1458, 2017.

[97] S. Coppo, B. B. Mehta, D. McGivney, D. Ma, Y. Chen, Y. Jiang, J. Hamilton, S. Pahwa, C. Badve, N. Seiberlich, *et al.*, "Overview of magnetic resonance fingerprinting," *MAGNETOM FLASH*, vol. 65, 2016.

[98] A. Panda, B. B. Mehta, S. Coppo, Y. Jiang, D. Ma, N. Seiberlich, M. A. Griswold, and V. Gulani, "Magnetic resonance fingerprinting–an overview," *Current opinion in biomedical engineering*, vol. 3, pp. 56–66, 2017.

[99] M. Davies, G. Puy, P. Vandergheynst, and Y. Wiaux, "Compressed quantitative MRI: Bloch response recovery through iterated projection," in *Acoustics, Speech and Signal Processing (ICASSP), 2014 IEEE International Conference on*, pp. 6899–6903, IEEE, 2014.

[100] M. Davies, G. Puy, P. Vandergheynst, and Y. Wiaux, "A compressed sensing framework for magnetic resonance fingerprinting," *SIAM J Imaging Sci*, vol. 7, no. 4, pp. 2623–2656, 2014.

[101] J. Assländer, M. A. Cloos, F. Knoll, D. K. Sodickson, J. Hennig, and R. Lattanzi, "Low rank alternating direction method of multipliers reconstruction for MR fingerprinting," *Magn Reson Med*, vol. 79, no. 1, pp. 83–96, 2018.

[102] P. A. Gomez, G. Buonincontri, M. Molina-Romero, J. I. Sperl, M. I. Menzel, and B. H. Menze, "Accelerated parameter mapping with compressed sensing: an alternative to MR fingerprinting," in *Proc Intl Soc Mag Reson Med*, p. #1167, 2017.

[103] J. Assländer, S. J. Glaser, and J. Hennig, "Pseudo steady-state free precession for MR-fingerprinting," *Magn Reson Med*, vol. 77, no. 3, pp. 1151–1161, 2017.

[104] B. Rieger, F. Zimmer, J. Zapp, S. Weingärtner, and L. R. Schad, "Magnetic resonance fingerprinting using echo-planar imaging: Joint quantification of T1 and $T2^*$ relaxation times," *Magn Reson Med*, vol. 78, pp. 1724–1733, 2016.

[105] P. Su, D. Mao, P. Liu, Y. Li, M. C. Pinho, B. G. Welch, and H. Lu, "Multiparametric estimation of brain hemodynamics with MR fingerprinting ASL," *Magn Reson Med*, vol. 78, no. 5, pp. 1812–1823, 2017.

[106] K. T. Block and J. Frahm, "Spiral imaging: a critical appraisal," *J Magn Reson Imaging*, vol. 21, no. 6, pp. 657–668, 2005.

[107] J. H. Lee, B. A. Hargreaves, B. S. Hu, and D. G. Nishimura, "Fast 3D imaging using variable-density spiral trajectories with applications to limb perfusion," *Magn Reson Med*, vol. 50, no. 6, pp. 1276–1285, 2003.

[108] G. H. Glover and A. T. Lee, "Motion artifacts in fMRI: comparison of 2DFT with PR and spiral scan methods," *Magn Reson Med*, vol. 33, no. 5, pp. 624–635, 1995.

[109] P. Gatehouse and D. Firmin, "Flow distortion and signal loss in spiral imaging," *Magn Reson Med*, vol. 41, no. 5, pp. 1023–1031, 1999.

[110] D. G. Nishimura, P. Irarrazabal, and C. H. Meyer, "A velocity k-space analysis of flow effects in echo-planar and spiral imaging," *Magn Reson Med*, vol. 33, no. 4, pp. 549–556, 1995.

[111] G. Cruz, T. Schneider, T. Bruijnen, A. S. Gaspar, R. M. Botnar, and C. Prieto, "Accelerated magnetic resonance fingerprinting using soft-weighted key-hole (MRF-SOHO)," *PLOS One*, vol. 13, no. 8, p. e0201808, 2018.

[112] K. Koolstra, J.-W. M. Beenakker, P. Koken, A. Webb, and P. Börnert, "Cartesian MR fingerprinting in the eye at 7T using compressed sensing and matrix completion-based reconstructions," *Magn Reson Med*, vol. 81, no. 4, pp. 2551–2565, 2019.

[113] O. Cohen, M. Sarracanie, M. S. Rosen, and J. L. Ackerman, "In Vivo Optimized Fast MR Fingerprinting in the Human Brain," in *Proc Intl Soc Mag Reson Med*, p. #430, 2016.

[114] C. R. Wyatt, J. Grinstead, and A. Guimaraes, "In Vivo T1 and T2 Mapping using Single-Shot EPI Fingerprinting," in *Proc Intl Soc Mag Reson Med*, p. #3895, 2017.

[115] M. Weigel, S. Schwenk, V. Kiselev, K. Scheffler, and J. Hennig, "Extended phase graphs with anisotropic diffusion," *J Magn Reson*, vol. 205, no. 2, pp. 276–285, 2010.

[116] M. Weigel, "Extended phase graphs: dephasing, RF pulses, and echoes-pure and simple," *J Magn Reson Imaging*, vol. 41, no. 2, pp. 266–295, 2015.

[117] T. Christen, N. Pannetier, W. W. Ni, D. Qiu, M. E. Moseley, N. Schuff, and G. Zaharchuk, "MR vascular fingerprinting: a new approach to compute cerebral blood volume, mean vessel radius, and oxygenation maps in the human brain," *Neuroimage*, vol. 89, pp. 262–270, 2014.

[118] D. F. McGivney, E. Pierre, D. Ma, Y. Jiang, H. Saybasili, V. Gulani, and M. A. Griswold, "SVD compression for magnetic resonance fingerprinting in the time domain," *IEEE Trans Med Imaging*, vol. 33, no. 12, pp. 2311–2322, 2014.

[119] C. C. Cline, X. Chen, B. Mailhe, Q. Wang, J. Pfeuffer, M. Nittka, M. A. Griswold, P. Speier, and M. S. Nadar, "AIR-MRF: accelerated iterative reconstruction for magnetic resonance fingerprinting," *Magn Reson Imaging*, vol. 41, pp. 29–40, 2017.

[120] M. Golbabaee, Z. Chen, Y. Wiaux, and M. E. Davies, "Cover tree compressed sensing for fast MR fingerprint recovery," in *2017 IEEE 27th International Workshop on Machine Learning for Signal Processing (MLSP)*, pp. 1–6, 2017.

[121] S. F. Cauley, K. Setsompop, D. Ma, Y. Jiang, H. Ye, E. Adalsteinsson, M. A. Griswold, and L. L. Wald, "Fast group matching for MR fingerprinting reconstruction," *Magn Reson Med*, vol. 74, no. 2, pp. 523–528, 2015.

[122] C. Badve, A. Yu, M. Rogers, D. Ma, Y. Liu, M. Schluchter, J. Sunshine, M. Griswold, and V. Gulani, "Simultaneous T1 and T2 brain relaxometry in asymptomatic volunteers using magnetic resonance fingerprinting," *Tomography*, vol. 1, no. 2, p. 136, 2015.

[123] C. Badve, A. Yu, S. Dastmalchian, M. Rogers, D. Ma, Y. Jiang, S. Margevicius, S. Pahwa, Z. Lu, M. Schluchter, *et al.*, "MR fingerprinting of adult brain tumors: initial experience," *Am J Neuroradiol*, vol. 38, no. 3, pp. 492–499, 2017.

[124] D. Ma, Y. Jiang, Y. Chen, D. McGivney, B. Mehta, V. Gulani, and M. Griswold, "Fast 3D magnetic resonance fingerprinting for a whole-brain coverage," *Magn Reson Med*, vol. 79, no. 4, pp. 2190–2197, 2018.

[125] C. Liao, B. Bilgic, M. K. Manhard, B. Zhao, X. Cao, J. Zhong, L. L. Wald, and K. Setsompop, "3D MR fingerprinting with accelerated stack-of-spirals and hybrid sliding-window and GRAPPA reconstruction," *Neuroimage*, vol. 162, pp. 13–22, 2017.

[126] A. C. Yu, C. Badve, L. E. Ponsky, S. Pahwa, S. Dastmalchian, M. Rogers, Y. Jiang, S. Margevicius, M. Schluchter, W. Tabayoyong, *et al.*, "Development of a combined MR fingerprinting and diffusion examination for prostate cancer," *Radiology*, vol. 283, no. 3, pp. 729–738, 2017.

[127] Y. Chen, Y. Jiang, S. Pahwa, D. Ma, L. Lu, M. D. Twieg, K. L. Wright, N. Seiberlich, M. A. Griswold, and V. Gulani, "MR fingerprinting for rapid quantitative abdominal imaging," *Radiology*, vol. 279, no. 1, pp. 278–286, 2016.

[128] M. A. Cloos, F. Knoll, T. Zhao, K. T. Block, M. Bruno, G. C. Wiggins, and D. K. Sodickson, "Multiparametric imaging with heterogeneous radiofrequency fields," *Nat Commun*, vol. 7, pp. 1–10, 2016.

[129] N. A. Pannetier, M. Sohlin, T. Christen, L. Schad, and N. Schuff, "Numerical modeling of susceptibility-related MR signal dephasing with vessel size measurement: Phantom validation at 3T," *Magn Reson Med*, vol. 72, no. 3, pp. 646–658, 2014.

[130] R. Tibshirani, "Regression shrinkage and selection via the lasso," *Journal of the Royal Statistical Society: Series B (Methodological)*, vol. 58, no. 1, pp. 267–288, 1996.

[131] I. Daubechies, M. Defrise, and C. De Mol, "An iterative thresholding algorithm for linear inverse problems with a sparsity constraint," *Communications on Pure and Applied Mathematics: A Journal Issued by the Courant Institute of Mathematical Sciences*, vol. 57, no. 11, pp. 1413–1457, 2004.

[132] A. Beck and M. Teboulle, "A fast iterative shrinkage-thresholding algorithm for linear inverse problems," *SIAM J Imaging Sci*, vol. 2, no. 1, pp. 183–202, 2009.

[133] J. Yang and Y. Zhang, "Alternating direction algorithms for $\ell 1$-problems in compressive sensing," *SIAM journal on scientific computing*, vol. 33, no. 1, pp. 250–278, 2011.

[134] D. L. Donoho, A. Maleki, and A. Montanari, "Message-passing algorithms for compressed sensing," *Proceedings of the National Academy of Sciences*, vol. 106, no. 45, pp. 18914–18919, 2009.

[135] L. M. Brègman, "Finding the common point of convex sets by the method of successive projection," in *Doklady Akademii Nauk*, vol. 162, pp. 487–490, Russian Academy of Sciences, 1965.

[136] D. C. Youla and H. Webb, "Image Restoration by the Method of Convex Projections," *IEEE transactions on medical imaging*, vol. 1, no. 2, pp. 81–94, 1982.

[137] M. Murphy, M. Alley, J. Demmel, K. Keutzer, S. Vasanawala, and M. Lustig, "Fast ℓ1-SPIRIT Compressed Sensing Parallel Imaging MRI: Scalable Parallel Implementation and Clinically Feasible Runtime," *IEEE Trans Med Imaging*, vol. 31, no. 6, pp. 1250–1262, 2012.

[138] G. Rath and A. Sahoo, "A comparative study of some greedy pursuit algorithms for sparse approximation," in *2009 17th European Signal Processing Conference*, pp. 398–402, IEEE, 2009.

[139] S. G. Mallat and Z. Zhang, "Matching pursuits with time-frequency dictionaries," *IEEE Transactions on signal processing*, vol. 41, no. 12, pp. 3397–3415, 1993.

[140] Y. C. Pati, R. Rezaiifar, and P. S. Krishnaprasad, "Orthogonal matching pursuit: Recursive function approximation with applications to wavelet decomposition," in *Proceedings of 27th Asilomar conference on signals, systems and computers*, pp. 40–44, IEEE, 1993.

[141] S. Chen, S. A. Billings, and W. Luo, "Orthogonal least squares methods and their application to non-linear system identification," *International Journal of control*, vol. 50, no. 5, pp. 1873–1896, 1989.

[142] T. Blumensath and M. E. Davies, "Iterative hard thresholding for compressed sensing," *Appl Comput Harmon Anal*, vol. 27, no. 3, pp. 265 – 274, 2009.

[143] T. Blumensath and M. E. Davies, "Gradient pursuits," *IEEE Transactions on Signal Processing*, vol. 56, no. 6, pp. 2370–2382, 2008.

[144] T. Blumensath, M. E. Davies, G. Rilling, Y. Eldar, and G. Kutyniok, "Greedy algorithms for compressed sensing," in *Compressed sensing: theory and applications*, pp. 348–393, Cambridge Univ. Press, 2012.

[145] L. Landweber, "An iteration formula for Fredholm integral equations of the first kind," *American journal of mathematics*, vol. 73, no. 3, pp. 615–624, 1951.

[146] E. J. Candes, J. K. Romberg, and T. Tao, "Stable signal recovery from incomplete and inaccurate measurements," *Communications on pure and applied mathematics*, vol. 59, no. 8, pp. 1207–1223, 2006.

[147] S. S. Vasanawala, M. T. Alley, B. A. Hargreaves, R. A. Barth, J. M. Pauly, and M. Lustig, "Improved pediatric MR imaging with compressed sensing," *Radiology*, vol. 256, no. 2, pp. 607–616, 2010.

[148] T. Zhang, S. Chowdhury, M. Lustig, R. A. Barth, M. T. Alley, T. Grafendorfer, P. D. Calderon, F. J. Robb, J. M. Pauly, and S. S. Vasanawala, "Clinical performance of contrast enhanced abdominal pediatric MRI with fast combined parallel imaging compressed sensing reconstruction," *J Magn Reson Imaging*, vol. 40, no. 1, pp. 13–25, 2014.

[149] S. Rapacchi, F. Han, Y. Natsuaki, R. Kroeker, A. Plotnik, E. Lehrman, J. Sayre, G. Laub, J. P. Finn, and P. Hu, "High spatial and temporal resolution dynamic contrast-enhanced magnetic resonance angiography using compressed sensing with magnitude image subtraction," *Magn Reson Med*, vol. 71, no. 5, pp. 1771–1783, 2014.

[150] U. Tariq, A. Hsiao, M. Alley, T. Zhang, M. Lustig, and S. S. Vasanawala, "Venous and arterial flow quantification are equally accurate and precise with parallel imaging compressed sensing 4d phase contrast mri," *J Magn Reson Imaging*, vol. 37, no. 6, pp. 1419–1426, 2013.

[151] A. Hsiao, M. Lustig, M. T. Alley, M. Murphy, F. P. Chan, R. J. Herfkens, and S. S. Vasanawala, "Rapid pediatric cardiac assessment of flow and ventricular volume with compressed sensing parallel imaging volumetric cine phase-contrast mri," *American Journal of Roentgenology*, vol. 198, no. 3, pp. W250–W259, 2012.

[152] O. N. Jaspan, R. Fleysher, and M. L. Lipton, "Compressed sensing MRI: a review of the clinical literature," *The British journal of radiology*, vol. 88, no. 1056, p. 20150487, 2015.

[153] H. Wang, Y. Miao, K. Zhou, Y. Yu, S. Bao, Q. He, Y. Dai, S. Y. Xuan, B. Tarabishy, Y. Ye, *et al.*, "Feasibility of high temporal resolution breast dce-mri using compressed sensing theory," *Medical physics*, vol. 37, no. 9, pp. 4971–4981, 2010.

[154] S. D. Sharma, C. L. Fong, B. S. Tzung, M. Law, and K. S. Nayak, "Clinical image quality assessment of accelerated magnetic resonance neuroimaging using compressed sensing," *Investigative radiology*, vol. 48, no. 9, pp. 638–645, 2013.

[155] P. W. Worters, K. Sung, K. J. Stevens, K. M. Koch, and B. A. Hargreaves, "Compressed-sensing multispectral imaging of the postoperative spine," *J Magn Reson Imaging*, vol. 37, no. 1, pp. 243–248, 2013.

[156] I. Marshall, G. Rilling, Y. Tao, C. Du, S. Varma, D. Job, A. Farall, and M. Davies, "Radiological and quantitative assessment of Compressed Sensing reconstruction of undersampled 3D brain images," in *Proc Intl Soc Mag Reson Med*, p. #2497, 2015.

[157] F. Knoll, C. Clason, C. Diwoky, and R. Stollberger, "Adapted random sampling patterns for accelerated mri," *MAGMA*, vol. 24, no. 1, pp. 43–50, 2011.

[158] S. Vasanawala, M. Murphy, M. T. Alley, P. Lai, K. Keutzer, J. M. Pauly, and M. Lustig, "Practical parallel imaging compressed sensing MRI: Summary of two years of experience in accelerating body MRI of pediatric patients," in *2011 IEEE International Symposium on Biomedical Imaging: From nano to macro*, pp. 1039–1043, 2011.

[159] E. Levine, B. Daniel, S. Vasanawala, B. Hargreaves, and M. Saranathan, "3d cartesian mri with compressed sensing and variable view sharing using complementary poisson-disc sampling," *Magn Reson Med*, vol. 77, no. 5, pp. 1774–1785, 2017.

[160] M. Lustig, M. Alley, S. Vasanawala, D. Donoho, and J. Pauly, "Autocalibrating parallel imaging compressed sensing using $\ell 1$-SPIRiT with Poisson-Disc sampling and joint sparsity constraints," in *ISMRM Workshop on Data Sampling and Image Reconstruction*, pp. 25–28, 2009.

[161] M. Jones, R. Frayne, and R. M. Lebel, "Image quality impact of randomized sampling trajectories in MRI: Implications for compressed sensing," in *Proc Intl Soc Mag Reson Med*, p. #1424, 2017.

[162] O. Cohen and J. R. Polimeni, "Optimized inversion-time schedules for quantitative t1 measurements based on high-resolution multi-inversion epi," *Magn Reson Med*, vol. 79, no. 4, pp. 2101–2112, 2018.

[163] P. Tsialios, M. Thrippleton, and C. Pernet, "Evaluation of mri sequences for quantitative t1 brain mapping," *BioRxiv*, p. 195859, 2017.

[164] M. del C. Valdés Hernández, A. Glatz, A. J. Kiker, D. A. Dickie, B. S. Aribisala, N. A. Royle, S. Muñoz Maniega, M. E. Bastin, I. J. Deary, and J. M. Wardlaw, "Differentiation of calcified regions and iron deposits in the ageing brain on conventional structural mr images," *Journal of Magnetic Resonance Imaging*, vol. 40, no. 2, pp. 324–333, 2014.

[165] R. A. Jones, S. Palasis, and J. D. Grattan-Smith, "Mri of the neonatal brain: optimization of spin-echo parameters," *American Journal of Roentgenology*, vol. 182, no. 2, pp. 367–372, 2004.

[166] P. Hou, K. M. Hasan, C. W. Sitton, J. S. Wolinsky, and P. A. Narayana, "Phase-sensitive t1 inversion recovery imaging: a time-efficient interleaved technique for improved tissue contrast in neuroimaging," *Am J Neuroradiol*, vol. 26, no. 6, pp. 1432–1438, 2005.

[167] J.-S. Han, K.-R. Dong, W.-K. Chung, J.-H. Cho, J.-W. Shin, and Y.-J. Kim, "Quantitative analysis of t1 weighted images due to change in ti by using the inversion recovery in 3.0 t brain mri examination," *Journal of Magnetics*, vol. 17, no. 2, pp. 158–162, 2012.

[168] M. Nazarpoor, "The effect of inversion times on the minimum signal intensity of the contrast agent concentration using inversion recovery t1-weighted fast imaging sequence," *Medical journal of the Islamic Republic of Iran*, vol. 28, p. 128, 2014.

[169] P. A. Bottomley, T. H. Foster, R. E. Argersinger, and L. M. Pfeifer, "A review of normal tissue hydrogen nmr relaxation times and relaxation mechanisms from 1–100 mhz: dependence on tissue type, nmr frequency, temperature, species, excision, and age," *Medical physics*, vol. 11, no. 4, pp. 425–448, 1984.

[170] A. J. V. Benjamin, W. Bano, G. Mair, M. Davies, and I. Marshall, "Sampling order optimization preserves contrast and improves clinical diagnostic utility of accelerated prospective 3D brain MRI: a radiological assessment study on healthy volunteers," in *Proc Intl Soc Mag Reson Med*, p. #3189, 2018.

[171] Z. Wang, A. C. Bovik, H. R. Sheikh, E. P. Simoncelli, *et al.*, "Image quality assessment: from error visibility to structural similarity," *IEEE transactions on image processing*, vol. 13, no. 4, pp. 600–612, 2004.

[172] N. Venkatanath, D. Praneeth, M. C. Bh, S. S. Channappayya, and S. S. Medasani, "Blind image quality evaluation using perception based features," in *2015 Twenty First National Conference on Communications (NCC)*, pp. 1–6, IEEE, 2015.

[173] B. Girod, "What's wrong with mean-squared error?," *Digital images and human vision*, pp. 207–220, 1993.

[174] A. M. Eskicioglu and P. S. Fisher, "Image quality measures and their performance," *IEEE Transactions on communications*, vol. 43, no. 12, pp. 2959–2965, 1995.

[175] M. P. Eckert and A. P. Bradley, "Perceptual quality metrics applied to still image compression," *Signal processing*, vol. 70, no. 3, pp. 177–200, 1998.

[176] L. W. Mann, D. M. Higgins, C. N. Peters, S. Cassidy, K. K. Hodson, A. Coombs, R. Taylor, and K. G. Hollingsworth, "Accelerating mr imaging liver steatosis measurement using combined compressed sensing and parallel imaging: a quantitative evaluation," *Radiology*, vol. 278, no. 1, pp. 247–256, 2015.

[177] C. Lazarus, P. Weiss, A. Vignaud, and P. Ciuciu, "An empirical study of the maximum degree of undersampling in compressed sensing for t2*-weighted mri," *Magnetic resonance imaging*, vol. 53, pp. 112–122, 2018.

[178] K. Khare, C. J. Hardy, K. F. King, P. A. Turski, and L. Marinelli, "Accelerated mr imaging using compressive sensing with no free parameters," *Magnetic Resonance in Medicine*, vol. 68, no. 5, pp. 1450–1457, 2012.

[179] S. Ramani, Z. Liu, J. Rosen, J.-F. Nielsen, and J. A. Fessler, "Regularization parameter selection for nonlinear iterative image restoration and mri reconstruction using gcv and sure-based methods," *IEEE Transactions on Image Processing*, vol. 21, no. 8, pp. 3659–3672, 2012.

[180] R. Otazo, D. Kim, L. Axel, and D. K. Sodickson, "Combination of compressed sensing and parallel imaging for highly accelerated first-pass cardiac perfusion MRI," *Magn Reson Med*, vol. 64, no. 3, pp. 767–776, 2010.

[181] K. H. Jin, D. Lee, and J. C. Ye, "A general framework for compressed sensing and parallel MRI using annihilating filter based low-rank Hankel matrix," *IEEE Transactions on Computational Imaging*, vol. 2, no. 4, pp. 480–495, 2016.

[182] E. Milshteyn and X. Zhang, "The Need and Initial Practice of Parallel Imaging and Compressed Sensing in Hyperpolarized 13C MRI in vivo," *OMICS journal of radiology*, vol. 4, no. 4, 2015.

[183] M. Kayvanrad, A. Lin, R. Joshi, J. Chiu, and T. Peters, "Diagnostic quality assessment of compressed sensing accelerated magnetic resonance neuroimaging," *J Magn Reson Imaging*, vol. 44, no. 2, pp. 433–444, 2016.

[184] S. Sirin, S. L. Goericke, B. M. Huening, A. Stein, S. Kinner, U. Felderhoff-Mueser, and B. Schweiger, "Evaluation of 100 brain examinations using a 3 Tesla MR-compatible incubatorsafety, handling, and image quality," *Neuroradiology*, vol. 55, no. 10, pp. 1241–1249, 2013.

[185] A. J. V. Benjamin, W. Bano, G. Mair, G. Thompson, M. Davies, and I. Marshall, "The clinical condition to be assessed by radiological assessment significantly influences the radiological scores of compressed sensing accelerated 3d brain mri," in *Proc Intl Soc Mag Reson Med*, p. #2992, 2018.

[186] B. M. Ellingson, M. Bendszus, J. Boxerman, D. Barboriak, B. J. Erickson, M. Smits, S. J. Nelson, E. Gerstner, B. Alexander, G. Goldmacher, *et al.*, "Consensus recommendations for a standardized brain tumor imaging protocol in clinical trials," *Neuro-oncology*, vol. 17, no. 9, pp. 1188–1198, 2015.

[187] A. J. V. Benjamin, P. A. Gómez, M. Golbabaee, Z. Mahbub, T. Sprenger, M. I. Menzel, M. Davies, and I. Marshall, "Multi-shot Echo Planar Imaging for accelerated Cartesian MR Fingerprinting: An alternative to conventional spiral MR Fingerprinting," *Magn Reson Imaging*, vol. 61, pp. 20–32, 2019.

[188] H. Vrenken, J. J. Geurts, D. L. Knol, L. N. van Dijk, V. Dattola, B. Jasperse, R. A. van Schijndel, C. H. Polman, J. A. Castelijns, and F. Barkhof, "Whole-brain t1 mapping in multiple sclerosis: global changes of normal-appearing gray and white matter," *Radiology*, vol. 240, no. 3, pp. 811–820, 2006.

[189] E. Canu, D. G. McLaren, M. E. Fitzgerald, B. B. Bendlin, G. Zoccatelli, F. Alessandrini, F. B. Pizzini, G. K. Ricciardi, A. Beltramello, and S. C. Johnson, "Mapping the structural brain changes in Alzheimer's disease: the independent contribution of two imaging modalities," *J Alzheimers Dis*, vol. 26, no. s3, pp. 263–274, 2011.

[190] V. M. Ferreira, S. K. Piechnik, E. Dall'Armellina, T. D. Karamitsos, J. M. Francis, R. P. Choudhury, M. G. Friedrich, M. D. Robson, and S. Neubauer, "Non-contrast T1-mapping detects acute myocardial edema with high diagnostic accuracy: a comparison to T2-weighted cardiovascular magnetic resonance," *J Cardiovasc Magn Reson*, vol. 14, no. 1, pp. 42–53, 2012.

[191] S. Hofer, X. Wang, V. Roeloffs, and J. Frahm, "Single-shot T1 mapping of the corpus callosum: a rapid characterization of fiber bundle anatomy," *Front Neuroanat*, vol. 9, pp. 1–6, 2015.

[192] M. J. Knight, B. McCann, D. Tsivos, S. Dillon, E. Coulthard, and R. A. Kauppinen, "Quantitative T2 mapping of white matter: applications for ageing and cognitive decline," *Phys Med Biol*, vol. 61, no. 15, pp. 5587–5605, 2016.

[193] D. Verhaert, P. Thavendiranathan, S. Giri, G. Mihai, S. Rajagopalan, O. P. Simonetti, and S. V. Raman, "Direct T2 quantification of myocardial edema in acute ischemic injury," *JACC: Cardiovascular Imaging*, vol. 4, no. 3, pp. 269–278, 2011.

[194] H. Nishioka, E. Nakamura, J. Hirose, N. Okamoto, S. Yamabe, and H. Mizuta, "MRI T1ρ and T2 mapping for the assessment of articular cartilage changes in patients with medial knee osteoarthritis after hemicallotasis osteotomy," *Bone Joint Res*, vol. 5, no. 7, pp. 294–300, 2016.

[195] A. Watrin-Pinzano, J.-P. Ruaud, Y. Cheli, P. Gonord, L. Grossin, P. Gillet, A. Blum, E. Payan, P. Olivier, and G. Guillot, "T2 mapping: an efficient MR quantitative technique to evaluate spontaneous cartilage repair in rat patella1," *Osteoarthr Cartil*, vol. 12, no. 3, pp. 191–200, 2004.

[196] M. Salerno and C. M. Kramer, "Advances in parametric mapping with CMR imaging," *JACC: Cardiovascular imaging*, vol. 6, no. 7, pp. 806–822, 2013.

[197] J. Warntjes, O. D. Leinhard, J. West, and P. Lundberg, "Rapid magnetic resonance quantification on the brain: optimization for clinical usage," *Magn Reson Med*, vol. 60, no. 2, pp. 320–329, 2008.

[198] G. Buonincontri and S. J. Sawiak, "MR fingerprinting with simultaneous B1 estimation," *Magn Reson Med*, vol. 76, no. 4, pp. 1127–1135, 2016.

[199] T. Hong, M. Kim, D. Han, and D. Kim, "Analysis of estimation error from system imperfection in mrf," in *Proc Intl Soc Mag Reson Med*, p. #437, 2016.

[200] M. Sarracanie, O. Cohen, and M. S. Rosen, "3D balanced-EPI magnetic resonance fingerprinting at 6.5 mT," in *Proc Intl Soc Mag Reson Med*, p. #3385, 2015.

[201] O. Cohen and M. S. Rosen, "Algorithm comparison for schedule optimization in MR fingerprinting," *Magn Reson Imaging*, vol. 41, pp. 15–21, 2017.

[202] M. A. Bernstein, K. F. King, and X. J. Zhou, "Chapter 16 - echo train pulse sequences," in *Handbook of MRI Pulse Sequences*, pp. 702 – 801, Academic Press, 2004.

[203] F. Farzaneh, S. J. Riederer, and N. J. Pelc, "Analysis of T2 limitations and off-resonance effects on spatial resolution and artifacts in echo-planar imaging," *Magn Reson Med*, vol. 14, no. 1, pp. 123–139, 1990.

[204] F. Hennel, "Multiple-shot echo-planar imaging," *Concepts Magn Reson Educ J*, vol. 9, no. 1, pp. 43–58, 1997.

[205] J. P. Wansapura, S. K. Holland, R. S. Dunn, and W. S. Ball, "NMR relaxation times in the human brain at 3.0 tesla," *J Magn Reson Imaging*, vol. 9, no. 4, pp. 531–538, 1999.

[206] T. Prasloski, B. Mädler, Q.-S. Xiang, A. MacKay, and C. Jones, "Applications of stimulated echo correction to multicomponent T2 analysis," *Magn Reson Med*, vol. 67, no. 6, pp. 1803–1814, 2012.

[207] C. L. Lankford, R. D. Dortch, and M. D. Does, "Fast T2 mapping with multiple echo, caesar cipher acquisition and model-based reconstruction," *Magn Reson Med*, vol. 73, no. 3, pp. 1065–1074, 2015.

[208] B. Zhao, K. Setsompop, E. Adalsteinsson, B. Gagoski, H. Ye, D. Ma, Y. Jiang, P. Ellen Grant, M. A. Griswold, and L. L. Wald, "Improved magnetic resonance fingerprinting reconstruction with low-rank and subspace modeling," *Magn Reson Med*, vol. 79, no. 2, pp. 933–942, 2018.

[209] D. L. Collins, A. P. Zijdenbos, V. Kollokian, J. G. Sled, N. J. Kabani, C. J. Holmes, and A. C. Evans, "Design and construction of a realistic digital brain phantom," *IEEE Trans Med Imaging*, vol. 17, no. 3, pp. 463–468, 1998.

[210] C. A. Cocosco, V. Kollokian, R. K.-S. Kwan, G. B. Pike, and A. C. Evans, "Brainweb: Online interface to a 3D MRI simulated brain database," in *NeuroImage*, Citeseer, 1997.

[211] D. Ma, S. Coppo, Y. Chen, D. F. McGivney, Y. Jiang, S. Pahwa, V. Gulani, and M. A. Griswold, "Slice profile and B1 corrections in 2D magnetic resonance fingerprinting," *Magn Reson Med*, vol. 78, no. 5, pp. 1781–1789, 2017.

[212] T. Hong, D. Han, M.-O. Kim, and D.-H. Kim, "RF slice profile effects in magnetic resonance fingerprinting," *Magn Reson Imaging*, vol. 41, pp. 73–79, 2017.

[213] S.-C. Chiu, T.-M. Lin, J.-M. Lin, H.-W. Chung, C.-W. Ko, M. Büchert, and M. Bock, "Effects of RF pulse profile and intra-voxel phase dispersion on MR fingerprinting with balanced SSFP readout," *Magn Reson Imaging*, vol. 41, pp. 80–86, 2017.

[214] Y. Jiang, D. Ma, K. E. Keenan, K. F. Stupic, V. Gulani, and M. A. Griswold, "Repeatability of magnetic resonance fingerprinting T1 and T2 estimates assessed using the ISMRM/NIST MRI system phantom," *Magn Reson Med*, vol. 78, no. 4, pp. 1452–1457, 2017.

[215] J. G. Sled and G. B. Pike, "Correction for B1 and B0 variations in quantitative T2 measurements using mri," *Magn Reson Med*, vol. 43, no. 4, pp. 589–593, 2000.

[216] N. Ben-Eliezer, D. K. Sodickson, and K. T. Block, "Rapid and accurate T2 mapping from multi–spin-echo data using bloch-simulation-based reconstruction," *Magn Reson Med*, vol. 73, no. 2, pp. 809–817, 2015.

[217] L. Czervionke, D. Daniels, F. Wehrli, L. Mark, L. Hendrix, J. Strandt, A. Williams, and V. Haughton, "Magnetic susceptibility artifacts in gradient-recalled echo MR imaging.," *Am J Neuroradiol*, vol. 9, no. 6, pp. 1149–1155, 1988.

[218] D. Holland, J. M. Kuperman, and A. M. Dale, "Efficient correction of inhomogeneous static magnetic field-induced distortion in Echo Planar Imaging," *Neuroimage*, vol. 50, no. 1, pp. 175–183, 2010.

[219] D. A. Feinberg and K. Oshio, "Phase errors in multi-shot echo planar imaging," *Magn Reson Med*, vol. 32, no. 4, pp. 535–539, 1994.

[220] J. Schlemper, J. Caballero, J. V. Hajnal, A. N. Price, and D. Rueckert, "A deep cascade of convolutional neural networks for dynamic MR image reconstruction," *IEEE Trans Med Imaging*, vol. 37, no. 2, pp. 491–503, 2017.

[221] M. Akçakaya, S. Moeller, S. Weingärtner, and K. Uğurbil, "Scan-specific robust artificial-neural-networks for k-space interpolation (RAKI) reconstruction: Database-free deep learning for fast imaging," *Magn Reson Med*, vol. 81, no. 1, pp. 439–453, 2019.

[222] C. M. Hyun, H. P. Kim, S. M. Lee, S. Lee, and J. K. Seo, "Deep learning for undersampled MRI reconstruction," *Physics in Medicine & Biology*, vol. 63, no. 13, p. 135007, 2018.

[223] M. Seitzer, G. Yang, J. Schlemper, O. Oktay, T. Würfl, V. Christlein, T. Wong, R. Mohiaddin, D. Firmin, J. Keegan, *et al.*, "Adversarial and perceptual refinement for compressed sensing MRI reconstruction," in *International Conference on Medical Image Computing and Computer-Assisted Intervention*, pp. 232–240, Springer, 2018.

[224] D. Jiang, W. Dou, L. Vosters, X. Xu, Y. Sun, and T. Tan, "Denoising of 3D magnetic resonance images with multi-channel residual learning of convolutional neural network," *Japanese journal of radiology*, vol. 36, no. 9, pp. 566–574, 2018.

[225] F. Pesapane, C. Volonté, M. Codari, and F. Sardanelli, "Artificial intelligence as a medical device in radiology: ethical and regulatory issues in europe and the united states," *Insights into imaging*, vol. 9, no. 5, pp. 745–753, 2018.